Geophysical Investigation of Coastal Roads Vulnerable to Erosion, Bay Bulls, Newfoundland and Labrador

by

Marzieh Arshian

Submitted to the School of Graduate Studies

In partial fulfillment of the requirements

For the degree of

Master of Science (Geophysics)

Department of Earth Sciences

Memorial University of Newfoundland

Fall 2023

St. John's, Newfoundland and Labrador

Abstract

In the town of Bay Bulls, on the east-facing coast of the Avalon Peninsula, Newfoundland, coastal roads run close to the steep, rocky shoreline on both sides of a deep bay. Three sections of road, each about 100 m in length, have been identified as vulnerable to erosional processes. To image the surface and subsurface structure in these three areas, two geophysical methods: ground penetrating radar (GPR), direct current resistivity/induced polarization (DCR/IP), and real-time kinetics global positioning system (RTK) were used. The primary aims of this study were to characterize the subsurface in these three vulnerable areas and to test the utility of the geophysical methods in identifying structural weaknesses.

On the north side of the bay, at "Bread and Cheese", the road dips down over a culverted creek in a highly fractured area. At "the Cliff", the road has been widened bay-ward with the use of a wooden retaining wall. "The Quays" is on the south side of the bay, where a narrow inlet with steep cliffs comes very close to the road. At all three sites, RTK data revealed locations where the road surface sloped bay-ward, suggesting undesirable creepage in the roadbed. Also, at all three sites, DCR data from deeper levels showed broad (10s of m) variations in the steeply dipping strata of the bedrock, possibly related to their ease of erosion. At Bread and Cheese, GPR showed depth to bedrock and the horizontal extent of the weaker, fractured region, while DCR measurements suggest the most fractured location is to the west of the culvert. At the Cliff, GPR profiles and 3D imaging identified the locations and lengths of wooden beams extending from the retaining wall under the widened road. At the eastern parts of the Quays, GPR identified shallow bedrock following the along-road topography of the road. To the west, the road appears to cover sediments.

Analysis of the geophysical data and geological information indicates that the hard bedrock and the shape and orientation of the bay mean that wave action is not a major factor affecting the stability of coastal roads and that the overland flow of water and groundwater is more of a concern at the three vulnerable sites.

Acknowledgments

I would like to take this opportunity to express my deep gratitude and appreciation to the individuals who have played a pivotal role in the completion of this thesis. Their unwavering support, guidance, and encouragement have been invaluable throughout this journey.

First and foremost, I would like to sincerely thank my supervisor, Dr. Alison Leitch. Her continuous support, guidance, and valuable insight have shaped this project's direction and success. Her exceptional compassion and patience not only facilitated my academic growth but also push me beyond my comfort zone.

I extend my heartfelt appreciation to my committee member, Dr. Colin Farquharson, for his time, dedication, and expertise. His insightful feedback and constructive criticism have been instrumental in improving my work and expanding my knowledge.

I am deeply grateful to Melanie Irvine for her valuable guidance and feedback on my thesis which greatly contributed to its improvement.

I would love to express my deep gratitude to Roberta Hicks and Masters's student Jason Sylvester for all of their commitment and hard work in the field by assisting me with the survey grid set-up and data collection.

I want to convey my profound appreciation to my examiners Dr. Chares Hurich and Prof. S. Christian Dupuis for their invaluable revisions that have significantly enhanced my thesis. Their contribution have been essential in evaluating the quality of my work, and I am thankful for their dedicated efforts.

Lastly, I want to express my heartfelt gratitude to my family, who have been a constant source of support and encouragement throughout this journey, even though they are physically distant. Their unwavering belief in me and their continued support has played a crucial role in my perseverance and drive to achieve the goals I had set for myself. Despite the challenges I faced as an international student, they have been my pillars of strength, motivating me to keep going. I am genuinely grateful for their love, understanding, and constant presence in my life.

Table of Contents

List of Figures

List of Tables

List of Appendices

1 Introduction

In this study, the primary aim is to determine the subsurface structure of coastal roads in three areas prone to erosion in the town of Bay Bulls, which is situated around a deep bay on the Avalon Peninsula, Newfoundland and Labrador (Figure 1-1and Figure 1-2). Three geophysical techniques were utilized, namely ground-penetrating radar (GPR), direct current resistivity (DCR), and induced polarization (IP). This study used Real Time Kinetics GPS (RTK) and also includes information based on geological and coastal geomorphological observations. This research pioneers geophysics studies in Newfoundland in the examination of erosion-impacting factors in Bay Bulls.

To address storm-water runoff, overland flow, and coastal erosion, the municipality of Bay Bulls recently established a Climate Adaptation Plan (Smith, 2019). Hydrologic and hydraulic models are being developed to assess infrastructure susceptible to storm-water in the town, emphasizing the effects of infrastructure development and climate change. There is high-resolution LiDAR (light detection and ranging) data available that provides an elevation map of the Bay Bulls coast and near-shore. Integrating hydrologic modeling and elevation maps provides crucial information about surface processes that may affect coastal erosion. However, subsurface vulnerability must also be determined to thoroughly assess the potential for erosion. Information about the subsurface can facilitate the development of long-term strategies to mitigate the effects of climate change, such as rising sea levels and severe storms.

This chapter describes the goals and motivations of the research. It provides reviews of previous studies conducted using similar methods, highlighting the existing knowledge gaps. A review of the topography, bedrock geology, and landforms of the region is presented to provide insights into the area's dynamics and evolution, and to help in the interpretation of geophysical models. Lastly, an overview of the thesis structure is provided, guiding readers through the organization and flow of the document.

Figure 1-1) Location map of Bay Bulls on the Avalon Peninsula.

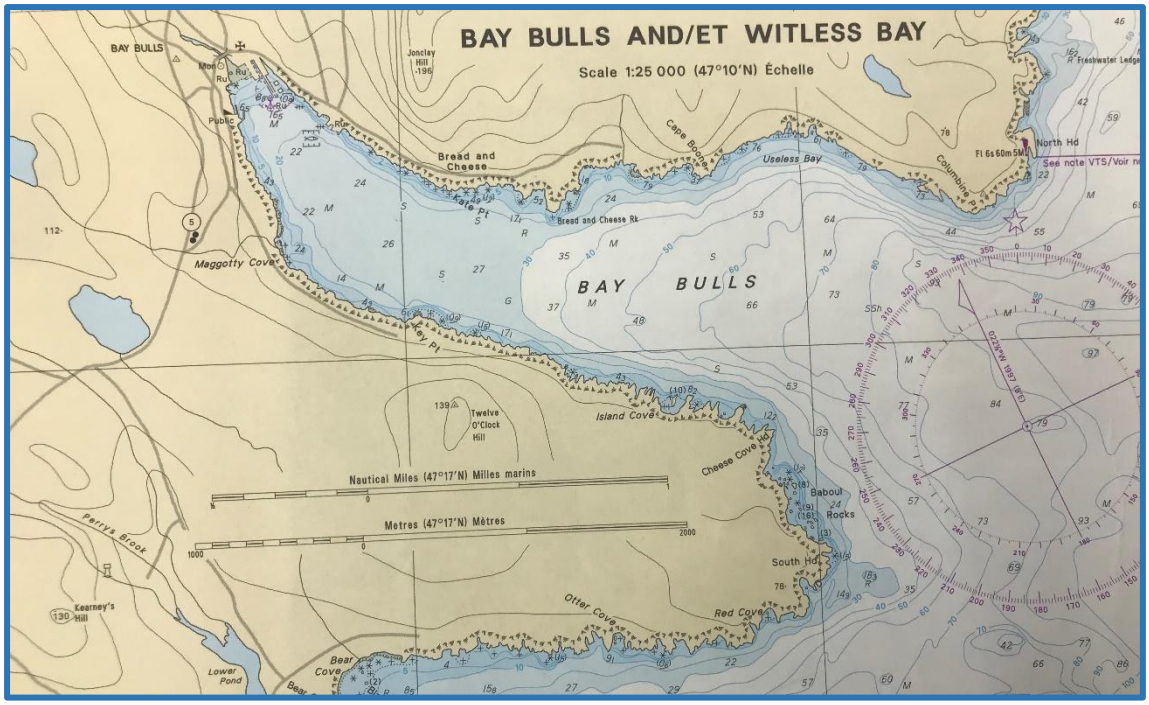

Figure 1-2) Bay Bulls bathymetry map (I-Boating : Free Marine Navigation Charts & Fishing Maps, n.d.)

1.1 Research Objectives

This study examines three sites in Bay Bulls where coastal roads are built on ground susceptible to erosion, which may have bedrock transitions, such as faults, concealed by Quaternary sediment (Figure 1-3). These sites are named: "Bread and Cheese," after a historic village; "Cliff," for the nearby terrain; and "Quays," after the road.

The study aims to address the following goals:

1. Identify the impacting variables and mechanism responsible for erosion/destabilization in three coastal areas in Bay Bulls.
2. Characterize the physical properties of the surface and subsurface of the road sections using the geophysical methods.
3. Evaluate and compare the effectiveness of the geophysical methods for recognizing areas subject to erosion in the three selected sites.
4. Utilize site observation and elevation data to provide valuable context and supplementary information to enhance the understanding of erosion process.

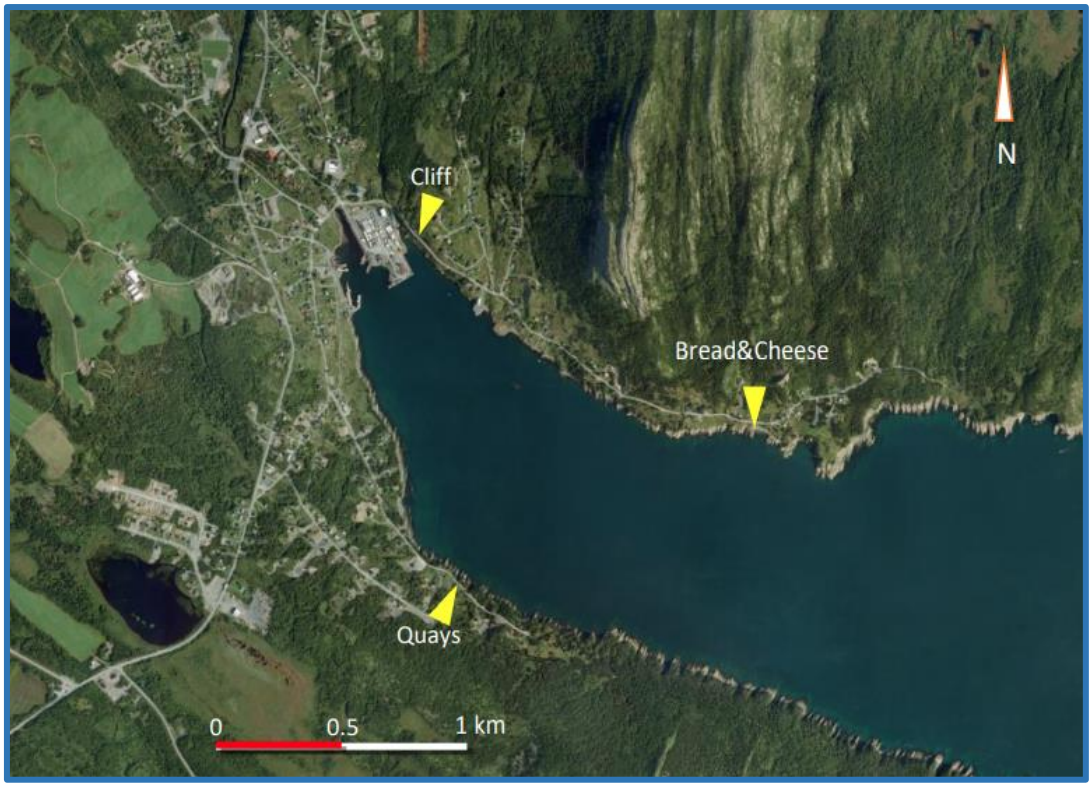

Figure 1-3) Air photo of Bay Bulls; the three study areas are depicted by the yellow arrows.

1.2 Literature Review

Coastal erosion is a problem in Newfoundland, and it is caused by a variety of natural and human-induced factors (to be discussed in the next chapter) which vary in their relative importance depending on local conditions.

Understanding these factors is crucial for developing effective management strategies to mitigate the impacts of erosion on coastal communities. To measure and evaluate the coastal process, a multidisciplinary approach is required, involving various fields such as oceanography, geology, climatology, meteorology, hydrology, geomorphology and geomatics. Many studies have been carried out to investigate the contributing factors in coastal erosion based on previously mentioned approaches, while only limited number of studies have been conducted utilizing the integration of geomorphology, geology, and geophysics methods. In this literature review, previous studies carried out on coastal erosion in Newfoundland and elsewhere will be discussed, along with those which used integrations of geophysics methods.

To understand the development of coastal cliffs, researchers can analyze the extent of their retreat over time. Pierre and Lahousse (2006) worked on the role of groundwater in the instability

of the soft chalk cliffs on the English Chanel. They described cliff retreat at Cap Blanc-Nez, France in relation to structural and topographic factors. Using highly accurate maps, the authors determined the amount of retreat depends on the mechanical behavior of the rock, which is controlled by the runoff-infiltration balance. They suggested that rainfall and piezometric surface data can help in understanding the stability of the cliff and managing risk.

According to Gatto (1995), freeze-thaw cycles cause sediment particles on slopes to undergo the process of frost heaving, destabilization, erosion, and redeposition. The extent of this process depends largely on the spacing of the joints, which determines the size of the rock fragments involved. Although the emphasis is on the importance of joint spacing as a key factor, the nature of the rock mass and particle size should not be overlooked in understanding the behaviour of sediment in such environments. The clasts heaved during this process become more susceptible to gravitational transport as they lose their shear strength. Rainfall, either overland or downslope flow, can also transport these particles. Furthermore, the combination of wind, wave action, and current can also affect the movement of these vulnerable clasts (Gatto, 1995).

Spooner et al. (2013) discussed deaths in Newfoundland coastal areas caused by mass movements, debris flows, rotational slumps, and rock falls. Matsuoka and Sakai (1999) investigated rock falls related to freeze-thaw cycles. Most rock falls that were not related to rainfall happened ten days after melt-out. Intense rainfall combined with freeze-thaw cycles can lead to more intense debris flows and rock falls.

Geomorphological studies of coastal erosion

In Newfoundland, researchers have made substantial progress in assessing the vulnerability of the coastline using geological and geomorphological methods. These studies are summarized here to provide broad background context to the present study.

One notable study on this topic was conducted by Catto (2011), who examined the Newfoundland coastline's sensitivity to erosion and petroleum contamination. Shoreline classification, short-term coastal erosion, longer-term factors of erosion, and sensitivity to sea-level rise are discussed. A combination of field observation, topographic survey, and remote sensing data was conducted to assess the vulnerability of the coastal communities in the province. Catto (2020) conducted a study about geomorphology and anthropogenic activity on the Avalon Peninsula, Newfoundland. The coastline is dominated by swash activity and reflective wave

conditions due to the coastal configuration and is marked by frequent storm activity. According to Catto (2020) the shapes of headlands are directly connected to the history of tectonic activity and the underlying geological structures. The landscape is characterized by bedrock erosional features due to repeated glaciation. Overall the region is a complex mixture of geological and biological process as well as human influences (Catto, 2020).

Another important study, conducted by Irvine (2015), was a coastal monitoring program at 112 coastal locations to identify areas vulnerable to coastal hazards and quantify rates of coastal change. The program began in 2011 and was built upon earlier work by the provincial and federal geological surveys. Fieldwork was conducted at 48 of 112 sites during 2014, and ongoing work will involve monitoring the sites at regular intervals to provide reliable estimates of coastal change and to identify areas vulnerable to erosion.

The program used RTK equipment to collect precise location data and establish transects to align survey markers perpendicular to the shoreline. Rates of coastal change vary, with certain areas displaying high rate of erosion due to factors such as wave action, groundwater flow, surface runoff and wind. Predicting coastal evolution is challenging, but the current erosion is likely to continue due to climate change projection and relative sea-level rise.

In 2018 Irvine used UAV data, together with control points precisely positioned using Real Time Kinetics GPS (RTK), to assess coastal erosion, terrain stability and flood-risk mapping in St. David's, Newfoundland. The photographs were processed to create point clouds, 3-D models, and orthophotos. The study identified a cliff top erosion rate of 52 cm between the years 2013 to 2017. Groundwater, surface water, and wind were identified as the main causes. The high-resolution data allowed for the computation of yearly erosion rate and the identification of erosional agents. The study also delineated areas prone to flooding, demonstrating the applicability of UAVs for measuring coastal change and mapping hazard-prone areas. These studies are all part of the same long-term coastal monitoring program.

Geophysical investigations of coastal processes

This study is one of the first to use geophysical techniques to assess coastal vulnerabilities in Newfoundland. One previous study is that by Kilfoil et al. (2018) on the west coast of Newfoundland, as part of the coastal monitoring program carried out by the Geological Survey of Newfoundland and Labrador. Direct Current Resistivity (DCR) and Ground Penetrating Radar

(GPR) were used to evaluate the usefulness of these technologies in delineating subsurface geology in the Daniel's Harbour and Parson's Pond areas on the Great Northern Peninsula (Figure 1-4). The GPR picks up the sloping interface between loose soil and sand and underlying more resistive and compact sand and gravel (Figure 1-4). The DCR images three distinct layers, including a deeper conductive layer of clay or shale that resulted in cliff instability in the region.

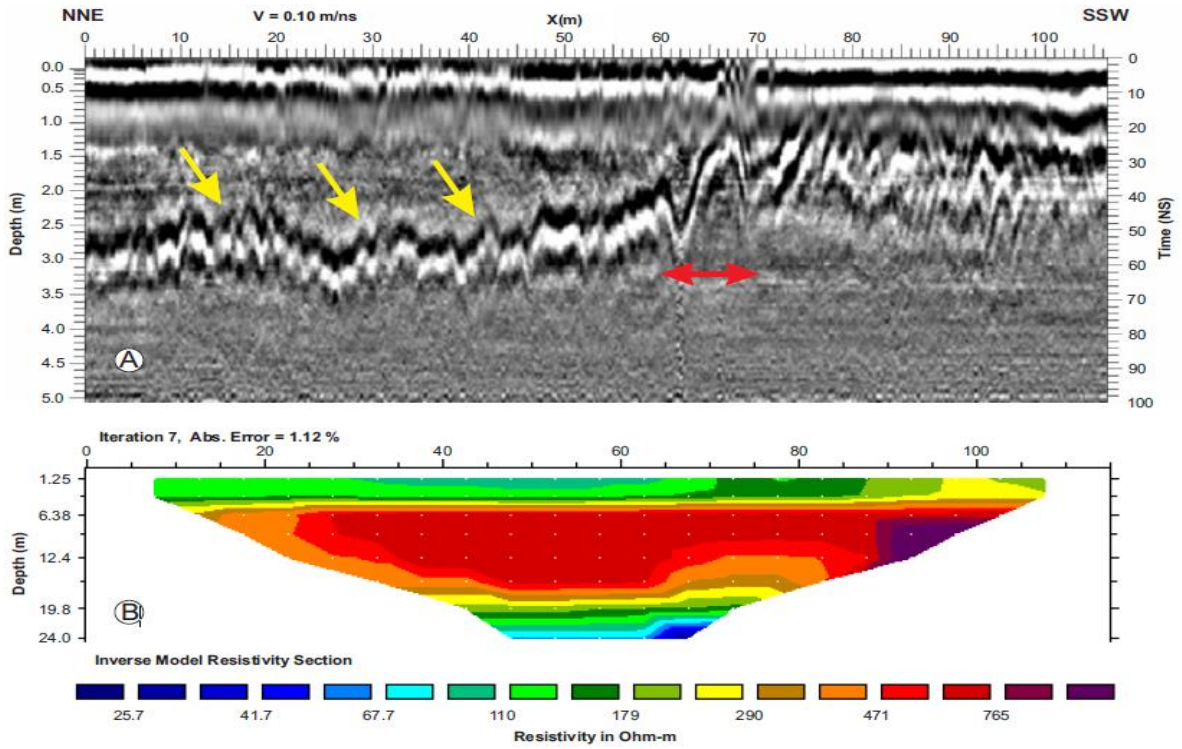

Figure 1-4) Geophysical sections from a profile in Parson's Pond, western Newfoundland (Kilfoil et al., 2018). (A) GPR. A wave velocity of 0.10m/ns was obtained from a hyperbola at the 2.5 m interface which is indicated by the yellow arrows. The red arrows show the location of a gully in the topography. (B) DCR. Inverted resistivity section.

Geophysical techniques have been used in other parts of the world to investigate the properties and vulnerabilities of coastlines.

Leucci (2006) carried out integrated geophysical, geological, and geomorphological surveys over the limestone Roca Cliffs in Lecce, Italy, to evaluate erosion. Geophysical surveys involving seismic refraction tomography, electrical resistivity tomography (ERT, another name for DCR), and ground penetrating radar (GPR) techniques were used to examine the physical and mechanical characteristics of the rock mass behind the cliff face. Stability evaluation was based on observations of the cliff morphology as well as on a structural study of the rock mass. Geophysical methods were also applied as geophysics can detect rock properties at depth while structural observations

are limited to surface or near-surface features. Geophysics also offers a three-dimensional view of the subsurface, allowing for a more comprehensive assessment. Geophysics is non-invasive and does not disturb the rock mass. Geophysics has the potential to enhance the overall comprehension of fracture distribution by supplementing structural observations.

For the electrical survey Leucci (2006) carried out three overlapping profiles using two array configurations (Figure 1-5b and Figure 1-5c). Dipole-Dipole was performed to obtain a resistivity image of buried features such as cavities. The Wenner configuration was used to acquire stratigraphic information. The result of ERT, illustrated in Figure 1-5 b and c, depict areas with high resistivity in the deep subsurface (A) corresponding to a fractured system with NW-SE alignment. The ERT, GPR, and seismic results were compared to integrate the results and to eliminate the inherent ambiguity of each method. The result of seismic refraction tomography, electrical resistivity tomography, and ground penetration radar showed velocity gradients and low-quality rock mass, high resistivity variations, and a fractured system. The GPR survey identified reflectors spatially correlated with the tops of near-vertical fractures identified from other methods. The data suggested the presence of a cliff-parallel fracture set that divided the cliff into two parts. The integrated analysis of geological, geomorphological, and geophysical data suggests the potential presence of a microfracture system and cavity beneath the Roca Cliffs.

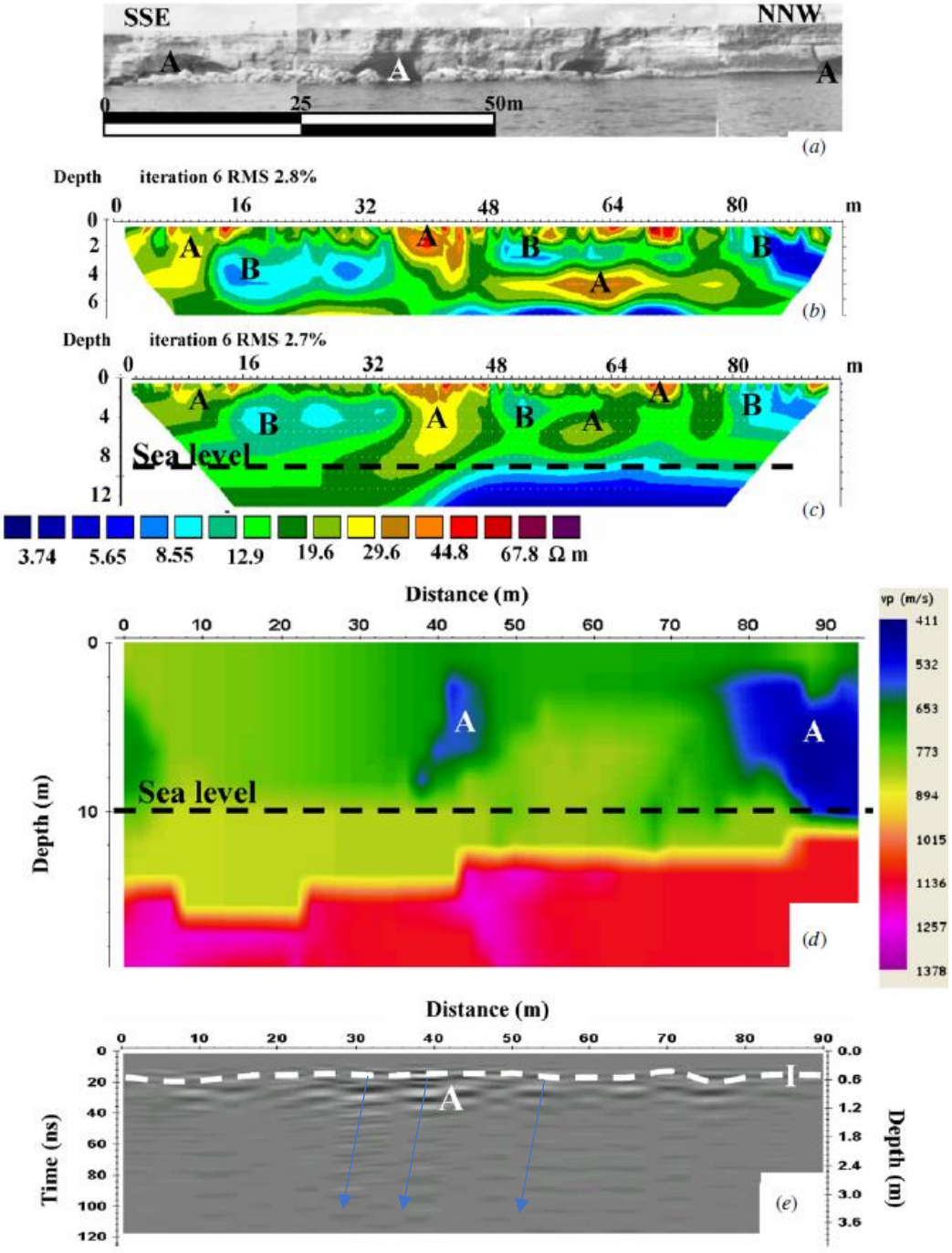

Figure 1-5) a) Photo of the Roca Cliff, b) resistivity model obtained using Dipole-Dipole array, the zones labeled A with a resistivity of 50 Ωm are likely to correspond to the presence of cavities filled with clay or salty water. Zones B with a resistivity less than 10 Ωm might be related to material soaked with salty water. c) Resistivity model obtained using Wenner array, d) Seismic wave velocity model, e) processed GPR section using a 100MHz antenna. Dashed line "I" was interpreted as horizon over a series of vertical open fractures (blue arrows) in this line. Feature A, corresponds to high amplitude anomalies in both resistivity and p-wave velocity (Leucci, 2006).

Margiotta et al. (2012) studied another coastal geophysical hazard (sinkholes) using geomorphology, geophysical and stratigraphy methods. This study outlines a methodology used to map vulnerability in coastal areas in the town of Casalabate, situated in the Apulia region in southern Italy. ERT and GPR were the geophysical methods that helped in the assessment of the sinkholes. ERT was carried out with different combinations of Dipole-Dipole and Wenner electrode configurations. The interpreted GPR data was combined with ERT and borehole results for more accurate interpretation (Margiotta et al., 2012).

These studies demonstrate the utility of Electrical Resistivity Tomography (ERT/DCR) (in particular using the Dipole-Dipole and Wenner array configurations) and Ground Penetrating Radar (GPR) in evaluating coastal hazards, over similar length scales and depths of investigation as the present study. Additionally, the studies emphasize the significance of integrating data with the geomorphological observations to enhance the accuracy of their interpretations. These factors encouraged the author to apply similar methodologies in the present study.

1.3 Study Area

1.3.1 Location

Bay Bulls is located along the Irish Loop scenic road on the east coast of the Avalon Peninsula, on the Southern Shore, Newfoundland and Labrador, Canada. It is situated 29 km south of the provincial capital St. John's (Figure 1-1) (Government of Canada, 2001).

The three sites of potential concern for coastal erosion are on roads built on steep slopes (Figure 1-3). Bread and Cheese site is located on Gunridge Road. The Cliff site is near the northwest end of Northside Road, where a wooden retaining wall was built when the road was widened westward over a steep slope. The Quays is the third site which is located approximately 70 m NE of Maggoty Cove on Quays Road, on the south side of Bay Bulls. In this location the road is close to a steep cliff face (Figure 1-3 and Figure 1-6).

1.3.2 History

Bay Bulls first appeared on a map in 1592, when it was utilized by the French, and provided an excellent area for early Atlantic convoys by 1635. It was used by English fish harvesters after fortification by Governor David Kirke in 1638, and it was attacked by Dutch Admiral De Ruyter

in 1665. During the Anglo-French struggle for Newfoundland's fisheries, the French attacked Bay Bulls in 1696, 1697 and 1762. In the last attack on September 29, 1796, French Admiral Richery burned Bay Bulls instead of St. John's, which he found too well-defended. During the 1800s, local fish businesses were introduced. During World War 2, when the facilities for repairing vessels in St. John's harbour became too crowded, Bay Bulls harbour was introduced as a second option. It is close to St. John's and has deep bathymetry. Smaller ships were constructed there to service the larger vessels in St. John's (Dohey, 2016).

Some of North America's oldest shipwrecks are found here. Subsequently, Bay Bulls grew into a local business center and shipping port (*History*, n.d.).

The population growth rate has increased from 1% between 2011 and 2016 to 4.4% between 2016 and 2021. In 2021 Bay Bulls had a population of 1,566 in a 30.60 km^2 land area (Government of Canada, 2001). This town also has seen an increase in residential housing. The population first settled in a linear pattern along Bay Bulls harbor and spread inland after the construction of roads and highways. Historically, Bay Bulls relied on the fishery as a source of income. However, the fishery has declined in recent years, and revenue is now largely dependent on tourism and servicing the offshore oil industry. Tourism has become a significant revenue source based on whale and bird watching as well as bed and breakfast places (*History*, n.d.).

Bay Bulls coastline’s historical importance combined with its maritime heritage, highlights its suitability for this study.

1.3.3 Topography

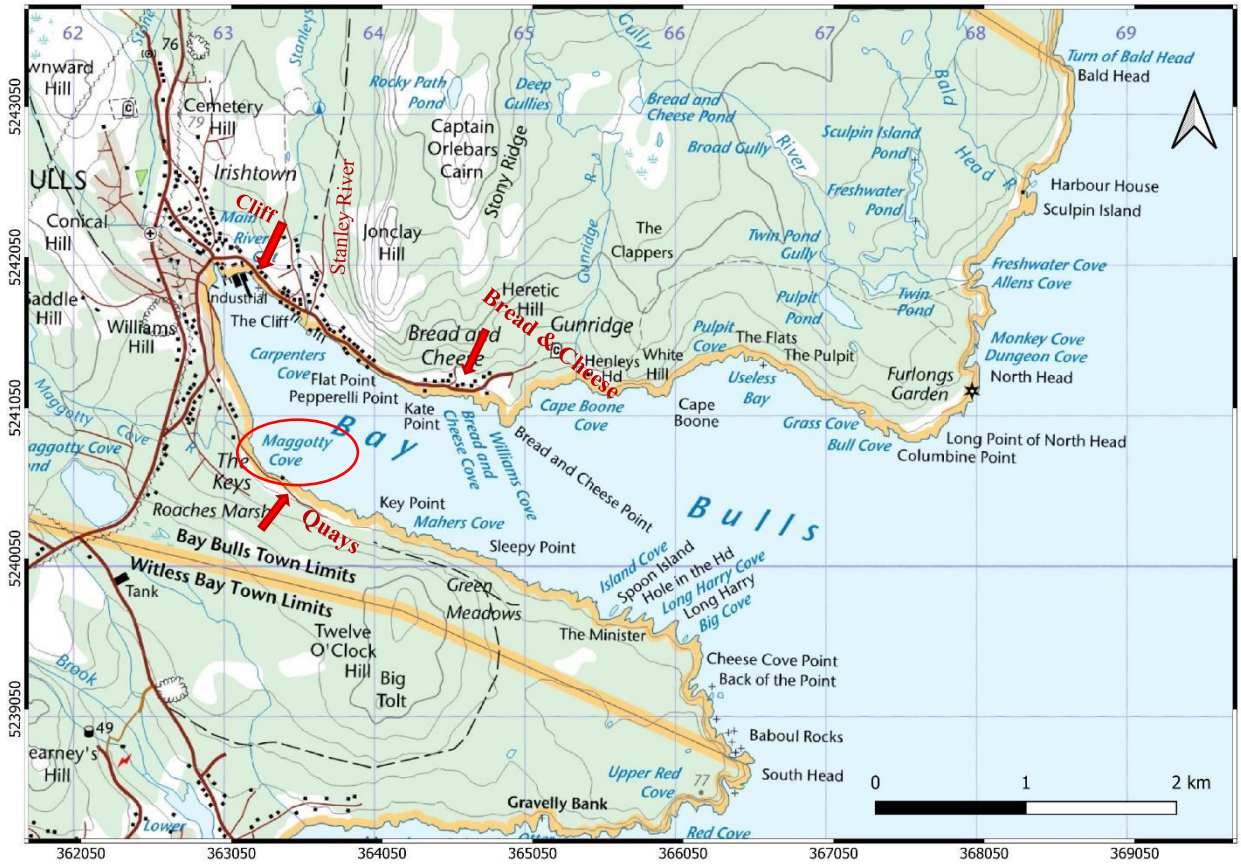

Figure 1-6) Topographic map of Bay Bulls, The grey contours are elevation contours at intervals of 20 m above sea level. Grid lines at 1 km intervals. Survey sites indicated by red arrows. NRCan- Canadian National Topography system (NTS) sheet.

Corresponding to the deep water bay (Figure 1-2), the topography of Bay Bulls includes the presence of high (around 10-20 m) and steep cliffs, in particular on the north side of the bay. Other features include headlands and inlets. Maggotty Cove River flows from Three Corner Pond, enters into the Ocean at Maggotty Cove located on the south side of Bay Bulls Harbour. Gunridge River flows into Cape Boone Cove, and Stanley River flows into Carpenter Cove near the old wharf on the north side (Figure 1-6).

The upland regions are undulating and hummocky. At the Cliff site, the hillside slopes on the northeast side are steep. Due to the steep, rocky slope to the northeast, fewer houses are close to the road compared to the Bread & Cheese site. Inland of the Quays site the land slopes at 10 degrees, less steep than on the northern side of the Bay. Quays road is very close to the cliff top here (less than 0.5 m) (Figure 1-6).

1.3.4 Bedrock Geology and Structure

Bay Bulls is underlain by the sedimentary rocks of the Signal Hill and St. John's Groups, which consist mainly of sandstones and siltstones (King, 1988) (Figure 1-7). The St. John's Group rocks are mainly dark shales exposed at the NW corner of the bay. The Signal Hill Group rocks are mainly sandstones. In the Gibbet Hill Formation, the lowest member of the Signal Hill Group, the rocks are broadly medium grained sandstones.

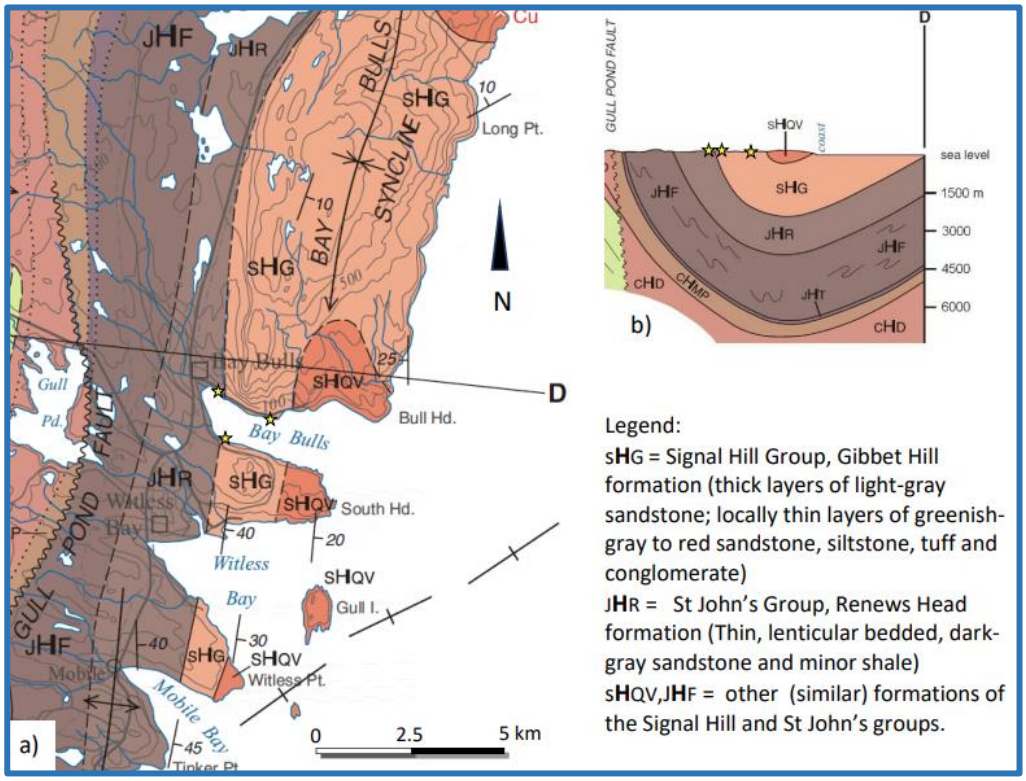

Figure 1-7) a) Bedrock geology of Bay Bulls region; b) cross-section from Gull Pond Fault (West) along profile D. Dashed and dotted lines indicate that boundaries are inferred, as their exact locations are hidden by vegetation and Quaternary sediment. The grey contours are elevation contours at intervals of 100 feet (about 30.5 m) above sea level (King, 1988).

The study site locations are on steep coastal cliffs, characterized by almost continuous bedrock exposure. Yellow stars in Figure 1-7 show the approximate locations of the key sites. The Cliff site is situated in the Renews Head Formation of the St. Johns Group. The Renews Head Formation is the youngest of three formations of the St. John's Group and is made up of thin, lenticular bedded, dark-grey sandstone, and minor shale. Shales and siltstones are prone to fracturing and are subject to erosion through freeze-thaw cycles. The Bread and Cheese site and the Quays are within the Gibbet Hill Formation of the Signal Hill Group, consisting of a thick layer of light gray sandstone

with locally thin greenish-gray to red sandstone bedding, argillite, tuff, and conglomerate (Figure 1-7).

Composition and rock types

Sandstones exhibit a wide range of strengths depending on variables such as porosity, grain composition, and cement type. Stronger sandstones contain stronger cement types and lower porosity. The strongest and most resilient sandstone form is silica cement, also called quartz cement. This particular variety of sandstone generally is formed from deposits in environments marked by transportation and reworking, such as beaches, marine bars, and sand dunes. Shale is typically less resistant to shear stress than sandstone, due to its smaller grain size (Wyllie, 2017). Thus, shale layers within sandstone may act as sliding surfaces. Water penetrating interbedded sandstone and shale can concentrate along the sandstone-shale contacts, further weakening the rock (Bell et al., 2007).

In a representative thin section from the Gibbet Hill Formation of the Signal Hill Group (Figure 1-8), there is an approximately bimodal distribution of grains (D. Lowe, pers. comm. 2022), with some larger sub-rounded grains (~0.5 mm,) of quartz and feldspar, and smaller grains (~150 microns) which are sub-angular. There are also a few small clasts of volcanic and sedimentary origin. The feldspars are altered and likely dominated by K feldspar, judging by the relatively few which show albite twinning. The sandstone is 'tight', i.e. compacted with no visible porosity. The rock is matrix poor, cemented with thin quartz overgrowths and a few patches of black material which may be clay and organics. Generally, the rock is clay poor. The Gibbet Hill sandstones, with low porosity and quartz cement, are relatively strong and resilient.

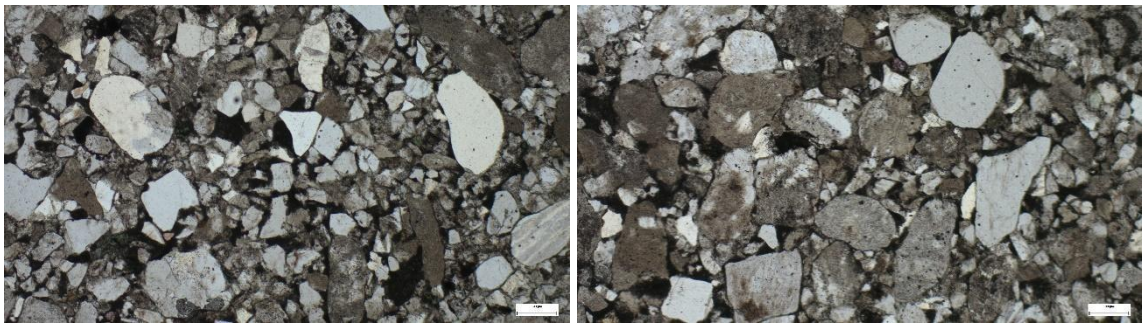

Figure 1-8) Photomicrographs from a thin representative section of the Gibbet Hill sandstone unit. The scale is 200µm (D. Lowe, with permission).

A significant structural feature is the Bay Bulls syncline, likely formed in the Devonian (D. Lowe, Memorial University, personal communication, 2022), with a fold axis running approximately parallel to the coast and with the eastern limb steeper than the western limb (Figure 1-5). The Renews Head Formation rocks, being much weaker than the Gibbet Hill Formation rocks due to higher shale content (Wyllie, 2017) took up most of the strain with small scale folds and offsets, so that the Gibbet Hill layers mostly deformed like an elastic beam.

As the thick sedimentary package of Gibbet Hill rocks bent, the layers separated along bedding planes (as required by geometry), often at contacts between layers with different grain sizes (Figure 1-9 and Figure 1-10). These contacts may be the locations of small amounts of shale or other weak minerals, in thin layers. These bedding parallel fractures thus have their origin in the tectonic forces which caused the syncline to form. Other fractures, at high angles to the bedding planes, may be related to bending forces near hinges (limits of elasticity) or to decompression.

A major set of fractures along bedding planes suggest that tectonic forces were involved in the fracturing. The sandstone layers are likely more porous to water and may help localize the fracture planes (Figure 1-10)

The layering and primary fracture planes in the bedrock dip to the north (Appendix A). This implies that overland and groundwater flow in the overlying Quaternary sediments is more effective than flow through the bedrock. Water seeping into these fractures, on the other hand, might enhance bedrock fracturing by frost wedging. Grass and tree roots within fractures (Figure 1-9, Figure A 3 to Figure A 9) would also promote break-up of rocky slopes. Slabs of rock spalled off the rock face may be observed at the bottom of outcrops (e.g. Figure 1-9), as can slickensides connected with their detachment.

Figure 1-9) Bedrock outcrop of Gibbet Hill Formation (363280 mE, 5241880 mN). Professor Norm Catto for scale.

Figure 1-10) Close-up of sandstone layers overlying a significant fracture. Above the sandstone layers is finer-grained argillite with less recognizable layering.

On the shoreline below the outcrop shown in Figure 1-9 and Figure 1-10, the rocks show a steeper slope to the north. Such variations in dip are not unusual. Along the road, there are also shifts in bedding orientation, including a shallow fold-over at a distance of around 100 m and shorter wavelength variations within it.

Because the folding pressures created weaknesses at 90° to the fold axes, Bay Bulls formed at 90° or normal to the general coastline. The structure does not appear to change across the bay from north to south. Measurements of strike and dip of the same bedding unit on both sides of the bay were the same (D. Lowe, pers. comm., 2022).

1.3.5 Landforms and Surficial Geology

A surficial geology map of Bay Bulls is shown in Figure 1-11. A key to the classification is provided in Table 1-1.

In Bay Bulls the source material is mainly rock (R), colluvial (C = coarse-grained material derived from bedrock) and glacial (T). The landforms are classified mainly as veneer (v, any deposit less than 1.5 m thick), often dissected and eroded (e) or concealed by vegetation (c). Fluvial sediments are generally derived from eroded glacial and glacio-fluvial deposits. Overall, the shoreline is flanked by steep cliffs and bedrock outcrops with veneers of coarse glacial sediments, subject to erosion by terrestrial and marine processes.

Bread and Cheese site surficial material consists of a veneer of glacially derived material, which is eroded and vegetated, covering bedrock (Tve/Rc). Surficial geology at the Quays site is similar.

The surface at the Cliff site, in contrast, is covered by vegetated colluvial material overlying eroded, glacially derived material (Cv/Te). In some locations along the road cut, bedrock is exposed. There are also large boulders derived from rock fall, covered by vegetation (Figure 2-22).

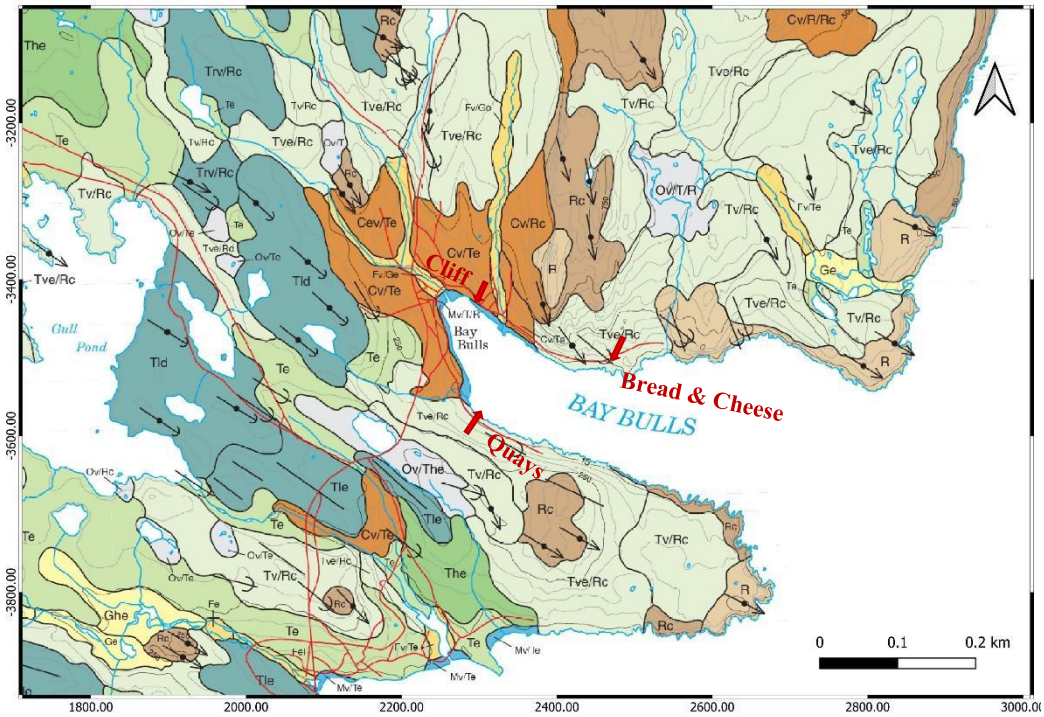

Figure 1-11) Surficial geology map of Bay Bulls. Grey contours are at 50 feet (15.24 m) intervals. The capital letters indicate the source material, and lower case letters the morphology. In the map, the straight lines indicate flutings; sharp arrows indicate roche moutonnées, and rounded arrows drumlinoid features. The rôche moutonnées and striations suggest that glacial ice moved southeast and eastward (Catto & Taylor, 1998).

Table 1-1) Simplified landform classification

GENETIC		MORPHOLOGY	
F	Fluvial	c	concealed by vegetation
C	Colluvial	d	Drumlinoid
G	Glaciofluvil	e	eroded and dissected
M	Marine	h	Hummock
T	Glacial	l	Lineated
O	Organic	v	Veneer
R	Rock		

1.4 Thesis Layout

The thesis is organized into six chapters.

Chapter 2 explores Newfoundland's geological hazard and coastal erosion, identifies the variables that impact coastal erosion, and describes the three sites in Bay Bulls with their geological context. Chapter 3 presents the theoretical basis of geophysical methods. Chapter 4 describes the procedures and techniques used for analyzing and processing geophysical data, and provides details of the geophysical surveys and geomorphological observations made at each site. The findings from each method are described in Chapter 5. A summary and discussion are presented in Chapter 6.

2 Background

2.1 Coastal Erosion

To evaluate the susceptibility of erosion in a specific coastal area, it is necessary to understand the variables that impact erosion and resulting failures, and the ways water – on the surface and in the subsurface, in liquid and solid form – interact with the sediments and rocks. Coastal erosion can result from the instability of cliffs as a result of wave impact during storms, from fracturing due to a freeze-thaw cycle, and from groundwater or surface-water flow, from development and natural sources. Increases in precipitation and sea level rise can exacerbate erosion, and human activities such as building houses, roads, and seawalls can cause shorelines to erode, endangering coastal development and infrastructure (Briguglio et al., 2009).

Salt spray is another coastal erosion contributing factor, which has a range of effects on local ecology, vegetation and infrastructure. One of the primary effects of salt spray is desiccation, or drying out of plants tissues due to the high salt content of the spray. This can lead to damage or death of vegetation in affected areas. Besides this, it can also contribute to soil salinization, as salt accumulates in the soil and reduces the ability of plants to take up water and nutrients. Salt spray can also corrode metal and concrete infrastructure, which lead to significant maintenance costs. Overall, the effects of salt spray depend on a range of factors such as the weather pattern, shoreline orientation and vegetation cover. So, assessing both climate and geological factors is necessary to analyze coastal cliff exposure to erosion.

Batterson et al. (1999) studied geological disasters of Newfoundland utilizing archival historical records. Many coastal communities have been built at the base of steep hills, making them prone to slope failures, storm damage, or coastal erosion. The entry of excessive amounts of water within fractures and the pore network of slopes, whether from rainfall or snowmelt, is frequently the cause of slope failures. Excess water stresses the slope material beyond its shear strength, causing point displacement.

In eastern Newfoundland, steep cliffs with fractured bedrock can be disrupted through frost wedging in a freeze-thaw cycle - the degree of which depends on the fracture pattern in the rocks, snowfall, and wind patterns - resulting in rock falls. Newfoundland's coasts are also often subject to high waves up to 30 m (Catto, 2011; Swail, 1997), strong winds (in excess of 61 km/h), and

alternating snow and rain, all of which make them vulnerable to erosion (Catto, 2011). Bay Bulls is most susceptible to rock falls, and debris flows (Batterson et al., 1999).

2.1.1 General Climate

Bay Bulls' climate is cold and mid-boreal. This climate is classed as Köppen-Geiger Dfb, which means fully humid with warm summers and cold, snowy winters (Kottek et al., 2006). Bay Bulls does not have a weather monitoring station for monitoring, forecasting, or climatological study. The nearest active weather monitoring site is at St. Johns airport, 33 km to the north (*Canadian Climate Normals*, 2011), therefore the values presented in Table 2-1 are from this station, compiled from data collected over the 30 year period from 1981 to 2010 (*Canadian Climate Normals*, 2011).

Table 2-1) Annual average of Climate Parameter (Canadian Climate Normals, 2011).

Climate Parameter	Value
Annual Average Temperature	5.0 °C
Extreme Maximum Temperature	31.5 °C on July 6th 1983
Extreme Minimum Temperature	-23.8 °C on March 10th 1986
Variation in monthly average Maximum and Minimum Temperature	About 20 °C
Annual Precipitation	1534.2 mm
Extreme Daily Rainfall	121.2 mm on July 27th 1949
Extreme Daily Snowfall	68.4 cm on April 5th 1999
Precipitation Variation between Driest and Wettest months	71 mm
Humidity Range	79% in January, 83% in July
Month with Higher Number of Rainy Days	December (16 days)
Month with Lowest Number of Rainy Days	July (10 to 11 days)
Average Depth of Snow Cover in St. John's (February)	32 cm
Extreme Snow Depth	180 cm on February 9th 2001
Days with Snow Depth Equal or Greater than 20 cm.	41.2 days/year

The depth of accumulated snow on the surface is measured at many points and averaged to be representative of the local area. The average value (1981-2010) in St. John's is 32 cm in

February. From May to October there is no snow cover. Greater snow depth produces more insulation of underlying substrate and prolonged snow cover reduces freeze-thaw activity.

The "Freezing-free Period" is the number of days between the last frost in the spring and the first frost in the fall for a given year. Any day where the minimum temperature (Tmin) is -5°C could result in freezing or frost occurrence (*Canadian Climate Normals*, 2011). In coastal environments, typically temperatures of -5°C must be maintained for 30-60 minutes in order to initiate freezing. The freezing point is depressed due to the brackish chemistry of coastal snowmelt, spray, and infiltrating water. As well, kinetics delay freezing (thawing) until the freezing temperature is maintained (ceases) for some time. The average frost free-period is 139 days, from May 30 until October 17.

2.1.2 Wind and Storm Surges

Table 2-2) 1981 to 2010 Canadian Climate Normals Station data (Wind).

Parameter	Measurement
Maximum hourly wind speed	>67 km/h in each month, 137 km/h in February 1959 (North)
Maximum gust speed	193 km/h in 1956
Dominant direction of maximum gust	Jan, Feb, Apr, Aug, Nov: SW Mar, Oct: NW; May: N; Jun: NE; Jul: SE; Sep, Dec: S.
Average of days with wind speed >52 km/h	46.6 days /year
Average of days with wind speed>63 km/h	16.1 days/year

Understanding the historical wind patterns and extreme wind events is important in assessing the potential impact of wind-driven wave and storm surges in coastal areas. This information helps researchers anticipate erosion risks and develop mitigation strategies.

According to the Environment Canada Normal data, the wind speed averaged over a 24 h period at St. John's is about 20 km/h, with stronger winds in the winter (in January it is 26 km/h). However there may be significant variations within a 24 hour period, especially in coastal areas. The wind most commonly comes from the west, however there is significant variability in wind direction on all timescales. The wind is influenced by local topography, resulting in funneling around headlands and into valleys and down sloping, as observed, for example, in Ferryland by Watton (2016). Due to the numerous embayments, steep and long valleys, and multiple high-elevation headlands, winds along the eastern Avalon coast are unpredictable.

Anecdotal evidence from the tour boat operator Joseph O'Brien indicates that winds from the southeast, east, and northeast bring significant wave action. Two fishermen, Mr. Ernie Mulcahy and Mr. Harley Williams, who have been fishing for more than 40 years in Bay Bulls, were interviewed on November 7, 2022, regarding the weather. According to them, in the summer the usual prevailing winds are from the west or southwest. In late August, the hurricane season starts and the winds are variable. In the winter, winds are stronger and mostly from the north or northwest, though sometimes there are easterly winds, some of the strongest from the southeast. Some northeast winds can blow for a week.

2.1.3 Wave Activity and Tidal Regime

Both wave and tidal activity can contribute significantly in coastal erosion, but the extent of their impact depends on various factors such as the type of coastline, local topography, geology and weather conditions.

Waves are typically an important cause of coastal erosion of sediment bluffs, as they generate a considerable amount of energy that can erode and transport sediment along the shoreline. The power of waves is determined by their height, frequency, direction and fetch (the length of open-ocean where winds blow on one direction without any obstruction from land or islands, (Komen et al., 1996)), so the geometry and orientation of costal areas relative to common wind directions affects their susceptibility to erosion. Wind speed, wind activity duration, and fetch all influence wave height (Catto, 2011; Komen et al., 1996). Long durations of wind activity are required to get the waves moving by overcoming the frictional energy losses between the atmosphere and ocean as well as the inertia of the water. Small waves occur when the wind is moving slowly, irrespective of the fetch or duration of the wind activity. Even if the wind is strong and the fetch is infinite, no significant waves will form if the wind blows only for a short period of time (Catto, 2011). Additionally, no large waves arise when strong winds blow for a long time but over a short fetch. Only when all three components come together do large waves develop (Catto, 2011). In 2011, a winter storm combined with high tide threw cobbles from the sea bed onto a wharf on the Bay's south side. Subsequently, the wharf was raised and armored with boulders brought in for the purpose (E. Mulcahy, pers. comm., 2022).

The mean height calculated for significant waves may be influenced by unusual storm waves (Cardone et al., 1996). The mean deep ocean wave heights offshore of the open eastern Avalon

coast are 7-8 metres (Neu, 1982). The 100-year height is roughly 15 m, and the 10-year significant wave height is predicted to be 11 m (Catto, 2006).

In addition to issues of variable wind direction along the coast, waves do not necessarily move in the same direction as the initiating wind. Generally, bays facing northeast are more exposed to northeasterly winds, and those facing south and southwest are exposed to wave attacks driven by hurricanes (Catto et al., 2003). Waves generated by southwest winds may impact coasts not directly facing the wind (e.g., north side of Bay Bulls Harbour). East to southeast winds are more frequent at St. John's during summer (*Canadian Climate Normals*, 2011). When the wind blows from the land (as is often the case (Table 2-2)), there is less intense wave action.

Bay Bulls opens to the ESE, like many bays on the Avalon's Southern Shore (Figure 1-1 and Figure 1-7) and, its theoretical fetch is the width of the North Atlantic. This means that wind blowing from the southeast can generate large waves and generate significant wave action, as confirmed in interviews with local fishermen, Mr. Mulcahy and Mr. Williams (November 7, 2022). The wave ranges from calm conditions to large long-period swells depending on the water depth and direction of the wind. The typical wave periods of the open eastern Avalon coast range from 6 to 8 seconds (Catto, 2011; Forbes, 1984).

The fetch and wind direction determine the strength of the approaching waves and their velocities and wavelengths. Generally, when most large swells and waves reach shallow bathymetry, their velocity reduces, wave movement is retarded, and wavelength progressively decreases while wave height increases, eventually leading to the waves breaking (Catto, 2011).

Generally the steepness of seafloor determines whether waves are reflective or dissipative. Reflective coasts are systems where the shoreline morphology reflects the majority of the wave energy because little wave energy is dissipated through breaking offshore (Guza, 1974). Typically, reflective coastlines feature steep cliffs or rocky outcrops. The embayed nature of the coast results in reflective, moderate-to-very high energy, wave-dominated shorelines in most embayments. Bay Bulls is a deep bay with maximum water depth varying from 25 m to 65 m from west to east (Figure 1-2). Bay Bulls' steep coastline exhibits mostly reflective behavior in response to wave regimes. This reflective nature of the coastline means that wave action is not a key factor of the erosion in Bay Bulls' coastline.

Tides are generated by the gravitational pulls of the Moon and Sun and cause changes in water level and currents that can lead to the movement of sediment and erosion in certain areas. The

nearest tide gauge data to Bay Bulls is in St. John's Harbour. The tidal regime at Bay Bulls is mostly micro-tidal (less than 2 m range) and mixed, semi-diurnal, which means that there are two high tides and two low tides each day, with roughly equal height. The tidal range in St. John's can vary from highest high water of 2.5 m and lowest low water of -0.5m (Government of Canada, 2019).

2.1.4 Sea Level change

The glacial history of the region, which provides information about isostatic rebound, is an essential component of the study of sea level rise. As the glaciers melt and retreat during deglaciation, the crust gradually rebounds or uplifts. This rebound affects local sea level. Understanding the timing and magnitude of this rebound is essential for the accurate calculation of sea level rise in past glaciated areas. Glacial activity can also shape coastal landscapes, creating features like fjords, inlets and coastal plains. This includes the directional imprint of ice movement and sediment deposition during deglaciation. According to Catto (2011), relative sea level change results from an increase in the volume of water, or ground subsidence, or a combination of both depending on the location. Sea-level rise can submerge coastal areas, altering the exposure of sediments and influencing their preservation or erosion. To make accurate long-term sea level projection it is important to consider historical trends and geological records.

Three phases in a glacial succession have been identified by investigation of ice flow indicators on the Avalon Peninsula and the Isthmus of Avalon between initial glacial accumulation 120,000 years ago and deglaciation (some time before 10,100±250 BP)(Catto, 1992, 1993, 1994, 1998).

Phase 1 involved accumulation at several centres located along the axes of the sub-peninsulas and the isthmus. Ice expanded radially from these centres, resulting in glaciation of all parts of the Avalon Peninsula. Ice thickness reached a maximum during Phase 2, completely covering all area affected by earlier Phase 1. At some time before 10,100±250 BP, phase 3, deglaciation of the Avalon Peninsula, began (Catto, 1998).

Glacial-isostatic depression resulted from the weight of the glacial ice that covered the province during the most recent glaciation, which began around 120,000 years ago. Due to the massive amounts of water incorporated into the land glacial ice during the glaciation, the volume of sea water decreased at the same time (Batterson & Liverman, 2010; Catto, 2011).

When the glaciers started melting, about 14,000 years ago, the sea was able to flood the depressed coastal topography due to the melting glaciers' discharge of meltwater to the ocean.

Many locations saw a significant rise in the relative sea level. Cores taken in St. John's Harbour suggest that sea level at this time was at least 14 m lower than it is today.

Throughout the Holocene, the relative sea level in St. John's Harbour seems to have stayed below the current level. During explorations in downtown St. John's, no raised sea sediments have been found (Bruckner, 1969; Catto & St Croix, 1998). Newfoundland started emerging from the glacio-isostatic depression ca. 10,000 years ago. While ongoing melting added new water to the ocean, the accompanying glacio-isostatic rebound raised the land, resulting in overcompensation and causing a decline in the relative sea level. As a result, eastern Newfoundland's relative sea levels were lower than they are today (Shaw & Forbes, 1995). Depending on the location, the ground started to subside from the overcompensated positions between 3,000 and 8,000 years ago, which led to a new rise in sea level. Increased erosion on many Newfoundland beaches and inundation of trees and peat bogs on land are indications of transgression brought on by relative sea level rise.

To obtain a comprehensive record of sea level change over an extended period (over 40 years), various methods (including C^{14} dating of tree stumps currently below mean sea level, tide gauge data (from St. John's) and archaeological data at Ferryland and Placentia) have been utilized in several Avalon Peninsula locations (Batterson & Liverman, 2010; Catto, 2006, 2011, 2020; Catto et al., 2003; Watton, 2016). Catto (2011, 2020) reports that the rate of sea-level rise over the past 60 years, between St. John's and Ferryland is (18-20 m)(Catto, 2020; Watton, 2016). According to Batterson and Liverman (2010), by the year 2099, sea levels are expected to rise by about 100 cm along the Avalon Peninsula's coastlines.

2.1.5 Effects of climate change

In Bay Bulls, changes in precipitation and temperature influence the frequency and intensity of rock fall and other slope failures. Snow cover insulates the ground from changes in temperature. Frost wedging phenomena increase when snow cover declines or the number of oscillations around the critical freezing point increases. Warmer winter temperatures might cause a reduction in snow cover and lead to more water available for future freezing. Increased wind activity could blow away snow, exposing the region to a more intense freeze-thaw cycle.

According to Hardy et al. (2001), climate change is expected to result in warmer temperatures leading to less snowfall which could lead to increased soil freezing due to lack of an insulating

snow cover. While a region like St. John's may experience less snow precipitation and more rain, extreme snow cover duration or snowfall may still occur due to small temperature changes (Finnis & Daraio, 2018). In summary, this suggest that areas like the Avalon Peninsula may experience fewer but heavier snowstorms and more frequent heavy rainfall during winter.

Daily mean temperatures are anticipated to increase all over the province with a largest shift in winter time. However, as this variable is closely linked to temperature, coastline and areas located near open water, like the Avalon peninsula, will experience less change due to the fact that open water changes temperature slowly, keeping climate moderate (Finnis & Daraio, 2018).

Daily minimum temperatures are also predicted to increase throughout the province with greater changes in mean and maximum temperatures during winter (3 to 6 ℃ in NL). As a predictor of frost events during the growing season (late spring to early fall) and thaws during the cold season, the mean daily minima are useful. Regions with daily minima close to 0 ℃ in a relevant season can anticipate more of these events.

It is anticipated that fewer days will have temperatures below freezing, particularly in the spring and fall. The largest reduction is expected in areas/seasons with temperatures that are close to freezing (such as the Avalon Peninsula in spring). Freezing occurrences (frosts, re-freezes, etc.) become less frequent and/or shorter as frost days decline; however, reduced snow cover enhances the possibility of frost penetration on frost days.

On a daily basis, daytime highs, and nighttime low temperatures are anticipated to rise at a constant rate, through the middle to end of the century (Finnis & Daraio, 2018). In the coldest season and regions, the greatest change is expected to be in the minimum nighttime low. In general the coldest temperatures are predicted to warm up the quickest. Winter is going to bring about the most shift (Finnis & Daraio, 2018). With the largest change anticipated in regions and seasons where daytime temperatures are projected to rise above near-freezing, the number of days with frost is predicted to decrease (Finnis & Daraio, 2018). Although the number of days with frost (i.e. < 0 ℃) will decrease, it does not necessarily mean that frost activity will decrease or be less effective. In fact irregular fluctuation around -5 ℃ can lead to more pronounced frost effects compared to a consistent colder temperature (Finnis & Daraio, 2018). In addition, the combination of reduced snow cover with warmer (but still below 0) temperatures results in more regelation and freeze-thaw. Changes in freeze-thaw cycles and winter thaw events are probably going to follow a similar trend.

Mean daily precipitation is projected to increase throughout the province. Although the projected increases are low, the variations are substantial when considered for the entire season. A 10% variation (increase) in the total seasonal precipitation for a place like St. John's is expected. By the end of the century, Newfoundland should see widespread increases in mean daily precipitation, frequently in the range of 1 mm during severely impacted seasons (winter and fall). The number of days in a year with significant precipitation, defined as 10 mm or more is expected to increase by 1-4 days depending on the location and season. This increase in precipitation can lead to flooding and erosion depending on the intensity of the rainfall. During winter, 10 mm of rain can turn into 10-100 cm of snow, depending on the temperature (Finnis & Daraio, 2018).

Most climate change impact predictions have focused on temperature and precipitation, with little information available on other variable such as wind and snow. This is due to the lack of downscaled data and limited understanding of how to assess change in these variables (Finnis & Daraio, 2018)

2.2 Three areas susceptible to erosion

The three sites of concern that are the subject of this research are stretches of roadway located on the north and south of Bay Bulls (Figure 1-3): Bread and Cheese, the Cliff and the Quays, situated about 1.5 to 2 km apart. Brief descriptions of the history, anthropogenic activities and the geomorphology observation of each site are given below. Official records of road work in Bay Bulls are sparse (J. Aspell, pers. comm. 2021), essentially non-existent from before the town was incorporated in 1986, and incomplete in subsequent years.

2.2.1 Bread and Cheese

The Bread and Cheese site is located on Gunridge Road (Figure 1-1 and Figure 2-1), where the road dips in elevation as it crosses a highly fractured region. The fractured region is marked by a creek running down the nearby hillside. On the north side of the 6 m wide road there are residential houses (Figure 2-2). Creek water (and sewage effluent from neighbouring houses) is carried under the road through a culvert with its top surface about 1 meter below the road surface, onto the western side of a pocket beach.

According to Gary O'Driscoll, a town employee and local resident, in heavy storms the waves reach 10 m asl, as high as the road surface, and water flows landward through the culvert.

Gary O'Driscoll reports that while he was a boy in the mid to late 1960s, a one-lane paved road along the north side of the bay, including Gunridge Road, was upgraded to two lanes, and fresh bitumen was laid on top of the old surface. Further roadwork was carried out about 13 or 14 years ago (~2009). Rip rap was also brought to reinforce the scarp next to the east of the culvert (Figure 2-3). The timing of this is unknown.

Figure 2-1) Bread and Cheese site. The arrow points to the culvert. The blue line shows the creek flow in the highly fractured area.

Figure 2-3 depicts the pocket beach at the Bread and Cheese site. Rip rap and the bay end of the culvert is seen to the left.

Figure 2-2) Gunridge Road, looking east. Field assistant Jason Sylvester is holding the RTK rover near the west end of the GPR survey grid. (1 April 2021).

Figure 2-3) View of the beach at the Bread and Cheese site, looking east. Rip-rap and the bay end of the culvert are seen to the left. (1 April 2021).

2.2.1.1 The culvert

Field assistant Jason Sylvester crawled through the culvert within the survey area (Figure 2-4 and Figure 2-5) to assess its condition. Figure 2-4 shows the creek and landward opening of the culvert. Cobbles and boulders from the creek or the banks surrounding the culvert are shown near the mouth of the culvert.

Interior views of the culvert are shown in Figure 2-5. Evidently, the culvert is made up by two sections with different diameters. The northern section, about 380 cm (~150" = 12.5') long, has a diameter of about 150 cm (~60"). The southern section has a wider diameter of about 180 cm (~72"). Angular rocks are seen in the gap where the two sections meet. Both sections appear slightly compressed in the vertical direction. This is particularly evident at the northern end of the northern section (Figure 2-4, bottom right). Much of the bottom of the culvert is covered by rocks and dirt, which progress to mud with some algae at the southern, bay end (Figure 2-6a).

Figure 2-4) Left: The boulder-strewn creek north of the Bread and Cheese culvert. Photo taken from the road, looking north. Right: The north end of the culvert, taken from the west bank of the creek (top), and from the creek bed looking south (bottom). (22 April 2021)

The bottoms of both sections of the culvert are corroded, with some parts in the southern section rusted through (Figure 2-5b). There is also 'crevasse corrosion' around all rivets, leading to rusting of the rivets (e.g. Figure 2-5b).

Figure 2-5) Inside the Bread and Cheese culvert, looking north toward the creek opening. Left: measurements of internal diameter of northern section. Right: measurements of internal diameters of southern (bay ward) section. (22 April 2021.)

We speculate that the northern section of the culvert was installed when the road was first constructed, and the larger diameter southern section was installed when the road was widened in the mid to late 1960's.

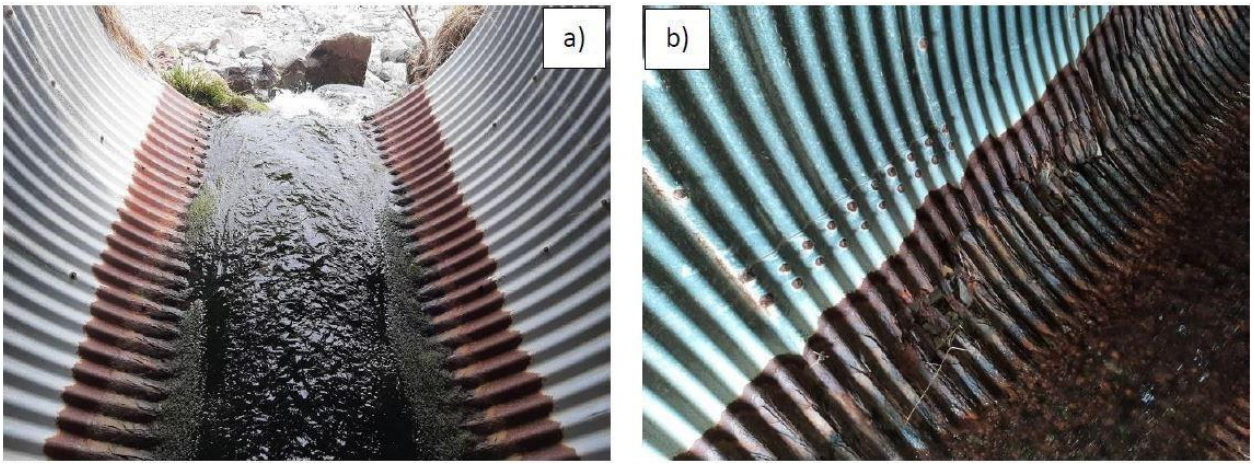

Figure 2-6) a) The bay-ward side of the culvert, looking south from inside the culvert. b) Close-up showing corrosion of rivet and pipe in the northern section of the culvert. (22 April 2021.)

2.2.1.2 Geomorphology observations

There is a small (19.4 m long) gravel pocket beach (Figure 2-7) in this area with natural bedrock headlands on both sides bearing 240° toward the south. The eastern headland is smaller while the west one is more extended ocean-ward affecting the direction of the waves and subsequent sediment transport on the beach. From the steep slope of the beach and the almost perpendicular incidence of the waves, this is a reflective beach, meaning that most of the wave energy is reflected back offshore.

The effect of wave action can be seen in the photograph of the pocket beach (Figure 2-7). Here, the beach rocks are grey pebbles, rounded and sorted in size over the first several meters. In the upper part of the beach (toward the cliff face), however, the rocks are more angular and varied in shape, indicating that wave action does not commonly reach very far up the beach. Figure 2-8, taken off the headland just to the west of the area shown in Figure 2-7, shows pebbles and cobbles of various sizes and shapes overlying the bedrock. This heterogeneous collection indicates that wave action is not the dominant process at this elevation. The rounded pebbles would have been washed up from the beach onto this location by storms. The more angular fragments would have come from higher elevations.

Another indication of the limits of wave action is the vegetation, which would be killed by common exposure to seawater. The small trees seen in Figure 2-8 likely grew after the last major storm soaked the slope in salty water.

A view from the east end of the pocket beach in Figure 2-9 shows, to the left (east), a rugged headland that would protect the beach somewhat from wave action, and in the middle right, between the trees, a flat outcrop which has been smoothed by the action of waves. This image also shows vegetation and some broken wooden structures that have collapsed toward the beach.

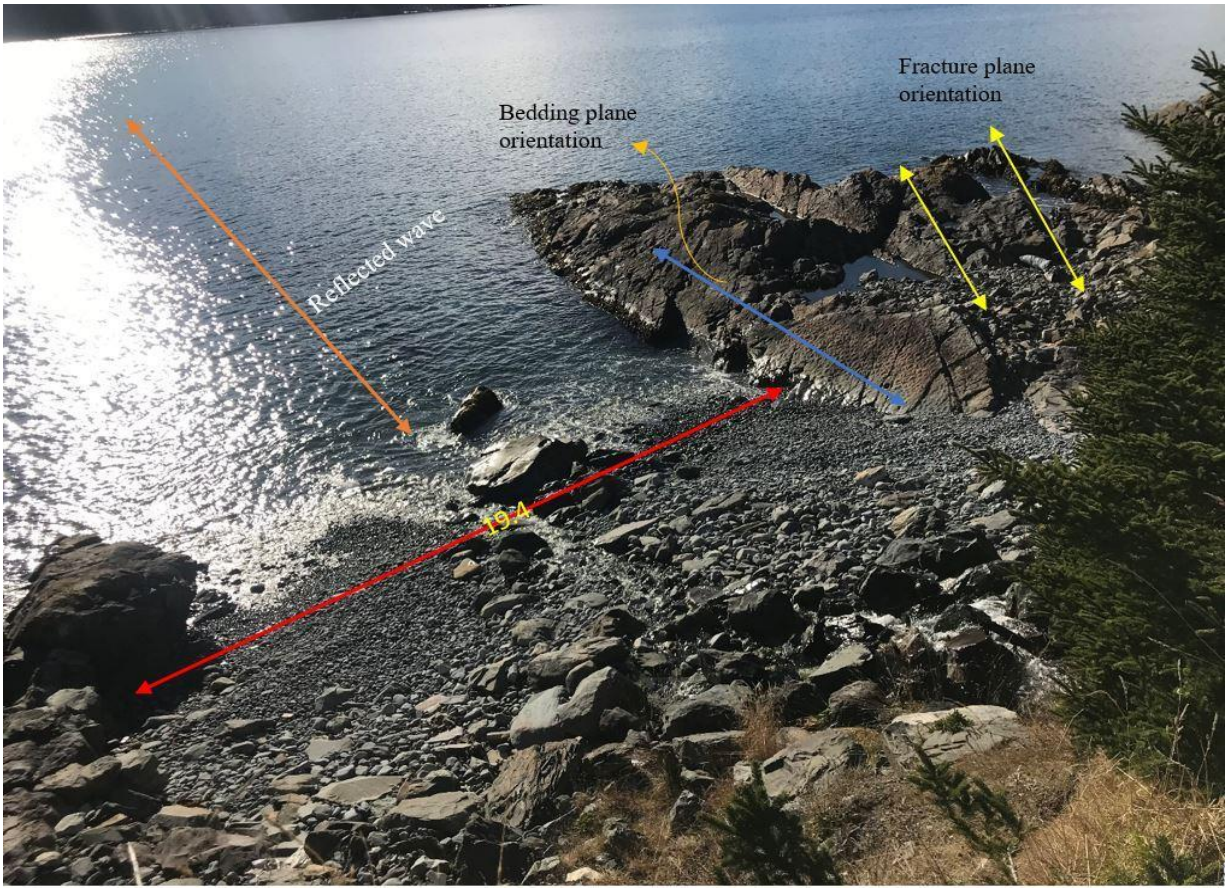

Figure 2-7) Ocean-ward photo of the pocket beach, taken from Gunridge Road facing southwest. The strike of the bedrock is shown with the blue arrow, yellow arrows represent the orientation of the fractured planes, the orange curved arrow depicts the direction of the waves, perpendicular to the beach.

Figure 2-8) Western headland of pocket beach at Bread and Cheese site. Photo taken from Gunridge Road, about 10 m east of Figure 2-7, facing southwest.

Figure 2-9) View from east end of pocket beach at Bread and Cheese site, about 25 m east of Figure 2-7. 21 April 2022.

The strike and dip of bedrock outcrop was measured on both sides of the pocket beach. Three measurements were taken, the longer headland on the right side and two smaller ones on the left side of the beach (Table 2-3). The strike measurements were all roughly the same.

The fractured plane's strike and dip also were taken (Table 2-3). These indicate the orientation of the weaknesses in the bedding (Figure 2-7, Figure 2-10).

Table 2-3) Strike and dip of the bedding outcrops Strike and dip of the fractured plane

Bedding outcrop			Fractured plane	
ID	Strike	Dip	Strike	Dip
1	010	32	223	51
2	360	31	240	55
3	008	34		

Figure 2-10) Photo of rocky headlands to the west of the pocket beach. Taken from Gunridge Road about 25 m west of Figure 2-7, facing southwest. Yellow arrows represent the orientation of fractured plane.

Although from the evidence of growing trees and unsorted rocks, wave action is commonly restricted to the near shoreline, storms influence the bank's stability. Overland saturation of the sediments and subsequent creep is important. To the east of the culvert, the turf can be seen detaching from the top of the slope (Figure 2-11 and Figure 2-12). In 2021, the area above the detachment was recognized as an erosion hazard. Recently (2022), this region was filled in, and a new railing was constructed on the south side of the road, inside the old railing over the culvert area where coastal erosion has brought the edge of the bank dangerously close to the road (Figure 2-13).

Figure 2-11) Lack of coherence in the Quaternary cover is depicted, as shown by the yellow arrow. The culvert opening appears on the left. Left and bottom: boulders (rip rap) have been brought there to stabilize the road. Photo taken from the beach, facing northeast.

Figure 2-12) An expanded view of separations shown in Figure 2-11. Average amount of separation was 50 cm and the distance from the top of the bank was roughly 95cm.

Figure 2-13) New railing constructed inside older railing. Looking east, Bread & Cheese, 21 April 2022.

Figure 2-14) Clifftop erosion because of surface water and danger sign at the cliff top above the eroded area.

2.2.2 The Cliff

The Cliff site is near the northwest end of Northside Road (Figure 1-3 and Figure 2-15). The marine terminal across from the Cliff site was built before 1945 as evidenced by an air photo of Bay Bulls in 1945 depicting the terminal. It has been used to serve the offshore oil and gas industry, including supply vessel berthing, crew changes, and cargo handling since the 1970s. Building the marine terminal caused the Cliff site to be sheltered from wave action.

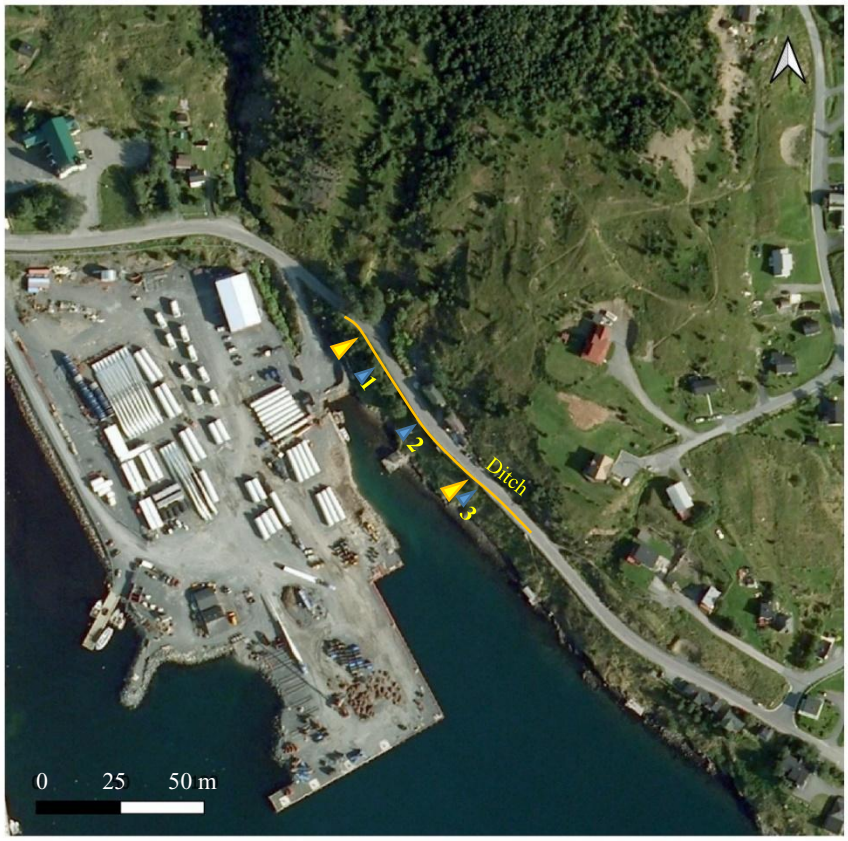

Figure 2-15) Cliff site overlooking the marine terminal. The yellow line indicates the centre line of the GPR grid survey, and the yellow arrows point to the north and south ends of the wooden retaining wall. The smaller blue arrows point to culverts, designated from 1 to 3 starting in the northwest. Air photo from the Government of Newfoundland.

There are three culverts along the surveyed area, numbered 1 to 3 from the northwest and indicated by blue arrows (Figure 2-15). Culvert 1 (Figure 2-16 b and Figure 2-17) is ~30 cm (12”) in diameter and does not appear to be in current use. According to Gary O'Driscoll, there used to be a drainage ditch on the NW of the road, and water was diverted into Culvert 1. This ditch no

longer exists due to the more recent construction. However, there is a ditch further to the NE of the road, and surface water is now flowing into culvert 3 and over and down the road.

2.2.2.1 Wooden retaining wall

When the road was converted from one lane to two lanes in the mid to late 1960's, a retaining wall was built to allow the road to be extended westward over a steep slope. When it was a one-lane road, it was separated from the cliff by a cable held up by metal poles. The remnants of this construction can be observed on the steep slope along the bay.

The retaining wall is 99 m long, with its northwest end about 59 m from the STOP sign at the start of the access road to the marine terminal. The wall is constructed of approximately horizontal beams of wood, which, according to interviews with local residents, were soaked in creosote for preservation. (For environmental reasons, this method is no longer used.) Wooden supporting beams extend perpendicularly from the wall under the road, presumably reaching the original slope's edge. The space between the wall and the original slope was filled with rocks and sediment. The construction of the wooden retaining wall was overseen by local resident Bobby O'Keefe in the late 1960s.

The top of the wall is about 0.5 m from the edge of the asphalt on the road, and wooden posts holding up metal guard rails are located on the inside (road-ward) side of the wooden wall. Representative images from the first ~40 m of the wooden wall (measured from the NW end) are shown in (Figure 2-16). Further to the SE, the bay-ward slope was too steep to safely navigate to take pictures. The beams making up the wall are square in cross-section, ~15 cm (~6") in width and height, and vary in length from ~1 m to > 3 m. On the wall, they are sometimes separated by the square ends of the support beams that extend under the road (Figure 2-16). As the road rises in elevation to the southeast, additional beams were added to increase the height of the wall (e.g., see the top of the wall near the center in Figure 2-16 b and Figure 2-16 c).

Past about 40 m (to the SW), it appears that the wall slopes inward, as it was probably first constructed. Over the first 10 m, however, the wall is approximately vertical, and over a section from 10 to 30 m the top few beams are dislocated outward, as seen in Figure 2-16 c and Figure 2-16 d and Figure 2-17. This is presumably due to the creeping motion of material under the road surface. Note, from Figure 2-17, that one of the boards under Culvert 1 is also displaced. To the

southeast of the wooden retaining wall, the road is supported by a galvanized iron retaining wall. The metal retaining wall was constructed later, in 1986 or 1988.

a) NW end of wall, from 0 to ~4.5 m. Field assistant Ms Hicks is indicating a distance of 3m from the first guard rail post (yellow arrow).

b) Wall near culvert 1. NW to SE. Photo ~7.4 m wide, centred ~16 m from NW end of wall.

c) Wall, centred ~24 m from NW end of wall.

d) Wall, centred ~ 30 m from the NW end of wall

Figure 2-16) Wooden retaining wall at the Cliff site. Photographed from the steep slope southwest of Northside Road.

Figure 2-17) side view of the wall near culvert 1.

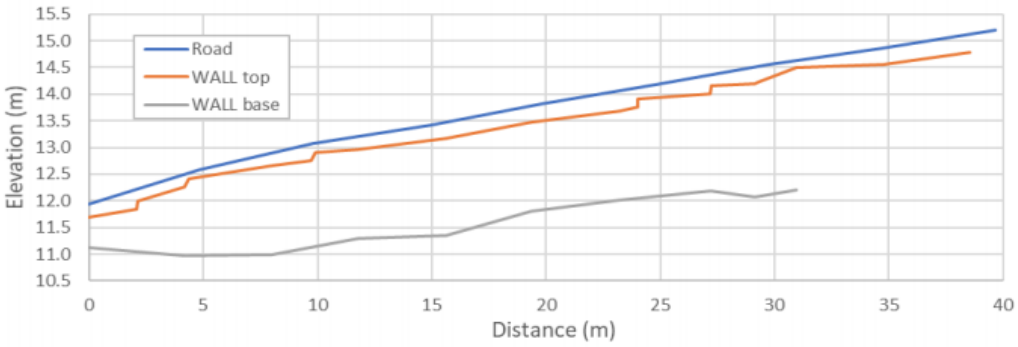

Figure 2-18) An elevation profile of the first ~40m of the wall.

2.2.2.2 Geomorphology observations

Field observations reveal that the steeply sloped hillside at the Cliff site is covered with a thin veneer of glacially derived sediment (~1-2 m at most) over the bedrock (Figure 2-19 and Figure 2-20). The veneer is creeping downward over the slopes, as can be seen from the hummocky appearance of the grass. In Figure 2-20, a ridge can be seen near the top of the slope, where the overburden has sunk downward, and underneath this ridge a bulge where the sunken material has collected. An indication of the thinness of the sediments is the exposure of bedrock in Figure 2-21.The hummocky appearance can also be seen in the even steeper slope below the road (Figure 2-22).

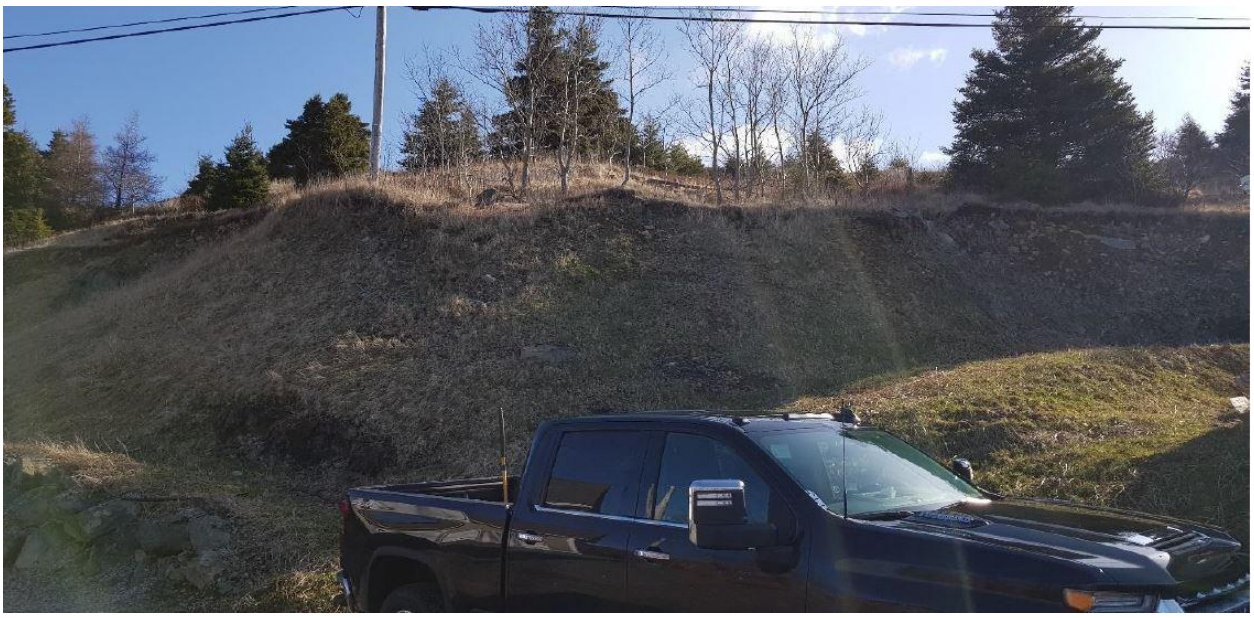

Figure 2-19) Hillside slopes on the north side of Northside Road. The Cliffs site, April 21 2022.

Figure 2-20) Hillside slopes on the north side of Northside Road. Photo taken looking southeast from ~UTM 363230E, 5241925N. The Cliffs site, April 21 2022.

Figure 2-21) Bedrock showing underneath vegetative cover on the slope above Northside Road, Cliff site, a few metres southeast of the deck shown in Figure 2-20.

A few 10s of meters east of the locations in Figure 2-21, it can be seen that the till has accumulated behind a power pole (Figure 2-22), as this obstacle is impeding the downward motion of the near surface sediments. Trees also act as obstacles, as seen Figure 2-23. In addition to the surficial downslope movement, some bedrock has detached, and boulders have descended. Such

boulders are shown in Figure 2-22 and Figure 2-24. Note that their angular shape indicates that they have not moved far. Bedrock is exposed next to the path of flowing water in Figure 2-24.

Figure 2-22) Creeping of surficial turf, with some accumulation behind the street light pole seen on the right in Figure 2-20. Some boulders are seen within the grassy slope.

Figure 2-23) Looking downslope (to the southwest) from the edge of Northside Road at ~ UTM 362205 E, 5241945 N. 21 April 2022. Yellow rectangle indicates area of Figure 2-25.

The importance of upland water flow in this area can be observed in sites such as (Figure 2-24). The weight of water and its effect on diminishing internal cohesiveness of Quaternary glacial derived cover undoubtedly contribute to its creeping downslope movement (Figure 2-22). Groundwater infiltrating underneath the road may jeopardise the road, causing lengthwise fractures, as seen in Figure 2-25.

Figure 2-24) Vegetated sediment containing many angular boulders, near a fourth culvert to the southeast of the survey area (~ UTM 363300 E, 5241850 N). 21 April 2022.

Figure 2-25) A crack in the pavement is another indication of shoreward motion of the land in this location. UTM 363253E, 524900 N. Photo taken looking south.

Changes in the geomorphology of the Cliffs site are mainly due to terrestrial processes, as wave-action has little effect. This was likely the case even before the dock was built. Winds here come mainly from the northeast, so this side of the bay, overlooked by a steep slope, is particularly sheltered. The relative unimportance of wave action can be seen on the shoreline (Figure 2-26). The rocks here are angular and poorly sorted, with no apparent gradation in size closer to the shore and no sign of shingling. Some rocks are lying at steep angles to each other. Wave action on shale debris would be expected to result in rounded, disc-shaped pebbles. The appearance of seaweed at the water line is another indication of how relatively undisturbed by wave action the shoreline is in this location.

Figure 2-26) Shoreline below the Cliff site. Close-up of region shown in Figure 2-22.

2.2.3 The Quays

The third survey site is on the south side of the bay. It is located to the southeast of Maggoty Cove (see Figure 1-6) on Quays road. The particular areas of interest are two inlets where the road runs close to steep drop-offs to pebbly beaches (Figure 2-27). Figure 2-28 and Figure 2-29 show seaward views from Quays Road at the western inlet, dubbed 'the Inlet' and the site of most concern, as the road edge is less than 0.5 m from the steep drop-off.

Recent anthropogenic activity at the Quays road site, consists of the relocation of the road from the coastline. According to local fisherman, Ernie Mulcahy, Quays Road suffered a collapse of an approximately 2 m section of the Quaternary cover under the road at Stone's Gulch (yellow star in Figure 2-27a). When the road was repaired in 2014, it was relocated away from the coastline at Stone's Gulch up to 10 m, presumably over ground in less danger of washout. The location of the new road is shown in Figure 2-27b and indicated by the yellow dots in Figure 2-27a. In Bay Bulls, such road works are dealt with using local contractors, and the town lacks detailed records of the work. The washout was localized, only a few meters wide, and it involved the removal of unconsolidated sediment under the road. There is a significant thickness of sediment over the bedrock in this area. The repair involved resurfacing the road, the introduction of guard rails, and concrete curbs.

Figure 2-27) a) Air photo of the Quays site, taken before the relocation of the road in 2014. The orange arrows indicate the inlets. Yellow dots indicate the location of the southwest edge of the new road. The star is the location of Stone's Gulch. b) Lower resolution Google Earth image of the same region, after the relocation of the road. Image date 8/2014.

Figure 2-28) Looking landward opposite the Inlet across the Quays road.

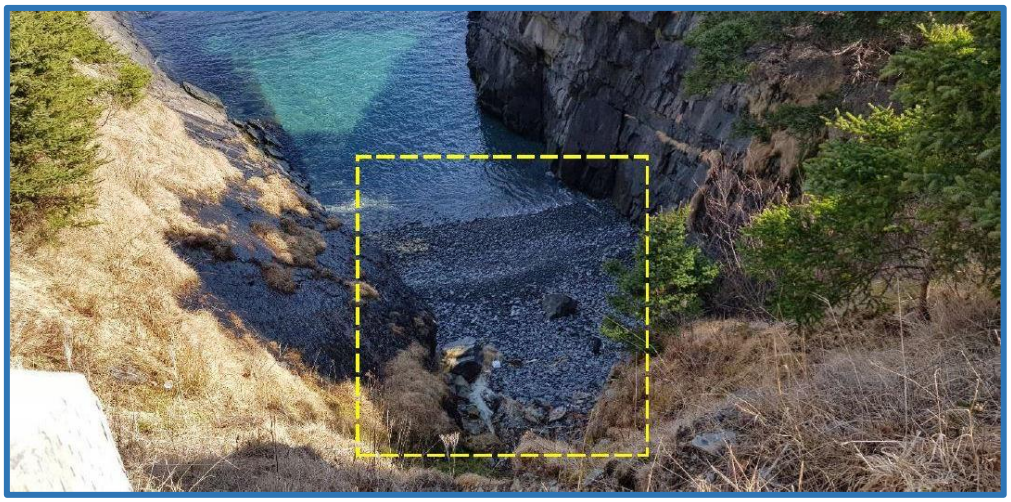

Figure 2-29) Looking down at the Inlet from the edge of Quays Road (bay-ward). April 21 2022. Yellow rectangle expanded in Figure 2-30.

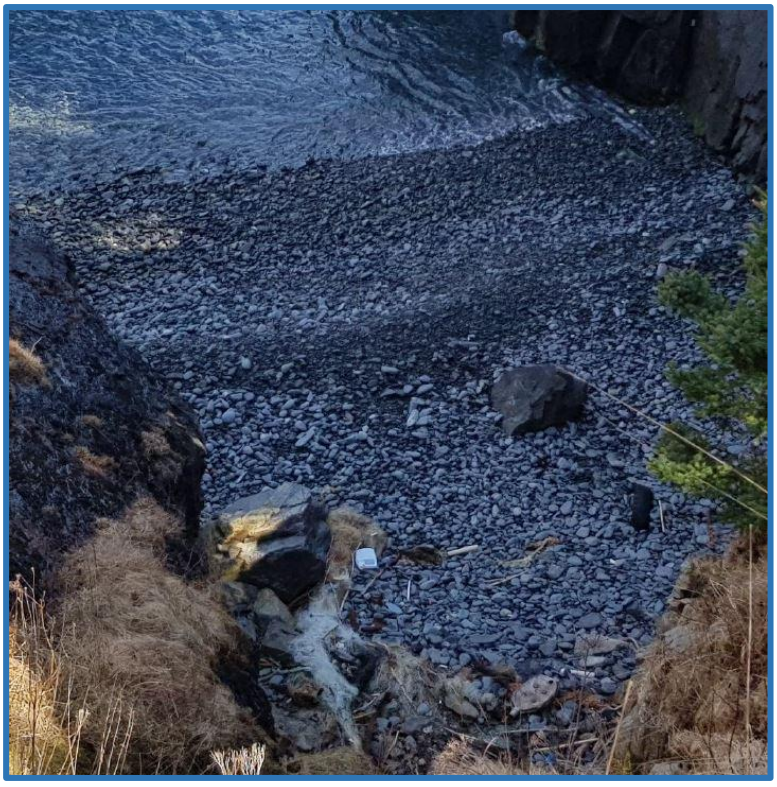

Figure 2-30) Close-up image of the beach of the Inlet from Figure 2-29.

At the Inlet, the road is bordered by a double galvanized iron guard rail 19 m long bay-ward-of the road. Opposite the guard rail, there is a concrete curb on the house side (north side) of the road (Figure 2-28). Most recently (~2020), there has been construction (sea-view building) in an area where fill overlies the till, and a gravel road has been constructed, heading uphill at an angle.

There is a small diameter cement culvert located underneath the road opposite the first inlet (farthest southeast). There is a drainage ditch on the SE of the road, and water flowing into this culvert goes toward the cliff face. Another two culverts NW of the surveyed area are made of plastic.

2.2.3.1 Geomorphological observations

The Quays site features steep cliffs, an embayed coastline and particularly deeply incised embayments, the northern of which is designated ‘the Inlet’ (Figure 2-27). From what has been observed in the field, the ground near the top of the cliffs has a thin layer of vegetated Quaternary sediments covering the bedrock. Creepage of this material is evident on the left (west) side of the Inlet (Figure 2-31), where the grass mat extends over the bedrock. Parts of the mat have become

detached and are sliding down the steep rock face. Some parts of the mat have been deposited at the cliff toe and on the beach (Figure 2-30). The beach at the Inlet is a pocket beach, covered with predominately pebble-sized stones and some boulders. The width was estimated at about 20 m. Strike and dip were estimated at around 004/50. There is drainage from the land, in particular indicated by the ditch in Figure 2-28, and under the roadway. Seepage can be seen on the shoreside of the road down the steep embankment (Figure 2-31).

The rocks on the beach (Figure 2-30) are not as well-rounded or sorted as those on the Bread and Cheese beach (Figure 2-7). The steep, closely spaced headlands here protect the beach from waves from all directions except directly aligned with the Inlet, that is, from the northeast. That is a common wind direction in Bay Bulls (pers. comm. N. Catto), but the fetch across the bay is only ~ 1 km. Storm waves from the NE would lead to undercutting the high (14.5 m) bank, which is a matter of concern.

Figure 2-31) Shingle pocket beach of the Inlet with fractured headland and bedrock outcrop and diamicton cover on the top in Quays area.

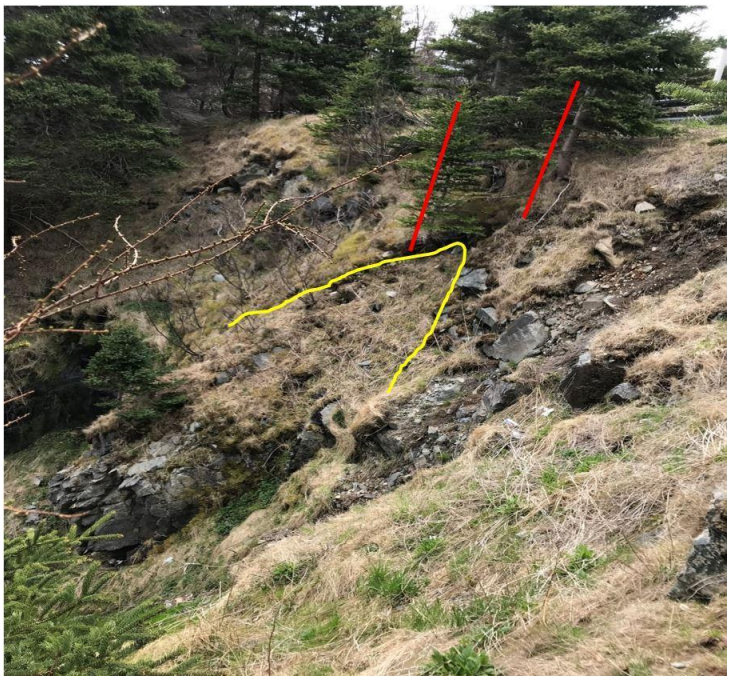

Figure 2-32) The yellow curve shows the soil creeping area (failure of soil cohesion), and the red line depicts that the tree is not straight yet. (Quays site, first eastern inlet.)

Trees are important to the stability of a landscape. Their roots help to hold quaternary cover together. It is noticeable that walking trails made by removing trees can become preferred paths for water flow and are easily eroded. Early settlers in Bay Bulls would have chopped down trees to make room for vegetable gardens, encouraging erosion of the diamicton (poorly sorted soil with pebbles and cobbles).

The embayment southeast of the Inlet (right arrow in Figure 2-27a) is of lesser concern. The headland to its SE (not shown) is not such a high feature as the SE headland of the Inlet, so waves could break over it instead of being funneled toward the beach. This embayment is also not as deeply incised, and it is closer to a high point on the shoreline road: on the landward (SW) side of the road, the ground is not as steep as it is opposite the Inlet, and it is thickly covered in trees, both factors which would reduce the surface and near-surface water flow toward the shoreline.

3 Methods

The three geophysical methods used to image the surface and subsurface of the vulnerable stretches of road were: ground penetrating radar (GPR), direct current resistivity/induced polarization (DCR/IP), and real-time kinetics global positioning system (RTK).

These methods were chosen largely because they are standard tools for investigating coastal erosion (Attwa et al., 2021; Kilfoil et al., 2018). DCR and IP were used in this study as they effectively characterise electrical properties of the subsurface including variation in soil composition, such as moisture content and pore space, which are a critical factors for sediment erodibility. IP can also help identify clay which aids in identifying high erosion risk areas. IP can be a complimentary method used in conjunction with resistivity and GPR to gain a comprehensive understanding of coastal subsurface properties. GPR is useful for detecting shallow subsurface structures such as interfaces related to road material layers or the occurrence of bedrock, while DCR can probe deeper, potentially revealing properties of the bedrock. The RTK was used to obtain detailed topographic information about the road surface, which can reveal features related to subtle ground movement under the road. This multi method approach enhances the accuracy of erosion assessment.

Other techniques, such as magnetics or electromagnetics were unsuitable in the study sites due to cultural noise from nearby houses and powerlines. The results of gravity surveys would be dominated by the morphology of the steep coastal slopes, and the differences in density between thin road cover and bedrock too small for meaningful interpretation. Shallow seismic methods, such as hammer seismic or vibro-seismics, survey procedures are more complicated and involved than DCR (and GPR), and the feature in the subsurface under the road and the slopes of the hill-side were expected to be complicated geometrically, both of which make seismics more effort than they are worth.

The instruments, what they measure and how they work are explained in the following.

3.1 Direct Current Resistivity (DCR)

The DCR method is one of the oldest geophysical techniques. It is used to estimate the subsurface resistivity distribution (Loke, 2012). Resistivity is the inverse of electrical conductivity and has units of ohm-m (Ω-m). The more resistive the ground, the harder it is for current to flow

through it. To demonstrate the utility of the DCR method (and the IP method, section 3.2) the electrical properties of Earth materials are first reviewed.

3.1.1 Electrical properties of rocks and minerals

The electrical properties of the subsurface are important in geophysical explorations using electrical and electromagnetic methods. These properties include natural electrical potentials, electrical conductivity/resistivity, and chargeability. Among these properties, electrical conductivity is the most important in resistivity surveys.

Electric current can spread in rocks and minerals via several mechanisms:

1- Electronic conduction

2- Electrolytic conduction

3- Dielectric conduction

In the context of soil and rock the primary mode of electrical conduction predominantly arises from the presence of fluids within this material, leading to ionic conduction. Contrary to other material like metal, where electronic conduction prevails due to the presence of free electrons, in soil and rocks, a relatively slow movement of ions in electrolytes plays a controlling role in facilitating the electrical conduction (Telford et al., 1996).

Dielectric conduction occurs in weak or non-conductors with very few or no free electrons. As a result of the external electric field, an atom's electrons move a little relative to its nucleus and dipolar molecules can re-oriented into the direction of the electric field. This relatively small separation of positive and negative charge, or reorientation of the dipole moment of the dipolar molecules results in a negative and positive charges known as the dielectric polarization of the material.

For the DCR method, which uses direct current in relatively long (0.5 to 1 second) alternating pulses, the most important conduction method is through electrolytic conduction. The main means of current flow for DCR data is electrolytic conduction in the water existing in the sediments, till, soil or fractures and cracks in the bedrock.

3.1.2 Resistivities of Earth materials

Resistivity depends on the material (Table 3-1), however, apart from the extremes of high (air) and low (metals), it is not particularly diagnostic of a particular material. In general, the resistivity of a material depends on the porosity (including the percentage of fractures in rocks) and whether air or water fills these spaces. Sedimentary rocks, which are usually porous and have higher water saturation, usually have lower resistivity. Clay soils usually have a lower resistivity than sandy soils or sandstone. Therefore, it can be said that the resistivity of porous rocks is primarily related to the amount of water in the rock, the amount of salts and solutes in the water (the chemical composition of the water in the rock), and the type of rock (Sheriff & Geldart, 1995). Depending on the above factors, specific values change from one ohm-meter or less for clay saturated with salt water to 10^8 ohm-meter or even more for igneous and hard crystalline rocks such as dense quartzites (Figure 3-1).

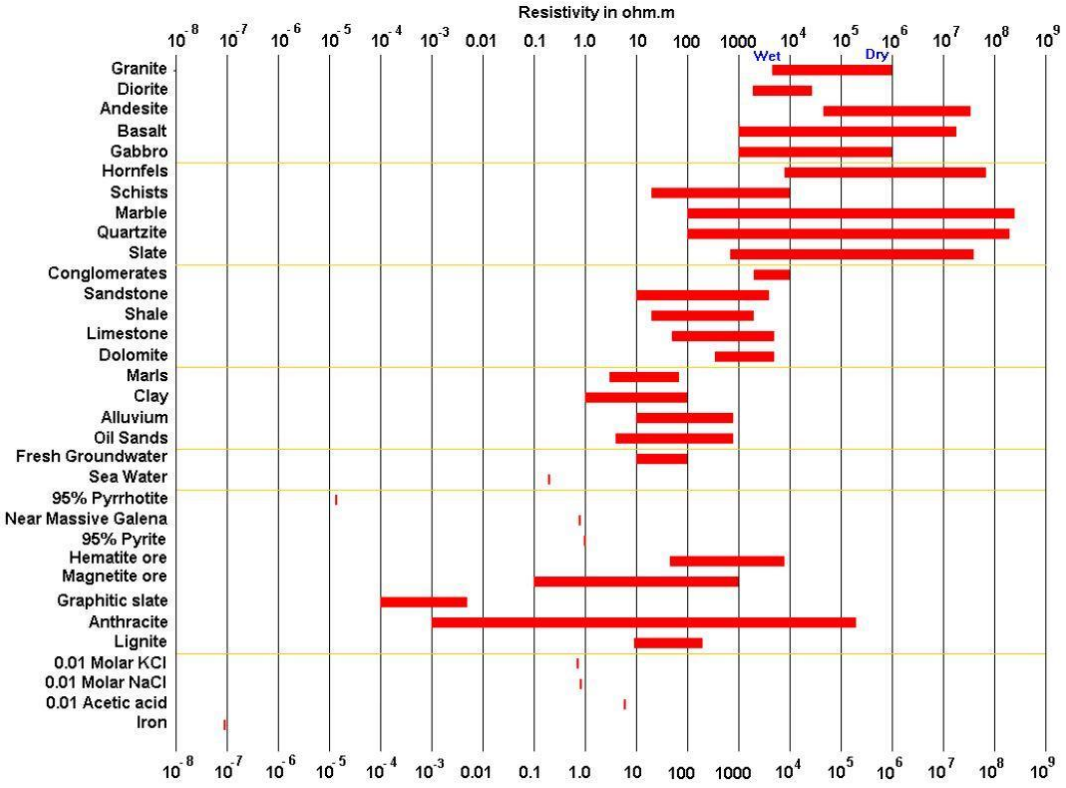

Figure 3-1) The range of resistivities of different materials (Loke, 2004).

Dry sandstone and gravel have a resistivity of several thousand ohm-meters, while if the same sediments are saturated with fresh water, their resistivity varies between 15 and 600 ohm-metres. The range of resistivities of different materials is shown in Figure 3-1 and Table 3-1. Resistivities

for given materials overlap in many cases, which can make it difficult to accurately interpret the data without additional information about the geology of the area. Within a given survey area, however, the expected range of resistivities for the different lithologies is much narrower, and resistivity can be a diagnostic tool.

Table 3-1) Resistivity of some types of geological materials (Domenico & Schwartz, 1997).

Common Geological Materials	**Resistivity (Ωm)**
Asmara limes	500 >= 1000
Cretaceous limes	200 – 500
Quartzite sandstone	300 – 500
Volcanic ash(Volcanic breccia)	20 – 100
underground water	10 – 100
Sea water	0.2
Limestone	50 – 5000
Shale	20 – 2000
Clay	1 – 100
Coarse-grain alluvium and conglomerate	300 – 10000
Medium grain alluvium	100 – 300
Fine-grained alluvium	50 – 100
Dry sand	1000 – 10000
Sand saturated with fresh water	50 – 500
Sand saturated with salt water	0.5 – 5

3.1.3 The DCR method

A DCR survey can show how the resistivity, hence subsurface composition whether sediment and soil or bedrock, varies with location along a profile and with depth into the ground. This method has been used in mining, hydrogeology, environmental purposes, and different types of exploration (Martínez et al., 2021).

Among the applications of the DCR method, the following can be mentioned:

1- The study of underground water to determine the water table level, the boundary of salt and fresh water, and the place of buried river channels (e.g., Jodry et al., 2019).

2- In civil engineering works, to determine the thickness of alluvium, the depth of the aquifer surface, the depth of bedrock, and the identification of clay layers (e.g., Diallo et al., 2019; Imani et al., 2021).

3-Mineral discoveries considering the low resistivity of metal minerals and identification of fractured and fault zones closely related to metal mineralization (e.g., Junaid et al., 2021).

DC resistivity survey configurations

In this method, a small electrical current, (for example, in the system used in this study, from a 12V battery), is directed into the ground through a pair of 'current' electrodes typically 30 cm long steel spikes that are hammered into the ground. The current spreads out from one electrode, radially (both down and sideways into the ground), and is returned to the other electrode, traveling between the two electrodes in a region that is roughly hemispheric if the ground is of uniform resistivity. There is a voltage field, in the ground and on the surface, associated with the current. This voltage is measured across another pair of 'potential' electrodes where their locations depend on the array configuration (Figure 3-2, see below).

The applied ‘direct’ electric current is, strictly speaking, an alternating current with a very low frequency (~1 Hz), typically with a square waveform.

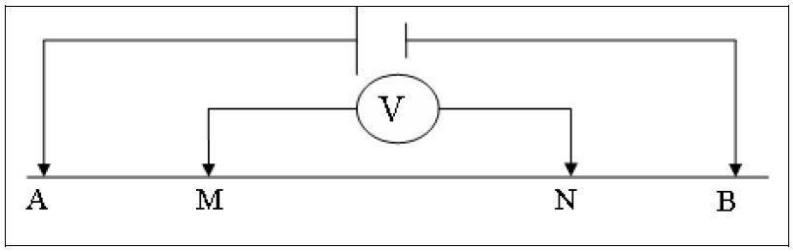

Figure 3-2) Four electrode configuration (for a Wenner-type array).

Current electrodes are labeled A and B, and N, M are the labels for the potential electrodes (Figure 3-2). The basic principle which is used in the DCR method is Ohm's law.

$$R = \Delta V/I \qquad (3.1)$$

After measuring the potential difference (ΔV) and the amount of injected current (I), resistance (R) is attainable. The 'apparent' resistivity is then calculated based on the R and the electrode locations using a geometric factor.

Apparent resistivity ρ_a has units of ohm-meters (Ω-m). If the ground is homogeneous, then the apparent resistivity measured is the actual resistivity of the ground. The following are the basic equations for calculating the apparent resistivity for a four electrode configuration.

$$\rho_a = K \frac{\Delta V}{I} \tag{3.2}$$

where the geometric factor (K) is given by the formula:

$$K = \frac{2\pi}{\left\{\left[\frac{1}{AM} - \frac{1}{BM}\right] - \left[\frac{1}{AN} - \frac{1}{BN}\right]\right\}} \tag{3.3}$$

Where AM, BM etc, are the distances between the current and potential electrodes (Figure 3-2). As seen in Equation 3.3, the geometric factor K depends only on these distances.

There are different arrangements of electrodes that have special applications. An electrode configuration is called an ‘array’. A series of measurements can be taken, with varying electrode positions and spacings to produce soundings or cross-sections, as described for selected array configurations below.

The depth of investigation of a DCR measurement depends on the separation between the current electrodes. The greater the current electrode spacing, the deeper the current penetrates the subsurface, allowing for determining resistivity for greater depth.

Different electrode arrays such as Wenner, Schlumberger and dipole-dipole, have varying electrode configurations and spacing and this affects their respective depths of investigation. Therefore the choice of array and electrode spacing is an important consideration in a DCR survey. The depth of investigation for different arrays is further described below.

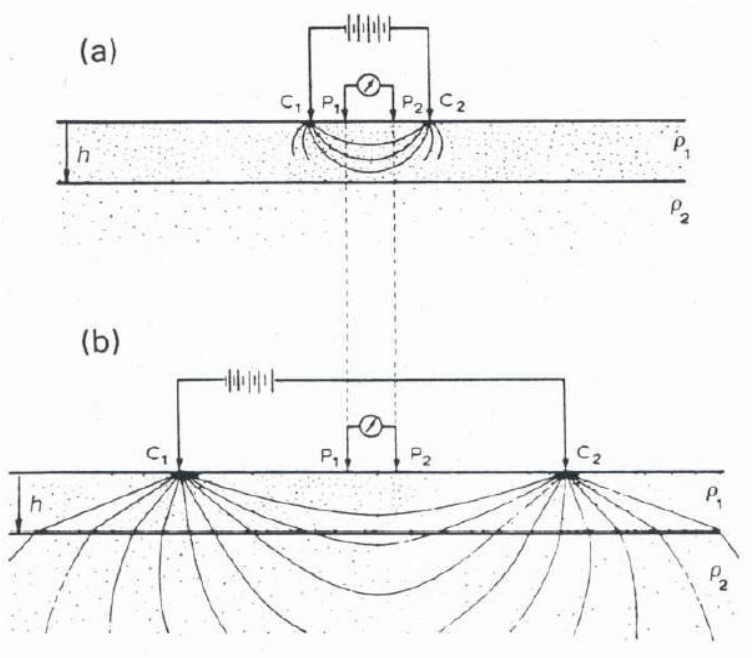

Figure 3-3)The Wenner-Schlumberger arrangement of the current and potential electrodes and how the current spreads into the ground (Telford et al., 1996).

Investigations of electrical resistivity are carried out by vertical electrical sounding (VES) and horizontal profiling (HP) methods.

VES is a method in which the resistivity of subsurface layers is evaluated in different depths, assuming that the ground is horizontally layered, whereas in HP, lateral changes of resistivity along the horizontal profile are measured. In VES, the investigation depth is increased by increasing the current electrodes' distances. In HP, the array is moved along the profile after each reading to track horizontal changes. A combination of VES and HP data can be collected in a region and the combined results analyzed.

Common electrode arrays

Based on the placement of the electrodes in relation to each other, there are different arrangements, such as Wenner, Schlumberger, and dipole-dipole arrays. In the following, these arrays are briefly compared. A summary of their key features is provided in Table 3-2.

Table 3-2) Comparison of the characteristics of different arrays (Carpenter & Habberjam, 1956; Loke, 2004).

Configurations	**Depth of investigation**	**Geometric factor**	**Key features**	**signal-to-noise**
Wenner	0.5 electrode spacing a	$K = 2\pi a$ (a = electrode spacing)	For surveys with multiple values of a, (good at detecting vertical boundaries between different resistivities)	High
Schlumberger	0.1 to 0.3 AB spacing	$K = \pi\left(\frac{a^2}{b}\right)\left(1 - \frac{b^2}{4a^2}\right)$ (a = half current electrode spacing b = potential electrode spacing)	Assuming minimal variation horizontally, finds the resistivity changes with depth.	Lower than Wenner ,higher than dipole-dipole
Dipole-dipole	Affected by both "a" spacing and "n" factor. Less than Wenner for a given injected current. Around 0.2 electrode spacing	$K = \pi an(n^2\text{-}1)$ (a = current electrode spacing = potential electrode spacing n = multiple of "a" between dipoles)	Sensitive to horizontal resistivity changes but fairly insensitive to vertical resistivity variations. Better horizontal data coverage than Wenner array for the same amount of work.	Low

Wenner configuration

In the Wenner arrangement, the electrodes are placed in a straight line with equal distances – designated 'a' – between them. This array was used for many early DCR surveys because of its simplicity (Carpenter & Habberjam, 1956).

The following equation depicts how apparent resistivity is calculated for the Wenner array:

$$\rho_a = 2\pi a(\Delta V/I) \quad (3.4)$$

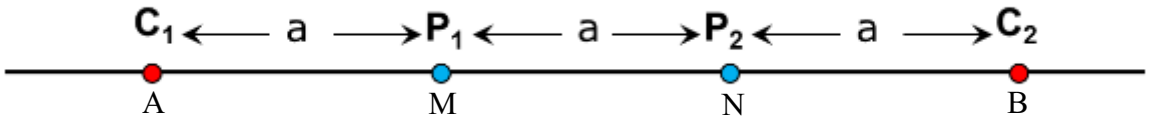

Figure 3-4) Diagram depicting the conventional geometry of the Wenner DCR array.

The sections shown in Figure 3.5 illustrate the sensitivity of the three Wenner configurations to the subsurface resistivity, under the assumption that variations in resistivity do not strongly affect the flow of current (Loke, 2004, 2012). Blue (negative) values indicate that anomalous ground will influence the apparent resistivity measurement in the opposite sense to the anomaly. The most sensitive areas in these arrays are near the surface between the electrodes.

The Wenner array is favored for noisy areas as the measurements have high signal-to-noise compared with other arrays. When Wenner's arrangement is used in depth soundings, the electrodes are extended around a fixed center, i.e., the a-spacing is increased many times, involving a change in location of all four electrodes. In lateral profiling, the a-spacing remains fixed, and all four electrodes move along line. Measurements along a profile using a Wenner array at one particular value of a, reveal variations in the horizontal between lithological units. If the a-spacing is systematically increased over the same profile, then the survey will reveal changes in resistivity with depth.

The Wenner Alpha array's depth of investigation is around 0.5 times the a-spacing, which is moderate in comparison to other arrays' investigation depth. The time taken using this array for 2-D surveys is one of its drawbacks, mainly when a limited number of electrodes is employed (Loke, 2004, 2012).

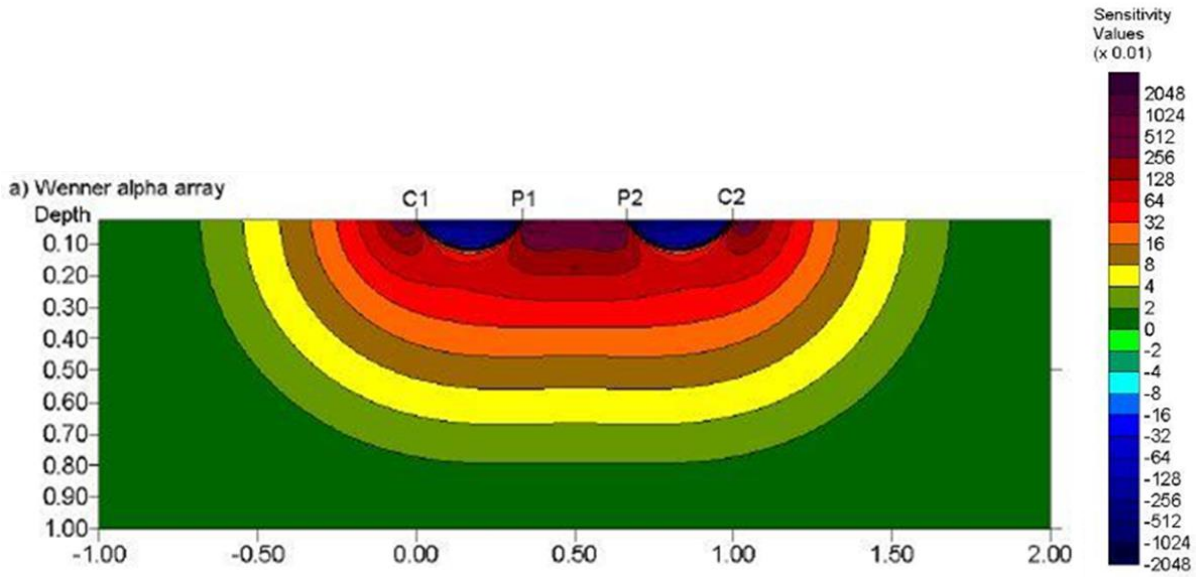

Figure 3-5) 2-D sensitivity sections for the Wenner array (Loke, 2004, 2012).

Schlumberger configuration

The standard Schlumberger arrangement is one of the most useful configurations for resistivity-sounding surveys. In the Schlumberger arrangement, the current electrodes are farther apart from each other than the potential electrodes (Figure 3-6). The geometric factor is equal to:

$$K = \pi\left(\frac{a^2}{b}\right)\left(1 - \frac{b^2}{4a^2}\right) \tag{3.5}$$

where a is the distance between current electrodes and the center of the array (x) and b is the distance between the potential electrodes (Figure 3-6).

Schlumberger-Wenner is a combination of Wenner and classical Schlumberger arrays, in that for the first measurement of a sounding the electrode spacings are the same ("a"), but for subsequent measurements the current electrodes are relocated outward a distance na. Compared to an expanding Wenner array, a Schlumberger sounding takes less time since only two electrodes need to be moved, but for the same strength of current its signal strength is weaker, since the potential difference is measured over a shorter horizontal distance. However, its signal strength is higher than dipole-dipole.

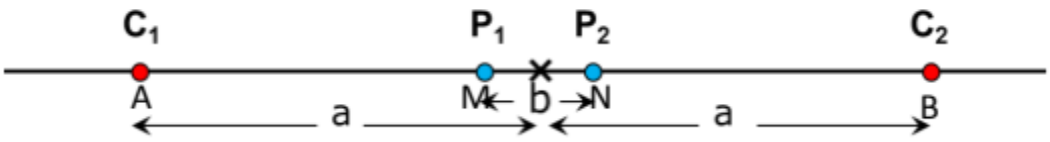

Figure 3-6) Diagram depicting the conventional geometry of the Schlumberger DCR array.

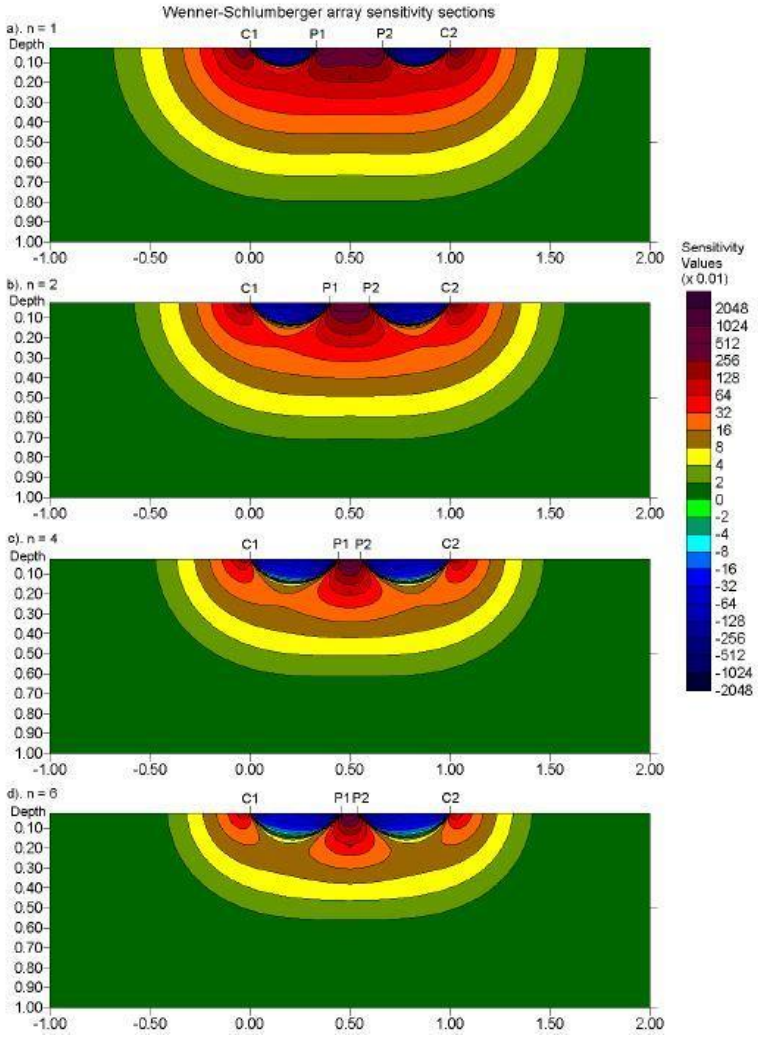

Figure 3-7) 2-D sensitivity sections for the Wenner-Schlumberger array. The sensitivity sections with (a) n=1, (b) n=2, (c) n=4, and (d) n=6 (Loke, 2004, 2012).

Dipole- dipole configuration

In this array, the spacing between potential electrodes ("a") is the same as the spacing between the current electrodes, and the potential electrodes are located outside the current electrodes (Figure 3-8). The distance between the inner electrodes (C1-P1 in Figure 3-9) is usually *na*, where n is an integer. A survey will start with n =1. The depth of penetration increases with the increase of "*n*." The current electrode positions A and B are often kept fixed (dangerously strong currents can be used to increase signal-to-noise), but they move along the line when the spread moves, and the potential electrodes are moved along a profile line by increasing *n*.

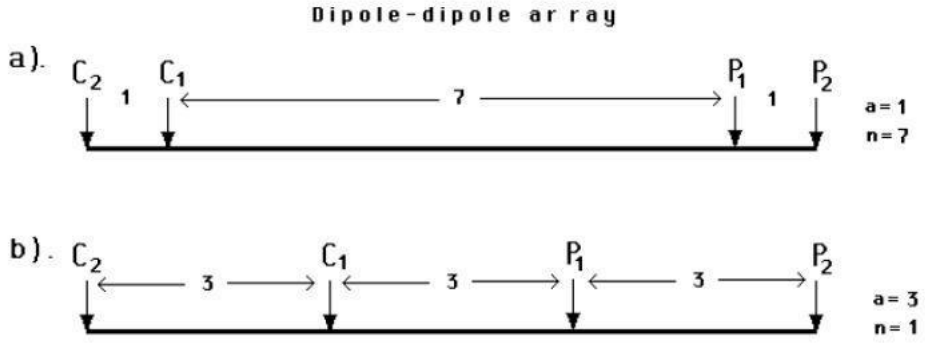

Figure 3-8) There are two dipole-dipole array alternative setups. The array lengths in both setups above are the same, but the "a" and "n" factors are different, resulting in drastically different signal intensities.

The dipole-dipole array is sensitive to variations in resistivity beneath each dipole pair (Figure 3-9). This array is highly sensitive to resistivity changes in the horizontal direction, as they contribute strongly to the measurement as the potential electrode pair passes over them. However, particularly as *n* increases, the measurements are less sensitive to the region between the dipoles and strong sensitivities being more concentrated under just the current and potential electrode pairs and so are relatively insensitive to vertical resistivity variations. As a result, surveys using the dipole-dipole array help detect vertical features like dykes and cavities but are not so effective at resolving vertical variation in resistivity such as occur for horizontal structures like different sedimentary layers.

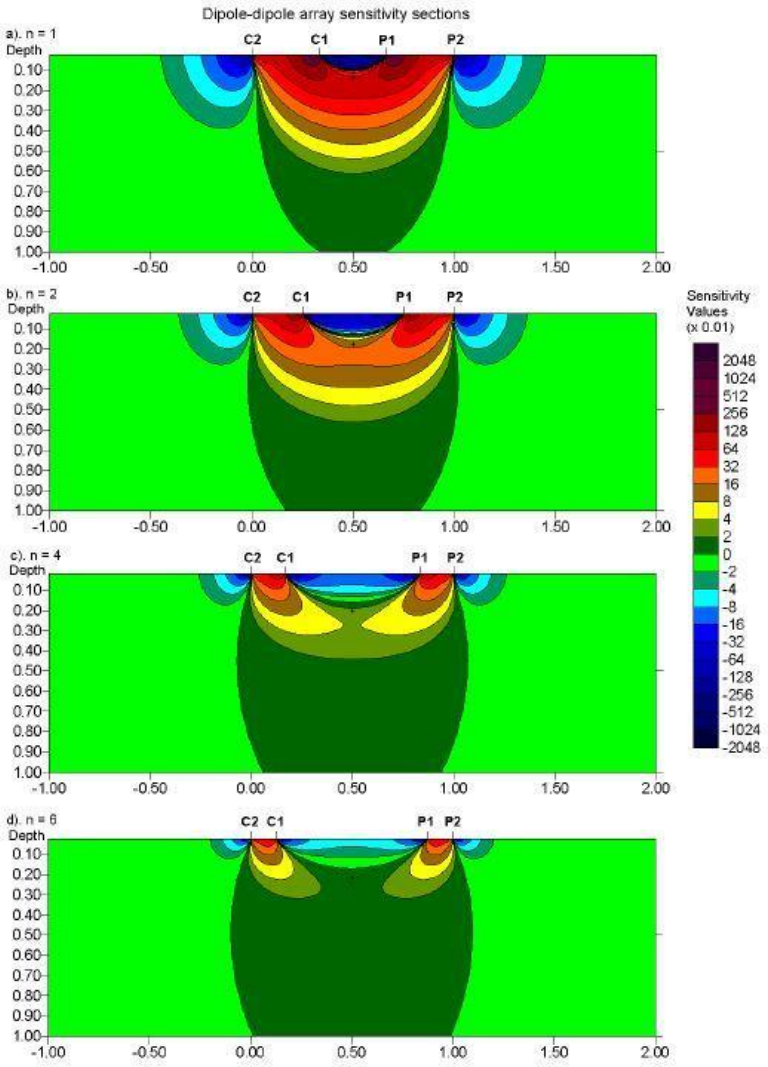

Figure 3-9)2-D sensitivity sections for the dipole-dipole array. The sections with (a) n=1, (b) n=2, (c) n=4 and (d) n=6(Loke, 2004, 2012).

Some advantages of using dipole-dipole configuration, in summary, are as follows:

1- Small distances between MN and AB reduce field work and increase work efficiency.

2- Current leakage is negligible due to the close distance between MN and AB electrodes.

Dispersion or unwanted spread of electric current might happen because of equipment and 'cable effects' (electromagnetic coupling between cables), nearby conductive material and ground water or conductive fluids. The small distance between current electrodes minimizes current leakage, meaning that the current stayed concentrated between the current electrodes, minimizing the potential for unwanted dispersion.

3- Electromagnetic coupling can be neglected due to the relatively large distance between the current and potential circuits (Telford et al., 1996).

This method also has disadvantages. The most important of these is (paradoxically) due to large distances between the dipoles: although this reduces electromagnetic coupling, it requires a large generator to inject current for deep investigation. This array's average depth of investigation is affected by both the "*a*" spacing and the "*n*" factor. When compared to the Wenner array, this array has a shallower depth of investigation for a given injected current and so to increase the investigation depth very high currents are used. This array provides better horizontal data coverage than the Wenner array for 2-D surveys for the same amount of work.

The relatively low signal strength for large values of the "*n*" factor is one potential downside of this array (Figure 3-9). The voltage is inversely proportional to the *square* of "*n*." Thus, the voltage decreases by a factor of 36 when *n* increases from 1 to 6. Increasing the *a* separation between the C1-C2 (and P1-P2) dipole pairs to lessen the drop in potential is a reasonable way to increase the depth of investigation when the total length of the array is expanded (Loke, 2004, 2012).

3.2 Induced polarisation (IP)

This measurement is taken with the same equipment and during the same survey as DCR. The resistivity of the ground is measured while the current is flowing, and the IP is measured when the current is switched off. If there is an IP effect, when a steady current between two electrodes is turned off, the voltage does not return to zero instantly. The way the voltage decays away with time tells us how much large-scale charge separation, i.e., polarisation occurred in the ground – between the patch of ground between the current electrodes (Figure 3-10). The charge is stored on the surfaces of conductive grains, such as sulphide or clays, which act somewhat like small capacitors dispersed within the ground (e.g., Parasnis, 2012). The charge on these surfaces builds up and decays relatively slowly as ions diffuse away from the surfaces (Telford et al., 1996).

The IP effect may be studied in two ways: in the time domain by detecting the voltage decay rate or in the frequency domain by measuring phase changes between sinusoidal currents and voltages.

The resulting potential measurement is depicted in Figure 3-10.

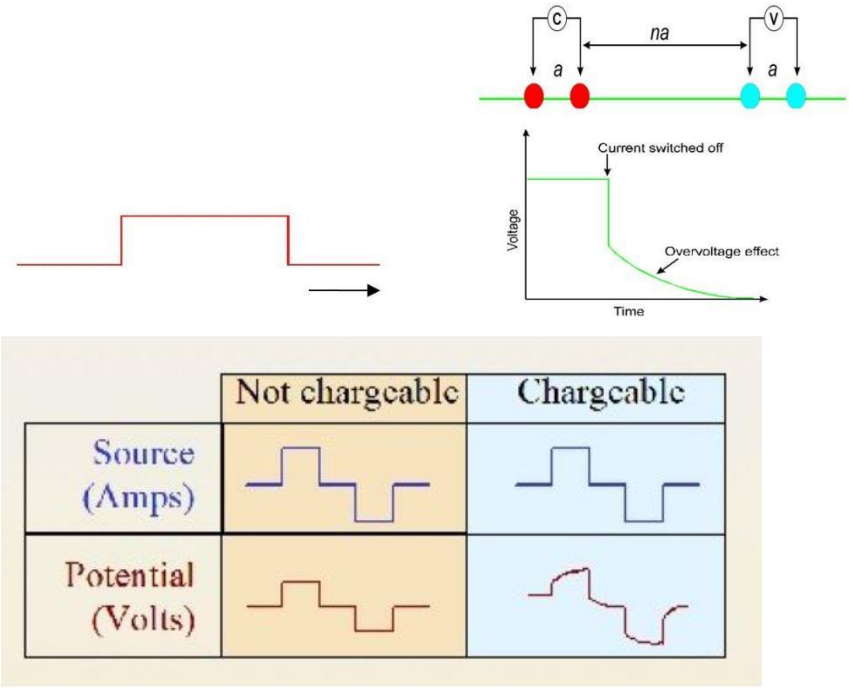

Figure 3-10) Demonstration of an induced polarization measurement using a standard arrangement of direct current four-electrode resistivity (Telford et al., 1996).

A graph of the measured potential along a 10-second current cycle is illustrated in Figure 3-11. The potential difference shortly before the current is shut off is the potential V_0. After the current is turned off, the potential is measured at many short periods (V1, V2, V3). This data is used to compute the chargeability M of the material in milliseconds (ms):

$$M = \frac{A}{\Delta V_{\mathrm{p}}} = \frac{1}{\Delta V_{\mathrm{p}}} \int_{t1}^{t2} V(t)\, dt \tag{3.6}$$

The chargeability measurement provided by Iris Syscal Junior is calculated as percentages or parts per thousand (ppt) of the voltage decay (V_0) that is measured after applying a current to the subsurface.

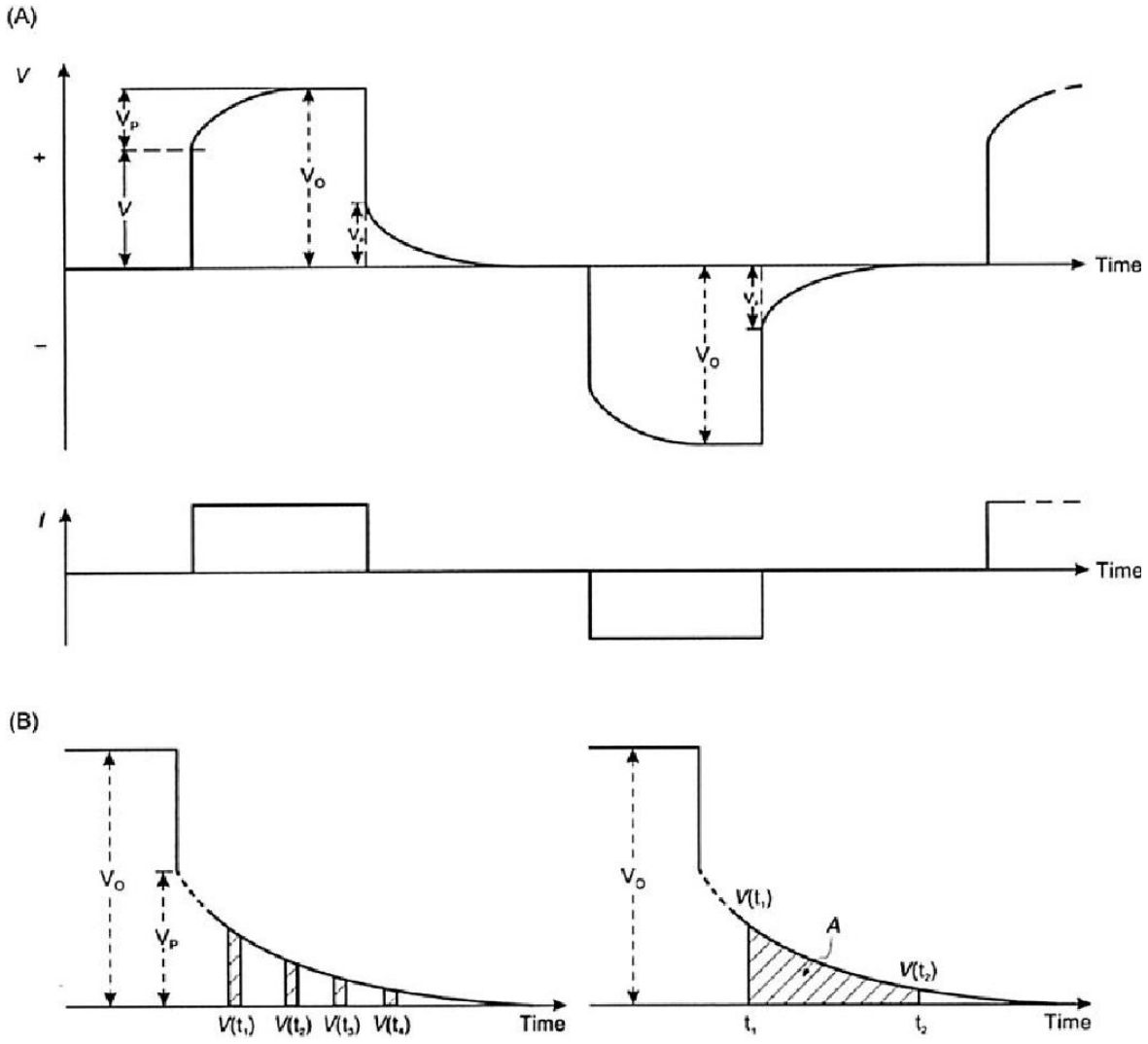

Figure 3-11)A) One application involves applying a pulsed current with alternating polarity and analyzing the effect of overvoltage (VP) and rise time on the voltage pulse's leading edge. B) Overvoltage can be measured at discrete time intervals (Vt) or by calculating the area A beneath the overvoltage curve (Reynolds, 2011).

IP is good for detecting certain types of ore deposits where the ore is scattered in small, disconnected pieces, (disseminated sulphides, common in Newfoundland), but also contamination in groundwater and clay.

It should be mentioned that the configurations used in resistivity measurements can also be used in the IP method, but mostly dipole-dipole (or pole-dipole) arrays are used because by using these two arrangements, the amount of electromagnetic coupling between current and potential circuits can be reduced to a minimum (Loke, 2004).

Induced polarization mechanisms

Although theoretically, energy can be stored in various forms - mechanical, electrical, and chemical - laboratory studies of polarization in different types of rocks have proven that chemical energy is far more important than others (Telford et al., 1996). This storage of chemical energy is the result of the following:

(a) Difference between electronic and ionic conductivity when metal minerals are present.

(b) Changing movement of ions in the fluids in the rock structure.

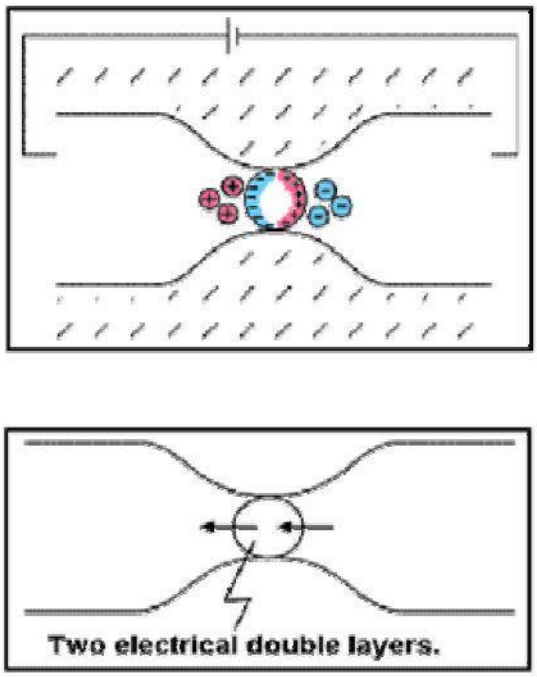

Figure 3-12) Electrode polarization

Electrode polarization happens (Figure 3-12), when an electric field is applied, and charges accumulate on the surfaces of the conductor metal particles. Spread throughout a non-conducting matrix, these conductors act as tiny capacitors. There are tiny accumulations of charge across the grain owing to the concentration of charged particles on either side. This is referred to as "electrode polarization" (Telford et al., 1996). This polarization is influenced by factors like mineral concentration, particle size and the characteristics of the surrounding rocks. The induced voltage can take up to several seconds to reach zero. Disseminated minerals, even in lower conductivity host rock, can produce strong induced polarisation respond (Telford et al., 1996). The more disseminated electronic conductors there are (the more surface area to collect charge), the longer this decay in potential takes place, which leads to higher chargeability values.

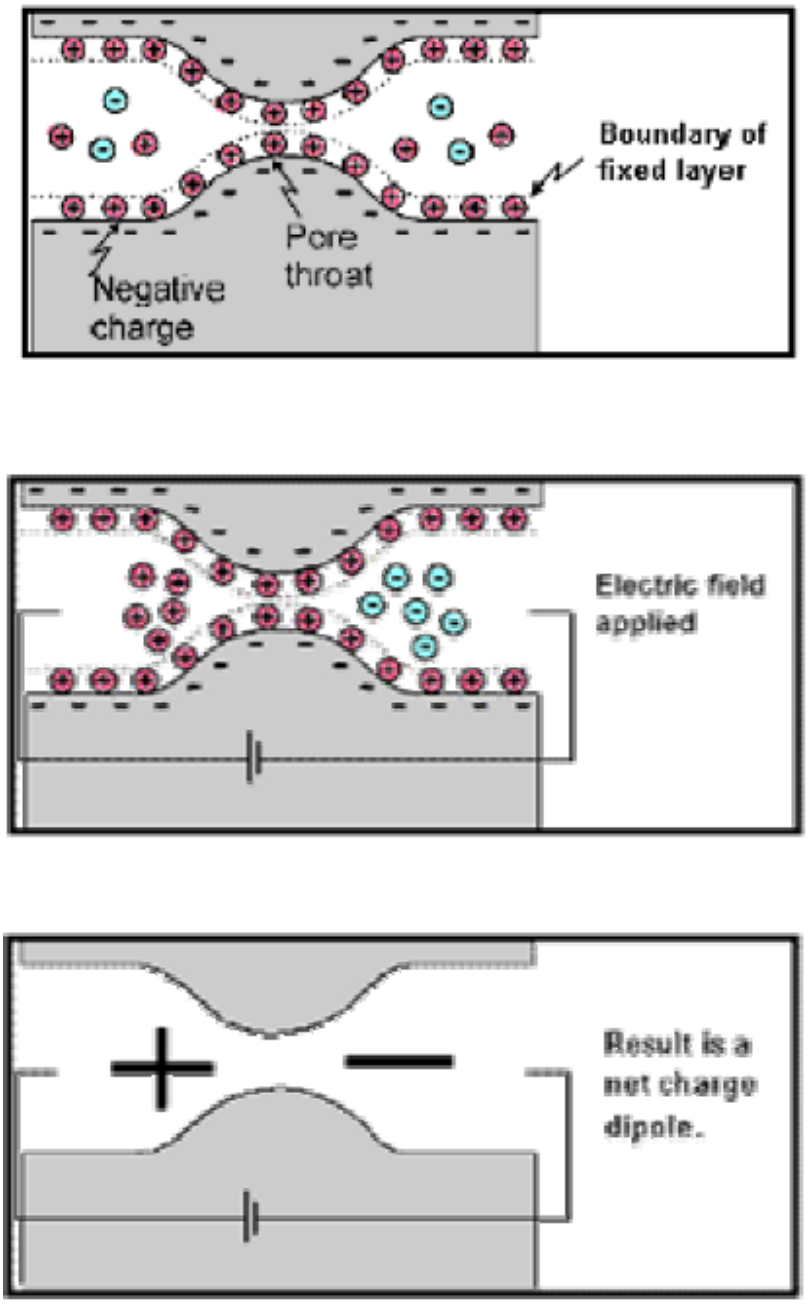

Figure 3-13)Membrane polarization (Jones, 2018).

Membrane polarization occurs when the blockage is insulators, with pore space narrowing to within several boundary layer thicknesses (Figure 3-13).

This effect may occur in rocks that do not contain metal minerals. This mechanism cannot be distinguished from electrode polarization by IP measurement unless the Spectral Induced Polarization (SIP) method is used (Telford et al., 1996).

Electrolytic conduction is the dominant factor in most Earth materials. When there are no good conductors such as metals, graphite or sulphide ores, and the frequency is low, this is the only form of conduction that exists. Therefore, the structure of the rocks must be somewhat porous to enable the current flow. Generally, clay minerals have a negative charge on the surface between the minerals and the fluid inside the pores. As a result, positive ions are attracted to this common surface, forming the 'Stern' layer. When a direct current potential is applied across a narrow capillary, the negative ions are stored on one side and move away from the other side of pores. As a result of such polarized distribution, the current flow is slow or, if the pore is blocked, interrupted. When the driving voltage is later turned off, the ion concentrations of like charges disperse over time (Figure 3-13).

The membrane IP effect is most evident in clay minerals because, in these minerals, the pores are microscopic. However, the degree of polarization does not increase uniformly with the density of the clay mineral, rather after reaching a maximum, it decreases again. This effect increases with the salinity of the fluid inside the pore. Because the polarization effect cannot be separated from the polarization of the electrode, which can lead to variation in the observed geological effects depending of the location and orientation of the electrodes. To minimise this effects careful attention must be paid to the electrode configuration and the interpretation of the resulting data (Telford et al., 1996).

3.3 Ground penetrating Radar (GPR)

GPR is a near-surface electromagnetic (EM) exploration method. GPR exploits contrasts in electromagnetic properties specifically dielectric permittivity and electrical conductivity to determine the physical boundaries of shallow structures. This method works by sending an EM pulse within the frequency range of 10 MHz to 2.6 GHz into the ground from a transmitter antenna while an adjacent receiver antenna (for bi-static GPR systems) records the pulses that are reflected from changes in the dielectric permittivity (ε) and electrical conductivity (σ) at the boundaries between rock types, or between rock and sediment, etc.

The receiver signals are recorded as a series of traces known as a radargram, similar to a seismic profile (Figure 3-14). Strong reflections show up as bright and dark bands.

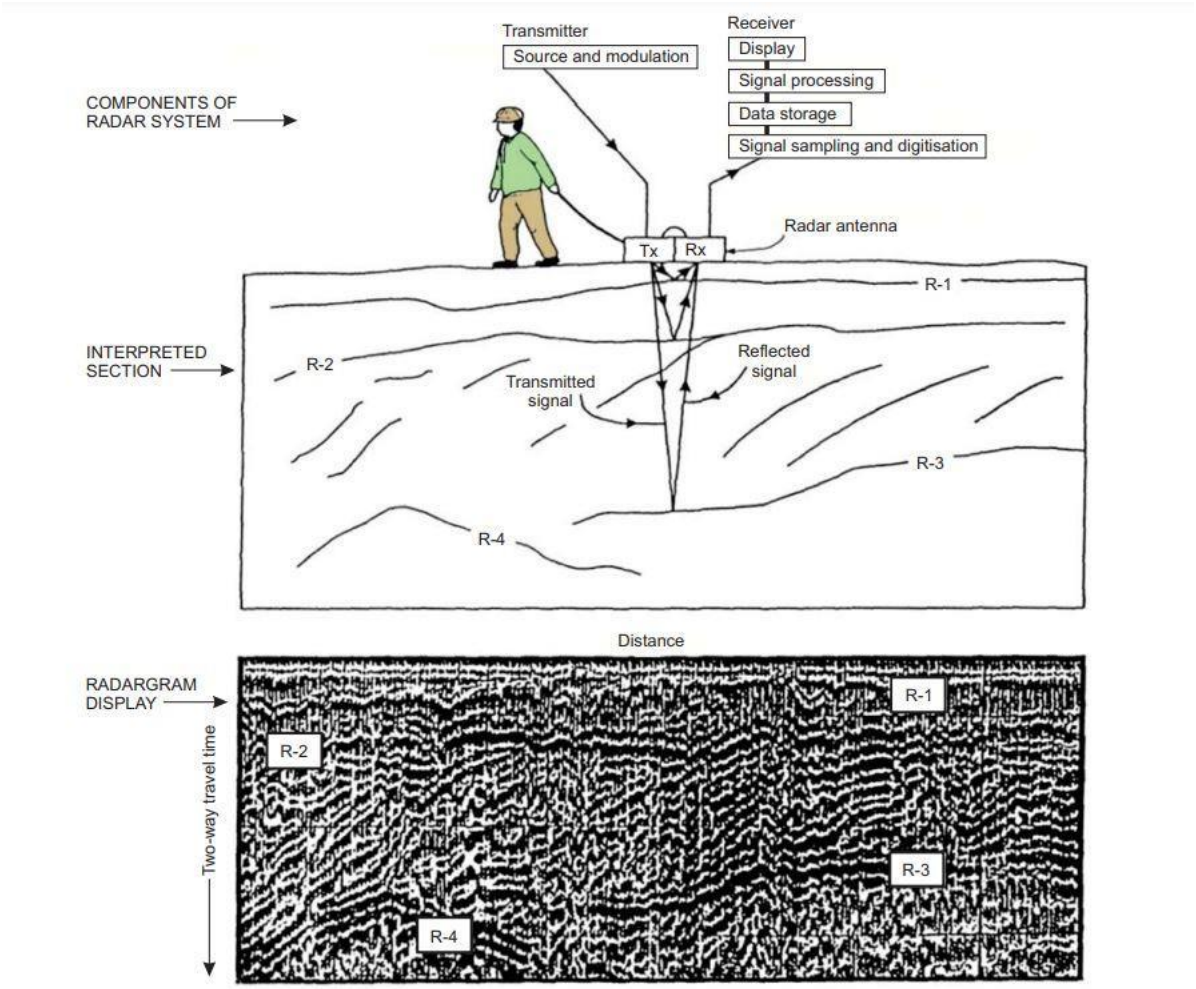

Figure 3-14) Illustration of the GPR surveying process (Reynolds, 2011).

The fundamentals of a GPR survey are illustrated in Figure 3-14 and Figure 3-15. The pair of GPR antennas consists of the transmitter (Tx) and receiver (Rx). Electromagnetic pulses are emitted from the Tx and received by the Rx after being reflected from a target object. Figure 3-16 illustrates that some of the emitted pulse is transmitted and some reflected. Reflection strength depends on the contrast in the electrical properties of the materials. Figure 3-17 is an example of a GPR survey over two tunnels, and the result shows two hyperbolae. The tunnels are easily detected because of the strong contrast between rock and air. This image includes other features, classified as noise that need to be removed for better data quality. In the next section, acquisition parameters will be discussed.

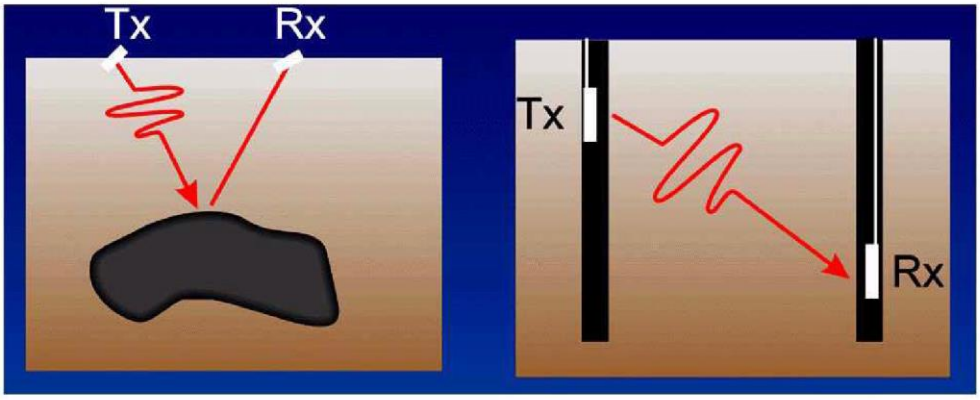

Figure 3-15) Fundamentals of a GPR survey (Annan, 2003).

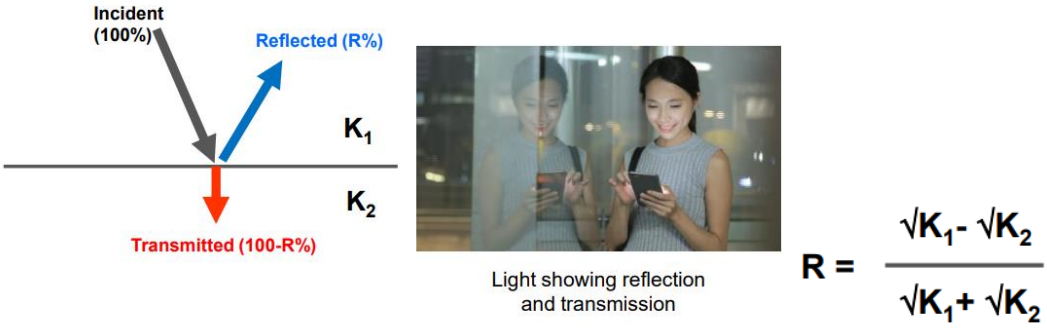

Figure 3-16) Reflections are created by the contrast.

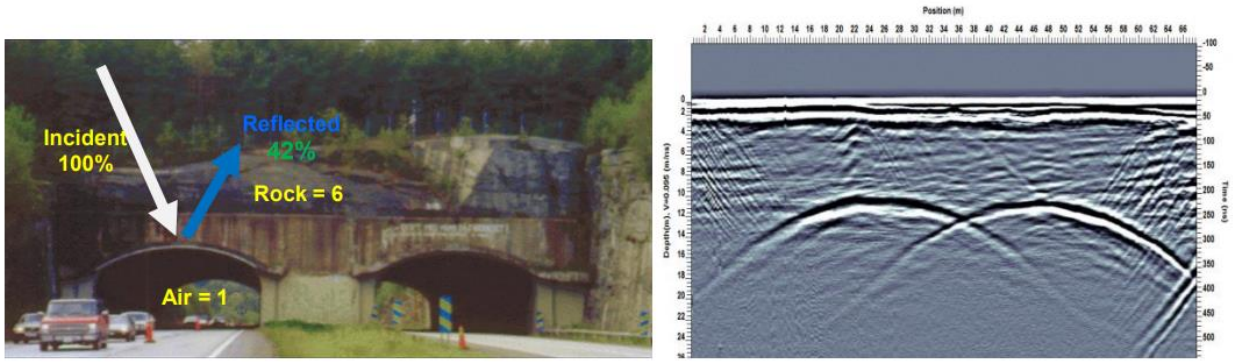

Figure 3-17) Example of GPR survey and the result using a 50 MHz GPR instrument. Reflection strength depends on the contrast of materials (Annan, 2003).

The fundamental physics behind the GPR method is based on the signal propagation of EM waves. When an alternating electric field is applied to a dielectric, the electric charges enclosed in

that material cannot translate in space but they can re-orient. They respond to that alternating field with tiny displacements of charge in the direction of the applied field, so-called polarization. The response of ions, electrons, and dipole molecules to these fields is different. In the case of non-polar molecules, the displacement occurs as a shift in the electron clouds relative to the nuclei. For polar molecules such as water, the molecules rotate in the direction of the applied field.

Loss of amplitude and penetration depth

There are several factors that decrease the amplitude of the GPR waves as they travel through subsurface environments and therefore how deep changes in material properties can be detected. These include geometrical spreading of waves, reflection when travelling through an interface, and scattering from items with size similar to the GPR wavelength. However, the main cause of energy reduction is "loss", which is a function of the electric and dielectric characteristics of the medium. The electromagnetic properties of materials depend on their composition and the amount of water in them, and these parameters significantly affect both the speed and loss of GPR waves. Some materials, such as polar ice, are nearly transparent to GPR waves, and these waves can pass through them without much dielectric and conductive losses. Other materials such as water-saturated soils, clays, and seawater are opaque to these waves and reflect or absorb most of their energy, so the waves are lost in a short distance (Reynolds, 2011).

A measure of signal loss is depicted by α, and its value is equal to 1/δ, where δ is the "skin depth", usually taken to mean the distance by which the amplitude is decreased by a factor of e. The loss "α" can be calculated by the following equation (Neal, 2004; Reynolds, 2011).

$$\alpha = \omega\left\{\left(\frac{\mu\varepsilon}{2}\right)\left[\left(1+\frac{\sigma^2}{\omega^2\varepsilon^2}\right)^{\frac{1}{2}}-1\right]\right\}^{\frac{1}{2}} \Rightarrow \delta = \frac{1}{\omega}\left\{\left(\frac{\mu\varepsilon}{2}\right)\left[\left(1+\frac{\sigma^2}{\omega^2\varepsilon^2}\right)^{\frac{1}{2}}-1\right]\right\}^{\frac{-1}{2}} \quad (3.7)$$

where ω is the fundamental GPR radial frequency (radians/s) being used. It can be seen from the above formula that the loss is directly dependent on the frequency, and the permeability (μ) and conductivity of the environment affect it. The ratio (σ/ε ω) is called the loss factor, and in low-loss environments such as pure sand, it is close to zero and can be ignored. In most geological conditions, conductivity has the greatest effect on the loss of GPR waves (Neal, 2004). For example, for a 500 MHz wave, the skin depth is only 1 cm for sea water and 2.2 cm for wet clay of conductivity 1 S/m (Singh, n.d.).

In areas where the formations are saturated with a conductive fluid, the high conductivity and relative permeability of liquid inside the formation increase the loss significantly. The presence of clay, due to the presence of water in its network structure, also has such an effect on energy loss (Reynolds, 2011).

The penetration depth – i.e., from how deep reflections can be detected before they are lost in the noise – is a few meters to a few 10's of meters (on glaciers it may be a few hundred meters), depending on the conductivity of the propagation medium, as well as the frequency of the wave used (Reynolds, 2011). Higher frequency antennas have shorter wavelengths, which can yield higher resolution but less depth of penetration. Lower frequency antennas have longer wavelengths that can yield a greater depth of penetration but lower resolution. For example, the penetration depth of the GPR survey carried out by the 250 MHz shielded antenna in July 2021 in Bay Bulls was about 5 meters. Figure 3-18 illustrates the relationship between different frequencies of antenna and depth of penetration and resolution.

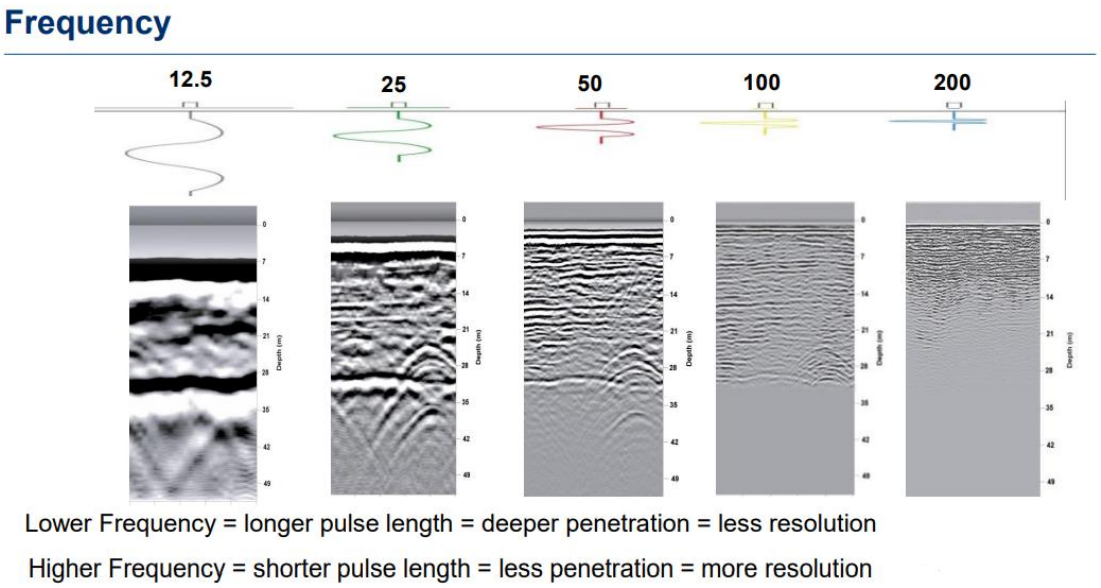

Figure 3-18) The relation between different frequencies and depth of penetration and resolution (Sensors & Software)

Electrical conductors, like metals, reflect the pulse back toward the surface so it cannot penetrate deeper than the top of the conductor. Though GPR can be an excellent tool for mapping the bottom of freshwater ponds and bogs, it is completely useless for targets below sea water as GPR signals are heavily damped in a conductor, with the dampening increasing as the conductivity increases and of very limited use over brackish water or on beaches where the sand is soaked with

salt water. Cobbles in the soil can scatter the pulse, so it is difficult to 'see' through many sorts of glacial till. Anthropogenic noise from power lines can also limit the penetration depth of unshielded antenna by overwhelming fainter signals coming from greater depth. Small size antennas (which radiate higher frequencies) are typically shielded from such noise, but the longer size antennas (which radiate lower frequencies) are too big for this to be practical. Figure 3-19 shows a summary of the typical penetration depths in various materials for various frequencies.

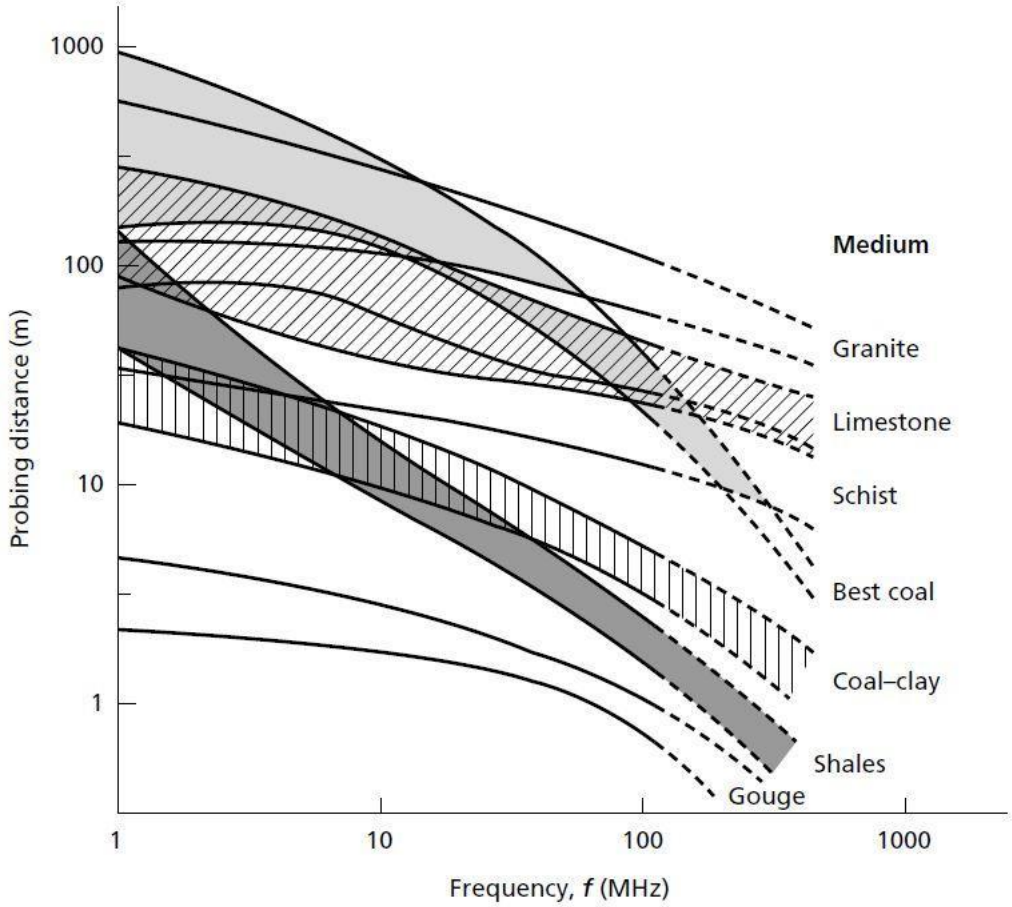

Figure 3-19) The maximum penetration depth available in different geological materials as a function of the frequency used (Reynolds, 2011) modified from (Cook, 1975).

In practice, using the GPR method in an area with high conductivity (greater than 0.01 S/m) is ineffective. This condition is seen in silty and clay environments and also in the presence of salty underground water (Van Overmeeren, 1994).

Wave velocity

The speed of GPR waves in subsurface environments is calculated by the following equation:

$$V = \frac{C_0}{\sqrt{\varepsilon_r \mu_r \frac{1+\sqrt{1+(\sigma/\varepsilon\omega)}}{2}}} \tag{3.8}$$

where C_0 is the velocity of electromagnetic waves invacuum, μ_r and ε_r depict magnetic permeability and dielectric permittivity relative to their values in vacuum, and ω is the fundamental GPR frequency being used. The impact of μ_r in a non-magnetized environment and at GPR frequencies is very small, so it is usually taken as 1. In low loss environments, the above formula becomes:

$$V = C_0/\sqrt{\varepsilon_r} \tag{3.9}$$

In using the above relationship, it should be considered that this relationship is not correct when dealing with materials with high conductivity such as sea water and some types of clays or when dealing with magnetic materials such as magnetite and hematite. Fortunately, this relationship can be used with a good approximation in most applications (Annan, 2001).

Resolution

Vertical resolution power is controlled by wavelength in GPR surveys (Kearey et al., 2002). The wavelength of electromagnetic waves is obtained from the following equation:

$$\lambda = v/f \tag{3.10}$$

In the above equation, v is the velocity of the GPR wave, and f indicates the frequency of that wave (in Hz).

Table 3-3 represents a theoretical resolution for typical sedimentary environments.

Table 3-3) Theoretical values for resolution of GPR in typical sedimental environments for different antennae. Values are λ/4-λ/2 (Sheriff & Geldart, 1995).

Antenna frequency	Lithology		
	Saturated sand 0.06 m/ns	Damp sand 0.1 m/ns	Dry sand 0.15 m/ns
50 MHz	0.3–0.6 m	0.5–1.0 m	0.75–1.5 m
100 MHz	0.15–0.3 m	0.25–0.50 m	0.375–0.75 m
200 MHz	0.075–0.15 m	0.125–0.25 m	0.1875–0.375 m

According to Knapp (1990), there are two ways that the concept of resolution in seismic reflection can be used with radar data. In the first definition, which deals with the ability to identify reflector location in space or time, vertical resolution is inversely proportional to frequency (Figure 3-18). The ability to distinguish between two tightly spaced features is described by the second definition (Knapp, 1990).

The best vertical resolution that can be achieved is one quarter of dominant wavelength (Sheriff, 1977). Then maximum vertical resolution recorded with high frequency (900 MHz) antennae is between 0.02 m and 0.08 m (e.g., Neal et al., 2002, 2003), which allows for the resolution of sets of laminae, beds and bed sets. For the 250 MHz antennae used in the present study, in typical overburden with a velocity of 0.1 m/ns, the resolution is about 10 cm.

Because higher frequencies are attenuated as waves travel through the subsurface (Bano, 1996; Jol, 1995), resulting in a longer average wavelength of the returning waves, the return centre frequency, which is the frequency that is most frequently detected or received by the antenna, is often used to determine realistic vertical resolution. The resolution of deeper reflections is slightly less because of the attenuation of energy in the higher-frequency antenna.

Reflection and transmission

At the interface of two materials with different electromagnetic properties, part of the electromagnetic wave passes through the interface, and the other part is reflected. Transmitted energy may be reflected by other interfaces below this layer. The relationship between the amount of energy transmitted and reflected is defined by the difference in EM wave impedance (Z). The formula for the impedance of an electromagnetic wave in free space is given by:

$$Z_0 = \sqrt[2]{\mu_0/\varepsilon_0} \tag{3.11}$$

where ε_0 is the permittivity of free space and μ_0 is the permeability of free space.

The impedance of an EM wave in a medium other than free space can be calculated using a modified formula that includes the relative permeability μ and relative permittivity ε_r of the medium:

$$Z = \sqrt[2]{\mu/\varepsilon_r} * Z_0 \quad (3.12)$$

If the wave hits the interface of two environments at 90 degree, the reflection (R) and transmission (T) coefficients, respectively, are expressed by the following relation:

$$R = (Z_2 - Z_1)/(Z_2 + Z_1) \quad (3.13)$$

$$T = (2Z_2)/(Z_2 + Z_1) \quad (3.14)$$

where Z_1 is the impedance of the first medium (from which the wave is coming) and Z_2 is the impedance of the second medium (into which the wave is entering) (Nabighian, 1988). These equations apply when an antenna is used as both transmitter and receiver (monostatic), basically for normal incidence wave. When two separate antennas (bi-static) are used to send and receive waves, the equations apply when the distance between the antennas is much smaller than the distance to the interface (Parasnis, 2012).

Changes in the type of fluid contained in a formation, small changes in porosity, changes in the type and shape of sedimentary particles, as well as their orientation and packing, are all good causes for reflections (Neal, 2004). As a result, phenomena such as water tables, sedimentary structures, and the boundary between rock units should be well revealed by the GPR method.

3.3.1 Data Acquisition

Proper data acquisition parameters are critical to the success of a GPR survey. These parameters impact the depth of investigation, resolution, and survey time. Several parameters should be considered during GPR profiling including:

Antenna frequency (center frequency of the antennas)

Step size

Time sampling interval

Trace stacking.

1) Antenna frequency*:* This is the main determinant of penetration depth and resolution for a given subsurface.

2) Step size (the distance between each data collection point). The step size of the GPR sampling should be chosen carefully based on the size of reflectors, image resolution, and so on. Figure 3-20 shows the effect of insufficient horizontal sampling in the horizontal resolution of sedimentary structures.

Generally, the step size should be a quarter to half of the wavelength in the host media. Increasing the step size reduces data volume and survey time. Assuming the typical EM wave velocity of rock is 0.1 m/ns, the recommended maximum step size for a 1 GHz GPR antenna is 2 cm, and for a 250 MHz antenna is 5 cm. If the step size is too large and exceeds the Nyquist sampling interval, a steeply dipping target cannot be defined properly (Jol & Bristow, 2003). Figure 3-21shows the effect of step size in resolving a layer with a 30° dip.

In this study, where the focus was on detecting metal culvert location, wooden supporting beams underneath the road, and determining the depth of till covering the bedrock and bedrock slope, the choice of appropriate step size in GPR data collection was crucial. These subsurface features have significant dimensions that can be detected effectively with a step size of 5 cm used for a 250 MHz antenna GPR. By selecting a 5 cm step size, the horizontal resolution to identify these features was achieved without sacrificing survey time.

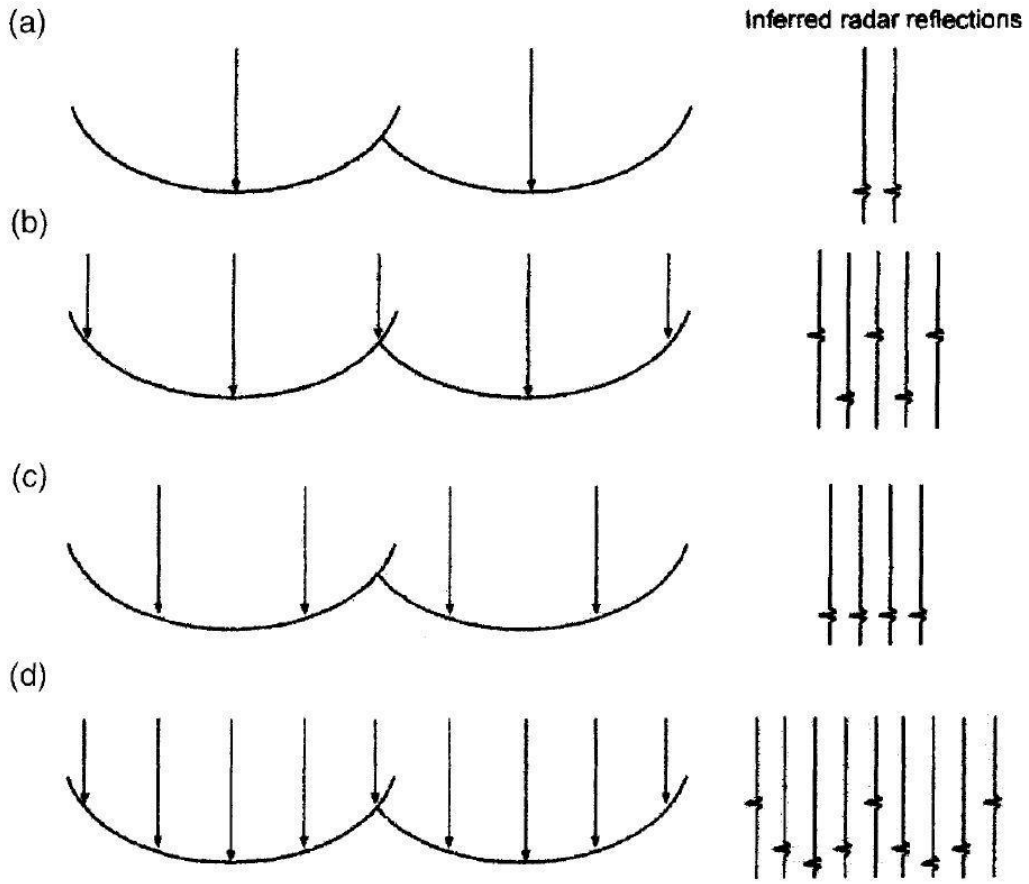

Figure 3-20) (a) A step size equal to trough width fails to image troughs; (b) a step size 1/2 of trough width causes spatial aliasing; (c) a step size 1/2 trough width but different sampling locations may be misinterpreted; (d) a step size 1/4 trough width, reflections start to resemble trough shapes. A step size of at least 1/4 trough width is necessary to depict troughs. Step size should ideally be as small as possible (Jol & Bristow, 2003).

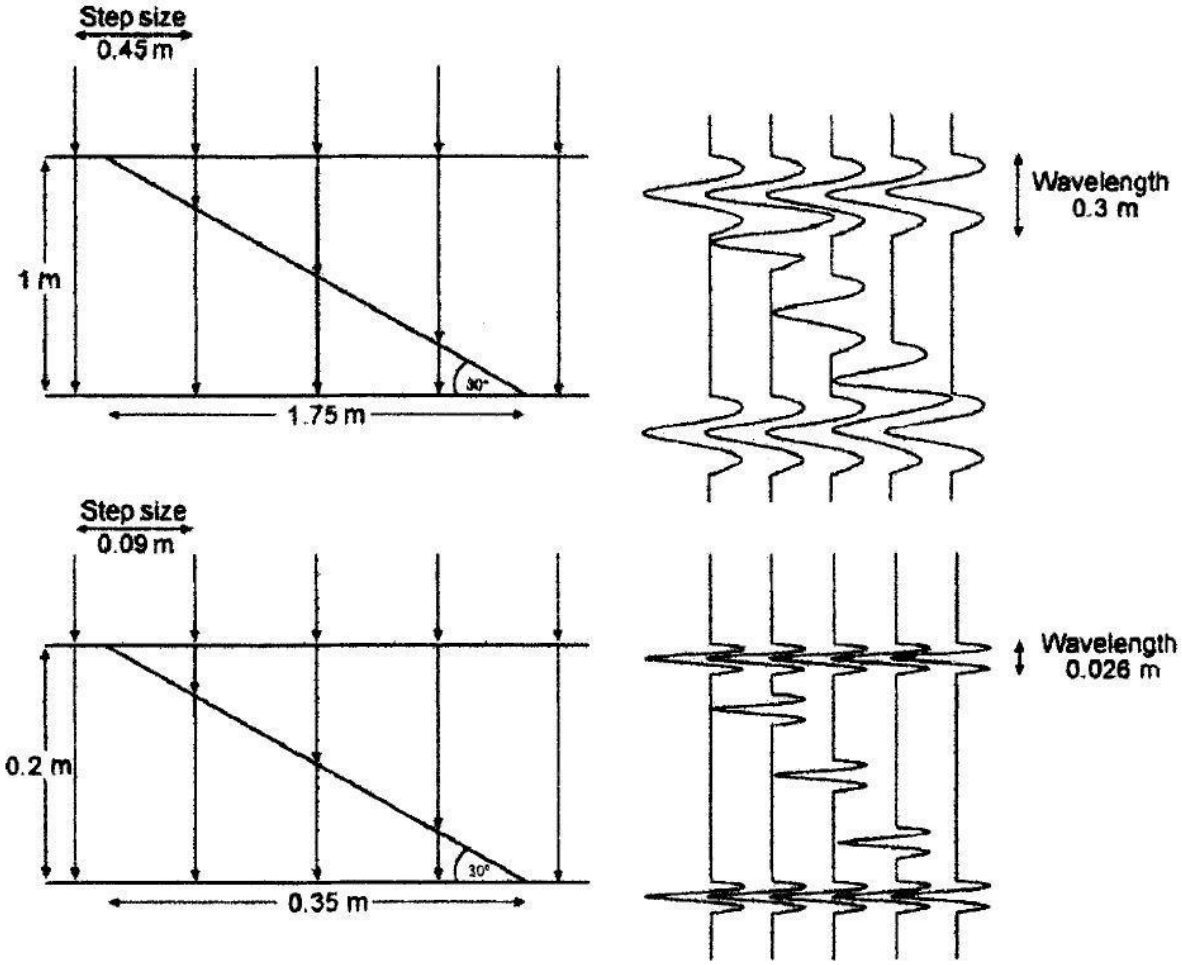

Figure 3-21) Effect of step size in the representation of a layer with a 30° dip. Top) It is possible to resolve the layer within a 1 m thick bed with a step size of less than 0.5 m and wavelength less than 0.5 m, Bottom) For a layer within a 0.2 m thick bed this requires a step size of less than 0.1 m and a wavelength of less than 0.1 m (Jol & Bristow, 2003).

3) The time sampling interval (sampling rate) is the rate at which the received signal is sampled. Based on the Nyquist principle, a higher sampling rate is required as the antennae frequency increases. If the time sampling rate is raised while the length of the time window remains constant, the data storage requirements will likewise grow (Jol & Bristow, 2003).

4) Trace stacking: The signal-to-noise ratio is increased by trace stacking. Random noise is reduced by averaging a set of repeated GPR shots. Figure 3-22shows the effect of stacking on the data quality (*Electromagnetic Geophysics*, 2015).

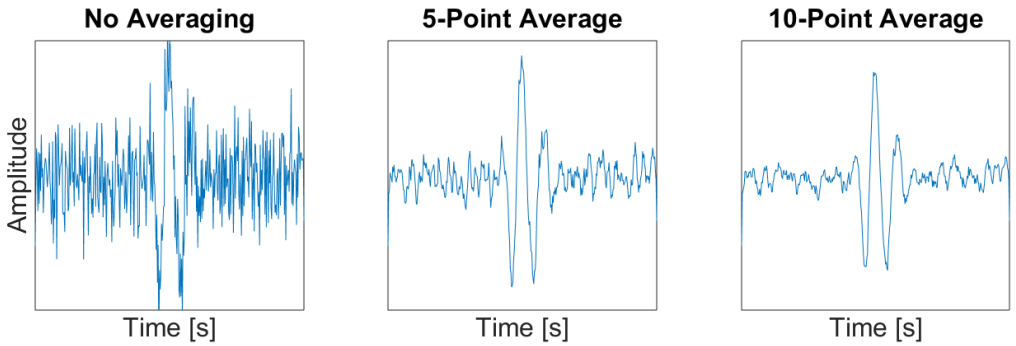

Figure 3-22) Example of how multiple averaging traces from the same Tx-Rx pair can improve the signal-to-noise ratio (Electromagnetic Geophysics, 2015).

GPR data acquisition methods

GPR data can be collected in 3 main ways: reflection profiling, common midpoint gathers, and tomography.

Reflection profiling or Common Offset

In this method, the antennas are kept at a fixed separation (a common offset) as they are moved along the ground. On a radargram, the propagation time of GPR waves to the reflector and the return to the receiver is shown on the vertical axis, while the location of the antennas is depicted on the horizontal axis (Figure 3-23). If the GPR wave velocity is measured independently or obtained from borehole data, the depth of the reflectors (subsurface targets) can be calculated. In the Common Offset method, different arrangements for the orientation of the antennas have been introduced, which can provide more information according to the purpose of the study. The most common arrangements of antennas are the arrangements with antennas parallel and perpendicular-broadside to the data collection lines (Annan, 2001).

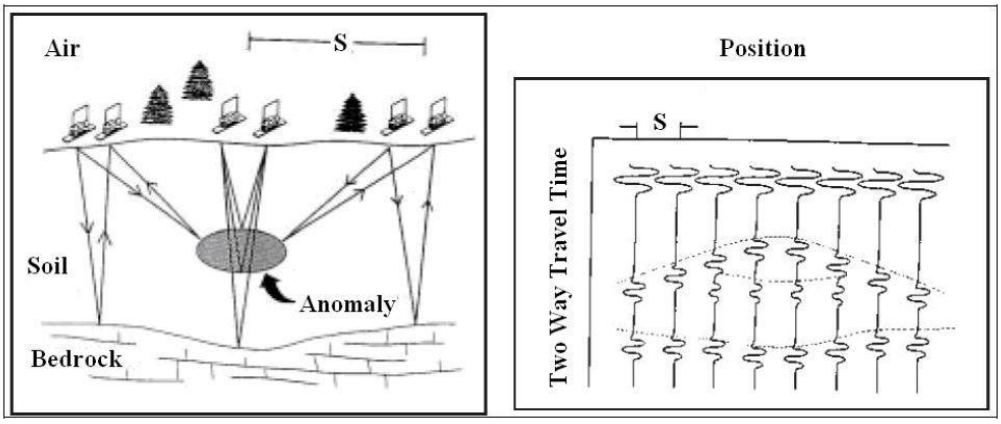

Figure 3-23) Schematic form of the profiling of the common offset (left side), along with its time section (right side) (Annan, 2001).

This profiling method, which is the most common data acquisition method, happens continuously or discretely. In the discrete profiling method, the antennas are placed in a fixed position on the ground, a trace is collected and then they are transferred to the next station. In this case, because the antennas are fixed, and there is more consistent coupling between the antennas and the ground, the reflections are seen clearly and also with a greater amplitude (Neal, 2004). Continuous profiling, the more commonly used method, involves moving the antennas while collecting data. This can provide a more comprehensive view of subsurface conditions in a shorter period of time, but may also introduce more noise and variability in the data.

CMP/WARR data acquisition

Common midpoint (CMP) and wide-angle reflection and refraction (WARR) measurements are used to obtain an estimate of the variation of GPR wave velocity with respect to depth (Annan, 2001). In the WARR arrangement, the transmitter is placed in a fixed position and the receiver is moved along the profile. This method of data acquisition should be done in an area where the main reflectors are flat and horizontal, and if they have a slope, their slope is very low. Also, in using this method, it is assumed that the subsurface reflectors' characteristics do not change throughout the study area. It is clear that such an assumption is not correct everywhere.

To avoid this assumption, the CMP arrangement should be utilized. In this method, both transmitter and receiver antennas move outward from a common fixed point. In this method, reflections from a common subsurface point are obtained, so the assumption of uniformity of the subsurface characteristics that were considered in the WARR arrangement is often met.

WARR arrangement was used in the early GPR systems, where metal cables were used for connections. But modern systems use optical fiber cables. Due to the advantages over the WARR arrangement, the CMP arrangement is the standard method of data collection to obtain the velocities in subsurface structures (Annan, 2001).

GPR Tomography

The GPR tomography method is based on the accurate measurement of wave travel time and pulse amplitude that propagates in the medium (Sensors & Software, 1999). This type of arrangement is not common as it requires significant processing and special operating conditions. In this method, transmitter and receiver antennas are placed on opposite sides of the volume to be

imaged. In this way, the antennas are placed in such a way that the waves travel directly through the investigation area, from transmitter to receiver antenna. As the antennas' distance is defined, the wave speed is calculated and using the input wave amplitude and GPR pulse period, the loss and propagation of waves in the environment are also calculated. Finally, in order to convert these values into desired parameters and prepare tomograms, processing is carried out on the data.

This method is used in various applications where it is possible to get transmitters and receivers on opposite sides of the investigation area, including investigations within borehole, assessment of man-made structures such as testing of concrete masses, and examination of columns and foundations of bridges (Reynolds, 2011). Additionally, in mining, it is utilized by placing the transmitter in a borehole and the receiver in another.

3.3.2 Post processing methods

The post-processing methods include time-zero correction and a moving average filter.

Time zero correction

Time zero correction is the first step in the processing of GPR data. It is not a constant value but depends on the surface material type and the antenna setup configuration (Yelf, 2006). The reason for applying this correction is to compensate for the time delay of the first arrival of the radar pulse at the receiver. Therefore by placing the first event in its actual location, the other events will also be in their actual positions. There are generally five points in traces to be selected as the starting point or zero points, as shown in Figure 3-24. Figure 3-25 shows the issues of traces with varying zero points, and processing was conducted to move all traces to a common zero point c.

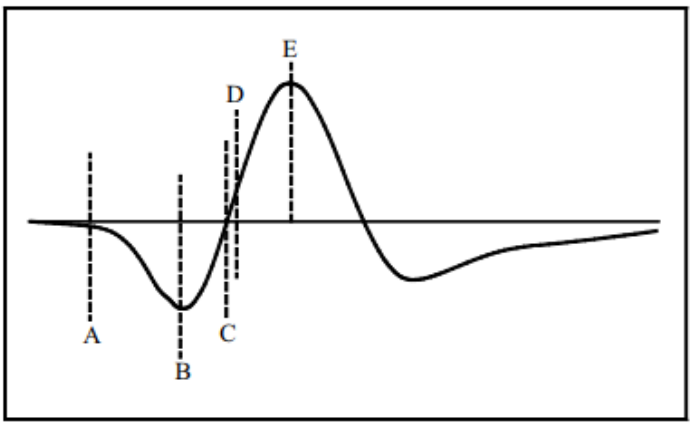

Figure 3-24)The options of picking the first arrival (Yelf, 2006).

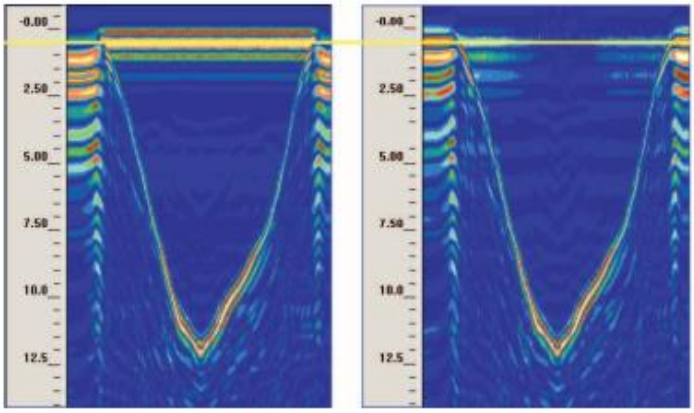

Figure 3-25) a) The traces move up, and b) the first points are shifted to the same start time using the first cross-over point c in Figure 3-24 (Yelf, 2006).

Signal saturation, Dewow

Due to the short time intervals between the pulses sent by the transmitter and arriving at the receiver directly through the air and along the ground surface, as well as the presence of reflections originating from shallow masses, the receiver is saturated with signals at early times (Neal, 2004).

Many GPR data show a significantly low-frequency component either due to inductive phenomena or possible instrument limitation. This low-frequency energy often yields a slowly time-varying component to the measured field data, causing the base level of the received signal to go up or down. This effect is known as baseline "wow" (Jol, 2008). The wow effect can make it difficult to distinguish between signal and noise in GPR data and can also affect the accuracy of the data interpretation. Therefore, it is important to be aware of this effect and take it into consideration. The process of removing this effect is referred to as "Dewow". A high-pass filter is usually applied to the data to remove this low-frequency noise. Sensors & Software offers two solutions to reduce these noises, the use of the Dewow filter and the DC-Shift filter. The Dewow filter works by estimating the base line and subtracting it from the original signal, effectively removing the wow effect. DC-shift filter on the other hand, is used to remove the DC component of the signal (caused by circuit biasing issue resulting from factors like sensor calibration or electronic noise, in the GPR system). This filter works by subtracting the mean value of the original signal. The choice of which filter to use may depend on the specific characteristics of the noise and the type of GPR survey being conducted. In Figure 3-26, a GPR cross-section is displayed before and after applying the Dewow filter.

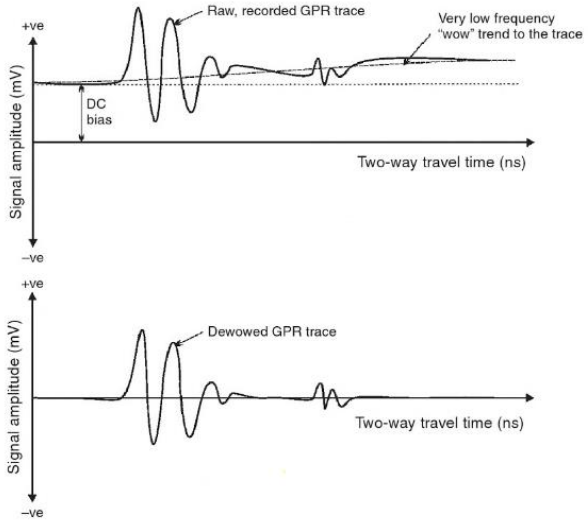

Figure 3-26) Raw GPR trace before Dewow (Top) and after (Bottom) (Jol, 2008).

In Figure 3-26 in the top illustration, signal saturation causes a DC offset or "bias" that creates a low-frequency trend in the data. In the bottom illustration, by applying the Dewow, the signal now has the desired mean amplitude of zero. The low-frequency trend is removed, and the high-frequency signal is preserved.

Figure 3-27 illustrates wow effect and Dewow filter on GPR data and how this filter can improve the data.

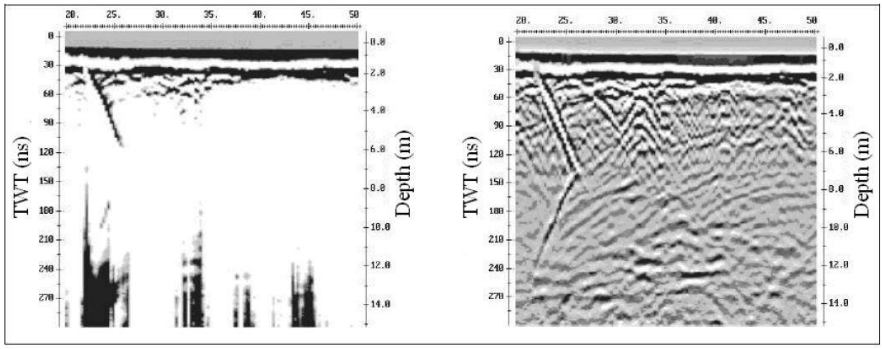

Figure 3-27) Wow effect on GPR data (left side). After applying the dewow filter reflections are well-defined (right side) (Jol, 2008).

Band-pass filtering

The GPR antennas transmit and receive a distribution of frequencies; when surveying with an antenna frequency of 250 MHz, the majority of the signal received will be within +/- 50 MHz of the frequency. However, the GPR also receives a small portion of the frequency distribution at the lower and higher ends of the spectrum. A high-pass filter cuts any frequencies below a specified

value out of the distribution. A low-pass filter cuts any frequencies above a specified value. These filters used together create a "band-pass filter" that cleans up the dataset and enhances the desired signal and removes undesired high and low-frequency noise from the center frequency of the frequency distribution (Sensors & Software Inc, 2015). Band-pass filtering is typically used to eliminate or reduce unwanted global background and system noise, leading to an enhancement in the signal-to-noise ratio (Xie et al., 2013). In Figure 3-28 the fundamentals of the band-pass filter in the frequency domain are illustrated.

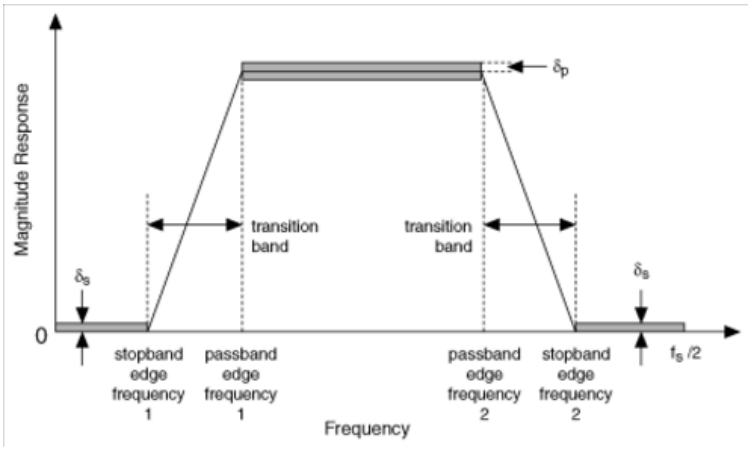

Figure 3-28) Illustration of the bandpass filter in the frequency domain (Sensors & Software Inc, 2015).

A good rule of thumb is to set the pass region symmetrically around the peak signal frequency with a bandwidth equal to 1.5 times its value. The recommended bandwidth for 1GHz is 250 MHz to 1750 MHz and for 250MHz it is 62.5 MHz to 437.5 MHz (Jol, 2008).

Gain algorithms

EM waves lose significant energy during propagation through the subsurface due to spherical spreading and intrinsic scattering attenuation. Therefore, these energy losses have to be compensated by applying gain. Manipulating the gain and attenuation variables allows the user to enhance attenuated reflections at depth (Annan et al., 1992). These gains help us restore and preserve the proportional amplitudes in the GPR data, making sure that the important information is not lost during data collection and processing process (Neal, 2004).

The SEC2 gain is the product of a linear time gain and an exponential time gain, with a defined maximum gain. This gain attempts to compensate for the spherical spreading losses and the exponential Ohmic dissipation of energy. Since GPR data is attenuated exponentially and the SEC2

is an exponential gain, it tends to be the gain closest to physical reality (Sensors & Software Inc, 2015).

In some cases, it may be necessary to manually adjust the gain of the GPR data to improve the visibility of weaker signals. This can be done by multiplying the data points by a user-supplied function, g (y) or g (t). This is known as time or spatial varying gain. This gain applies manually from the desired depth onwards. It is important to know that when manually adjusting the gain of the GPR data, it should be done with caution and consideration of the potential impact on the interpretation of the data. Over-gaining the data can result in a noisy and complicated profile, making it difficult to distinguish between signal and noise.

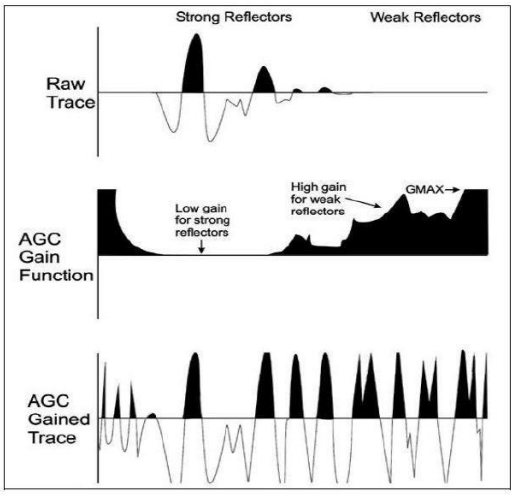

Figure 3-29) A single trace of a GPR profile before and after applying AGC to it (Sensors & Software, 1999).

Dealing with noise

GPR systems are generally wideband receivers. Hence they may encounter interference from man-made sources such as FM radio transmitters, mobile phones, their transmitter towers, and wireless and other radio instruments. Figure 3-30 shows a GPR profile taken near a military airport. Note the effect of high frequency radio waves, in the form of noisy bands within the top profile, (panel a). This is an unfiltered and unprocessed 100 MHz radar reflection profile which exhibits high frequency ambient noise caused by aircraft radio communications. Panel b) depicts the profile with the noise mostly eliminated by filtering the profile in the time domain with a low pass filter having a cut off of 125 MHz. Panel c) shows the profile with the lower frequency noise eliminated using spatial filtering with an alpha-mean trim filter (Neal, 2004).

In many cases, background and random noise are reduced by stacking traces when collecting data. In some cases, by choosing an antenna with a different frequency than the frequency of noise sources, such problems can be avoided. Of course, with the increase in the number of stacked traces in the collection stations, the time required for data acquisition increases, and choosing a frequency different from the samples may not be compatible with the primary objectives of the project, including the depth of penetration and the desired resolution (Neal, 2004).

In addition to random noise in the data, there is systematic and regular noise. One of the most common sorts of systematic noise is ringing. It is characterized by multiple reflection event that are dominated by a single frequency. These reflections can obscure the primary reflection and make it difficult to accurately interpret the data. This type of noise can be caused by several factors. It can be created when wire cables are used to connect transmitter and receiver to the console in a radar system. This is because the cable can act as a second antenna and pick up unwanted signal. Using fiber-optic cables can help decrease this effect (Annan et al., 1992). According to Neal (2004), a series of reflections (ringing) can occur when a radar signal bounces back and forth between an antenna and a highly conductive reflector, such as salty waters and conductive.

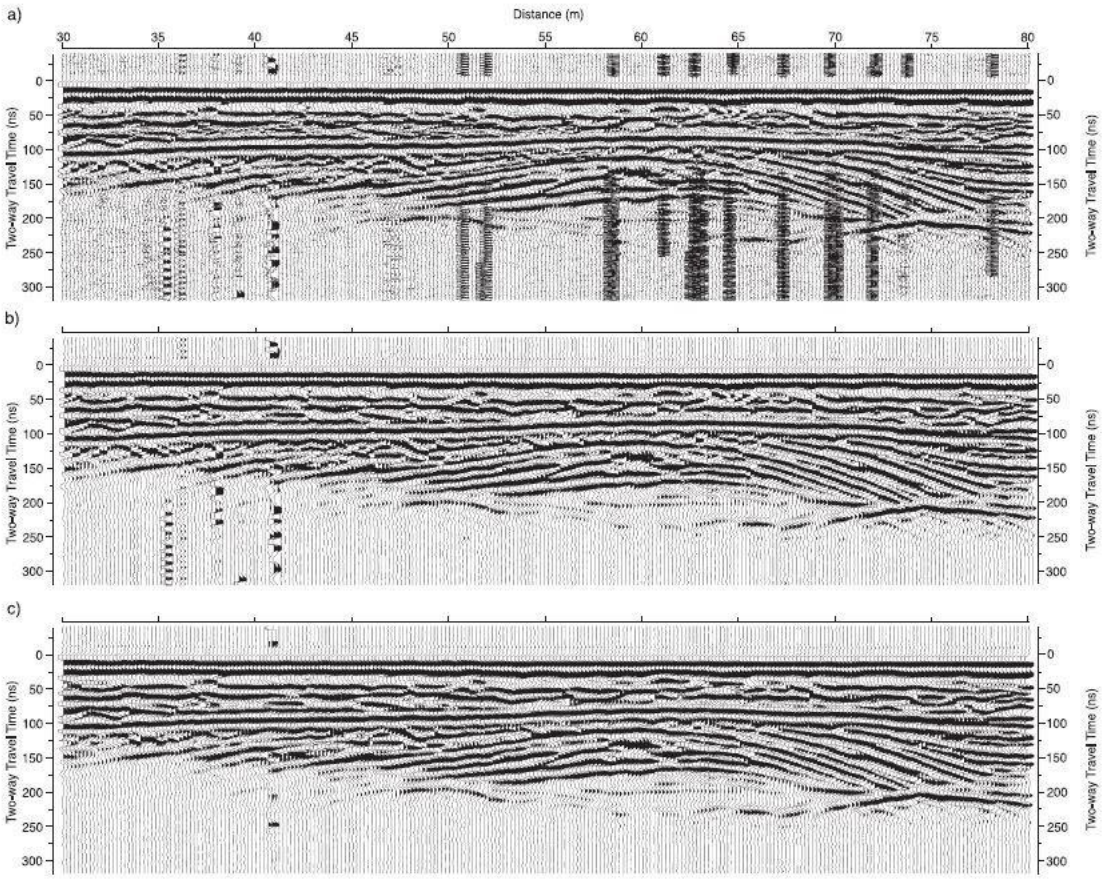

Figure 3-30) A GPR profile taken near a military airport. This filter is particularly effective in removing single 'bad' traces as reported by Sensors and Software (1998) The profile all have a minimum limiting AGC gain of 1000 (Neal, 2004).

Background removal or Background subtraction filter:

Background removal (or background average subtracting in Sensors and Software terminology) is used to subtract the average trace of the entire GPR line from each trace in the line. This process enhances localized events (such as hyperbolas from point targets) and suppresses horizontal or slowly varying events. The primary purpose of using this filter is to remove the system-induced irregularities. Background subtraction is similar to background removal but uses the running average over a localized set of traces and subtracts it from the center trace (Sensors & Software Inc, 2015). This can be very useful for removing localized flat-lying responses or signal from stationary objects in the surrounding environment that can contaminate the GPR data. This filter can help detect objects close to the surface that might be concealed by strong signal on top of the image. It can also improve the clarity of hyperbolas deeper in the data. However, it is important to note that using the background subtraction filter if your target is flat, as it can also remove other

flat responses and mask features of interest such as soil boundaries (Sensors & Software Inc, 2015). This is because the filter can remove both the near surface feature and the background signal from the surrounding environment, making it difficult to distinguish between the two.

3.4 Real Time Kinetics global positioning system (RTK)

Real-Time Kinetics (RTK) is a satellite navigation technique used to enhance the precision of position data from Global Positioning System (GPS) and other satellite navigation system. RTK is a method used to obtain locations in 3D with a precision of a few centimeters. These days, it is commonly used in infrastructure construction. It uses the same GPS satellites as handheld GPS units, but employs two GPS receivers: one, mounted on a tripod (Figure 3-31a) is a stationary 'base' which collects satellite data over a few hours in order to obtain a very precise location; the other, mounted on a staff (Figure 3-31b) is a 'rover', which the surveyor carries around the survey area, recording positions. The fixed base station and rover unit measure the difference between the satellite signal arrival-times at the two locations, enabling high precision positioning. The data collected at the base station can be post-processed to get the accuracy of its position, and a correction then applied to all the rover locations to get them just as accurate.

In RTK the base receives signals from GPS satellites and calculates its precise position using carrier phase measurements. The base station then transmits this position information in real-time to the receiver unit, which also receives signals from GPS satellites. The rover unit compares the carrier phase measurement it receives from the satellite with the carrier phase measurement it receives from the base station, allowing it to calculate its own precise position. The key to the RTK system’s accuracy is the use of carrier phase measurements, which provide a very precise measurements of the phase of the radio signal transmitted by the GPS satellites. These measurements are sensitive to variations in the signal strength caused by ionospheric and other atmospheric factors, as well as to any errors in the timing of the GPS signal. By using RTK, it is possible to achieve centimeter-level accuracy in real-time positioning, making it valuable tool for a variety of applications, such as surveying, mapping and construction.

Figure 3-31) a) RTK base receiver on a tripod. Bread and Cheese site, April 1, 2021. b) RTK rover receiver on staff. Operator Marzieh Arshian. The Cliff site, April 26, 2021.

4 Survey Procedures

4.1 Field Methods

4.1.1 Electrical method

Resistivity data can be acquired in 1-Dimensional, 2-Dimensional, and 3-Dimensional forms (Loke, 1999). A 2-D resistivity model that varies in resistivity in the horizontal and vertical direction is in general more accurate than a series of 1-D models over the same ground. 2-D electrical imaging survey results are complementary to those achieved by other geophysical methods. For instance, seismics can map subsurface undulating interfaces, but it has limitations in detecting discrete subsurface bodies (without using advance processing techniques), including boulders and cavities (Loke, 2012). On the other hand, GPR can provide a more detailed picture of them within a limited depth. 2-D electrical survey results can be integrated with seismic or GPR survey results, depending on the purpose of the study, to obtain complementary information about the subsurface (Loke, 2012).

A programmable Iris Instruments Syscal Junior DCR unit was used to collect both resistivity and chargeability data at the sites of interest in Bay Bulls. This instrument is an imaging system in which the two measurements can be made simultaneously for each pair of current electrodes (Loke et al., 2013). This resistivity meter can provide voltage of 0-400 V, a current of 0-1.250 mA, and has an auto controlled internal power of 100W DC/DC converter using a 12 V internal or external battery (*Syscal Junior*, n.d.).

Two 120 m long multi-core cables connect to the control box. Each cable can connect to twelve ~30 cm long stainless-steel electrodes at a maximum of 10 m spacing. For the present study, a 12 V external battery was utilized to boost the current. Saltwater was poured over each electrode to improve electrical contact with the ground. In order to increase the length of the survey, the first half of the spread (12 electrodes) was shifted forward to guarantee considerable data overlap (Figure 4-1). The control and storage unit was located in the middle of the spread (Figure 4-2), electrodes were hammered into the ground at 4 m intervals in a straight line (Figure 4-3), and once all the electrodes were connected to the cable 'take outs', the readings were taken, using four electrodes at a time, according to a pre-set sequence.

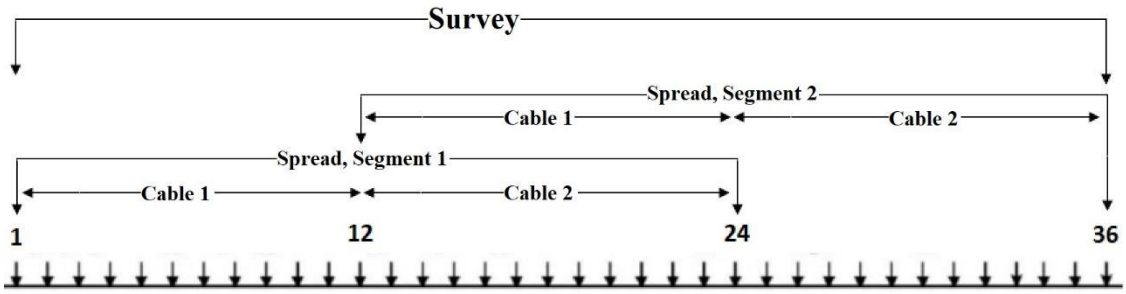

Figure 4-1) Depicts the DCR survey's spreads and segments.

Figure 4-2) Illustrates the programmable Iris Instruments Syscal Junior DCR unit used to collect data in Bay Bulls. The control and storage unit was located in the middle of the spread.

Figure 4-3) a) DCR multicore cable spread out along the road side. b) DCR multicore cable showing take out (orange) and a blue wire with bulldog clips each end, connecting callout to the top of a steel electrode (white arrow) hammered into the ground. The Cliff site, 26 April 2021.

4.1.2 Ground-Penetrating Radar

The GPR instrument consists of a Digital Video Logger (DVL), a pair of transmitter and receiver antennas, cables and a power supply. 250 and 100 MHz antennas were used in these surveys. The 100 MHz antennas require fibre optic cables because they are not shielded. The 250 MHz antennas utilize wire cables. The 250 MHz antennas are shielded and can 'see' down about 4 or 5 meters, while the 100 MHz antennas can see deeper. For effective data gathering, the DVL incorporates a high-resolution, sunlight-visible touchscreen. Figure 4-4 illustrates the product specifications in a chart.

To optimize the GPR survey, survey settings can be chosen specifying the survey type, antenna, stacking, and triggering. For this study, X and Y grid reflection surveys were carried out with the Smart Cart and odometer wheel triggering. The time-zero for the top of the trace (see section 3.3.2) was set by locating the first arrival in ‘Scope mode’ at the starting location of the survey. Default acquisition parameters were used.

Control Module

- Time Window: 0.5 to 200,000 ns
- Points per Trace: 10 to 31,000
- Hardware Stacking: 1 to 32768
- Software Stacking: Unlimited
- Signal Enhancement: DynaQ
- Hardware Temporal Sampling Increment: 5 ps
- Sampling: Digital Equivalent Time Sampling (DETS)
- Pulse Repetition Frequency (PRF): up to 100 kHz
- Data Quality Assurance: Active temperature and supply voltage compensation
- Power Consumption: 100 mA @ 12V
- Temperature Range: -50 to +50 C

Transmitter

- Emission Regulation-Compliant Transmitters: FCC, ETSI (EU) and Industry Canada
- Power Consumption: 150 mA @ 12V
- Temperature Range: -50 to +50 C

Receiver

- Receiver Sensitivity: 1.5µ V lsb
- Data Recording: 16 bit
- Power Consumption: 100 mA @ 12V
- Temperature Range: -50 to +50 C

System

- Maximum System Performance: 186 dB + 10*$\log_{10}$(#stacks) ex. 219 dB @ 2048 stacks
- Environmental: IP65
- Auxiliary Positioning: GPS, laser tracking

Figure 4-4) Product specification (Sensor and Software).

Table 4-1) Ekko Pulse Pro GPR default settings.

Setting	Value	Units
Nominal frequency	250	MHz
Sampling interval for receiver data	0.40	ns
Antenna step size	0.05	m
Time window for receiver data	90.00	ns
Assumed radar velocity	0.100	m/ns
Calculated depth window	4.05	m
TX-RX Antenna separation	0.38	m
System stacking	DynaQ*	
Pulse setting	PRO AUTO**	

* The number of stacks is calculated internally depending on the traverse speed.
** The shape of the pulse is the internal default.

GPR surveys were conducted over the study area using a Sensors and Software pulse EKKO PRO GPR, mounted on a Smart Cart. The system, with 100 and 250 MHz antennas, as shown in Figure 4-5.

Figure 4-5) Sensors & Software EKKO Pulse Pro GPR with (a) 100 and (b) 250 MHz antennas. Operated by Marzieh Arshian. The two yellow mounds in (b) are shields covering the transmitter (back) and receiver (front) antennas. A skid plate separates the antennas from the road.

4.1.3 Real Time Kinetic surveys

RTK surveys were carried out using a Topcon Hiper V system (Figure 3-31). At the three sites, detailed RTK location and elevation surveys were conducted over the GPR grids and along the DCR lines. At the start of each survey, the RTK base was set up near the survey area: at the Bread and Cheese site, on the headland east of the pocket beach; at the Cliff site, in a driveway to the east of the road; at the Quays, in a school-bus turn-around location at the south-eastern end of the site.

After the base receiver had been receiving satellite data for a few minutes, and established its approximate location, it was connected to the rover receiver. During the subsequent survey, the base receiver collected 'static' satellite location data for 3 to 4 hours and stored it in an SD card.

For the GPR grid surveys, long tape measures were laid out on either side of the road, and a shorter tape measure was used to connect the two long tape measures at selected intervals of a few metres. The road surface was marked with chalk at the intersections of the GPR x- and y-lines, and these locations were then recorded using the RTK rover. For the DCR line surveys, the locations of each of the electrodes was measured using the RTK rover after the electrodes were placed.

On returning to St. John's, the static data was downloaded from the base receiver's SD card, and converted from Topcon's proprietary format to the industry standard RINEX format using Topcon software Topcon Link. The RINEX file was uploaded to the Natural Resources Canada website for Precise Point Positioning (Government of Canada, 2003). Static results were returned by email, usually within a few minutes of submission. These included the location of the RTK base in latitude, longitude, UTMs, ellipsoid height and orthometric height, and uncertainties in meters. Uncertainties were always within a few cm (see Appendix E). The offsets between this precise position and the initial approximate position of the base receiver were used to correct the rover survey locations, which were originally determined relative to the location of the RTK base.

4.1.4 Site visits and local geomorphological surveys

Visiting the sites to observe features ranging from surficial geology, bedrock outcrops kinds, and deformation in bedrock, to fractures in the asphalt of the road provided significant in-site knowledge. Interviews with local residents provided information on previous hazardous phenomena, such as the date, strength, and direction of occurring hurricanes or prevailing wind, when and how infrastructures were built or reinforced, and what material was used for infilling road subsurface. These are useful when integrated with the geophysical model during the interpretation.

Local residents, fishermen, tourist operators, and municipality employees were contacted to ask about anthropogenic activities like road reinforcement, widening and relocating, storm conditions, and wave activity.

4.2 Geophysical Surveys

4.2.1 Bread and Cheese site

GPR, DCR/IP and RTK surveys were carried out at this site in the spring of 2021. Characteristics of the surveys are summarized in Table 4-2.

Table 4-2) Geophysical surveys conducted over the Bread and Cheese site

	Date	Characteristics
DCR/IP	March 23, 2021 bay side	92 m long, 4m electrode spacing, Wenner-Schlumberger array
DCR/IP	April 22, 2021 north side	92 m long, 4m electrode spacing, dipole-dipole and Wenner-Schlumberger array
GPR	April 1, 2021	Grid: 5 'Xlines' along the road, 96 m long and 1.5 m apart, and 25 'Ylines' across the road at 4 m intervals, 250 MHz
RTK	March 23, April 1, April 22, 2021	set up in a grassy area on the bay side of the road

The DCR/IP and RTK surveys

As summarized in Table 4-2, the DCR/IP surveys were conducted along profile lines, approximately 92 m long with 4m electrode spacing, using Wenner-Schlumberger on the south side (bay) on March 23, 2021, and both dipole-dipole and Wenner-Schlumberger configurations on the north side (hill) of the Gunridge Road, on April 22, 2021 (Figure 4-6). The 4 m spacing for the electrodes was chosen to allow an efficient collection of data over the length of road of interest (~100 m) to an appropriate exploration depth of about 15 m (i.e. at or below sea level), while allowing, reasonable horizontal resolution. The dipole-dipole array was used to investigate whether better resolution of any vertical structures could be obtained. The spreads were not perfectly straight lines because it was sometimes difficult to find a spot where the electrodes could be hammered in to sufficient depth. The spreads were offset to the east by about 10 m relative to the start of the GPR grid.

Maps showing the electrode locations are given in Figure 4-6. Two lines labelled P0 and P1 were taken parallel to each other on opposite sides of the road, P0 to the south and P1 to the north. Locations of all stations were obtained using a Topcon Hiper V Real Time Kinetic (RTK) system.

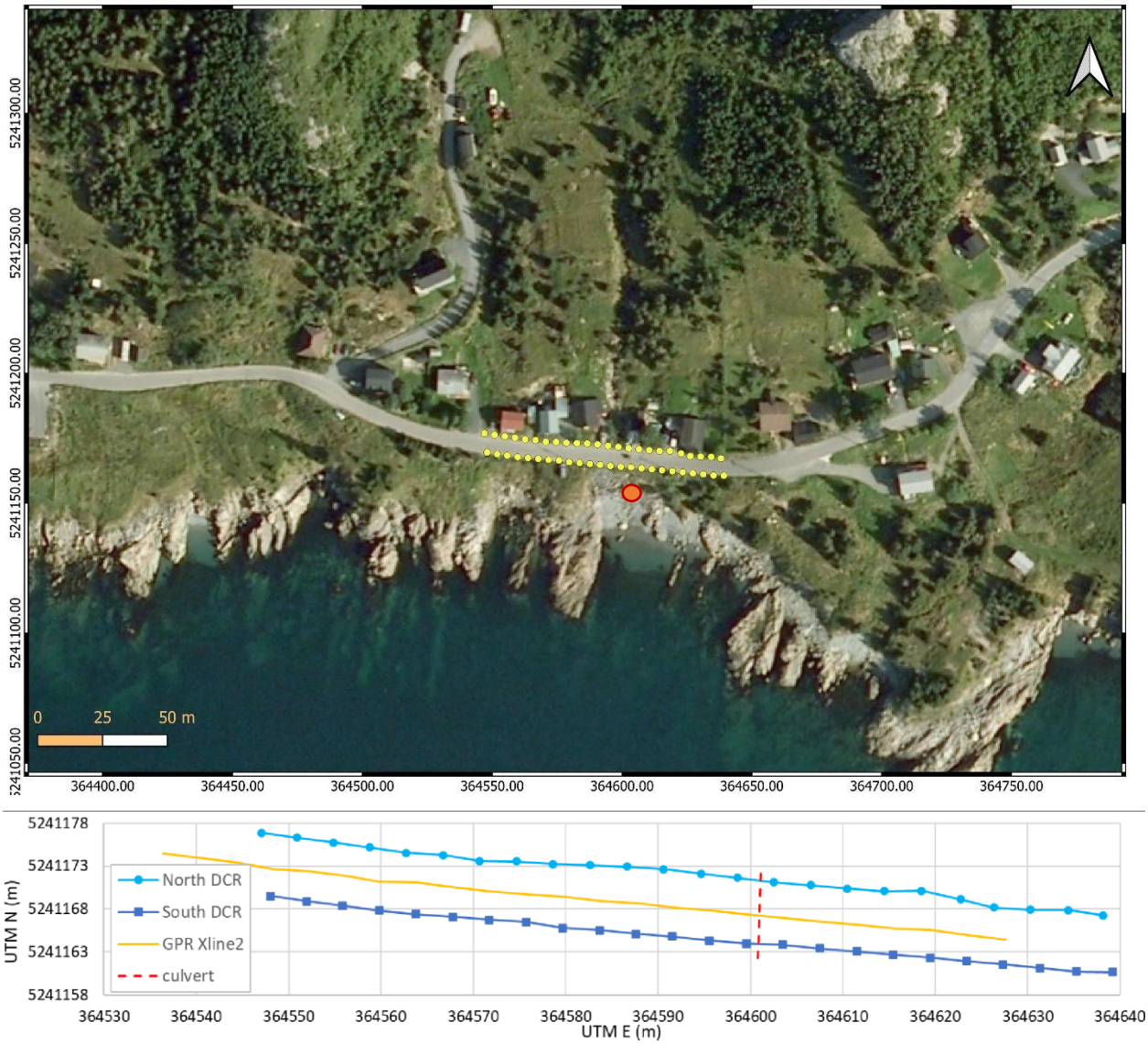

Figure 4-6) Maps of electrode location of DCR surveys at the Bread and Cheese site. Top: superimposed on air photograph. The location of each electrode is indicated, and the orange circle shows the location of culvert. Bottom: graph showing the location of each electrode of DCR survey and GPR Xline2 and the culvert.

GPR and RTK surveys

A survey grid was set up along the road at the Bread and Cheese site on April 1, 2021. It consisted of 5 'Xlines' along the road, 96 m long and 1.5 m apart, and 25 'Ylines' across the road at 4 m intervals (Figure 4-7). The grid length was chosen to cover the same stretch of road as the DCR survey (though there was an inadvertent offset of 10 m in the start position). An Xline spacing of 1.5 m was estimated as adequate to investigate continuity of subsurface features in the cross-road direction and suitable for documenting variation in the elevation of the road surface. More widely spacing Ylines serve as tie-lines.

The grid was set up by laying a long tape measure at the side of the road, marking off 4 m intervals with chalk, and then marking points at 1.5 m intervals across the road at each 4 m mark. These chalk marks, intersection points for the grid lines, were then precisely located by RTK. The RTK base was set up in a grassy area on the bay side of the road (red dot in Figure 4-6 and Figure 4-7).

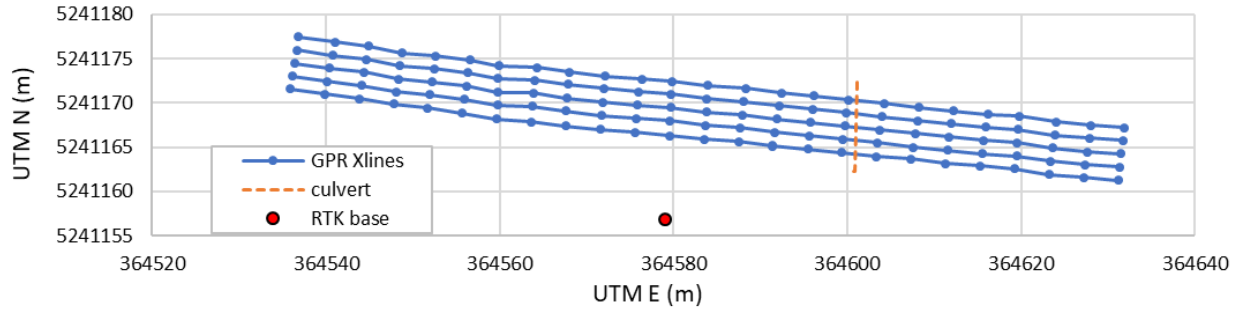

Figure 4-7) Map of GPR grid, Bread and Cheese site, 1 April 2021. Dots represent chalk markers indicating intersections with crossing Ylines.

4.2.2 The Cliff site

Characteristics of the geophysical surveys carried out at the Cliff site are summarized in Table 4-3.

Table 4-3) Geophysical surveys over Cliff site

Survey	Date	Characteristics
DCR/IP	April 26, 2021 NE side of road	140 m long in two overlapping spreads, 4 m electrode spacing, dipole-dipole and Wenner-Schlumberger array
GPR	April 23, 2021 May 28,2021	Survey 1: 150 m long, 250 MHz antennas. Survey 4: 40 m length, 250 MHz

GPR	April 23, 2021	Survey 2, Grid: 4 Xlines 2 m apart, 150 m long; 13 Ylines 12.5 m apart, 6 m long. 250 MHz
GPR	May 6, 2021	Survey 3, Parallel lines: 3 Xlines 2.5 m apart, 175 m long. 100 MHz antennas
GPR	May 28,2021	Survey 4, Grid: 13 Xlines 0.5 m apart, 40 m long; 9 Ylines 5 m apart 6 m long. 250 MHz antennas.

DCR/IP and RTK surveys

Two overlapping spreads of the DCR survey were conducted at the Cliff site on April 26, 2021, on the landward (NE) side of the road over 140 m with 4 m electrode spacing (Figure 4-8).

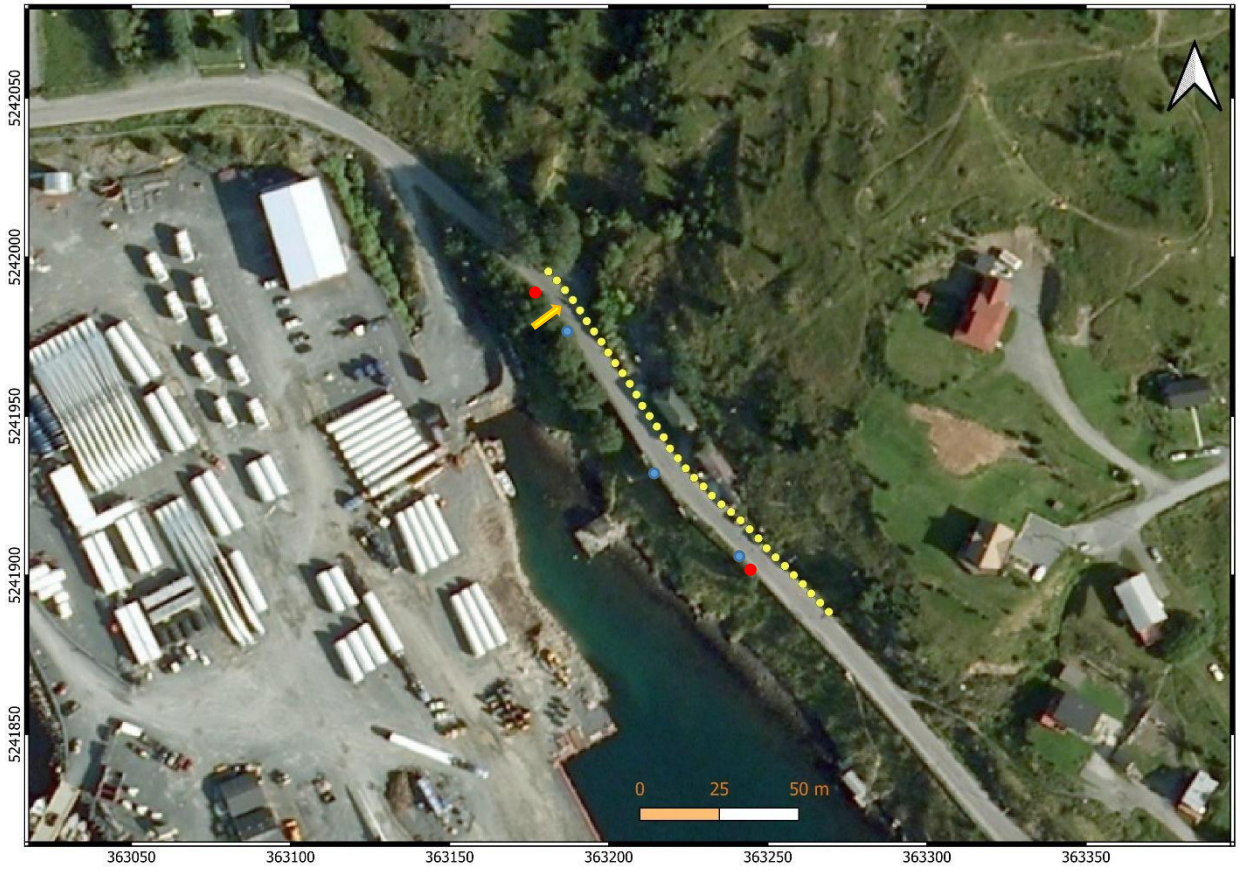

Figure 4-8) Air photo of Cliff site with DCR electrode locations marked as yellow dots. Red dots show the start and end locations of the wooden retaining wall and blue dots depicts the location of culverts.

GPR and RTK Surveys

Four GPR grid surveys were carried out over the Cliff site (Table 4-3). Survey 1 was a line survey along the centre of Northside road, starting from opposite the access road to the marine terminal; Survey 2 was a grid over 150 along the road and 6 m across the road; Survey 3 was three

parallel lines along the road using 100 MHz antennas; and Survey 4 was a detailed grid survey over a 40 m length of the road.

Surveys 1 and 2 are displayed in Figure 4-9, together with the locations of three culverts, designated Culvert 1, 2 and 3 starting from the northwest.

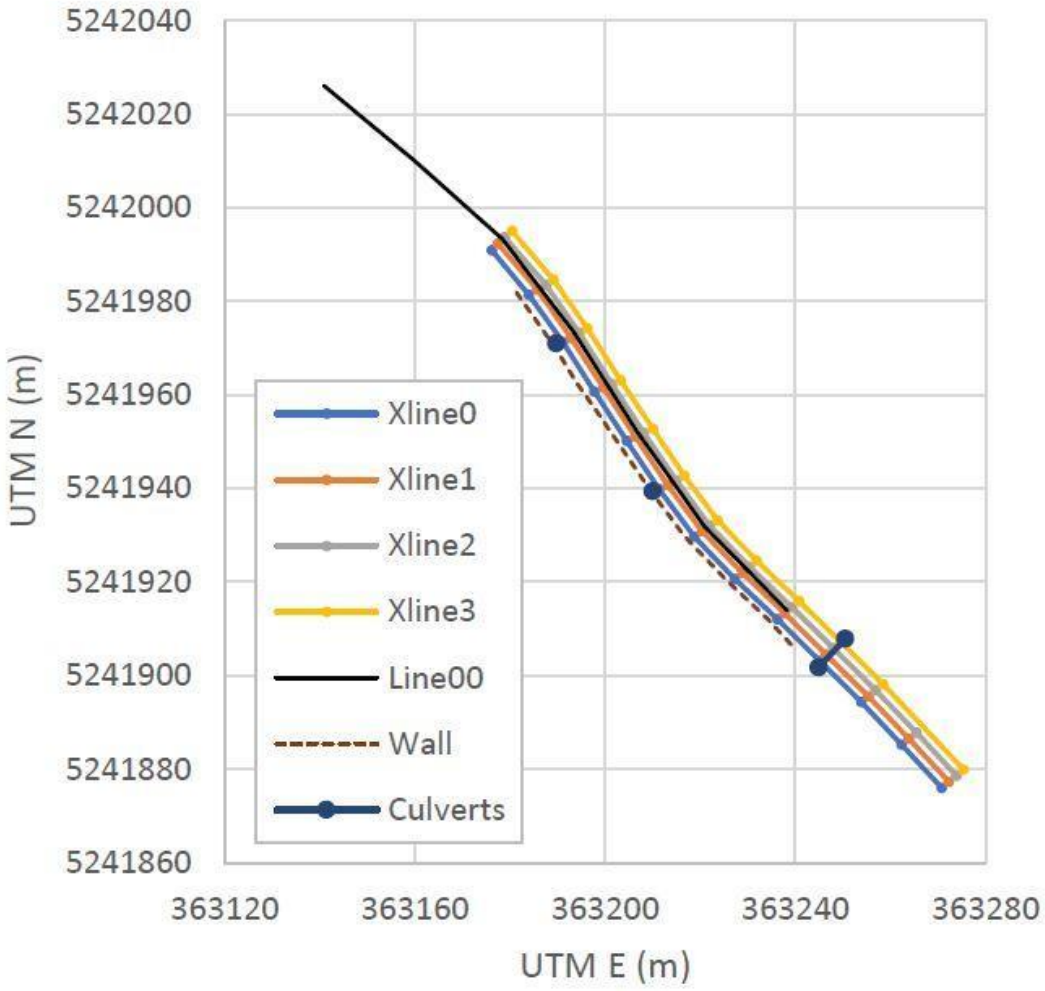

Figure 4-9) Map of GPR Surveys 1 and 2. The Cliff site. 23 April 2021.

4.2.3 Quays Site

Table 4-4) Geophysical surveys over the Quays site

DCR/IP	May 18, 2021	140 m long in 3 overlapping spreads, 4 m electrode spacing, dipole-dipole and Wenner-Schlumberger arrays
GPR	May 13, 2021	Grid: 4 'Xlines' along the road, 148 m long and 1.5 m apart, and 38 'Ylines' across the road at 4 m intervals
RTK	May 13, May 18, 2021	set up in bus turnaround area near NE end of grid on the bay side of the road

DCR and IP Surveys

The DCR surveys were undertaken on the southwest edge of Quays Road (Figure 4-10). Three overlapping spreads were carried out, covering a total of 140 m, with both Wenner Schlumberger and dipole-dipole arrays with 4 m electrode spacing. The survey line was longer than at the previous sites in order to cover the region where inlets were close to the road and also the region where the road was relocated. In the SE, the electrodes were hammered into the fine gravel verge. Farther to the NW where the road was curbed, the electrodes were hammered into grassy soil about half a metre back from the curb.

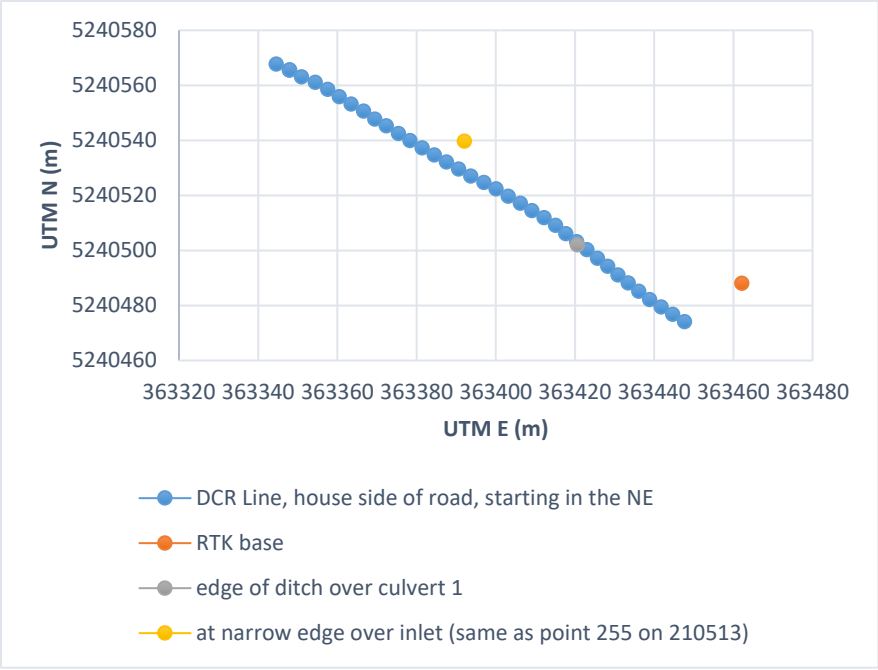

Figure 4-10) Top: Air photo of the Quays, from 2011 before the road was relocated. Yellow points illustrate the location of electrodes in DCR survey, along the existing road. Yellow arrows depict the location of concerning inlets. Bottom: Graph including electrode location of DCR surveys, RTK and, the culvert at the Quays site, May 18, 2021.

GPR Survey

The GPR grid at the Quays consisted of 4 parallel Xlines, 1.5 m apart and about 148 m long, and 38 Ylines spaced at 4 m (

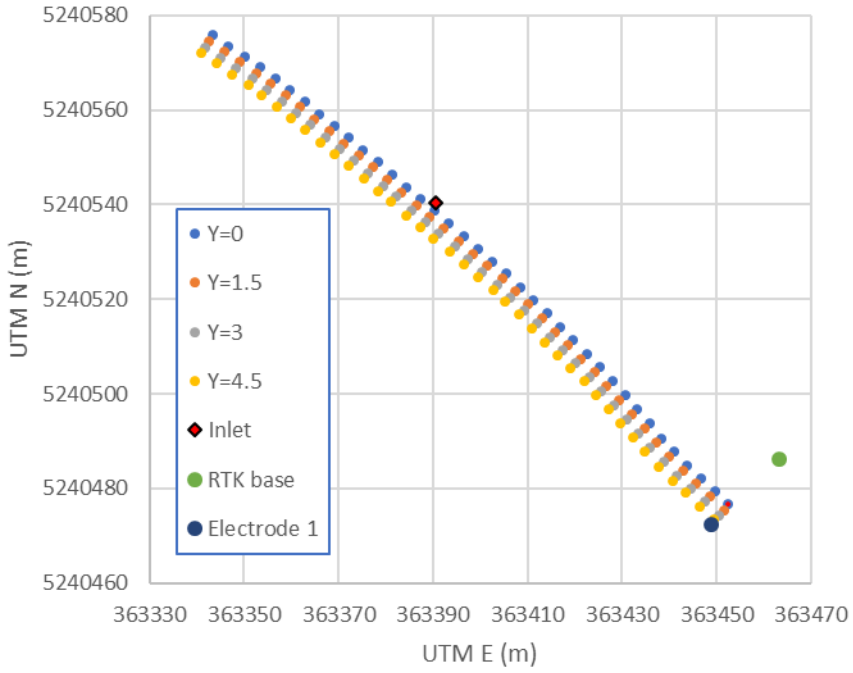

Figure 4-11). Beyond the first 50 m, the road was relocated landward, the largest offset occurring in the last 50 m (Figure 4-10).

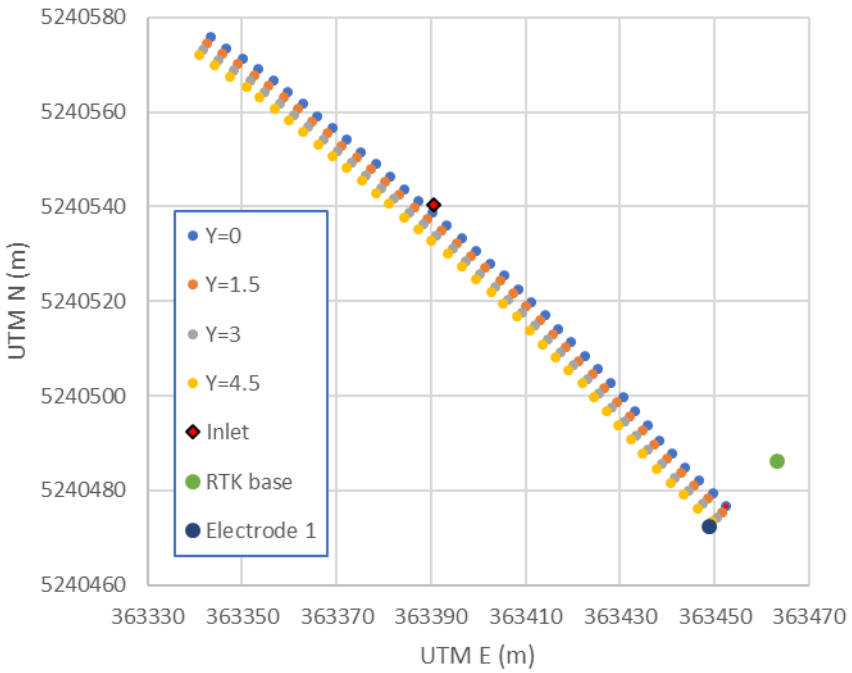

Figure 4-11) GPR Grid, the Quays. 13 May 2021.

4.3 Analytical Techniques and Processing

To convert raw data into accurate and relevant information about the subsurface, data processing is required. The data acquired as part of this research study was examined and modelled by using commercially available software.

4.3.1 GPR data processing

The GPR data were processed and analyzed using EKKO-Project 5 software from Sensors & Software Inc. The start-up GUI interface for this software is illustrated in Figure 4-12. This interface allowed a view of the grid layout and fiduciary marks in the MapView window, and previews of any selected line in the Line Preview window for basic quality control.

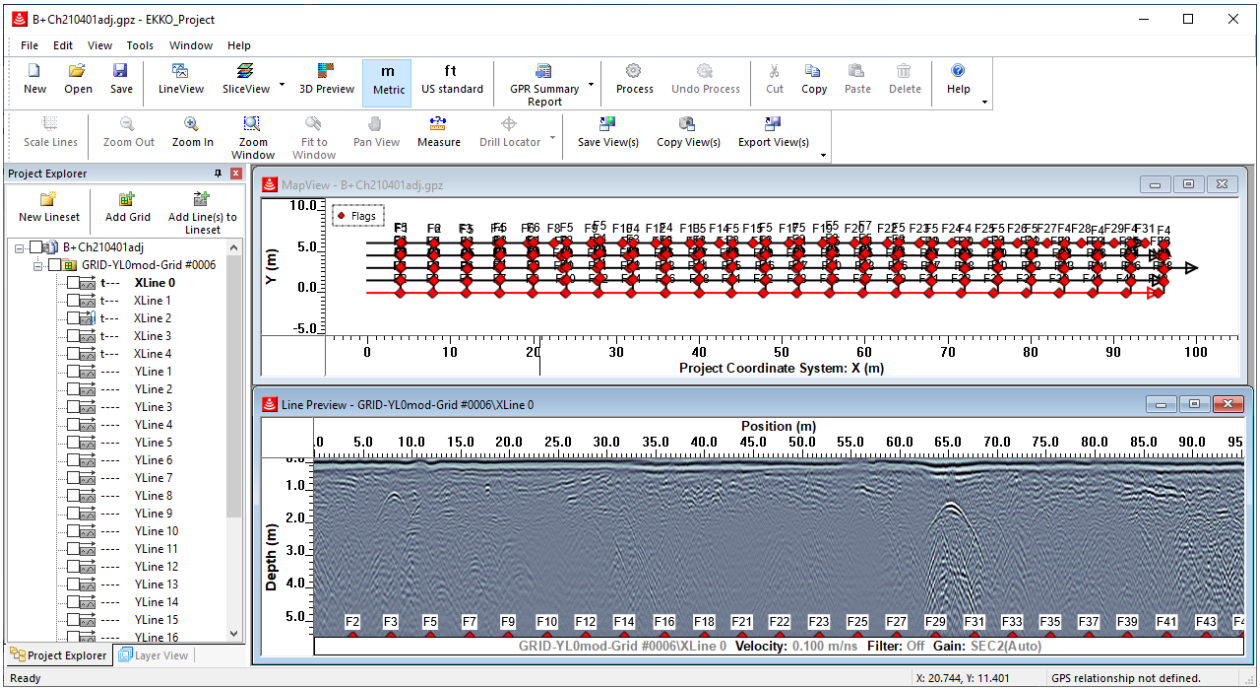

Figure 4-12) GUI interface for EKKO Project 5 software, illustrating the start-up window for the Bread and Cheese site GPR grid survey.

For processing the data, the GPR data is displayed in 'LineView', where single or multiple radargrams can be diplayed (Figure 4-13). Apart from various display options, such as showing or hiding fiduciaries and legends and changing fonts, some processing options are available in LineView. For the most part, the default settings and processes were used as they were found to be optimal. These defaults include Dewow, background subtraction and SEC2 gain (section 3.3.2). The parameters for the gain are: the start gain, the maximum gain and attenuation. The larger the attenuation parameter, the more rapidly the gain approaches the maximum. Typical default values for these parameters for the GPR surveys were: start gain between 1.3 and 2.3, maximum gain between 200 and 800, and attenuation between 3 and 6.

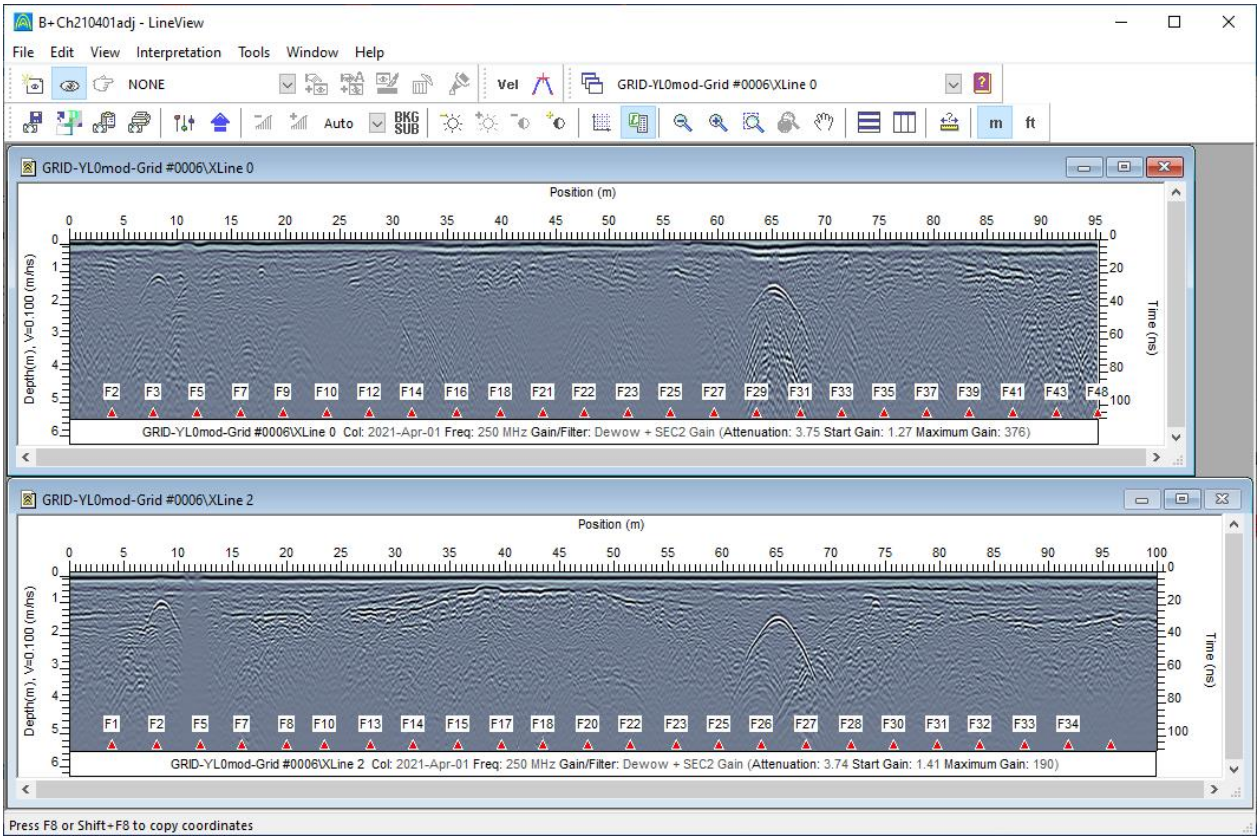

Figure 4-13) EKKO Project 5 LineView GUI.

The default velocity was 0.1 m/ns, generally appropriate for overburden. EKKO Project 5 enables the average velocity to be determined by fitting hyperbolas to such features in the radargrams. Hyperbola fitting of small features gave velocities between 1.25 and 0.085 m/ns within the same profile, so the default of 0.10 m/ns was kept. The depths of features are not claimed to be very accurate.

Topographic information was added to the profiles by attaching a text file (named XLine*nn*.top), containing x and elevation data, to the appropriate Xline. This operation simply moved the stacked traces up and down depending on the topography, which was extrapolated linearly between the data points provided in the *.top file.

Further processing options are available in the main GUI through the 'Process' button (near the centre of the top menu in the main GUI, Figure 4-12). Such options include adjusting the odometer calibration, line editing, time and spatial filtering, and cropping data. For the Bread and Cheese site, odometer recalibration was required. F-K migration is the simplest migration technique for collapsing diffraction hyperbola to the true surface position using Fourier Transforms

assuming a uniform subsurface velocity (e.g., Cassidy & Jol, 2009). For the Cliff site, FK migration was attempted, but was not found to be helpful.

Another viewing feature in Ekko Project 5 is 'SliceView' where horizons at equal depth could be displayed as maps. The maps are displayed with a colour code corresponding to the amplitude of the trace within a 10 cm interval of depth. Dark blue indicates a low amplitude and red a high amplitude. Values between profiles are determined by linear interpolation, so the maps are streaky in both grid directions. This feature was utilized for the Cliff high resolution survey (Figure 5-18) to locate the support beams under the road.

4.3.2 DCR data Processing

The collected data for DCR and IP surveys were processed, modeled, and analyzed using software, including *RES1DINV, RES2DINV, RESIPy, SURFER, GIS* and *Oasis Montaj. RES1DINV* and *RES2DINV* are one- and two-dimensional inversion modeling software produced by Geotomo, version 3.56.73, with a dongle allowing access to full features (Loke, 2011). The default values of inversion parameters were used, except that the model cells were refined to half the unit electrode spacing for optimum results: this is particularly useful when there are large variations in resistivity in the near surface (Loke, 2011). The default inversion method was least squares.

The starting model for the inversions was a uniform half space. At the start of the inversion a pseudo-section of the raw data is produced, where each apparent resistivity measurement was plotted at the distance of the centre of the array, and at a pseudo-depth of about a third of the array width. The differences between the starting model and a forward model based on the pseudo-section were then used to improve the model. Iterations continued until the differences between the measured and calculated pseudo-sections reached an acceptably small amount, generally a few %. The starting pseudo-sections, the final model sections, and the pseudo-sections calculated from the final models are shown for all surveys in Appendix B.

Prior to inversion, the raw data sets were inspected for quality control. The raw measurements themselves were repeatable. During acquisition, the measurements were stacked 3 times and the standard deviation of the apparent resistivity readings recorded. These were always "0 %" (i.e., < 0.5%). At the Bread and Cheese site, the cable inputs were reversed and the survey repeated to check the reliability of the cables. The results were almost identical. At the Cliff and Quays sites,

where overlapping spreads were utilized, the overlapping measurements could be compared. Again, these were highly repeatable, especially for apparent resistivity (Figure 4-14).

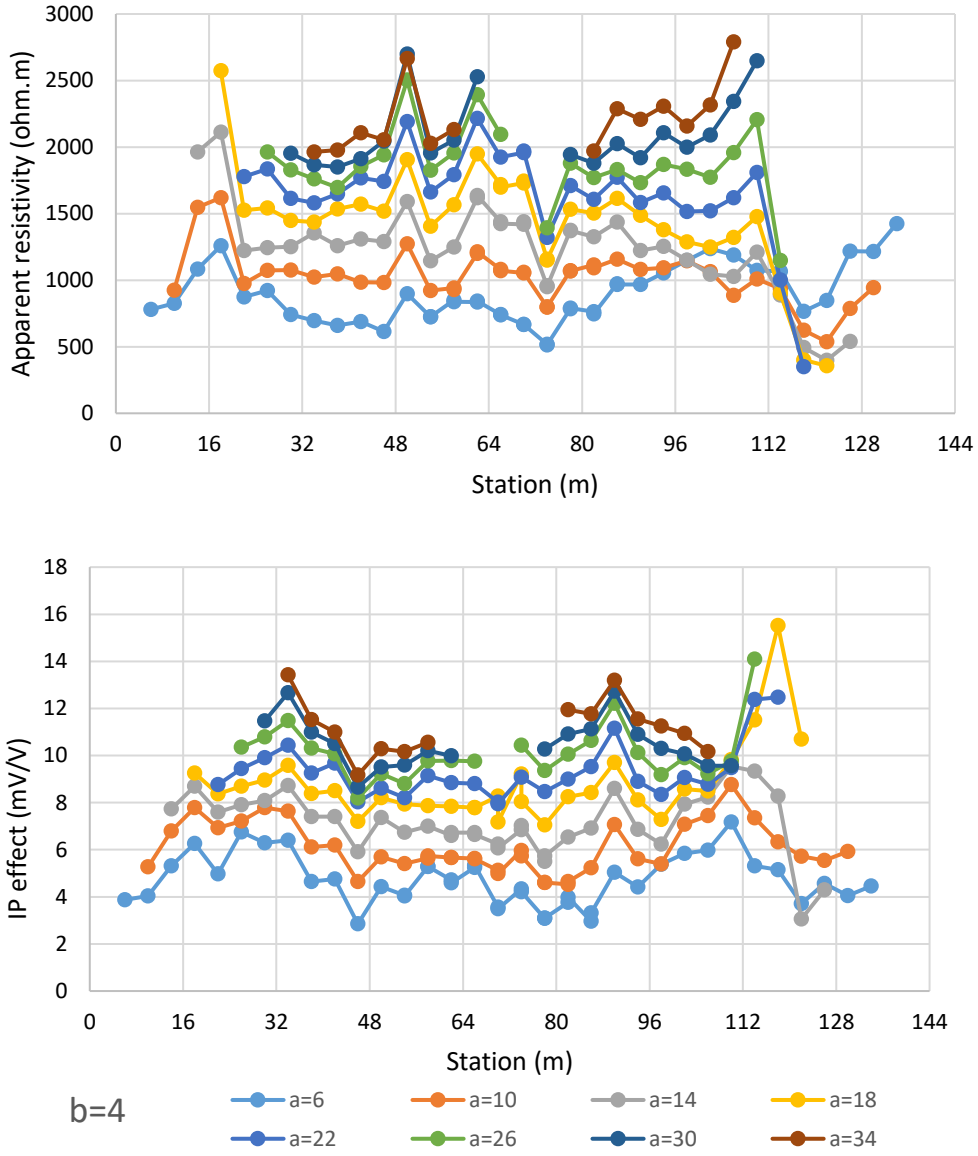

Figure 4-14) Raw data from Wenner-Schlumberger DCR/IP survey at the Cliff site: b=4 indicates the potential electrode spacing, 'a' is half the current electrode spacing. Top: Apparent resistivity measurements; bottom: IP measurements. Two spreads were taken, with 9 overlapping measurements for a=6 and one overlapping measurement for a=22.

RESIPy (Blanchy et al., 2020; https://resipy.org) is freeware which can accept some *RES2DINV* input files. It was used to find a measure of the depth of investigation for the DCR models. The RESIPy software was not used as the primary inversion tool for this thesis due to its inability to accommodate the format of the induced polarization (IP) data.

5 Analysis

5.1 Bread and Cheese

GPR and RTK Surveys

The elevation of the road surface at the RTK locations is displayed in Figure 5-1. Note the vertical exaggeration in the figure. It is seen that the road dips 1.2 m from the east end of the grid to the culvert area, and the road surface slopes slightly seaward in the middle stretch of the profile. Ideally, road surfaces are bowed up slightly in the middle so that water drains to both sides, mitigating ponding and erosion, and so that light from oncoming traffic headlights is reflected to the side rather than into the eyes of motorists (e.g., About Civil Engineering, 2023). The present seaward slant of the road at the lowest elevations could be the result of mass movement under the roadbed. This slant is problematic, as it will direct water toward the beach and onto the vulnerable bluff, promoting erosion of the bluff.

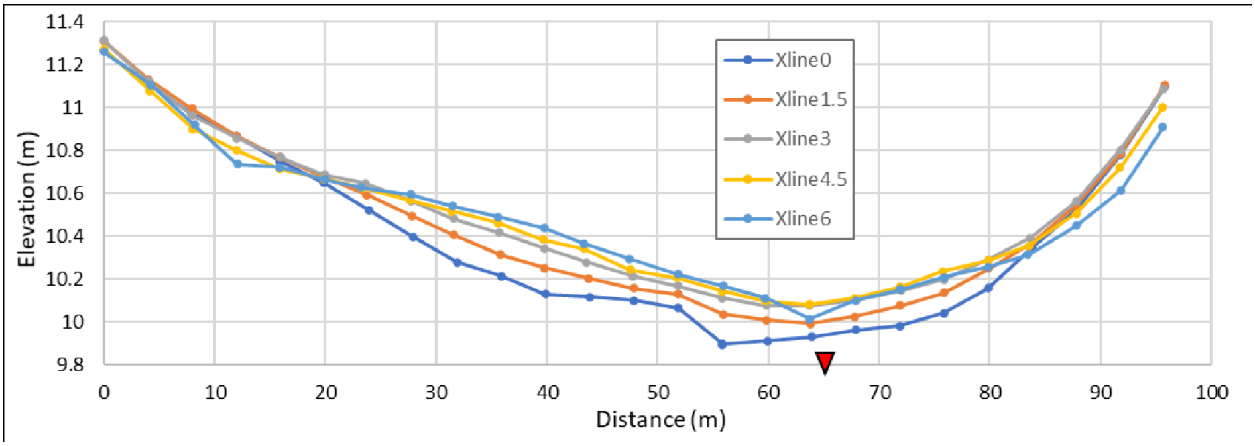

Figure 5-1) Elevation of the road surface along GPR grid Xlines. Xline0 is closest to the coast. Distance measured W to E. Red triangle indicates the location of the culvert (culvert top is ~1 m below road surface). Vertical exaggeration 20X.

The five GPR Xlines are displayed in Figure 5-2. These were collected using 250 MHz antennas. Dewow, background subtraction and default SEC2 gain settings were applied. There is little variation in the structure across the road, the main features are interpreted in Xline 2, down the centre of the road (Figure 5-3). In GPR profiles, interfaces between different materials show up as strong reflections, and point targets (small, localized, objects like pipes or boulders), appear as hyperbolas (arches).

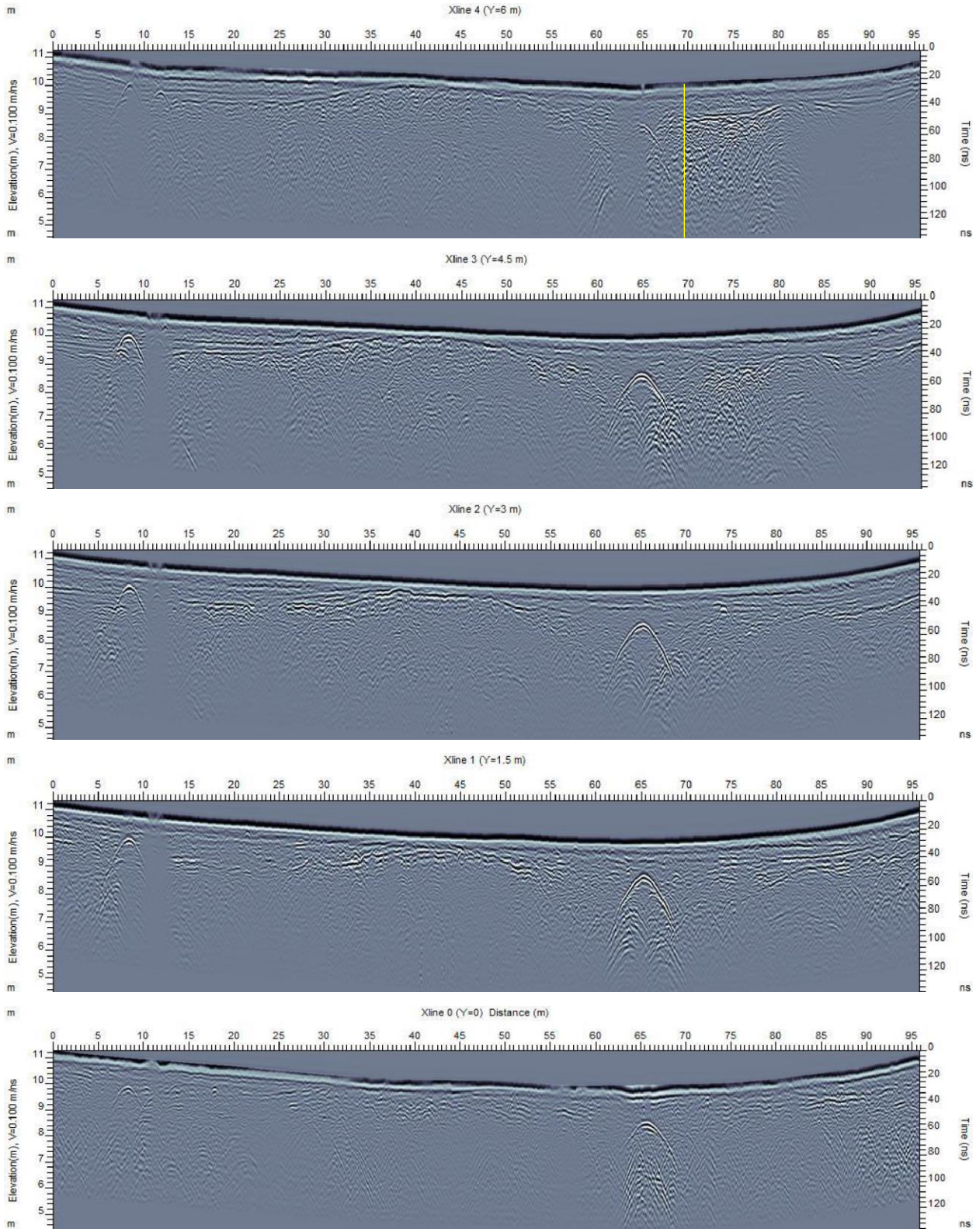

Figure 5-2) GPR profiles along Gunridge Road at Bread & Cheese site, Xline 0 is closest to the coast. Vertical exaggeration 3.5X. Yellow line in Xline 4 indicates missing data.

The top of the culvert shows up as a strong hyperbola with its peak ~1.2 m below the road surface, at distance ~65 m. (The hyperbola does not appear in Xline 4 top panel in Figure 5-2- because data is missing due to slippage of the odometer wheel.) Another hyperbola at distance 8.5 m, which is a smaller pipe, which can be seen in at least three sections. The blurry region at distance 10.5 m corresponds to a patch of new asphalt across the road, presumably cut to allow the laying of another pipe, most clearly seen in Xline 4 on the north side of the road. The small hyperbola at distance 74 m in Figure 5-3, and other fainter hyperbolas on this and other lines, are interpreted as boulders as they are not seen at the same locations on the other profiles.

The strong, irregular interface across the profiles is interpreted to be bedrock, and the interfaces parallel to the surface of the road above it as related to different materials laid down during the construction of the road. This is consistent with an aim of having a relatively smooth road surface. The dashed yellow line in Figure 5-3 indicates the approximate slope of the bedding plane, based on dip measurements taken on the nearby beach, if this plane is extrapolated back to a position under the road with the same orientation. This is consistent with this bedding plane, which defines the western edge of the beach, also defining the western edge of the fracture region. Its apparent very steep dip is the result of the vertical exaggeration in the figure.

From the GPR profile, it appears that there is a width of about 25 m where the pattern of reflections is irregular. We interpret this as the fracture region, where the ground is particularly susceptible to erosion. This region is similar to the width of the beach between its western edge and the next major outcrop, as seen in Figure 2-1.

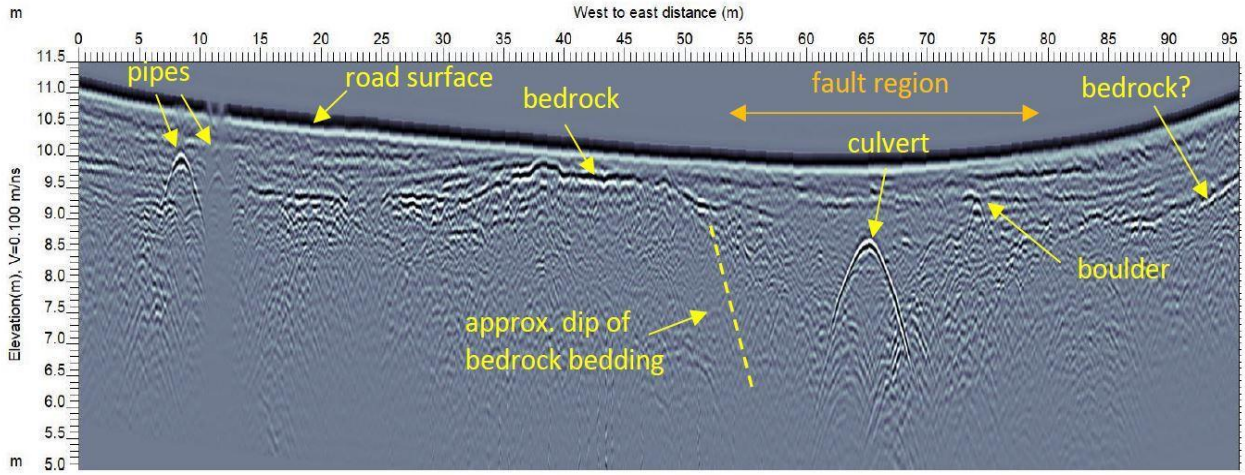

Figure 5-3) GPR profile Xline2 down the centre of the road, Bread and Cheese site. Elevation is meters above sea level. Freq: 250 MHz, Gain/ filter. Dwow+SEC2 Gain, (Attenuation 3.74) start gain 1.41, maximum gain 190). Vertical exaggeration 5X.

It should be noted from Figure 2-1 that there is a further stretch of beach to the east of this second outcrop, suggesting another portion of the coast particularly susceptible to erosion. Fortunately, the road is farther inland here, and there are outcrops in the water to help break the force of storms coming from the SW as they commonly do (Driscoll, pers. comm.; Catto, 2020).

DCR/IP and RTK

The elevation of the road surface at the RTK locations is depicted in Figure 5-4 (Vertical exaggeration of 10X applied in the figure). This figure shows similar features as Figure 5-1. The seaward slant to the road surface west of the culvert is not as apparent in Figure 5-4 because the DCR electrodes were located on the verges rather than on the road surface itself.

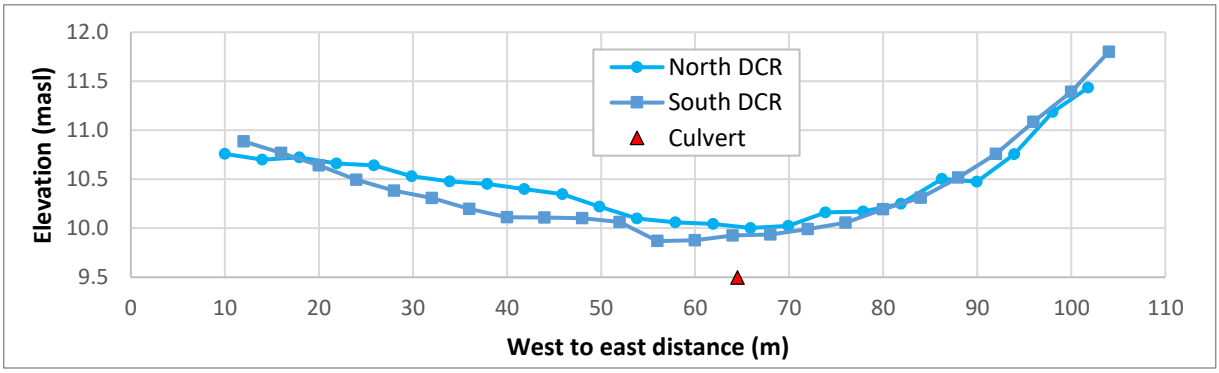

Figure 5-4) Elevation along DCR spreads at Bread and Cheese site. Red triangle indicates the location of the culvert. Vertical exaggeration 10X.

Figure 5-5 shows resistivity sections based on one dimensional inversions of the Schlumberger soundings using RES1D Inversion, on the south (bay) side of Gunridge Road. Normally, in a situation where significant lateral variations are expected, a 2D model would give better results. In this case, the 2D models were unstable (seeFigure B 3) 2D resistivity and IP modesl based on Wenner-Schlumberger survey on the south side of Gunridge Road, Bread and Cheese (23 March 2021).).

The existence of a decrease in electrical resistivity at x=38m to x=58 m is associated with highly fractured area in the culvert region, and particularly to the west of the culvert. Clay and ground water, particularly with salt content from road salt, within the fractures would lead to a lower resistivity. The metal culvert itself may also have an influence, though it is not obvious in which direction, since the culvert runs perpendicular to the current flow and is filled with resistant air. The high resistivity on either side of the fractured region, between stations 7-10 and 15-18 is presumably due to the presence of more resistant bedrock.

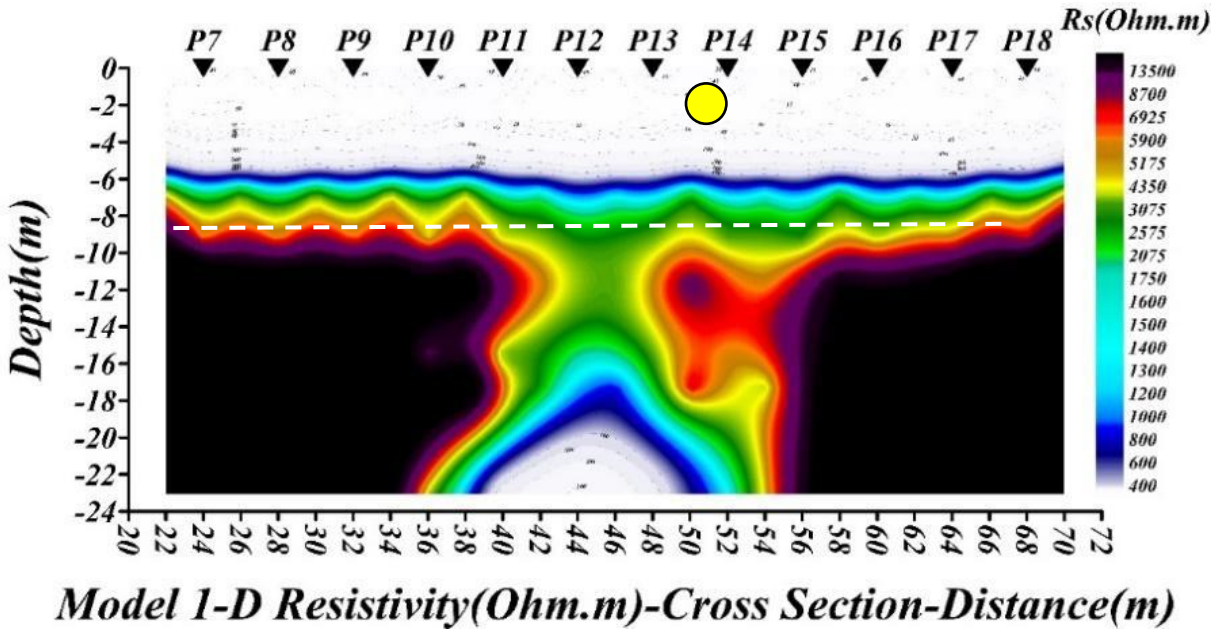

Figure 5-5) 1D model based on Schlumberger soundings along the south (bayward) side of Gunridge Road. Labeled arrows at the top of the figure refer to electrode locations. Scale at the bottom is distance from eastern-most Electrode 1, no vertical exaggeration.The yellow circle indicates the approximate location of the culvert, and the dashed white line is approximately sea level. Image produced using Surfer.

Figure 5-6 shows sections of the resistivity and IP (chargeability) for the survey on the north side of the road. This is thought to be more reliable than the model for the survey on the south (bay-ward) side of the road because the metal railing on the bay side is partly buried in earth and this could lead to current short circuiting through the railing rather than sampling the ground.

In both sections in Figure 5-6, red and purple indicate high values, and blue indicates low values. We expect solid bedrock to have high resistivity and low chargeability, and damp soil and clay to have low resistivity and high chargeability. Salt water has very low resistivity and low chargeability compared with fresh water.

The range of resistivities in Figure 5-5 and Figure 5-6 are similar, and both show a relatively low resistivity surface layer and an increase in resistivity below about 4 m above sea level. They also both show the lowest resistivity to the west of the culvert for about 8 m. This corresponds to the fractured region to the west of the culvert as seen in the GPR profiles (Figure 5-2) and to the region where the road slopes most steeply bay-ward (Figure 5-1). This is also the region where the bluff is covered in rip-rap (Figure 2-3). Though no records are available on timing, the rip-rap was presumably emplaced in response to rapid erosion in this location. Thus the low resistivity is likely

related to more porosity and/or clay in the fractured region, perhaps enhanced by the presence of deicing salt.

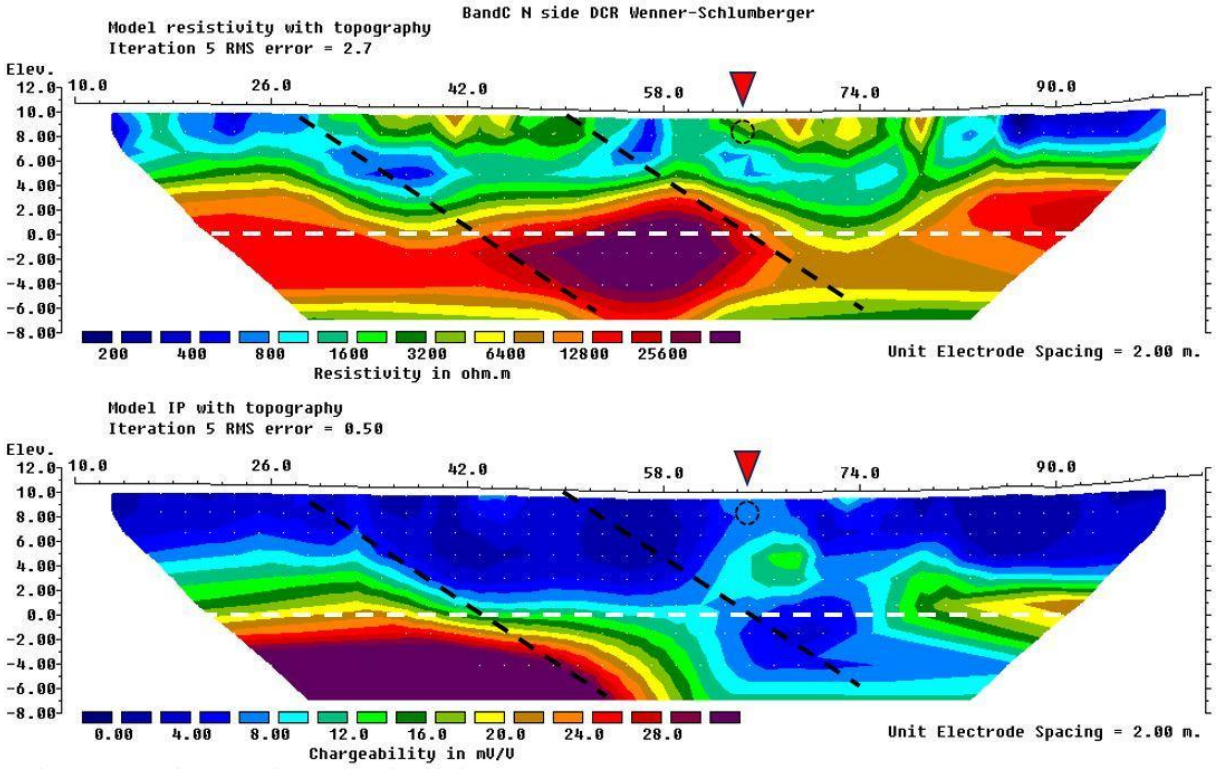

Figure 5-6) 2D resistivity and IP models based on the Wenner-Schlumberger survey along the south side of Gunridge Road, Bread and Cheese. The black dashed line indicate the orientation of exposed bedrock outcrops and the white line shows the sea level. There is no vertical exaggeration, and the profiles are measured from west to east. Models by RES2DINV. Measured and calculated pseudo sections are provided in Appendix B.

The resistivity varies significantly near the surface. It is moderately high where bedrock is interpreted to be close to the surface (34-48 m; 44-58 in Figure 5-6)This corresponds to where the road crosses over the headland to the west of the pocket beach. Near surface resistivity is also moderately high over the culvert and eastern portion of the fracture region. This maybe due to better drainage allowing drier sediments in the near road fill over the culvert, or conversely less porosity in the fractured region depending on whether air or more conductive material fill the porosity. The difference in properties east and west of the culvert is not obvious in the GPR profiles (Figure 5-2).

The low resistivity 'layer', seen as blue colours between the surface and 6-7 m deep at various distances in Figure 5-6, may be due to sideways flow of current through such anthropogenic features as fences or gardens from nearby houses or the buried guard rail in the ground (Figure 2-13). This is an unavoidable limitation of using the DCR method in an environment such as coastal roads with strong variations perpendicular to the survey lines. It is also possible that deicing road salt could have accumulated within brackish water at these depths. Variations along the profile could be due to variations in composition within the near-surface.

The depth of investigation (DOI) section for the resistivity model in Figure 5-6 is shown in Figure 5-7. DOI refers to the depth below which surface data become insensitive to the value of the physical property of the earth. In interpreting models resulting from any inversion process, it is important to determine this depth for DCR and IP surveys. The structure beneath that depth should not be interpreted geologically or the interpretation should be undertaken cautiously and in combination with other geophysical techniques. This model can provide an estimation of the depth of region below which the earth structure is no longer constrained by the data. This prevents over-interpretation of the inversion results (Oldenburg, 1999).

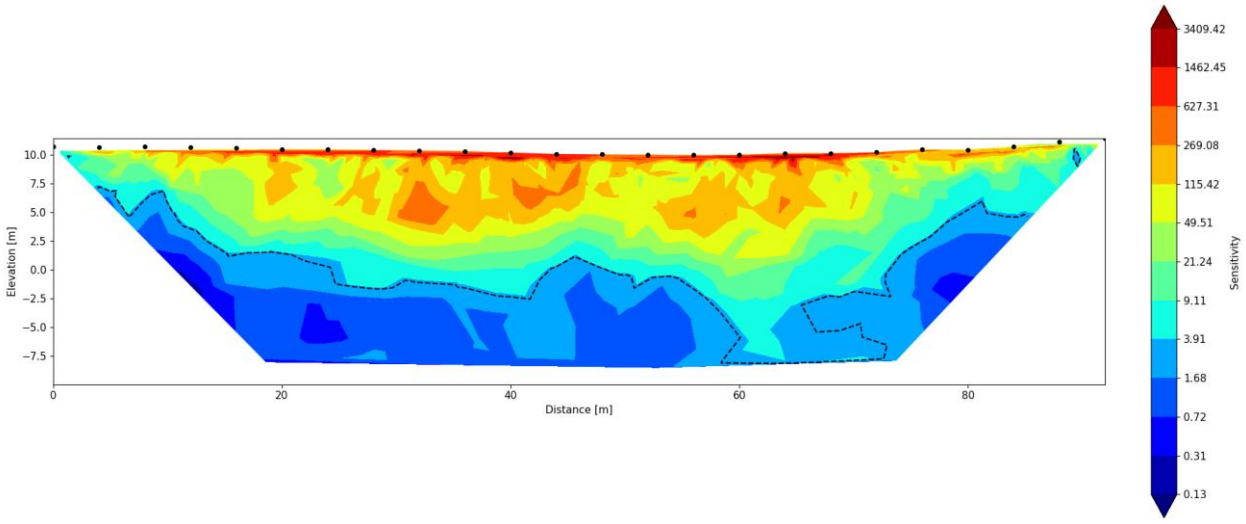

Figure 5-7) Relative sensitivity model and Depth of investigation (black dashed line) for the DCR survey (Wenner-Schlumberger configuration), at the Bread and Cheese site. RESIPy model.

From Figure 5-7 it is seen that the area most sensitive to the measurement values are located near the surface and centre of the spread, consistent with the higher current density in these locations. As well as being closer to the current electrodes, current density is concentrated in the

near surface because it is less resistive there. Accordingly, less confidence can be given to the model results greater depths and to the sides.

At depths below about 5 masl, the resistivity structure broadly follows the bedrock and fracture zone structure, being lowest over the fracture zone (Figure 5-3) and highest over the rocks which extend to the headland to the west of the pocket beach (Figure 2-1). However, based on the sensitivity model (Figure 5-7), the model below about sea level is not robust. The decrease in resistivity at the deepest level (at elevations of -4 m to -8 m) occurs mostly below the DOI and cannot be considered a reliable feature.

Above sea level, the chargeability (lower panel, Figure 5-6) is mostly low especially in the hard rocks of the headland, and except in the fracture zone follows a somewhat similar pattern as the resistivity. The chargeability is low to moderate in the fracture zone and is not correlated with the resistivity. Since signal to noise is significantly lower for IP than for resistivity, the chargeability pattern at depth (including the very high chargeablity to the left side of the model) cannot be regarded as reliable.

The results and the relative sensitivity and DOI model of the dipole-dipole survey in Bread and Cheese site, shown in Figure 5-8 and Figure 5-9, are generally consistent with the Wenner-Schlumberger model, though the values are more extreme. Dipole-dipole surveys are expected to be better at detecting vertical boundaries, however this is not apparent in the models, arguably because major interfaces are not vertical.

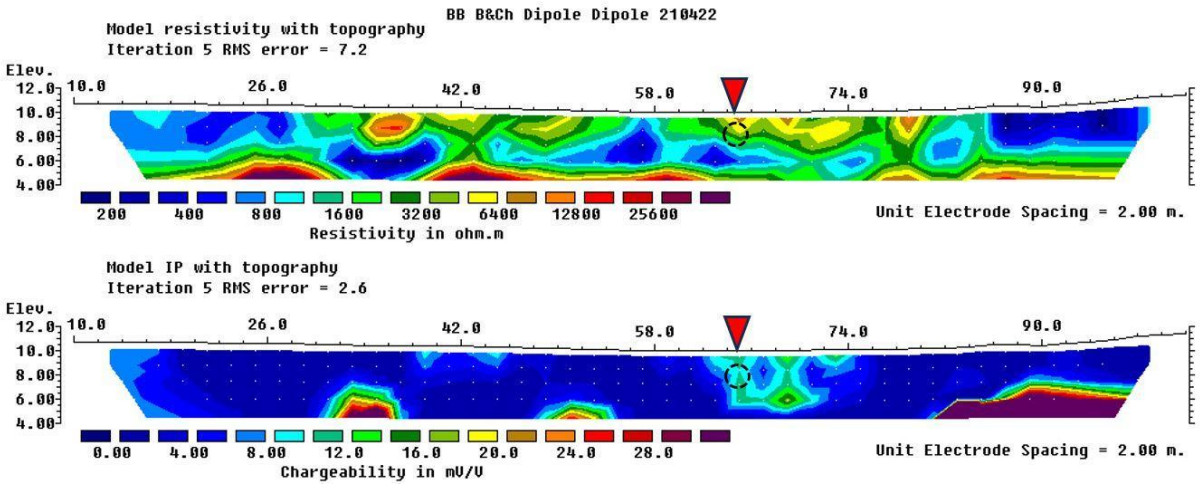

Figure 5-8) 2D resistivity sections based on Dipole-Dipole array along Gunridge Road, Bread and Cheese site. Top: resistivity; bottom: chargeability. Models by RES2DINV.

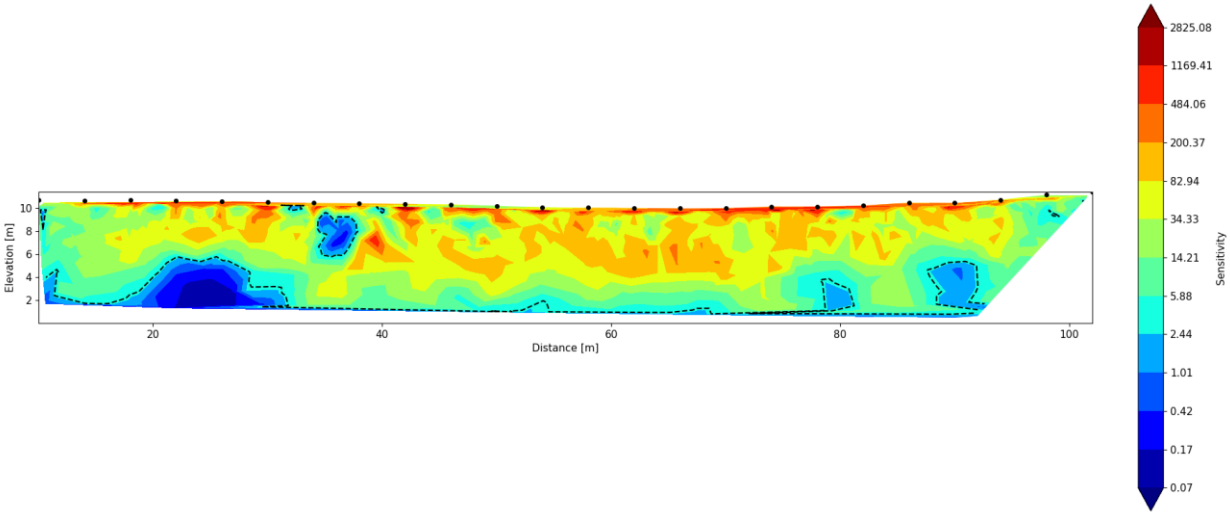

Figure 5-9) Relative sensitivity model and Depth of investigation (black dashed line) for the DCR survey (Dipole-Dipole configuration), at the Bread and Cheese site.

5.2 Cliff site

The geophysical surveys undertaken at the Cliff site are summarized in Table 4-2.

GPR and RTK surveys

Figure 5-10 shows elevation data for the Xlines (along the road) of grid Survey 2. Xline 0 (Y=0) is closest to the bay and Xline 6 (Y=6) is on the landward side of the road. The road rises in elevation to the SE then levels off at the SE end of the wooden retaining wall.

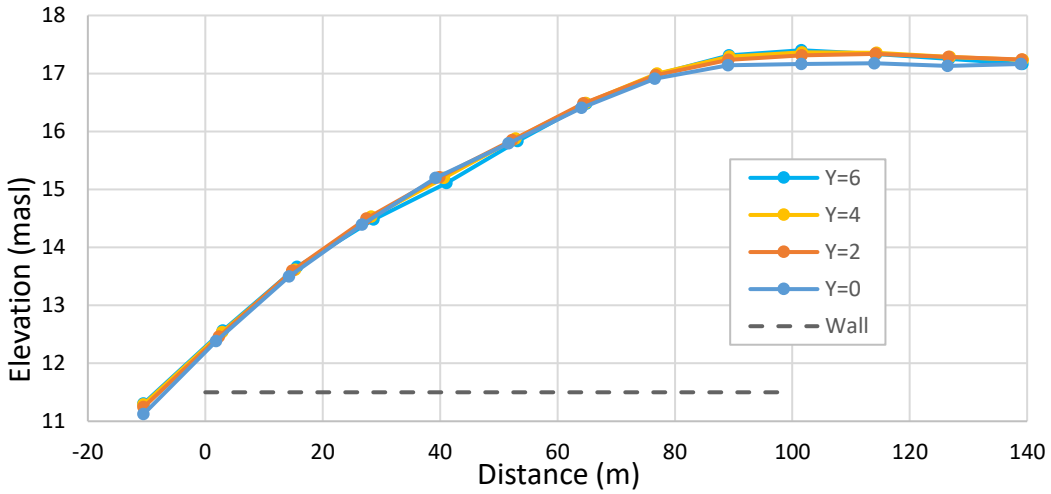

Figure 5-10) Elevation of Xlines in survey 2 along Northside Road, the Cliff site. The horizontal grey dashed line indicates the extent of the wooden retaining wall. Distance is measured from NW to SE. 23 April 2021. Vertical exaggeration 10X.

The dashed lines in Figure 5-11 show the change in elevation across the road relative to Xline 0. Positive numbers indicates the road surface slopes bay-ward, negative values indicate that it slopes landward. For rainwater to drain to the sides of the roads, Xlines 2 and 4 (brown and yellow dashed lines) should have the most positive values. This is the case past the end of the wooden retaining wall (Distance > 100 m). At each end of the wooden retaining wall, the road surface slopes bay-ward. At distance 40 m, the road surface is mostly flat but slopes landward at the landward edge. If the road was initially bowed up slightly in the centre (to shed rain water to both sides), then these measurements indicate subsequent movement of the road subsurface.

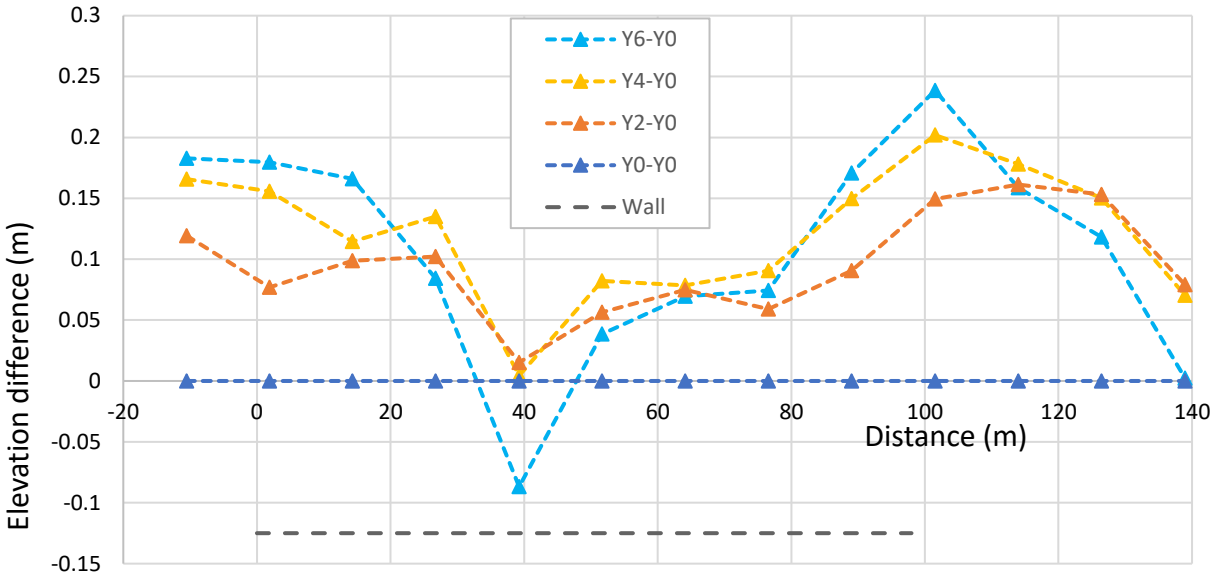

Figure 5-11) Survey 2 along Northside Road, the Cliff site. Dashed lines show the difference in elevation across the road, using Xline 0 (Y=0, close to the bay) as a reference. The horizontal grey dashed line indicates the extent of the wooden retaining wall. Distance is measured from NW to SE.

Figure 5-12 shows elevation data across the road (Ylines) for fine-scale Survey 4. Values of X correspond to the distance scale in Figure 5-11. These data further illustrate that the road surface slopes bayward at X=0 (magenta line), and landward at X=40 (red line) (cf. Figure 5-11).

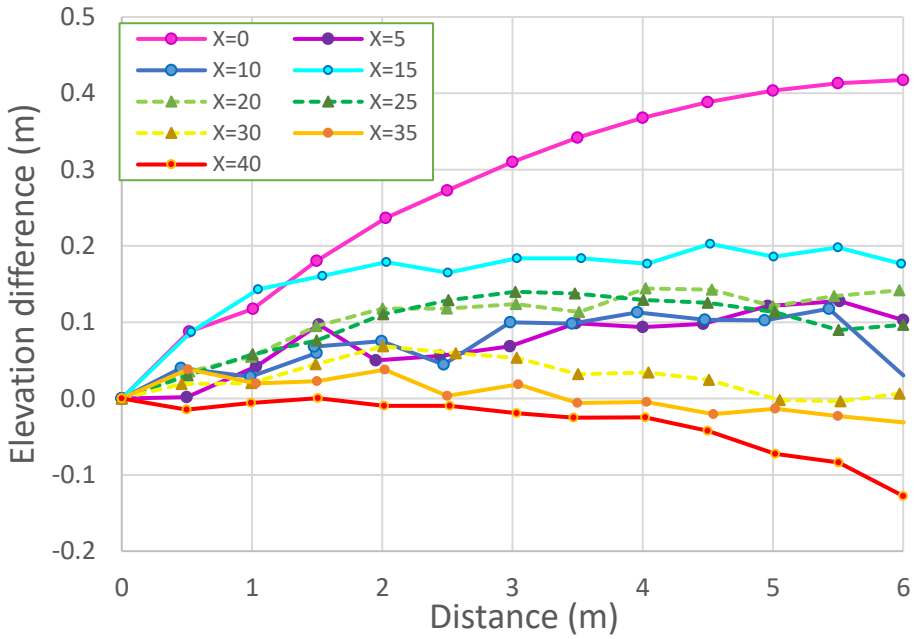

Figure 5-12) Difference in elevation across Northside Road in Survey 4, the Cliff site. Here distance is measured from the bay-side of the road and increases landward. Colours are in a roughly rainbow progression from NW to SE (increasing X). 28 May 2021.

GPR Survey 1 was taken along the middle of Northside Road, starting at the stop sign at the turn-off to the dock, 60 m from the NW end of the wooden retaining wall and extending to about 10 m from the SE end of the wooden retaining wall (Figure 4-9). Figure 5-13 shows there is some shallow layering under the road, probably related to its construction, and many hyperbolic signatures, particularly under the road supported by the retaining wall.

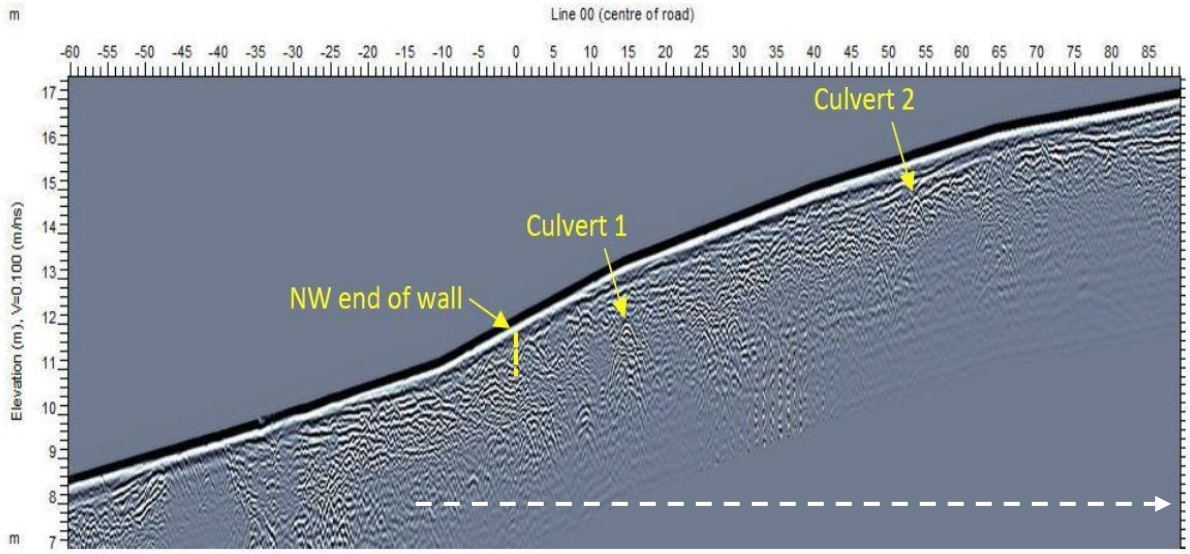

Figure 5-13) GPR profile survey 1, NW to SE, down the centre of Northside road, Cliff site. (250 MHz antenna, Gain/ filter. Dwow+SEC2 Gain, (Attenuation 3.74) start gain 1.41, maximum gain 190).). Elevation is metres above sea level. The white dashed line shows the location of GPR Survey2 (Figure 5-14)

GPR Survey 2 started 10 m from the NW end of the wooden wall and extended 55 m farther SE than Survey 1, where the road flattens and the bay-side retaining wall is composed of galvanised iron. The profiles from grid Survey 2, Figure 5-14 and Figure D 2, show a more complete story. In Xlines 0 (along the bay-side edge of the pavement) and 1 (2 m further toward the centreline of the road), the wooden support beams under the road show up as regular, double hyperbola. From the sharp, wavey reflections for distances greater than 98 m in Xline 0, it appears that the metal retaining wall is supported by some material that extends at least a short distance under the road. The Ylines, crossing the road parallel to the beams (e.g., Figure 5-15) are not very illuminating, though Yline 5 does pick up the top of abandoned Culvert 2, and Yline 10 suggests that supporting beams for the metal wall angle downward.

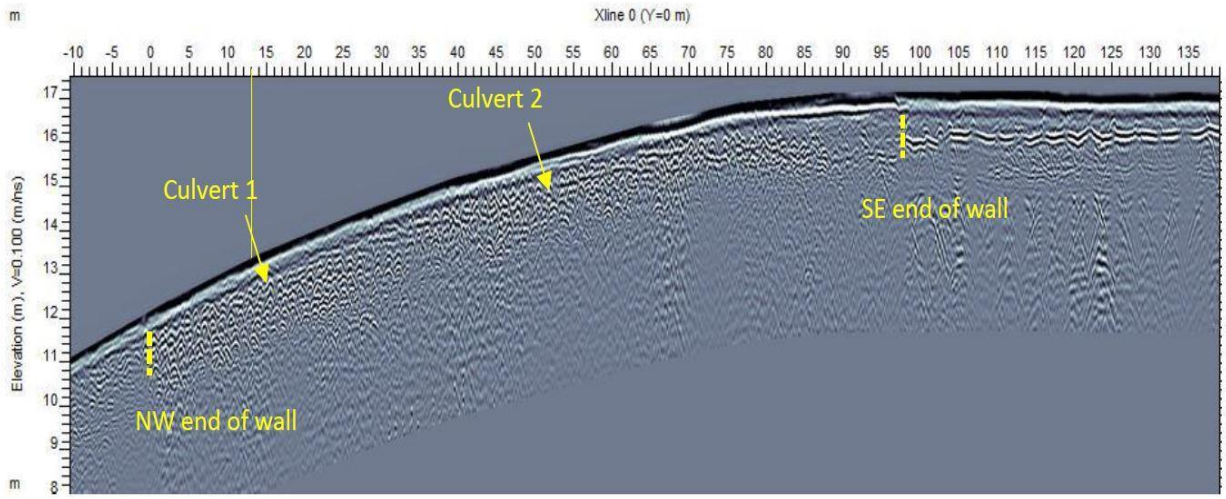

Figure 5-14) GPR profile along bayward side of road, Survey 2, the Cliff site, ~1.1 m from the retaining wall. Freq: 250 MHz, SEG default Gain settings. Vertical exaggeration 5X. 23 April 2021.

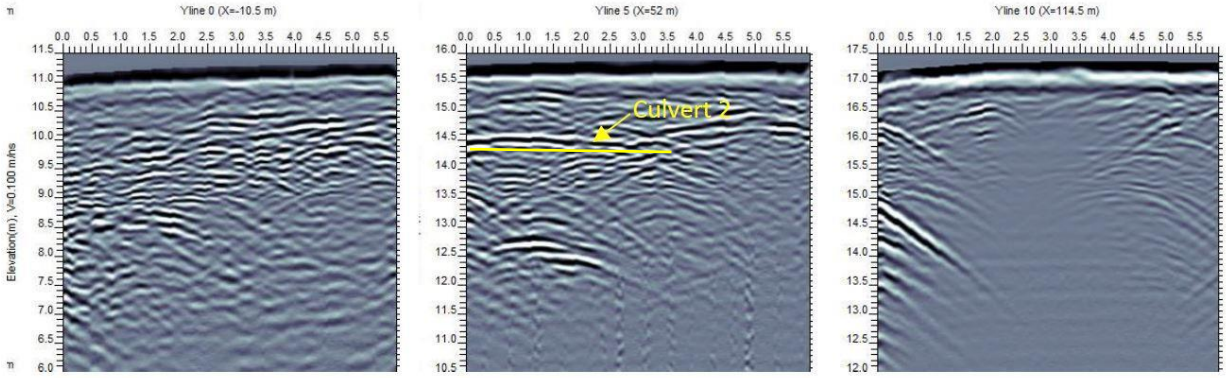

Figure 5-15) GPR profiles across the road. See Figure 5-14 for x locations. Left, Yline 0, 10.5 m NW of the start of the retaining wall; Centre, Yline 5 over (parallel) Culvert 2, So we wouldn't expect a point diffractor, but something more like an extended reflection from a layer; Right, Yline10 SE of the end of the retaining wall. The Cliff site. 23 April 2021. No vertical exaggeration.

Survey 3 was taken using longer antennas (100 MHz vs 250 MHz) in the hope of improving the depth penetration. However, because these antennas were not shielded from electromagnetic noise from power lines (and the RTK base!), the data were too noisy to be of use.

Survey 4 was taken to provide a higher spatial resolution for the first 40 m length of the retaining wall, where visual inspection revealed movement of the wall (Figure 2-16).

Figure 5-16 shows selected profiles along the bayside edge of the road and at two more landward distances from the wall. The full set of Xline profiles, without elevation corrections, are given in Figure D 2. Figure 5-16 a clearly shows the supporting beams, spaced at about 1.3 m, as a series of hyperbolas. There are about 5 layers of beams extending under the road from the wall:

it is difficult to distinguish the lower layers in the GPR profile. In Figure 5-16b, only one layer of beams is seen. Presumably, due to the slope of the original bank, the lower beams did not extend as far beneath the road as upper beams before encountering the bank. An indistinct layering seen in Figure 5-16b, roughly parallel to the road surface may indicate bedrock.

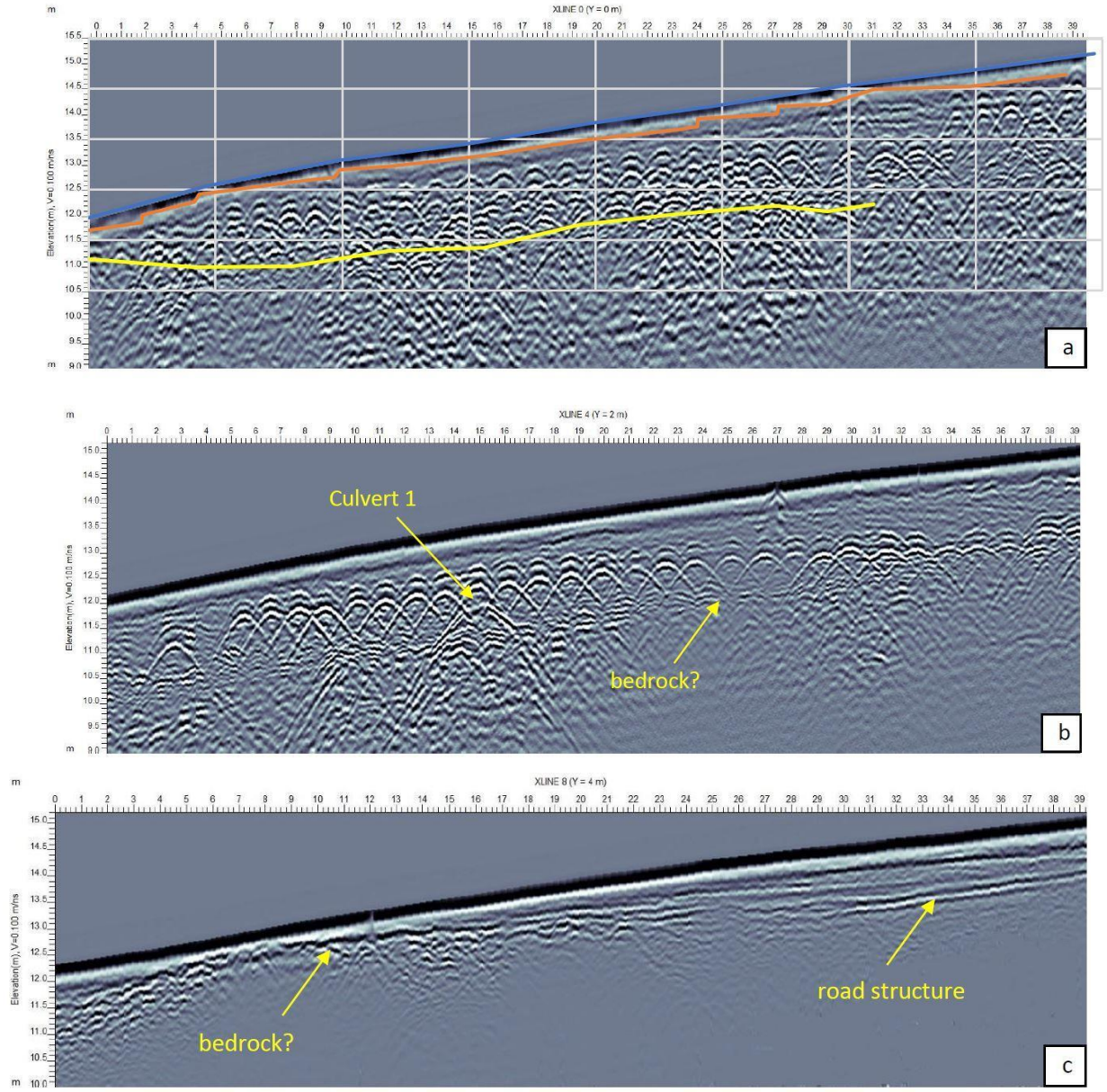

Figure 5-16) Selected GPR Xline profiles from Survey 4, along the first ~40 m of Northside Road adjacent to the wooden retaining wall. a) Xline 0, ~1.1 m from the retaining wall. Measurements of wall top (orange line) and bottom (yellow line) are superimposed. b) Xline 4, ~3.1 m from the retaining wall. c) Xline 8, ~5.5 m from retaining wall. Vertical exaggeration 2X.

Figure 5-16c is taken about 5 m from the wall, so about 1 m landward of the centre of the road. This would cover ground traversed by the original single-lane road. For distances from 0 to 20 m, it appears that bedrock is close to the surface. Farther to the SE, reflective interfaces parallel to the road surface are interpreted to indicate layering related to road construction. As seen in Figure D 3, profiles 0.5 m bay-ward and up to 2 m landward (Xlines 7 through 12) have a similar appearance.

An attempt was made to improve the localization of the beams using F-K migration, a process available using the software program *EKKO Project 5*. As shown in Figure 5-17, F-K migration, assuming a velocity of 0.1 m/ns, was successful in collapsing the hyperbolae from the top layer of support beams. However, the locations of deeper beams were obscured, so this was not seen as an improvement.

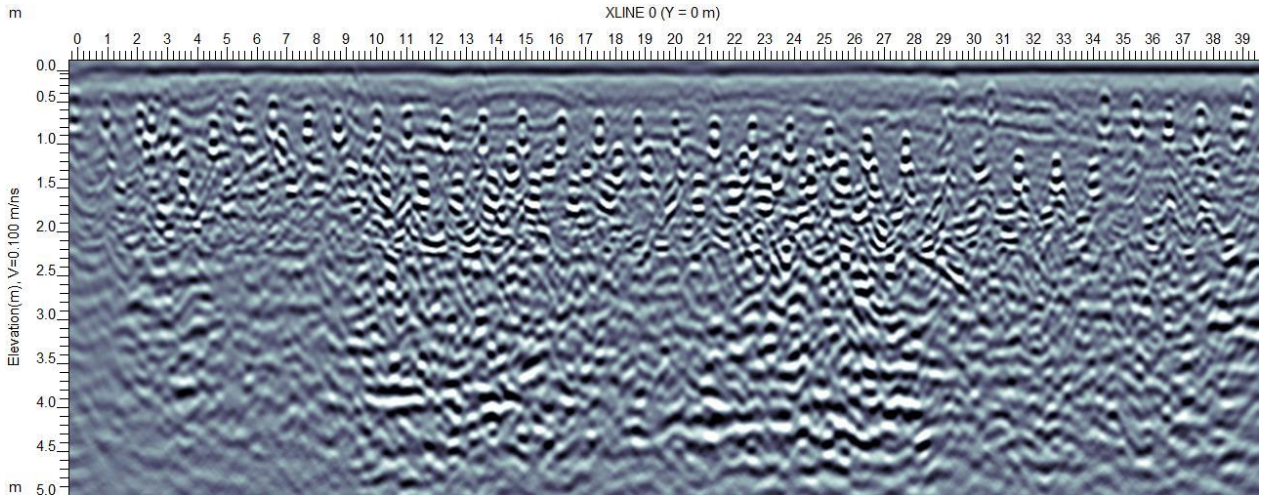

Figure 5-17) Xline 0 after F-K migration with velocity 0.1 m/ns. EKKO Project 5.

Comparing Figure 5-11 and Figure 5-16, it appears that a landward slope of the road surface is associated with a deeper layer of road construction material, and a bay-ward slope associated with shallower bedrock. As seen in Figure D 2, the area at distance ~20-50 m – where the retaining wall is warped outward, is associated with deeper bedrock on the landward side of the road.

The tight spatial resolution in Survey 4 allowed a 3D map of the grid region to be created using the Slice view option in Sensors & Software program EKKO Project 5. Figure 5-18 shows selected depth slices. Bright reflections are shown in red and orange colors. In the two first slices (0.5 to 0.6 m and 0.9 to 1.0 m depth) we can see that the bedrock is not even, and the culvert is in a space between two marked bedrocks occurances where there are no bright reflections. The beams are not all at a fixed distance from the surface, so they do not show up evenly at a given depth.

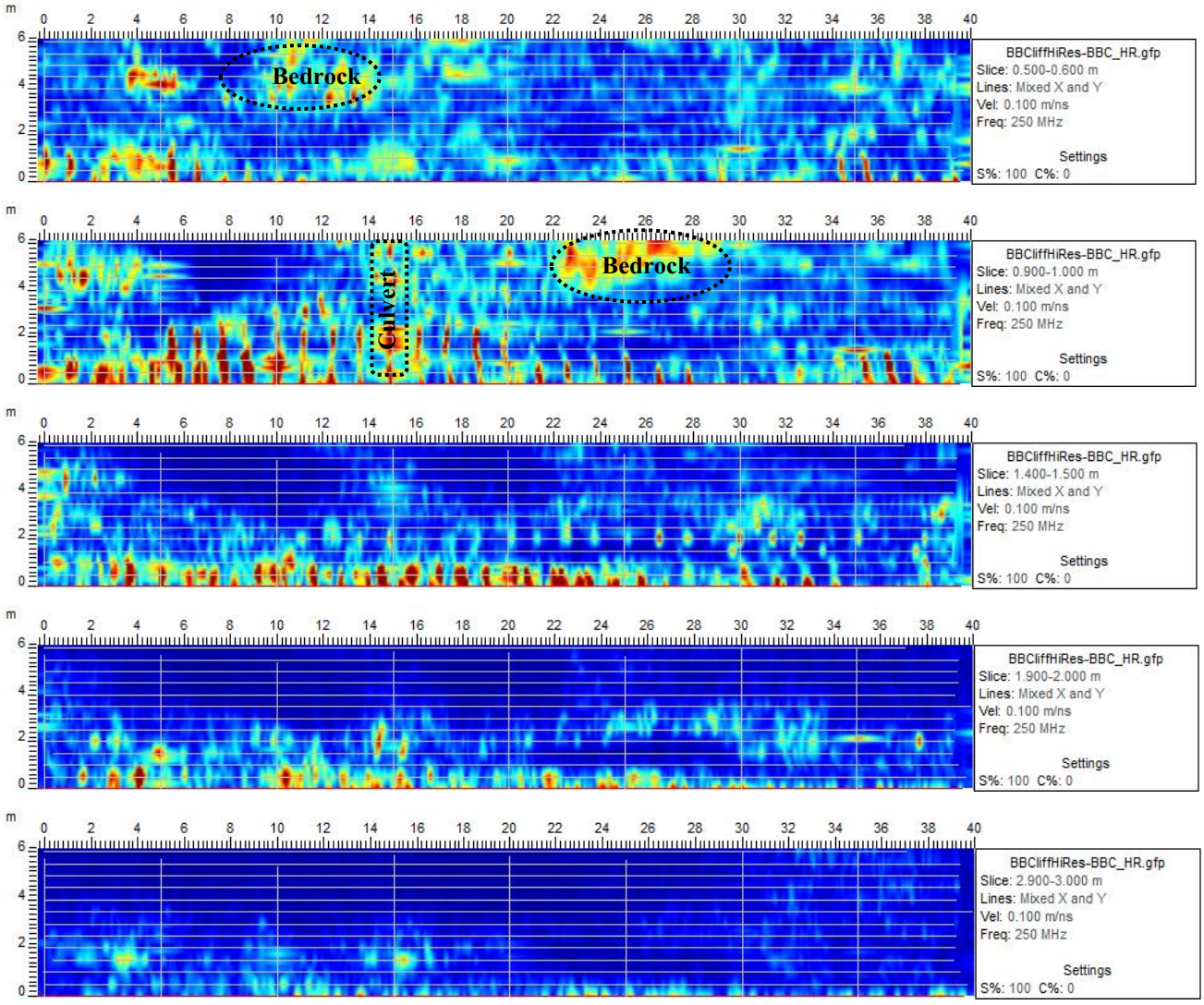

Figure 5-18) Depth slices (depth relative to the road surface) of reflectivity, GPR Survey 4. Slice View option in EKKO Project 5. F-K migration applied with velocity 0.1 m/ns.

From Survey 4 data, we can establish that the top layer of beams extends horizontally about 3.1 m from the wall underneath the road, so that they end about 2m from the bayside edge of the pavement. Survey 2 data have less spatial resolution (2 m vs 0.5 m) but they are consistent with this being the case for the entire stretch of the wooden retaining wall.

DCR and RTK surveys

Figure 5-19 depicts the elevation along DCR spreads on the landward side of the road at Cliff site using RTK data. This is consistent with the data taken during the GPR surveys (Figure 5-11).

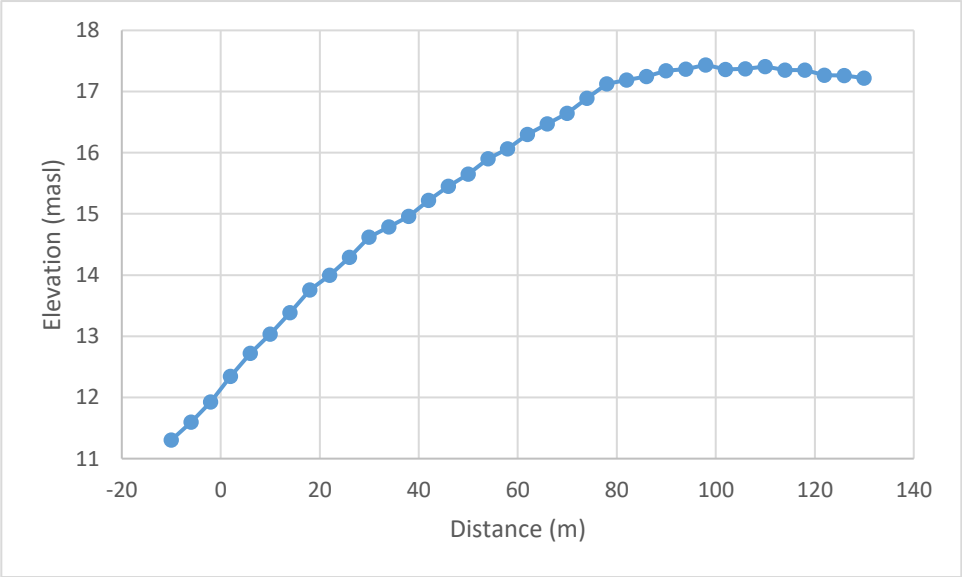

Figure 5-19) Elevation along DCR spreads at Cliff site. April 26, 2021.

As for the Bread and Cheese site, the DCR profile in the top panels of Figure 5-20 and Figure 5-22 show a surface layer a few meters deep which has generally low, though variable resistivity (blue colours). This corresponds to the road fill and overburden soil. The higher resistivity near-surface regions (green colours) corresponds to where the bedrock is closer to the surface: for example at stations ~10 m (see Figure 5-16c) and stations ~100 m.

At deeper levels, the bedrock has moderate to high resistivity (yellows to reds), with highs and lows over about a 20 m length scale. This variation is likely related to the bedrock properties, as for the Bread and Cheese site. The Cliff site is near the steeply dipping boundary between the St John's Group to the west and the more competent (less easily eroded) Signal Hill Group rocks to the east, so the highs and lows going from NW to SE are likely reflecting nearly vertical layers of rock, roughly 20 m thick, with different properties. The culverts (blue arrows) tend to be associated with dips in the resistivity. Possibly the culvert locations were chosen to be where the rock was weaker or the fill used to fill in the rest of the hole once the pipe of the culvert had been put in it is more conductive than the undisturbed, natural soil or glacial till elsewhere.

For stations >106 m, there is a region of very low resistivity at an apparent depth below the surface of ~5-10 m. This is interpreted as due to the effect of the metal retaining wall beyond the extent of the wooden retaining wall. Current crossing sideways across the road (~6 m) would be pulled into the very low resistivity metal, giving the false impression that there was a very low resistivity layer in the subsurface. The very high resistivity underneath this apparent very low resistivity layer is likely an overshoot artifact in the inversion program RES2DINV (see the sensitivity model and DOI dashed line in Figure 5-21).

The chargeability (lower panels in Figure 5-20 and Figure 5-22) is commonly related to the clay content where the ground is not mineralized. (The sedimentary bedrock here is not mineralized.) Chargeability is low (darkest blue) to moderate (other blues) for the top ~6 m of the subsurface and higher at greater depth. Near the surface it is lowest where the resistivity is also low. A lower clay content generally increases resistivity, this indicates that the low resistivity near the surface is due to water content rather than clay content. Perhaps including extra solutes from lingering road salt. At deeper levels, the correlation of resistivity and chargeability varies. Between distances 20 to 40 m, and 70 to 85 m resistivity and chargeability are correlated, whereas at other distances they are not. The highest chargeability occurs in areas where the resistivity is changing from lower to the NW to higher to the SE. This variation in correlation is interpreted to be due to differences in the composition or structure of the bedrock strata. For distances > 100 m, the effects of the metal wall make interpretation problematic. Figure 5-21 and Figure 5-23 show the relative sensitivity model and DOI of Wenner - Schlumberger and Dipole-Dipole array for the DCR surveys at this site.

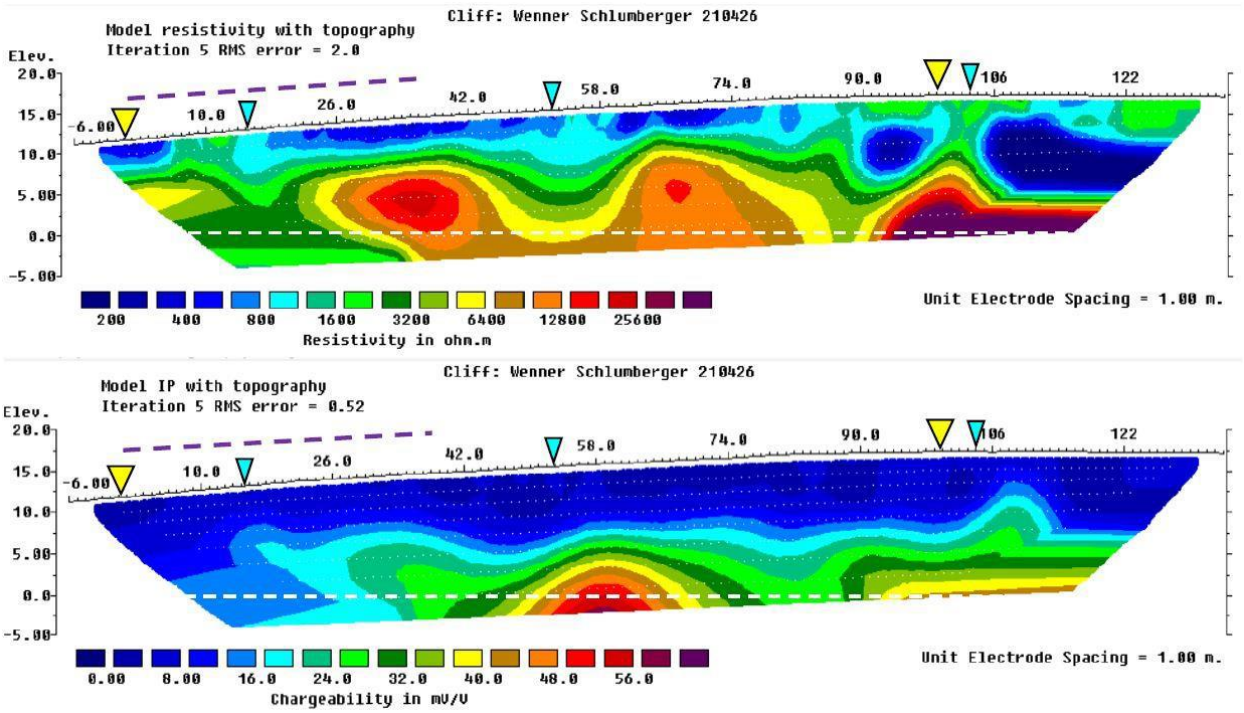

Figure 5-20) NW to SE DCR sections along Northside Road, Cliff site. Top: resistivity; bottom: chargeability. Yellow arrows indicate start and end locations of the wooden retaining wall. Blue arrow are locations opposite culverts 1, 2 and 3 (Figure 2-15). Dashed white line indicates sea level. Purple dashed line corresponds to GPR grid survey 4. 26 April 2021. No vertical exaggeration.

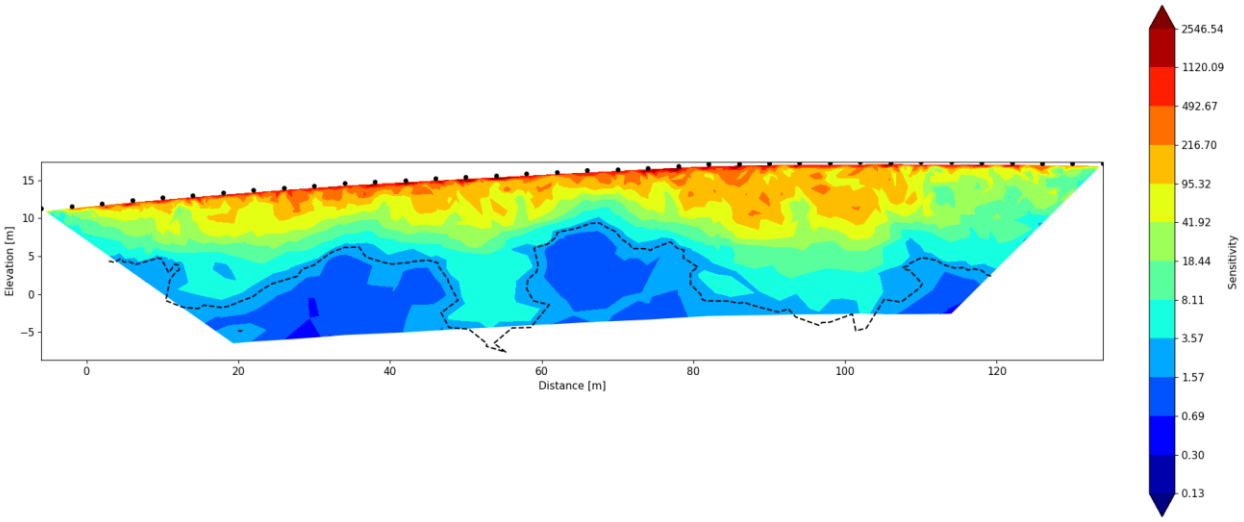

Figure 5-21) Relative sensitivity model and Depth of investigation (black dashed line) for the DCR survey (Wenner-Schlumberger configuration), at the Cliff site.

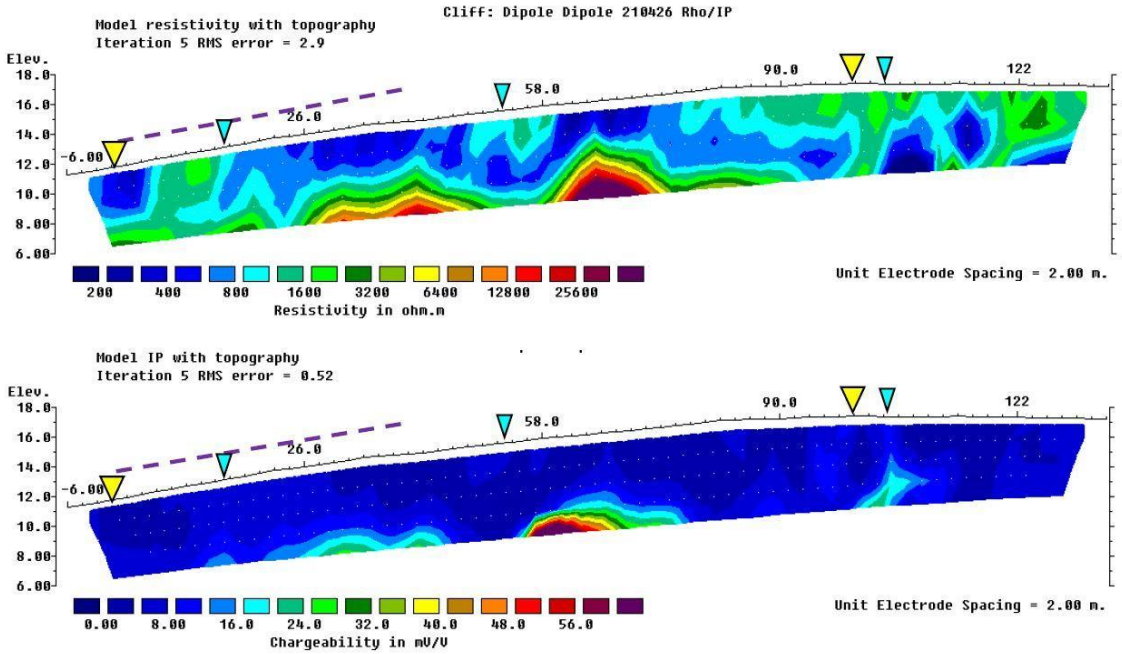

Figure 5-22) NW to SE dipole-dipole DCR sections along Northside Road to 6 m depth, Cliff site. Top: resistivity; bottom: chargeability. Yellow arrows indicate start and end locations of the wooden retaining wall. Blue arrow are locations opposite culverts 1, 2 and 3 (Figure 2-15). Purple dashed line corresponds to GPR grid survey 4. 26 April 2021. Vertical exaggeration 2X.

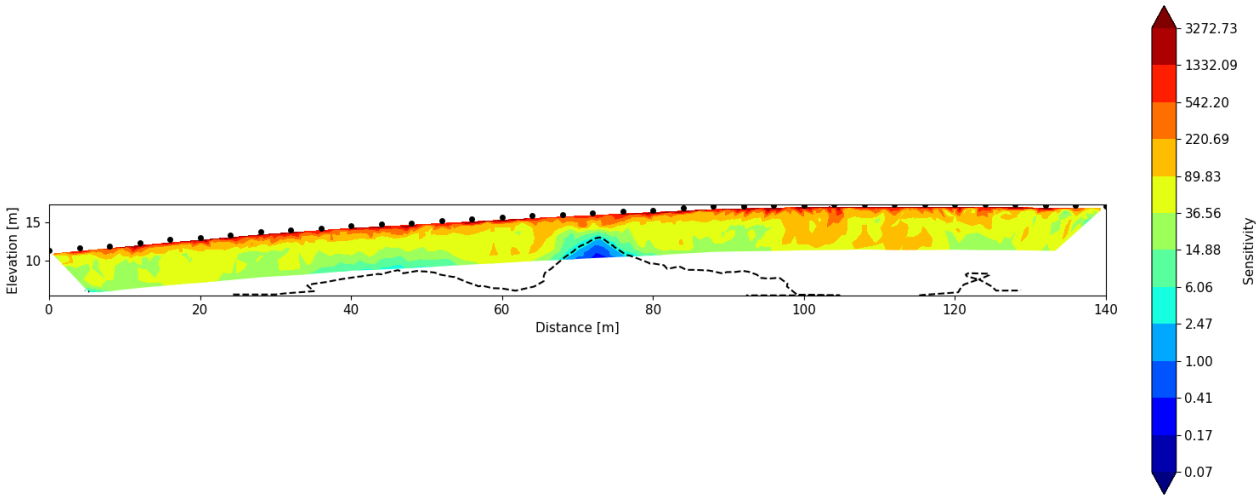

Figure 5-23) Relative sensitivity model and Depth of investigation (black dashed line) for the DCR survey (Dipole-Dipole configuration), at the Cliff site.

5.3 The Quays site

GPR and RTK surveys

RTK and GPR surveys were undertaken in a grid with lines along the road separated by 1.5 m. The elevation of the road surface is displayed along these lines in Figure 5-24. The road descends ~3.3 m to the NW, with a short section where it is almost flat, between distances 40 and 50 m. The last ~30 m of the profile, at the lowest elevation, is also nearly flat. Shown in the Figure 5-25 are the differences in elevation in the across road direction, relative to Xline 0 (Y=0, nearest to the coast). This figure indicates that the road mostly slopes toward the coast, except near the flat part, where it is flat in the cross direction as well as the along road direction. The bayward slope of the road surface is greatest opposite the main inlets (indicated by orange and yellow triangles).

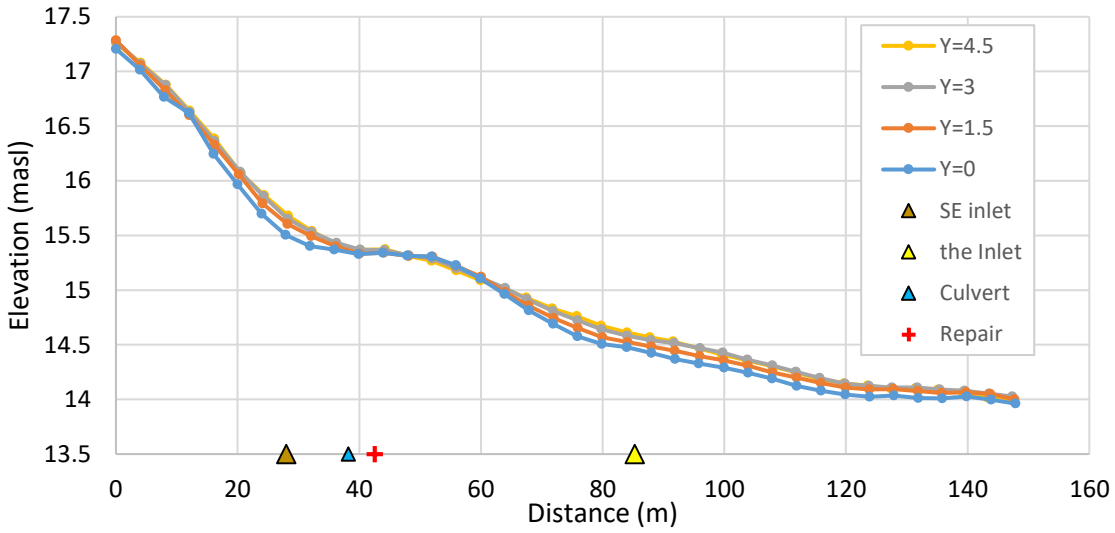

Figure 5-24) Elevation of Xlines of GPR grid along the road from SE to NW at the Quays site. Vertical exaggeration 18X. Location of additional features marked on the x-axis. 13 May 2021.

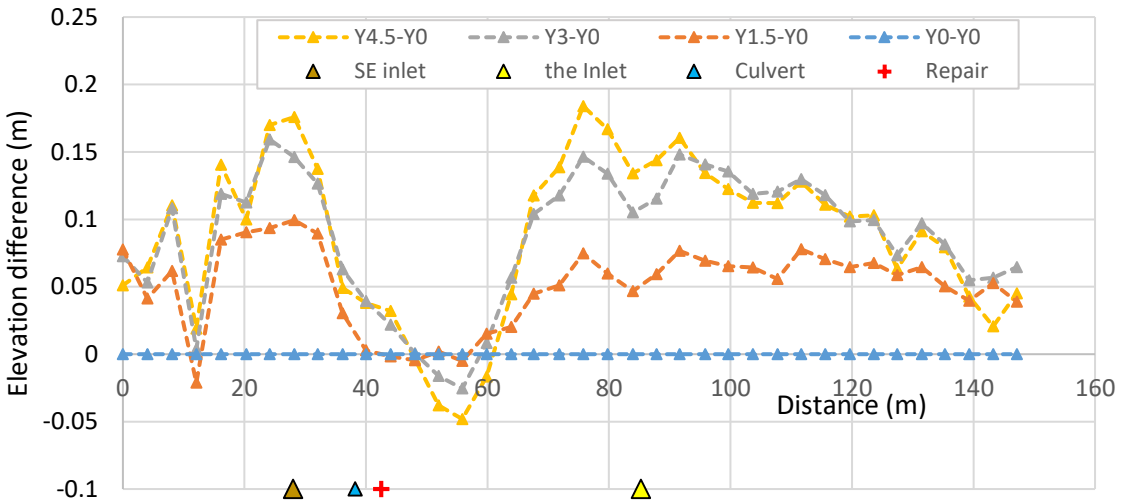

Figure 5-25) Differences in elevation of Xlines of GPR grid along the road from SE to NW at the Quays site. Relative to Xline 0, nearest to the coast. Location of additional features marked on the x-axis. 13 May 2021.

From the GPR profile, Figure 5-26, bedrock is very close to the surface at distance intervals 0 to 12 m, and 45 to 60 m. This is doubtless the reason for the shape of the road elevation in these regions, in particular why the road gradient flattens at ~50 m. Bedrock dips downward between 12 and 45 m, opposite the location of the SE inlet (Figure 5-25). The culvert (blue arrow) was placed in the overburden at ~38 m, at the base of the slope presumably in order to divert rainwater from flowing across the road.

From about 65 m onward, there are one or two strong sub horizontal interfaces that are likely related to the construction of the road. The bedrock may descend here: it is difficult to make out. It is possible that the sub-horizontal reflector from distances >100 m is bedrock, however if so it is unusually flat compared with what has been interpreted to be bedrock reflectors at the other sites. This stretch of the road at the lower elevations is underlain by Renews Head Formation, which is more easily eroded than the Gibbet Hill Formation underlying the higher elevations (Section 1.3.4), so we expect the bedrock interface to be relatively deep. This section of road was relocated inland due to a washout of unconsolidated material in 2011, supporting evidence that bedrock does not lie close to the surface in this location.

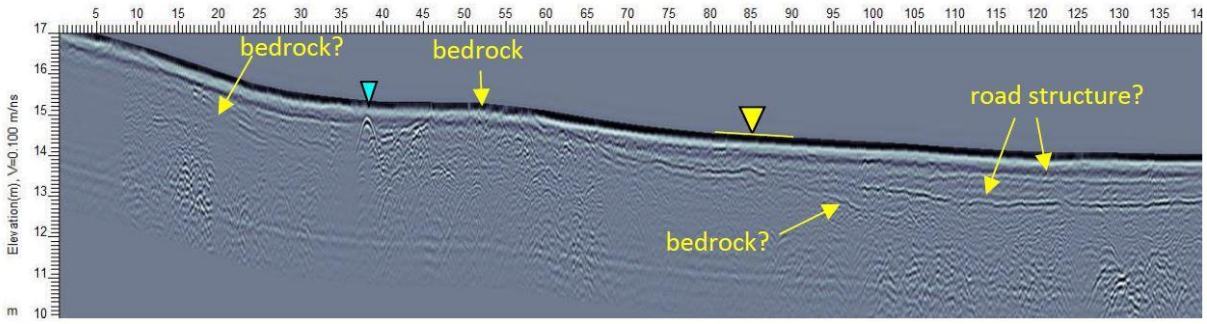

Figure 5-26) SE to NW GPR profile XLINE01 (Y=1.5), down Quays Road. Distances in metres. Elevation is metres above sea level. Blue arrow: culvert. Yellow arrow & bar: the Inlet. Vertical exaggeration 5X.

DCR and RTK surveys

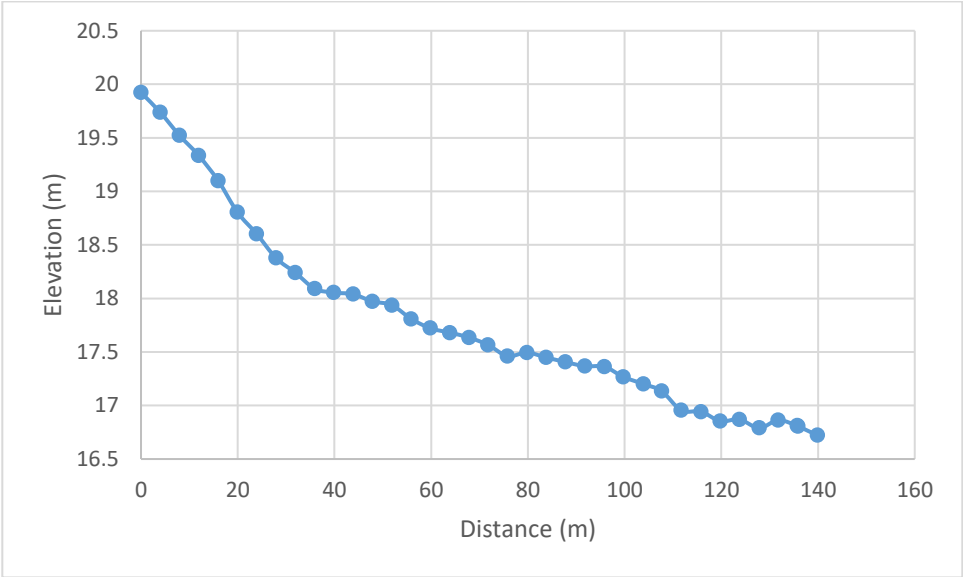

Figure 5-27) Elevation along DCR spreads at Quays site.

The elevation of the DCR electrodes, on the landward side of Quays Road, are given in Figure 5-26. The profile is similar to that for Xline 3 (Y=4.5 m), on the landward side of the road surface, though more irregular at larger distances, since some the electrodes there were placed on the landward side of the curbed road.

Figure 5-28 shows the results of the Wenner-Schlumberger survey, with no vertical exaggeration. The results of the dipole-dipole survey over the same profile but with lesser depth penetration and a vertical exaggeration of 5X are shown in Figure 5-30. As expected, the two

surveys show very similar results over their common depth range, though the dipole - dipole model shows higher resistivity contrasts in some locations.

As seen in Figure 5-28, at depth, the high resistivity occurs in three large blocks, with the boundaries occurring where there are inlets (see Figure 2-27) and so presumably weaker rock layers. The structure here, as at the Cliff site, is sub-vertical, though the rocks at the Quays are all within the stronger Signal Hill Group (Figure 1-7).

Relative sensitivity model and DOI for DCR survey for Wenner-Schlumberger array is depicted in Figure 5-29 which shows less sensitivity corresponding to lower resistivity at depth. Thus, the apparent reduction in resistivity (blue color) near and below sea level (white dashed line) is likely an artifact and not related to the composition of the subsurface.

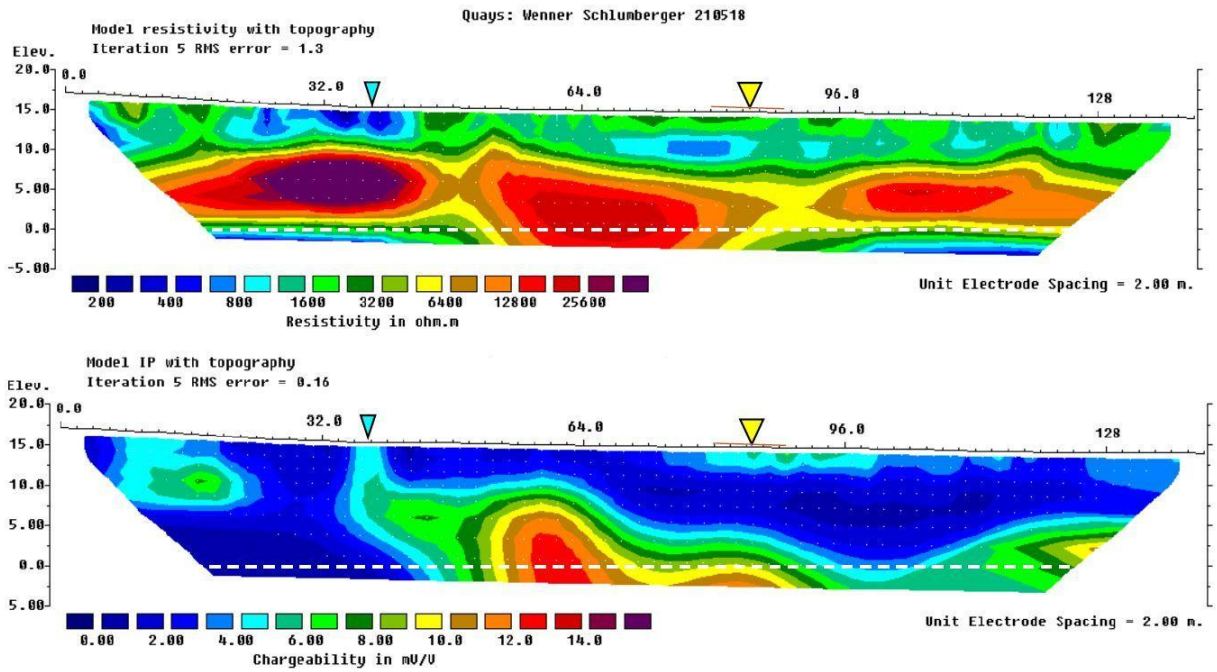

Figure 5-28) Illustrates the 2D resistivity and IP models of the DCR survey with Wenner-Schlumberger configuration along the Quays site. Models by RES2DINV.

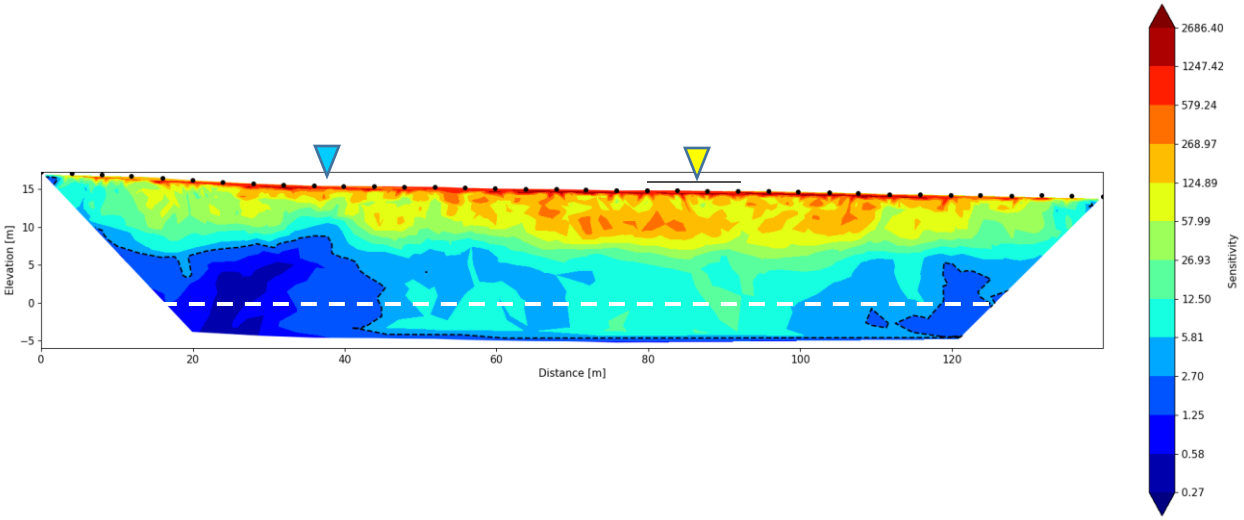

Figure 5-29) Relative sensitivity model and depth of investigation (black dashed line) for the DCR survey (Wenner-Schlumberger configuration), at the Quays site.

In the near surface there is significant variation in resistivity, with generally higher values than the other two sites. This is particularly the case where the bedrock is close to the surface (yellow colours, distances ~20 m and ~50 m). Low resistivity is seen near the culvert (cyan arrow) where the subsurface is looser and wetter.

The low resistivity layer between distances 12 and 42 m and at about 3 m apparent depth may be related to sideways flow of current and not to the underlying ground structure. There is a ditch to the SW of the road, with standing water in it at the time of the survey. The centre of the ditch is about 2.5 m distant from the electrodes and there may be similar reasons for the apparent low resistivity layer farther along the profile (distances > 64 m).

The chargeability at the Quays site is significantly lower than that at the other sites. Note that the scale for chargeability in Figure 5-28 and Figure 5-30 is 0 to 16, whereas at the other sites it is 0 to 64. The chargeability is high around the culvert. Otherwise, at shallower depths (Figure 5-30) it is mostly positively correlated with resistivity, as it is at the other sites (see Figure 5-6 and Figure 5-20). Deeper, high chargeability (Figure 5-28) correlates with high resistivity for the central headland (distance 50-85 m) but not for the other headlands.

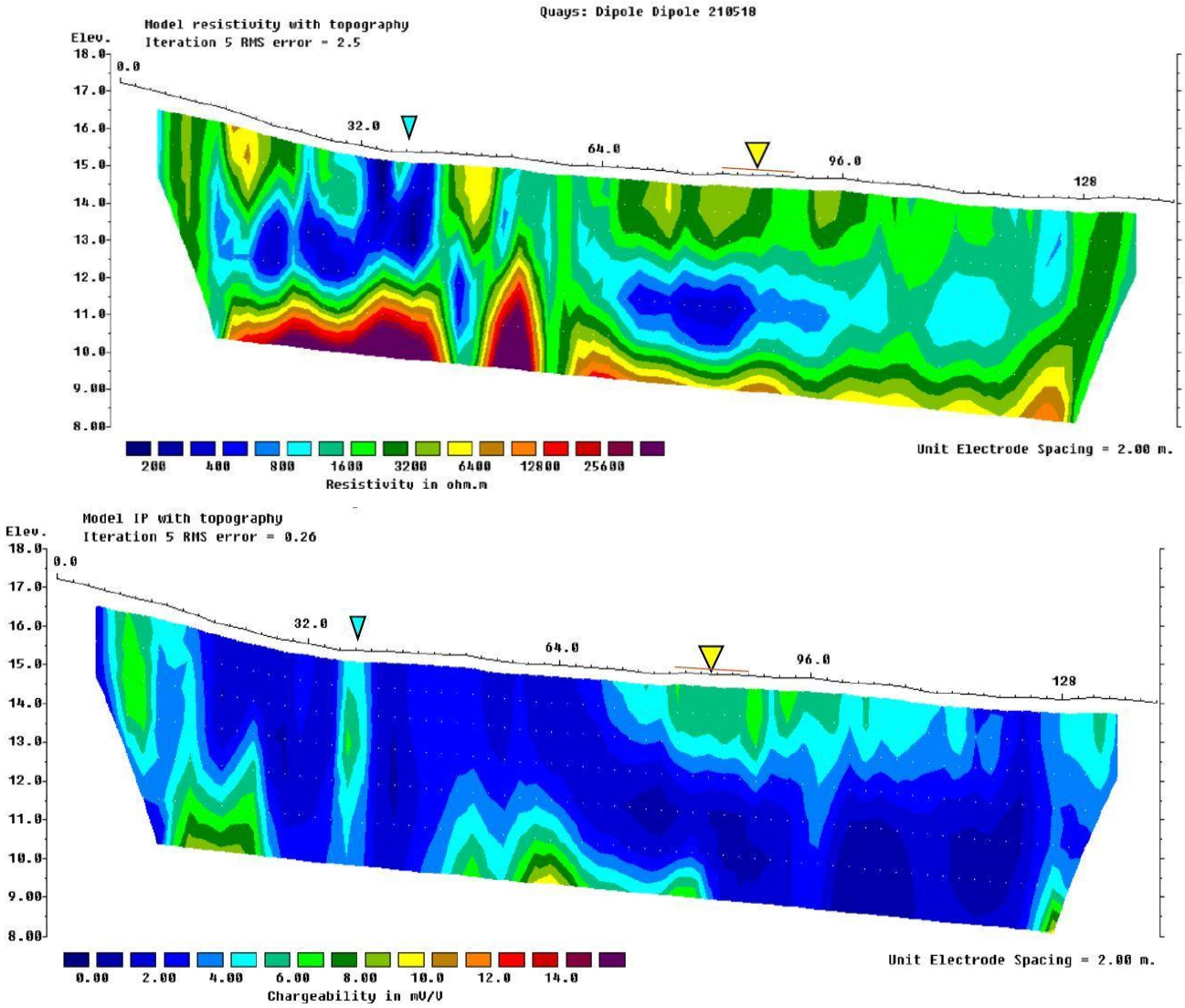

Figure 5-30) Shows the 2D resistivity and IP model of DCR survey with Dipole-Dipole configuration along the Quays.

Relative sensitivity of model and DOI for DCR survey Dipole-Dipole configuration is shown in Figure 5-31.

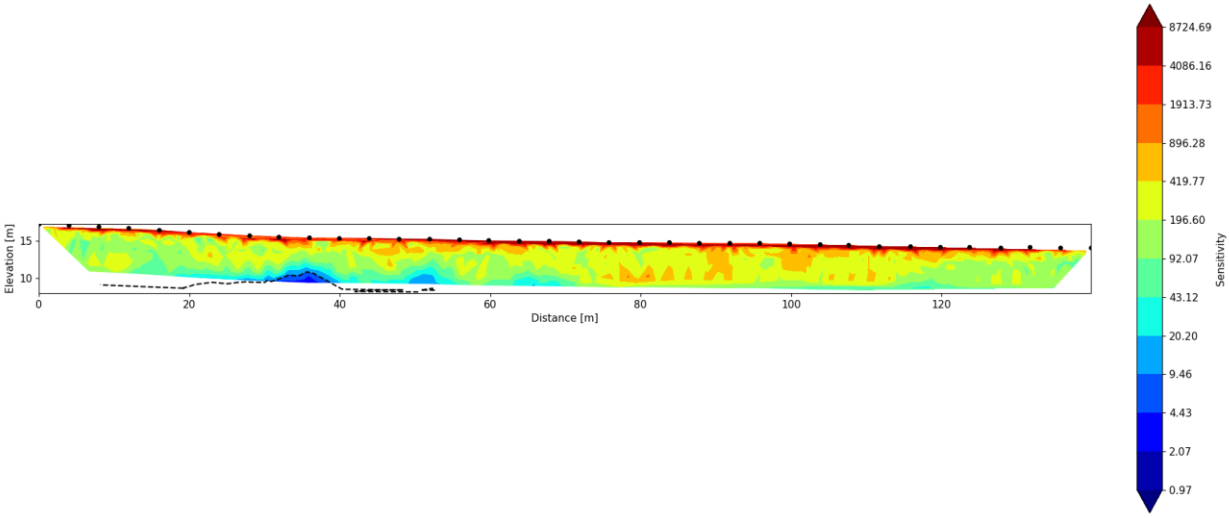

Figure 5-31) Relative sensitivity model and Depth of investigation (black dashed line) for the DCR survey (Dipole-Dipole configuration), at the Quays site.

6 Summary and discussion

6.1 The surveys

Determining subsurface properties can be useful for assessing the stability of roads. To accomplish this at three sites of concern on coastal roads in the town of Bay Bulls, this study employed an integrated approach that analyzed data from surveys using real-time kinetics GPS (RTK), 250 MHz ground penetrating radar (GPR), and direct-current resistivity/induced polarization (DCR/IP) combined with geomorphological observations. The three vulnerable sites were designated as Bread and Cheese, the Cliff, and the Quays (Figure 1-3). In this study, RTK and GPR surveys were conducted over sections of road about 6 m wide and 100 to 150 m long, while DCR/IP surveys were conducted along the landward side of the road sections.

Geomorphological observations complemented the geophysical results by providing information on the physical context and on past and ongoing changes in the environment. Bay Bulls is a deep (25-65 m) bay which opens to the southeast. Except in the west, its shores are characterized by steep slopes and sandstone cliffs overlain with a vegetated veneer of glacially derived diamicton. In the three survey areas, the bedrock strata dip steeply to the east. The bedrock is susceptible to erosion due to the freeze-thaw cycle, but creeping motion of the diamicton veneer due to overland groundwater flow is of more immediate concern.

The RTK surveys provided high-resolution elevation data, revealing slopes along and across the road surface. The GPR surveys investigated the subsurface to a depth of 4 or 5 m and provided information on the location and shape of subsurface structures, such as depth to bedrock and horizontal layering associated with road structure. The investigative depth of the DCR/IP surveys was up to 17 m. DCR measures the electrical resistivity of subsurface materials, which can be used to infer lithological information: for example, low porosity bedrock has a high resistivity, while damp sediments, fluid-filled fractures and salt water have lower resistivity. IP measures the ability of subsurface material to hold and transmit electrical charges, which can provide information on mineral and fluid content: clay minerals have high IP while salt water has low IP.

6.2 Limitations of the methods

Each of the three methods has its limitations. For GPR it was necessary to use relatively high frequency shielded antennae because of anthropogenic noise from power lines and houses along

the roads. This limited the depth of penetration to about 4 m at most. The strong contrast in properties between overburden and bedrock also meant that the GPR signal could not penetrate below the (often shallow) bedrock.

The location of the roads next to steep slopes presented a challenge for interpretation of the DCR models. It was not possible to carry out more that one profile parallel to the road, to investigate the influence of the 3D geometry. Unlike GPR signals, which come from a cone-shaped region directly underneath the antennae, currents from DCR electrodes spread out as much sideways as downward, particularly if the surface layers are relatively conductive. That this could be an issue is clear from the low resistivity artifact due to current flowing through the metal wall on the far side of the road at the Cliff site (distances > 100 m, Figure 5-20), and the low resistivity region arguably due to current flow through a water-filled ditch at the Quays site (distances 20-40 m, Figure 5-28). Such low resistivity features influence the resistivity model at greater apparent depths. Thus, the resistivity modelled below the ditch feature in Figure 5-28 is likely artificially high. The resolution and sensitivity of the DCR models decreases with depth, so the most reliable features of the DCR models are estimated to be from the near surface and middle depths.

The RTK surveys provided very precise (~1 cm) data on the road surface elevation over the survey grid. The limitation there is that measurements were taken at one time, so subsurface motions inferred from the measurements had to assume an ideal road profile sloping down to both sides.

6.3 Strengths of the methods

The RTK surveys were particularly useful in revealing subtle variations in the across-road profiles. Bay-ward, and occasional landward, slopes indicated areas where there has been undesireable creepage in the road subsurface (Figure 5-1, Figure 5-10, Figure 5-11, Figure 5-24, and Figure 5-25). Such slopes also indicate that rainwater would flow to one side of the road or the other, instead of to both sides as is optimal in road design. Elevation profiles along the roads often followed the elevation of underlying bedrock. GPR data was useful in determining where firm bedrock underlay the road and where there was a significant layer of less consolidated road fill and unconsolidated sediments under the road surface (e.g., Figure 5-26).

In addition to identifying depth to bedrock, the GPR surveys were useful in finding the location and depths of pipes and culverts, the extent of fractured rock at Bread and Cheese, and the lengths

and depths of wooden support beams under the widened section of road at the Cliff (Figure 5-3 and Figure 5-15). The limitation of GPR was its relatively shallow depth of penetration (4 to 5 m). Penetration depth, to a certain extent, increases with the size of the antennas. Surveys were carried out with longer (100 MHz vs 250 MHz) antennas, however the longer antennas could not be shielded from the electromagnetic noise of the powerlines along the road. The 100 MHz profiles showed less spatial resolution and, due to the noise, no better depth penetration.

The DCR surveys had a depth penetration of up to 17 m, enabling measurements below the reach of the GPR. Inherent to the method, the spatial resolution in the inverted models decreases with depth, as does the sensitivity to the resistivity values, especially for high resistivity regions. Resistivity values varied from ~200 Ωm, typical for unconsolidated surface sediments, to more than 20,000 Ωm, appropriate for a tight sandstone (Figure 5-6, Figure 5-20 and Figure 5-28). Measurements from deeper levels revealed large scale (10-30 m) horizontal variations resistivity in the steeply dipping strata of the subsurface, that correspond to the scale of headlands and inlets, and so are likely related to the erosional properties of the rock, though due to a lack of resolution and sensitivity in the models, any sharp boundary locations were blurred and the resistivity contrasts uncertain. Near surface (2-3 m depth) measurements showed variations linked to the properties under the survey line, for example showing higher resistivity where bedrock was close to the surface. However, in the DCR method the current flows sideways as well as downward. The inversion program assumes that the ground structure is two-dimensional, and that is not the case at the three coastal sites. The current could find low resistivity pathways through drainage ditches, low resistivity fill, fences or metal guard rails, potentially resulting in misleading models for intermediate (3-8 m) depths (e.g., at distances > 100 m in Figure 5-20).

The IP models (Figure 5-6, Figure 5-20 and Figure 5-28) mostly show low values (< 4 mV/V), reflecting the low clay content of the road material, the diamicton sediments and the sandstone bedrock. Anthropogenic features, like culverts, generated higher values, though not centred on the source (e.g., culverts in Figure 5-6, and Figure 5-28). The models showed some higher values of IP at apparent depths greater than ~ 10 m, possibly related to bedrock properties, however their significance is undetermined: note that signal to noise of IP is inherently less than for resistivity so the depth of investigation for IP is shallower than for resistivity. The combination of more conductive layer at top of a resistive layer, and the resistive layer itself, cause the current to not get as deep as it otherwise would. So, when there is no current at depth, the IP value is not valid.

6.4 Summary of results

The geophysical and geomorphological surveys revealed different features at the three sites. Figure 6-1 illustrates key profiles from the different surveys at one of the sites, Bread and Cheese. The Bread and Cheese site is located next to pebbled beaches and headlands, and the road section, about 10-11 masl, traverses a culvert that transports water from a stream to the beach. The GPR survey revealed the horizontal extent (~25 m) of the weak, fractured region under the road. This is similar to the width of the pocket beach into which the culvert drains. The results of the DCR survey suggest that the weakest point are to the west of the culvert (Figure 5-5 and Figure 5-6), where rip-rap has been deposited, and this also corresponds to an area where the road surface slopes bayward. The culvert under the road is composed of two segments with different diameters and an imperfect seal between them (Figure 2-6), which could lead to water infiltration under the road. The segments are rusted and deformed (Figure 2-4, Figure 2-5 and Figure 2-6) and will need to be replaced eventually.

The variation in the shapes of the pebbles on the beach and nearby headland (Figure 2-7 and Figure 2-8) indicate that wave action is commonly restricted to the near shoreline, except during storms. Such storms would play a role in erosion of the bluff (Figure 2-11 and Figure 2-12). Overland water is likely to be the main factor leading to instability of the surficial vegetated diamicton veneer and road material: recently (in late 2022 or early 2023), a new guardrail was constructed inside an older one (Figure 2-13) which had been carried bay-ward with creeping motion of surficial materials. To protect the road section nearest to shore, it would likely be necessary to armour the rest of the pocket beach.

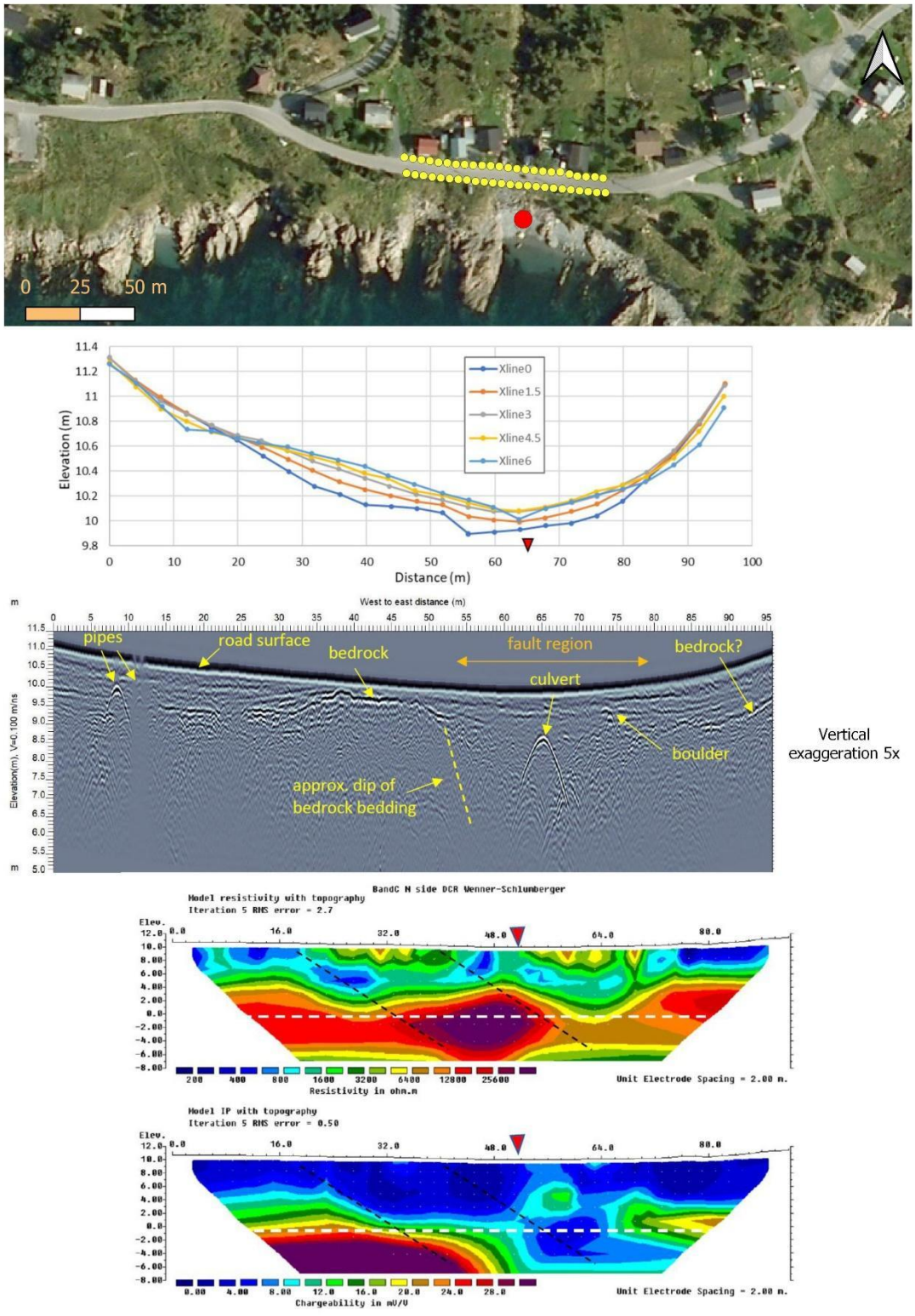

Figure 6-1) Illustration of the correlation of the geophysical results at Bread and Cheese. Note the different vertical exaggerations in the separate profiles.

The Cliff site underwent road widening in the 1960's with the construction of a wooden retaining wall, which is now displaced outward in some locations due to subsurface movement (Figure 2-17). This shift is evident in the shape of the wall and of the road surface (Figure 2-16 and Figure 5-10). Observations of longitudinal cracks in the pavement (Figure 2-25) were further signs of subsurface creepage. GPR survey data (Figure 5-16 and Figure 5-18) reveal the locations bedrock, road fill, and the beams extending from the wall under the road. This is useful information for planning the eventual replacement of the retaining wall, as there are no records of its construction.

The bedrock at this site contains the steeply dipping boundary between the shale-rich Renews Head Formation to the northwest and the more competent sandstones of the Gibbet Hill Formation (Figure 1-7, Appendix A). The DCR models (Figure 5-20) show low resistivity in the first several meters, reflecting the damp road fill or host to brackish waters from deicing salts. Below this, the resistivity changes from low for the first ~20 m in the northwest to higher, consistent with the bedrock geology transition (weaker to stronger).

The Cliff site is sheltered next to the marine terminal (Figure 4-8) and so wave action has very limited impact. However, creeping downward motion of the surficial colluvial material is evident on the steep slopes above and below the road (Figure 2-19 to Figure 2-24). It is likely that overland near surface water, which weakens and adds weight to the sediments, also seeps under the road and contributes to the subsurface motion there. Once the road is repaired, the main focus needs to be on preventing overland water from destabilizing the Quaternary cover, by enhancing the drainage system and vegetation management.

Quays road runs along the top of cliffs on the southern part of the bay, with the road edge overlooking two pocket beaches in the southeast and central regions of the survey area (Figure 2-27). The road runs very close to the cliff edge at 'the Inlet', over the central pocket beach. GPR data (Figure 5-26) shows that over the higher elevation, southeastern two-thirds of the survey area bedrock is close to the surface, providing a relatively stable foundation for the road. The road to the northwest of the Inlet is underlain by deeper road fill and sediments: the road here was relocated inland after a washout in 2011 (Figure 4-10). The DCR profile (Figure 5-28) shows a lower resistivity zone under the Inlet at about 5 m depth. This likely reflects weaker strata that eroded more easily to produce the Inlet.

Due to its location and orientation, the Inlet is more sheltered from storms than Bread and Cheese. Only waves from the northeast over only a 1 km fetch across the bay (Figure 1-3) would enter the Inlet directly. This is reflected in the beach rocks being less rounded and sorted (Figure 2-30). Landward of the Inlet, the ground slopes upward and has been cleared of many trees (Figure 2-28). A gully opposite the inlet ends in a ditch, and the road verge is curbed with no nearby culvert. Because the road runs very close (< 0.5 m) to the cliff edge here, seepage under the road from groundwater may endanger the road's stability. Turf and loose sediment from the road verge are seen on the beach below (Figure 2-30). Attention to drainage pathways and the planting of more trees may help delay erosional damage.

Erosion under the road opposite the southeastern inlet (Figure 4-10) is less concerning. Here the ground landward of the road is nearly flat so bay-ward flow of groundwater is less, and it is covered with trees, whose roots help to stabilize the landscape. The shoreline here is also less deeply incised.

6.5 Conclusions

In these three different sites of concern on coastal roads in Bay Bulls, a reasonable understanding of the subsurface characteristics has been achieved through the integration of the complementary GPR, DCR/IP and RTK methods. The results highlight the importance of local factors, including a general understanding of the geomorphological characteristics, in assessing erosion concerns.

Overall, Bay Bulls is located in a fortunate position, sheltered from all but easterly and southeasterly storms, with strong bedrock that is relatively resistant to wave action. Though the shores shows rocks displaced by the freeze-thaw cycle, local fishermen have not noticed any difference in the rocky shoreline over the last several decades (E. Mulcahy & H. Williams, pers. comm. 2022). However, roads over quaternary cover face vulnerability primarily due to overland water flow leading to creep in surficial materials at all three sites, and southeasterly storms pose an ongoing danger at the Bread and Cheese site. The predicted increase in precipitation and increased severity of storms associated with global climate change will exacerbate erosional effects at these sites. The effects of rising temperatures are uncertain, as less insulating snow cover and more melting of snow may lead to an enhancement of the freeze-thaw cycle, even if there are fewer days with frost (Finnis & Daraio, 2018).

7 References

Annan, A. P. (2001). Ground Penetrating Radar Workshop Notes, 197 pp. *Sensors and Software, Mississauga, Ontario, Canada*.

Annan, A. P., Davis, J. L., & Pilon, J. (1992). Design and development of a digital ground penetrating radar system. *Ground Penetrating Radar, Geological Survey of Canada Special Paper*, *90*(4), 15–23.

Attwa, M., El Mahmoudi, A., Elshennawey, A., Günther, T., Altahrany, A., & Mohamed, L. (2021). Soil Characterization Using Joint Interpretation of Remote Sensing, Resistivity and Induced Polarization Data along the Coast of the Nile Delta. *Natural Resources Research*, *30*, 3407–3428.

Bano, M. (1996). Constant dielectric losses of ground-penetrating radar waves. *Geophysical Journal International*, *124*(1), 279–288.

Batterson, M. J., & Liverman, D. G. E. (2010). Past and future sea-level change in Newfoundland and Labrador: Guidelines for policy and planning. *Current Research. Newfoundland and Labrador Department of Natural Resources Geological Survey, Report*, 10–11.

Batterson, M. J., Liverman, D. G. E., Ryan, J. M., & Taylor, D. M. (1999). *The assessment of geological hazards and disasters in Newfoundland: An update*. Goverment of Newfoundland and Labrador, Department of Mines and Energy ….

Bell, T., Daly, J., Batterson, M. J., Liverman, D. G. E., Shaw, J., & Smith, I. R. (2007). Late Quaternary Relative Sea-Level Change on the West Coast of Newfoundland*. *Géographie Physique et Quaternaire*, *59*(2–3), 129–140. https://doi.org/10.7202/014751ar

Briguglio, L., Cordina, G., Farrugia, N., & Vella, S. (2009). Economic Vulnerability and Resilience: Concepts and Measurements. *Oxford Development Studies*, *37*, 229–247. https://doi.org/10.1080/13600810903089893

Bruckner, W. D. (1969). Post-glacial geomorphic features in Newfoundland, Eastern Canada. *Ecologae Geologicae Helvetiae*, *62*(2), 417–441.

Canadian Climate Normals. (2011, October 31). Environment and Climate Change. https://climate.weather.gc.ca/climate_normals/index_e.html

Cardone, V. J., Jensen, R. E., Resio, D. T., Swail, V. R., & Cox, A. T. (1996). Evaluation of contemporary ocean wave models in rare extreme events: The "Halloween Storm" of October 1991 and the "Storm of the Century" of March 1993. *Journal of Atmospheric and Oceanic Technology*, *13*(1), 198–230.

Carpenter, E. W., & Habberjam, G. M. (1956). A tri-potential method of resistivity prospecting. *Geophysics*, *21*(2), 455–469.

Cassidy, N. J., & Jol, H. M. (2009). Ground penetrating radar data processing, modelling and analysis. *Ground Penetrating Radar: Theory and Applications*, 141–176.

Catto, N. (1992). Surficial geology and landform classification maps for the southwest Avalon Peninsula. *Newfoundland Department of Mines and Energy, Geological Survey Branch, Open File*, *2186*.

Catto, N. (1993). Surficial Geology and Landform Classification, northwestern Avalon Peninsula. *Government of Newfoundland and Labrador, Department of Mines and Energy, Open File*, *1*.

Catto, N. (1994). Surficial Geology and Landform Classification, eastern Avalon Peninsula. *Government of Newfoundland and Labrador, Department of Mines and Energy, Open File*, *1*.

Catto, N. (1998). The pattern of glaciation on the Avalon Peninsula of Newfoundland. *Géographie Physique et Quaternaire*, *52*(1), 23–45.

Catto, N. (2006). More than 16 years, more than 16 stressors: Evolution of a reflective gravel beach, 1989-2005. *Géographie Physique et Quaternaire*, *60*(1), 49–62.

Catto, N. (2011). *Coastal Erosion in Newfoundland*. 148.

Catto, N. (2020). The Avalon of Newfoundland: Geomorphology, People and Landscape. In O. Slaymaker & N. Catto (Eds.), *Landscapes and Landforms of Eastern Canada* (pp. 333–367). Springer International Publishing. https://doi.org/10.1007/978-3-030-35137-3_15

Catto, N., Scruton, D. A., & Ollerhead, L. M. (2003). *The coastline of eastern Newfoundland*. Department of Fisheries & Oceans Canada, Science, Oceans & Environment Branch.

Catto, N., & St Croix, L. (1998). Urban geology of St. John's, Newfoundland. *Urban Geology of Canadian Cities: Geological Association of Canada, Special Paper*, *42*, 445–462.

Cook, J. C. (1975). Radar transparencies of mine and tunnel rocks. *Geophysics*, *40*(5), 865–885.

Diallo, M. C., Cheng, L. Z., Rosa, E., Gunther, C., & Chouteau, M. (2019). Integrated GPR and ERT data interpretation for bedrock identification at Cléricy, Québec, Canada. *Engineering Geology*, *248*, 230–241.

Dohey, L. (2016, November 30). WWII Dockyard for Bay Bulls. *Archival Moments*. http://archivalmoments.ca/2016/11/30/wwii-dockyard-for-bay-bulls/

Electromagnetic Geophysics. (2015, 2018). EM GeoSci. https://em.geosci.xyz/content/geophysical_surveys/gpr/data.html

Finnis, J., & Daraio, J. (2018). Projected impacts of climate change for the province of Newfoundland & Labrador: 2018 update. *Memorial University of Newfoundland, St. John's, Nfld*.

Forbes, D. L. (1984). Coastal geomorphology and sediments of Newfoundland. *Geological Survey of Canada, Paper*, 11–24.

Gatto, L. W. (1995). *Soil freeze-thaw effects on bank erodibility and stability*.

Government of Canada. (2003). *Precise Point Positioning*. https://webapp.csrs-scrs.nrcan-rncan.gc.ca/geod/tools-outils/ppp.php?locale=en

Government of Canada. (2019, July 18). *Canadian Tide and Current Tables*. Canadian Tide and Current Tables. https://charts.gc.ca/publications/tables-eng.html

Government of Canada, S. C. (2001, January 15). *Census of Population*. https://www12.statcan.gc.ca/census-recensement/index-eng.cfm

Guza, R. T. (1974). *Excitation of edge waves and their role in the formation of beach cusps.* University of California, San Diego.

Hardy, J. P., Groffman, P. M., Fitzhugh, R. D., Henry, K. S., Welman, A. T., Demers, J. D., Fahey, T. J., Driscoll, C. T., Tierney, G. L., & Nolan, S. (2001). Snow depth manipulation and its influence on soil frost and water dynamics in a northern hardwood forest. *Biogeochemistry*, *56*, 151–174.

History. (n.d.). Baybulls. Retrieved August 2, 2023, from https://www.townofbaybulls.com/history

i-Boating: Free Marine Navigation Charts & Fishing Maps. (n.d.). Retrieved November 4, 2023, from https://fishing-app.gpsnauticalcharts.com/i-boating-fishing-web-app/fishing-marine-charts-navigation.html#12.5/37.8115/-122.3890

Imani, P., Tian, G., Hadiloo, S., & Abd El-Raouf, A. (2021). Application of combined electrical resistivity tomography (ERT) and seismic refraction tomography (SRT) methods to investigate Xiaoshan District landslide site: Hangzhou, China. *Journal of Applied Geophysics*, *184*, 104236.

Irvine, M. L. (2015). Monitoring coastal change in Newfoundland and Labrador: 2014 UPDATE. *Current Research Newfoudland and Labrador Department of Natural Resources Geological Survey, Report*, 15–1.

Jodry, C., Lopes, S. P., Fargier, Y., Sanchez, M., & Côte, P. (2019). 2D-ERT monitoring of soil moisture seasonal behaviour in a river levee: A case study. *Journal of Applied Geophysics*, *167*, 140–151.

Jol, H. M. (1995). Ground penetrating radar antennae frequencies and transmitter powers compared for penetration depth, resolution and reflection continuity1. *Geophysical Prospecting*, *43*(5), 693–709.

Jol, H. M. (2008). *Ground penetrating radar theory and applications*. Elsevier.

Jol, H. M., & Bristow, C. S. (2003). GPR in sediments: Advice on data collection, basic processing and interpretation, a good practice guide. *Geological Society, London, Special Publications*, *211*(1), 9–27.

Jones, F. (2018, May 15). *Chargeability*. https://www.eoas.ubc.ca/courses/eosc350/content/foundations/properties/2physprop-iag.htm

Junaid, M., Abdullah, R. A., Sa'ari, R., Ali, W., Rehman, H., Alel, M. N. A., & Ghani, U. (2021). 2D Electrical Resistivity Tomography an advance and expeditious exploration technique for current challenges to mineral industry. *Journal of Himalayan Earth Science*, *54*(1).

Kearey, P., Brooks, M., & Hill, I. (2002). *An introduction to geophysical exploration* (Vol. 4). John Wiley & Sons.

Kilfoil, G., Blagdon, A., Leitch, A., Campbell, H., Irvine, M., Batterson, M., Roberts, G., & Baker, B. (2018). The Application And Testing Of Two Geophysical Methods (Direct Current Resistivity And Ground-Penetrating Radar) As Part Of The Coastal Monitoring Program

To Assess Terrain Stability. *Current Research, Newfoundland and Labrador Department of Natural Resources Geological Survey, Report 18-1, 31-57.*, 28.

King, A. F. (1988). *Geology of the Avalon peninsula, Newfoundland*. Newfoundland Department of Mines and Energy, Mineral Development Division.

Knapp, R. W. (1990). Vertical resolution of thick beds, thin beds, and thin-bed cyclothems. *Geophysics*, *55*(9), 1183–1190.

Komen, G. J., Cavaleri, L., Donelan, M., Hasselmann, K., Hasselmann, S., & Janssen, P. (1996). *Dynamics and modelling of ocean waves*.

Kottek, M., Grieser, J., Beck, C., Rudolf, B., & Rubel, F. (2006). World Map of the Köppen-Geiger climate classification updated. *Meteorologische Zeitschrift*, *15*(3), 259–263. https://doi.org/10.1127/0941-2948/2006/0130

Lahousse, P. (2006). The role of groundwater in cliff instability: An example at Cape Blanc-Nez (Pas-de-Calais, France). *Earth Surface Processes and Landforms*, *31*(1), 31.

Leucci, G. (2006). Integrated geophysical, geological and geomorphological surveys to study the coastal erosion. *Int. J. Soil Sci*, *1*, 146–167.

Loke. (1999). Electrical imaging surveys for environmental and engineering studies. *A Practical Guide To*, *2*, 70.

Loke. (2004). *Tutorial: 2-D and 3-D electrical imaging surveys*.

Loke. (2012). *2-D and 3-D Electrical Imaging Surveys*.

Loke, M. H., Chambers, J. E., Rucker, D. F., Kuras, O., & Wilkinson, P. B. (2013). Recent developments in the direct-current geoelectrical imaging method. *Journal of Applied Geophysics*, *95*, 135–156.

Margiotta, S., Negri, S., & Parise, M. (2012). *Integration of geological, geomorphological and geophysical methods in the study of sinkholes*. 7693.

Martínez, J., Mendoza, R., Rey, J., Sandoval, S., & Hidalgo, M. C. (2021). Characterization of Tailings Dams by Electrical Geophysical Methods (ERT, IP): Federico Mine (La Carolina, Southeastern Spain). *Minerals*, *11*(2), 145.

Matsuoka, N., & Sakai, H. (1999). Rockfall activity from an alpine cliff during thawing periods. *Geomorphology*, *28*(3–4), 309–328.

Nabighian, M. N. (1988). *Electromagnetic methods in applied geophysics: Voume 1, theory*. Society of Exploration Geophysicists.

Neal, A. (2004). Ground-penetrating radar and its use in sedimentology: Principles, problems and progress. *Earth-Science Reviews*, *66*(3–4), 261–330.

Neal, A., Richards, J., & Pye, K. (2002). Structure and development of shell cheniers in Essex, southeast England, investigated using high-frequency ground-penetrating radar. *Marine Geology*, *185*(3–4), 435–469.

Neal, A., Richards, J., & Pye, K. (2003). Sedimentology of coarse-clastic beach-ridge deposits, Essex, southeast England. *Sedimentary Geology*, *162*(3–4), 167–198.

Neu, H. J. A. (1982). *II-year deep-water wave climate of Canadian Atlantic waters*. Canadian Technical Report of Hydrography and Ocean Sciences.

Parasnis, D. S. (2012). *Principles of applied geophysics*. Springer Science & Business Media.

Reynolds, J. M. (2011). *An introduction to applied and environmental geophysics*. John Wiley & Sons.

Sensors & Software. (1999). *Ground penetrating radar survey design*. Sensors & Software Mississauga.

Shaw, J., & Forbes, D. L. (1995). The postglacial relative sea-level lowstand in Newfoundland. *Canadian Journal of Earth Sciences*, *32*(9), 1308–1330.

Sheriff, R. E. (1977). *Limitations on resolution of seismic reflections and geologic detail derivable from them: Section 1. Fundamentals of stratigraphic interpretation of seismic data*.

Sheriff, R. E., & Geldart, L. P. (1995). *Exploration seismology*. Cambridge university press.

Singh, P. (n.d.). *Skin Depth Calculator*. Omni Calculator. Retrieved October 21, 2023, from https://www.omnicalculator.com/physics/skin-depth

Spooner, I., Batterson, M., Catto, N., Liverman, D., Broster, B., Kearns, K., Isenor, F., & MacAskill, W. (2013). Slope Failure Hazard in the Atlantic Provinces: A Review. *Atlantic Geology*, *49*, 1–14.

Swail, V. R. (1997). Analysis of climate variability in ocean waves in the northwest Atlantic Ocean. *Occas. Rep. Environ. Can.*, *9*, 313–318.

Syscal Junior. (n.d.). Retrieved August 2, 2023, from http://www.iris-instruments.com/syscal-junior.html

Telford, W. M., Geldart, L. P., Sheriff, R. E., & Keys, D. A. (1996). *1976, Applied geophysics, Cambridge Univ*. PrcSS.

Van Overmeeren, R. A. (1994). Georadar for hydrogeology. *First Break*, *12*(8).

Watton, E. C. (2016). *Coastal geomorphology, processes and erosion at the tourist destination of Ferryland, Newfoundland and Labrador* [PhD Thesis]. Memorial University of Newfoundland.

Wyllie, D. C. (2017). Rock strength properties and their measurement. In *Rock slope engineering* (pp. 117–162). CRC Press.

Xie, X., Zeng, C., & Wang, Z. (2013). GPR signal enhancement using band-pass and K–L filtering: A case study for the evaluation of grout in a shielded tunnel. *Journal of Geophysics and Engineering*, *10*(3), 034003. https://doi.org/10.1088/1742-2132/10/3/034003

Yelf, R. (2006). "Where is the True Time Zero?" *Electromagnetic Phenomena*, *7*(1), 158–163.

Appendices

Appendix A: Structural measurements on north coast of Bay Bulls

On the May 5, 2022, Marzieh Arshian, Roberta Hicks and Alison Leitch made structural observations and measurements of 7 bedrock outcrops on the north side of Bay Bulls. Measurements were taken on the Bread and Cheese beach in 2021. The locations of the observations are given in Table A 1, and illustrated in Figure A 1 and Figure A 2. Photographs of the outcrops are given in the following Figure A 3 to Figure A 11.

Fractures are mostly along bedding planes or sub-vertical. Fractures are mostly clean: some have grass growing in them (e.g., Figure A 3, Figure A 7 and Figure A 9). At location 1, north of the marine terminal, the bedding parallel fractures within the Renews Head Formation are warped on a scale of several metres (Figure A 3). At location 2, Renews Head Formation rocks show significant soft sediment deformation, presumably due to a high shale content. These rocks are dark, showing multiple recumbant folds and crenulations in muddier layers.

Strike and dip measurements (RHR) given in Table A 2, show that for fractures along the bedding planes, the strike is mostly within a few degrees of north, and dipping to the east, in agreement with the geological map, Figure 1-7. At location 4, a major road cut in the Gibbet Hill Formation, the bedding plane fractures occurred at vertical intervals of 0.6, 1.2, 2 and 3 m (see Figure A 7).

At location 7, opposite the Coady Memorial Park, the road-side outcrop displays changes in colour from greenish to pinkish, and in contrast to locations 4 to 6, has conchoidal fracturing (Figure A 10 and Figure A 11) indicating a higher silica content.

Table A 1) Locations of studied outcrops

Location	Description	Easting	Northing
1	E side of creek, NE of Marine Terminal	363120	5242045
2	Deformed shales, Renews Head Fm	363180	5242010
3	Bedrock in steep grassy slope	363240	5241920
4	Blasted roadside outcrop, Gibbet Hill Fm	363280	5241880

5	Up track, Gibbet Hill Fm	363295	5241865
6	Roadside outcrop, Gibbet Hill Fm	363310	5241845
7	Silica rich roadside outcrop, Gibbet Hill Fm	364060	5241285
8	Shoreline outcrops, Gibbet Hill Fm	364595	5241135

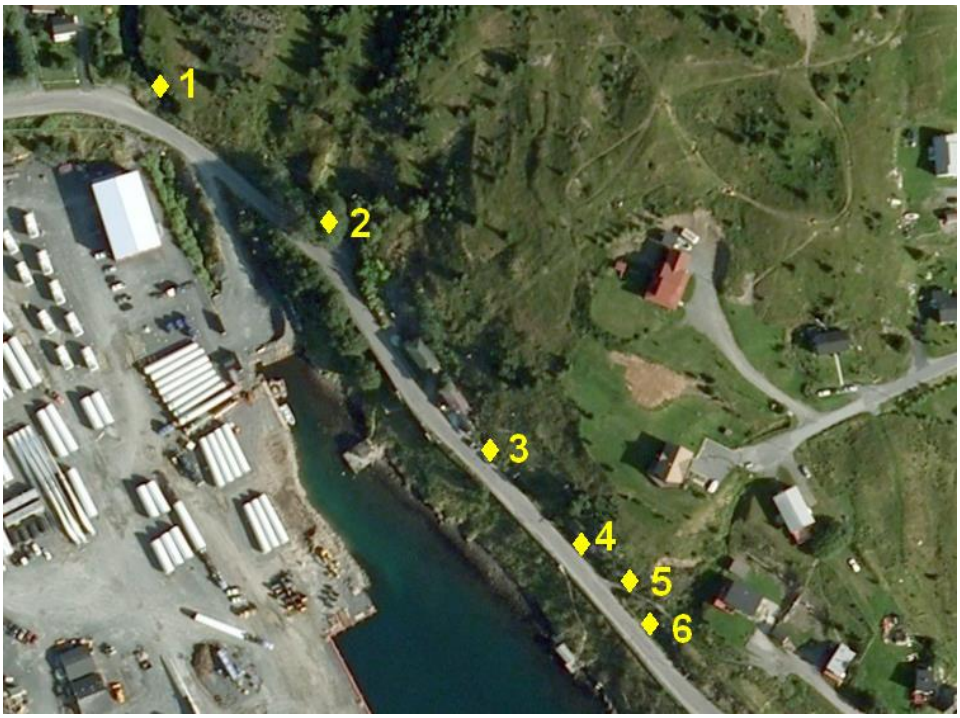

Figure A 1) Locations of structural observations 1 to 6 (yellow diamonds) along Northside Rd. Bay Bulls.

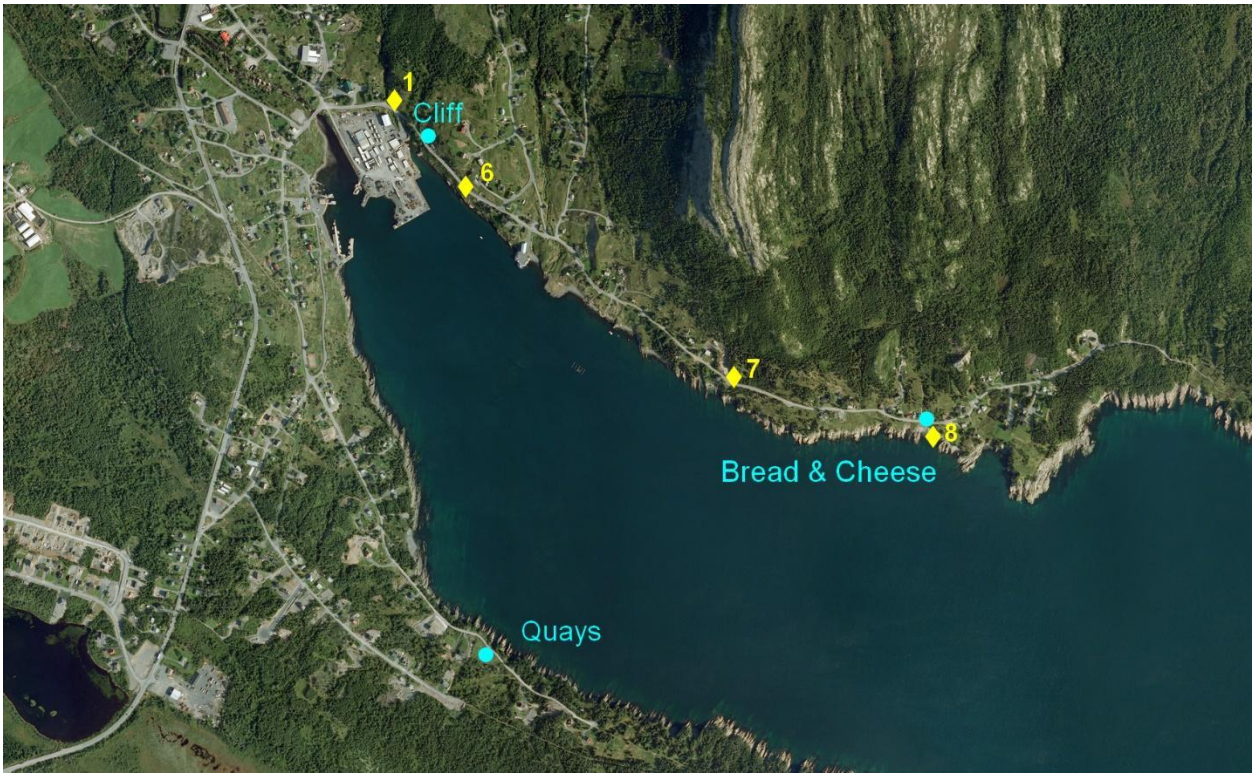

Figure A 2) Locations of structural observations 1,6, 7 and 8 (yellow diamonds) in Bay Bulls . Survey sites are indicated by blue dots.

Table A 2) Structural measurements (RHR)

Location	Description	Strike	Dip
1	Bedding parallel fractures, Renew Head Fm (Fig. A.3)	352	48
3	Bedding parallel fractures, Renew Head Fm (Fig. A.6)	008	56
4	Bedding parallel fractures, Gibbet Hill Fm (Fig. A.7)	001	38
4	Near vertical fracture, dipping to east	091	88
4	Vertical fracture	016	90
4	Near vertical fracture, dipping to east	198	74
4	Bedding parallel fracture	358	45
5	Bedding parallel fracture	356	48
6	Bedding parallel fracture (14 m SE of culvert 4)	004	48
6	Fracture (5 m to east)	236	58
6	Irregular fracture	210	75-90

6	Vertical fracture (2 m to east)	64	90
6	Fracture, SE end of outcrop	336	80
7	Bedding	340	45, 35
7	Bedding	360	38
7	Fracture	230	58
7	Fracture	231	59

Figure A 3) Location 1. Outcrop E of creek, NE of marine terminal. View to north. Renews Head Fm, St John's Group.

Figure A 4) Location 1. View to east. Renews Head Fm, St John's Group.

Figure A 5) Location 2. View to north. Outcrop of dark, shale-rich Renews Head Fm, St John's Group.

Figure A 6) Location 3. Outcrop at base of grassy slope, NE side of road. Dark, shale-rich Renews Head Fm, St John's Group.

Figure A 7) Location 4. Roadside outcrop. Gibbet Hill Fm, Signal Hill Group.

Figure A 8) Location 6. Roadside outcrop. Gibbet Hill Fm, Signal Hill Group.

Figure A 9) Location 6. Roadside outcrop, Right side of Fig. A.7. Gibbet Hill Fm, Signal Hill Group.

Figure A 10) Location 7. Roadside outcrop. Gibbet Hill Formation, Signal Hill Group.

Figure A 11) Location 7. Close-up of outcrop, illustrating concoidal fractures.

Appendix B: DCR Models

The programmable control box takes a sequence of measurements using 24 electrodes for different array types. Each sequence requires specific programming applied to the control box. The software utilized for this purpose is called “Electre II” (Figure B 1a).

The ELECTRE II software allows the user to create sequences of measurements for the multi electrode system (Figure B 1b). The first step is to select a cable set, which can be made of several segments. Once the cable set has been specified, the user chooses the acquisition parameters together with the geometric parameters of the sequence (electrode array, electrodes spacing, depth level), then the sequence can be created automatically (Figure B 1c).

The distribution of the report points of the measurements that will be done together with the total number of data point, can be seen from the graphical window (Figure B 1d), before loading the sequence into the unite.

a)

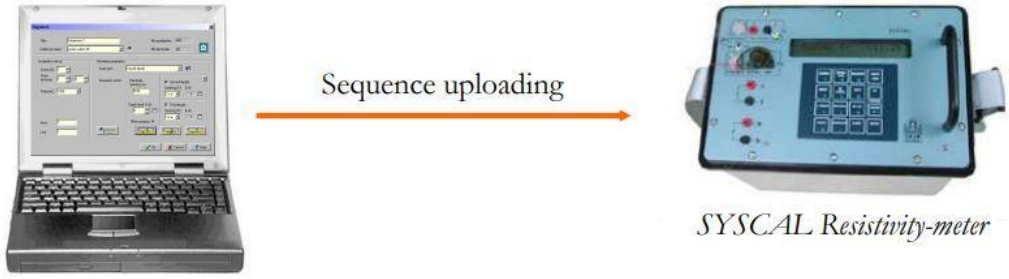

Electre II software

SYSCAL Resistivity-meter

b)

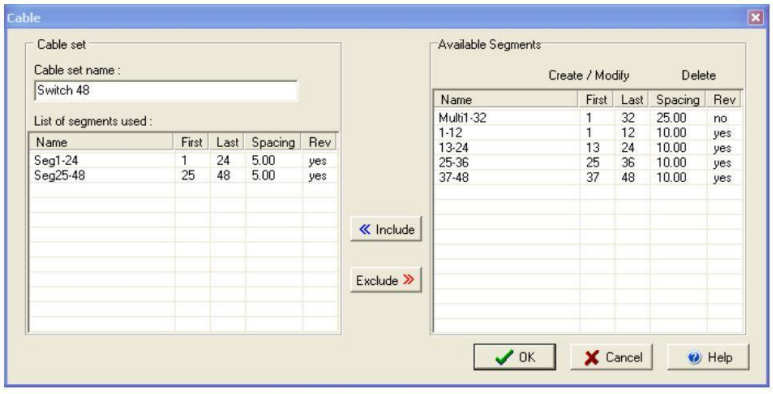

Cable definition

c)

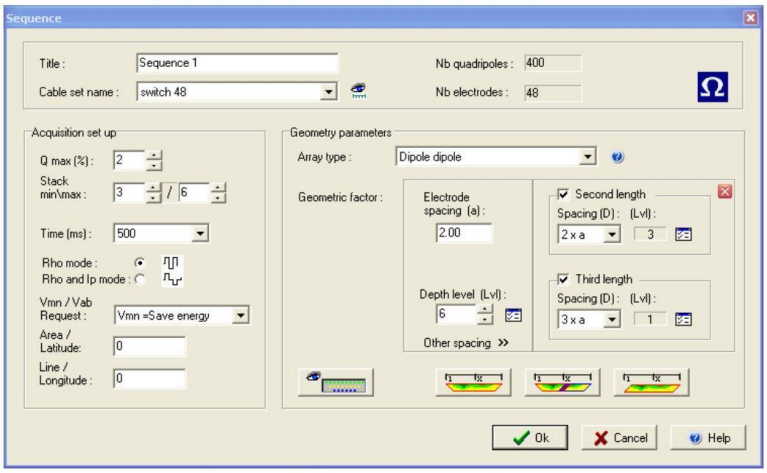

Master window: sequence creation

d)

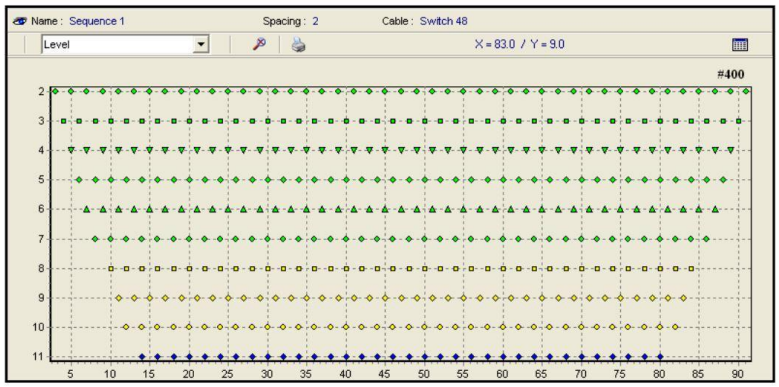

Graphical picturing of the sequence

Figure B 1) a, b, c, d, automatic sequence creation window in Iris Instruments Electre II DCR software (Syscal Junior, n.d.).

DCR Models South Side of Road, Bread and Cheese Site

The DCR/IP survey on the south (bay) side of Gunridge Road at the Bread and Cheese site resulted in apparent resistivity data that look reasonable in pseudo section (Figure B 1), with apparent resistivity values between 500 and 4500 ohm.m, increasing with a-spacing (pseudodepth), and anomalously low values in the fractured region over the creek. The IP pseudo section is more irregular, particularly at smaller a-spacings (shallower depths). It shows highest values at depth toward the edges of the fracture zone.

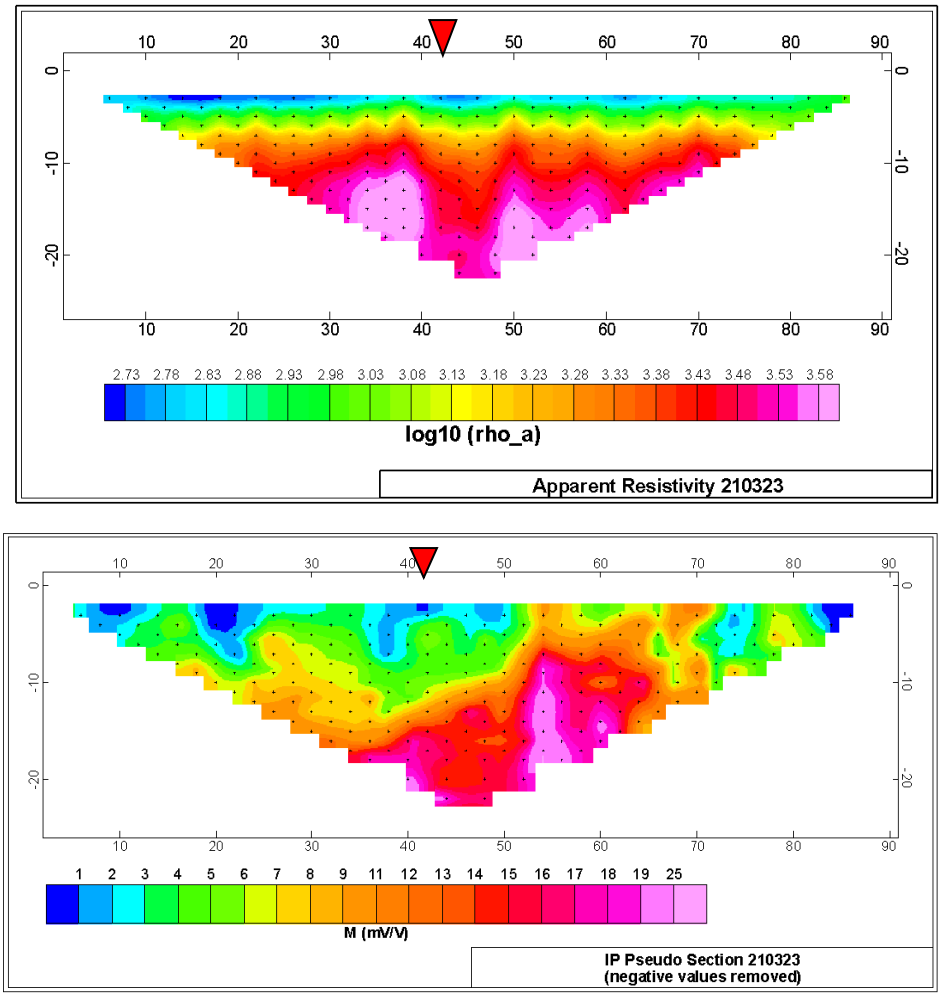

Figure B 2) Pseudo-sections of apparent resistivity and IP for DCR/IP survey on south side of Gunridge Road, Bread and Cheese site (23 March 2021). Units on y axis -a/2 (m). Units on x axis are distance along the survey line (m). Red arrow indicates location of the culvert. Graphs generated in Oasis Montaj.

In general, inversions of Wenner-Schlumberger DCR surveys produce models that show similar features to the pseudo-sections, with a greater range of resistivity compared with apparent resistivity. The 2D inversion models corresponding to the surveys on the south side of Gunridge Road (Figure B 2) were generated with warnings about the instability of the inversions, and bear little resemblance to the pseudo sections. A layer with very large resistivity (> 1.6×10^6 ohm.m) covers the central part of the section. Changing parameters for the inversion, such as damping factors, and flatness ratios generated different models but none that did not give warnings about instability or looked any more geologically reasonable.

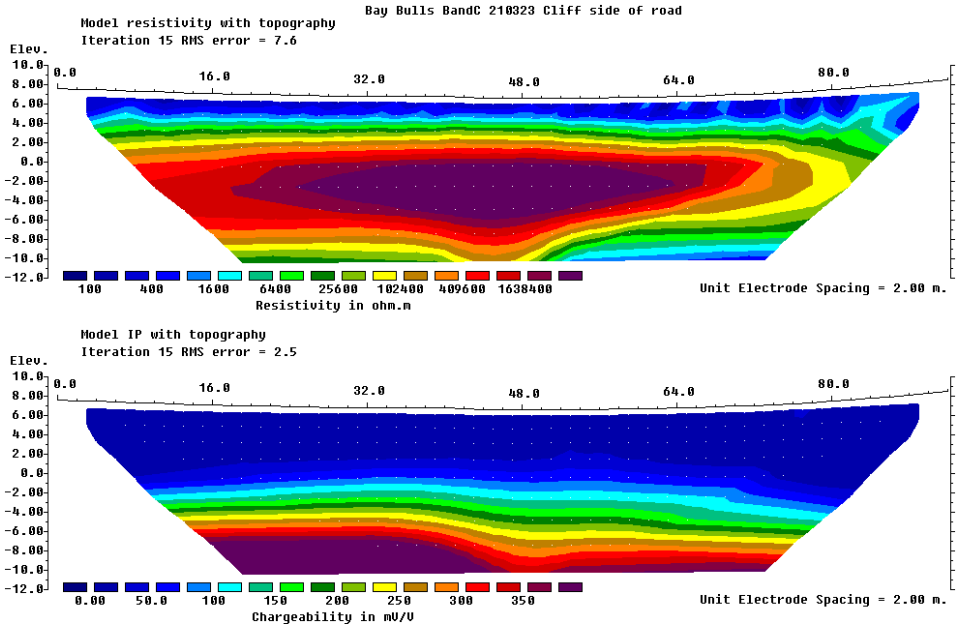

Figure B 3) 2D resistivity and IP modesl based on Wenner-Schlumberger survey on the south side of Gunridge Road, Bread and Cheese (23 March 2021).

We speculate that the data were influenced by 3D effects to the extend that the assumption of 2D geometry was violated to too great a degree. In particular, the ends of the metal guard rail between the survey line and the scarp were embedded into the ground so that current at larger a-spacings would have channeling through it. It is possible that the low apparent resistivity values seen over the fractured region are due to the current channeling through the guard rail and not to a decrease in resistivity over the fractured region.

Pseudo-sections of the Wenner-Schlumberger and the Dipole-Dipole survey of all three sites illustrates as below.

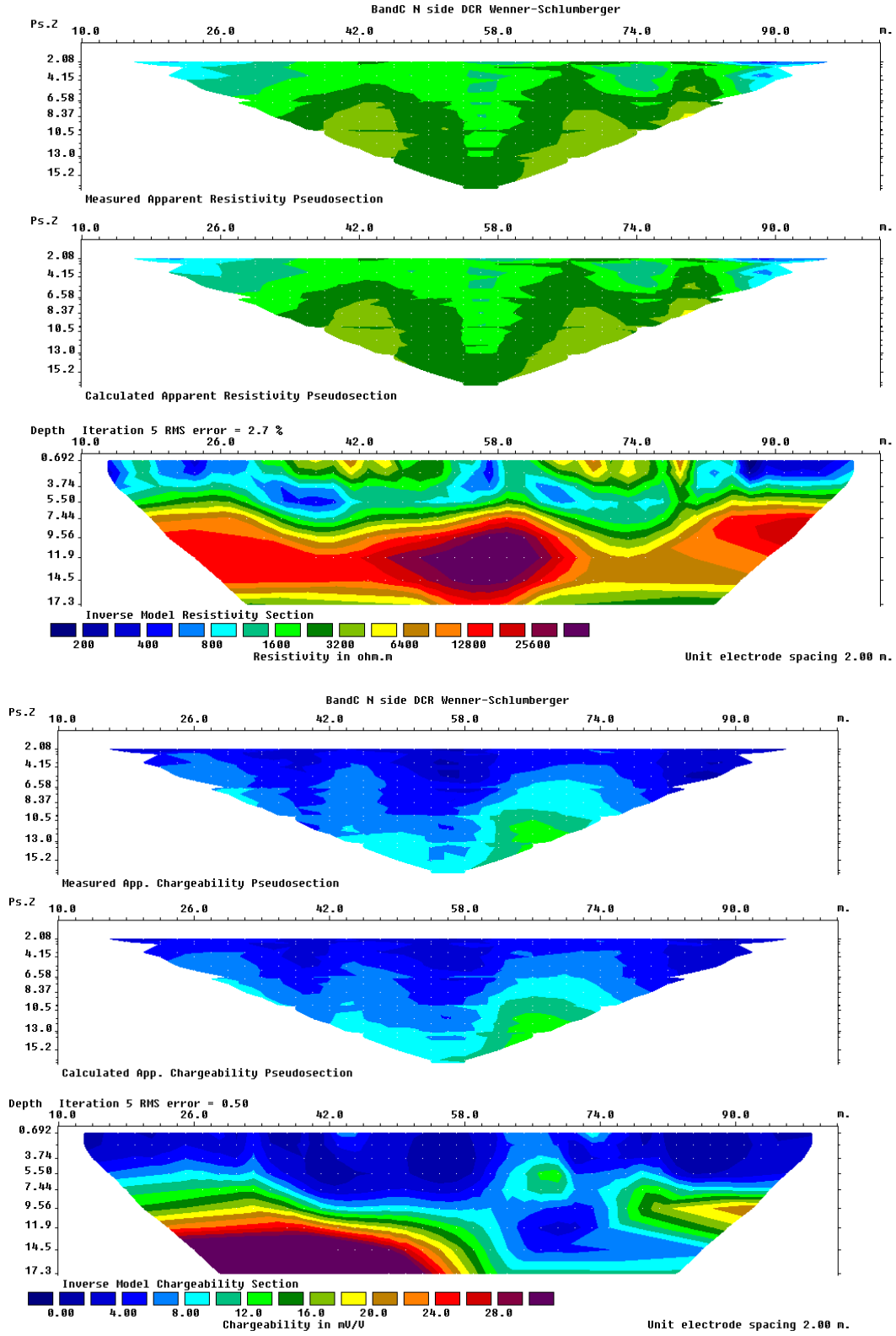

Figure B 4) Bread & Cheese, north side of road. Wenner-Schlumberger survey: pseudo-section, section calculated from model, inverse model section.

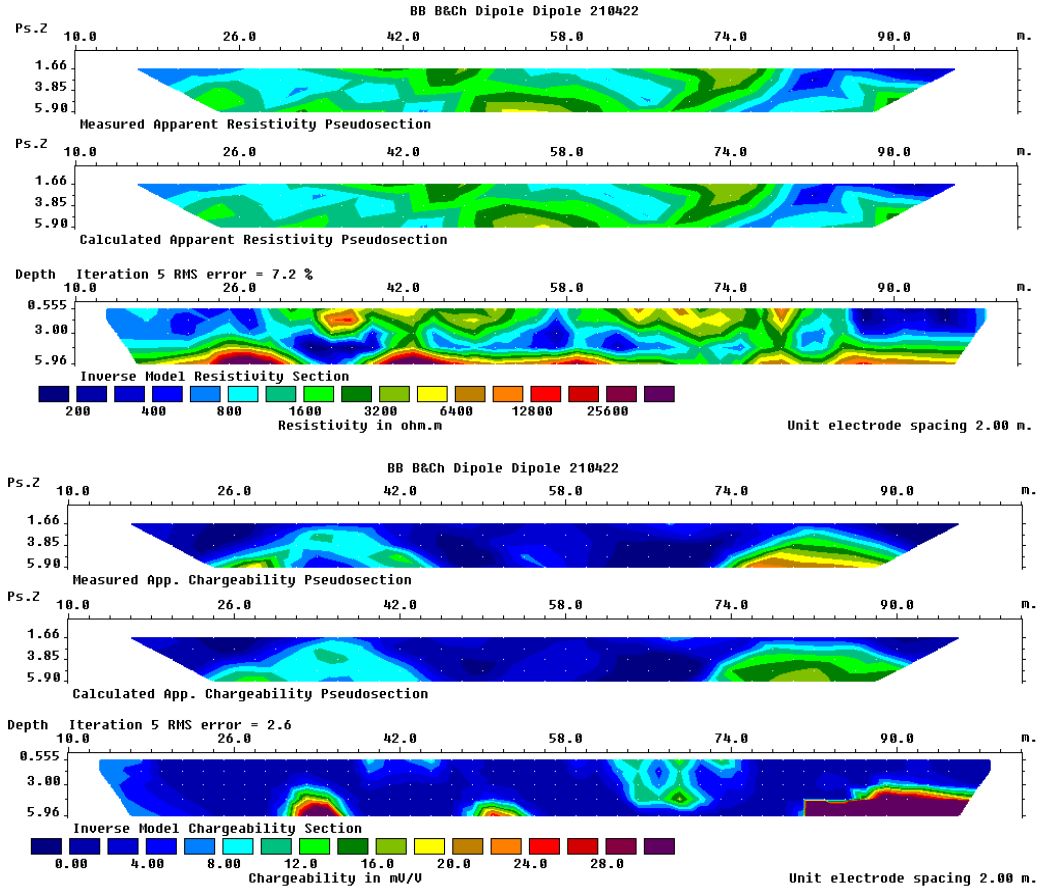

Figure B 5) Bread & Cheese, north side of road. Dipole-dipole survey: pseudo-section, section calculated from model, inverse model section

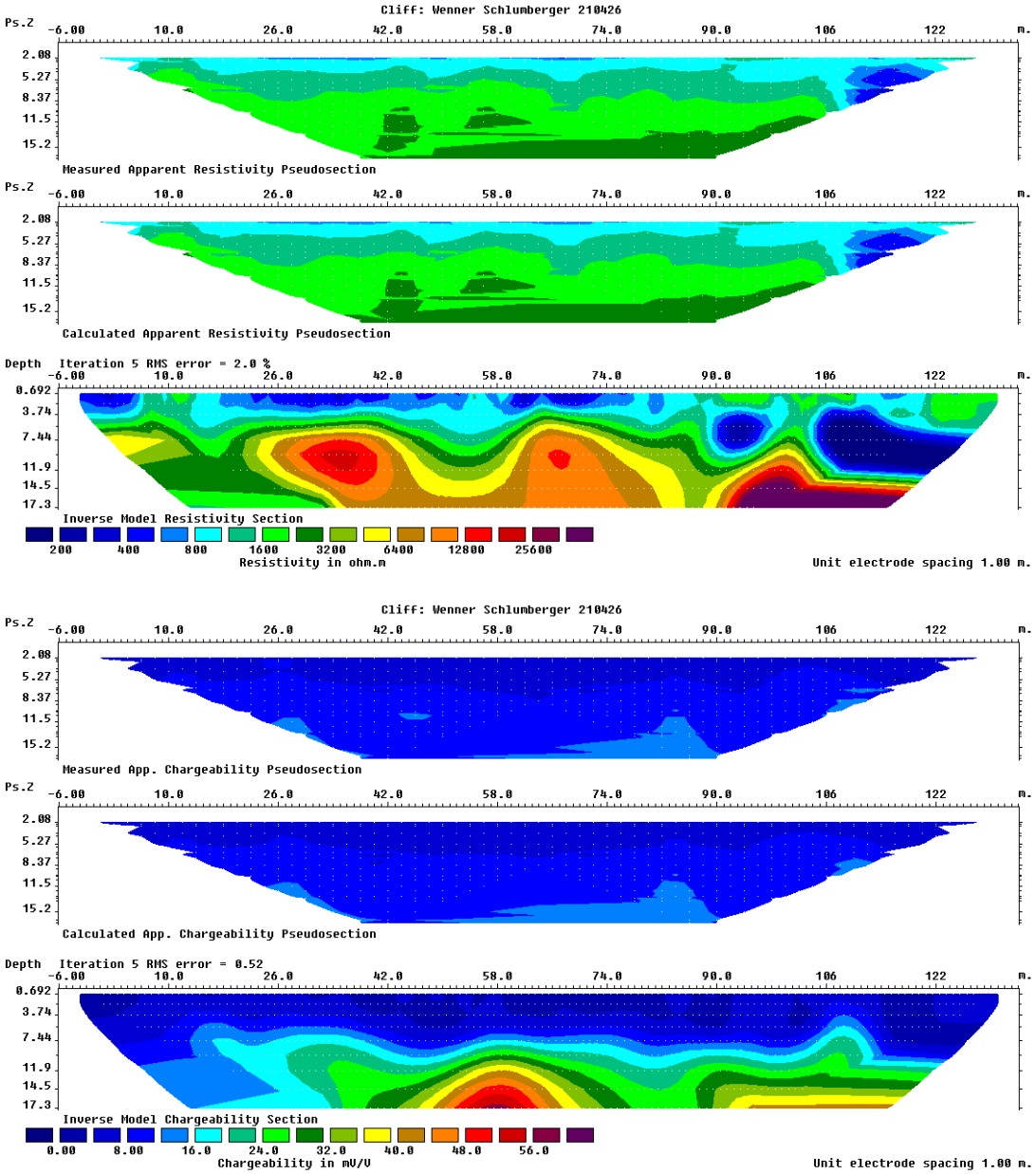

Figure B 6) The Cliff, northeast side of road. Wenner-Schlumberger survey: pseudo-section, section calculated from model, inverse model section.

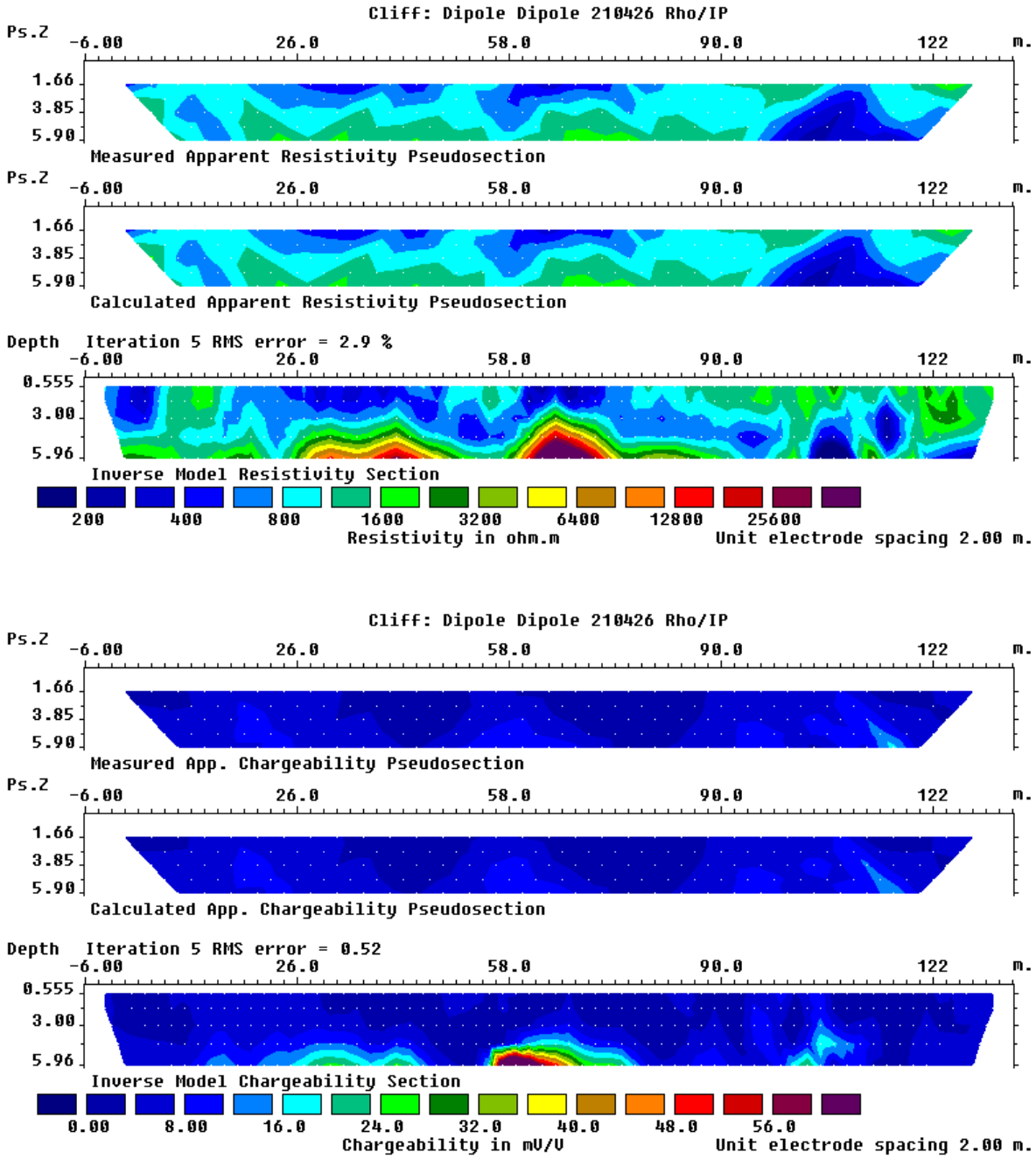

Figure B 7) The Cliff, northeast side of road. Dipole-dipole survey: pseudo-section, section calculated from model, inverse model section. 2X vertical exaggeration.

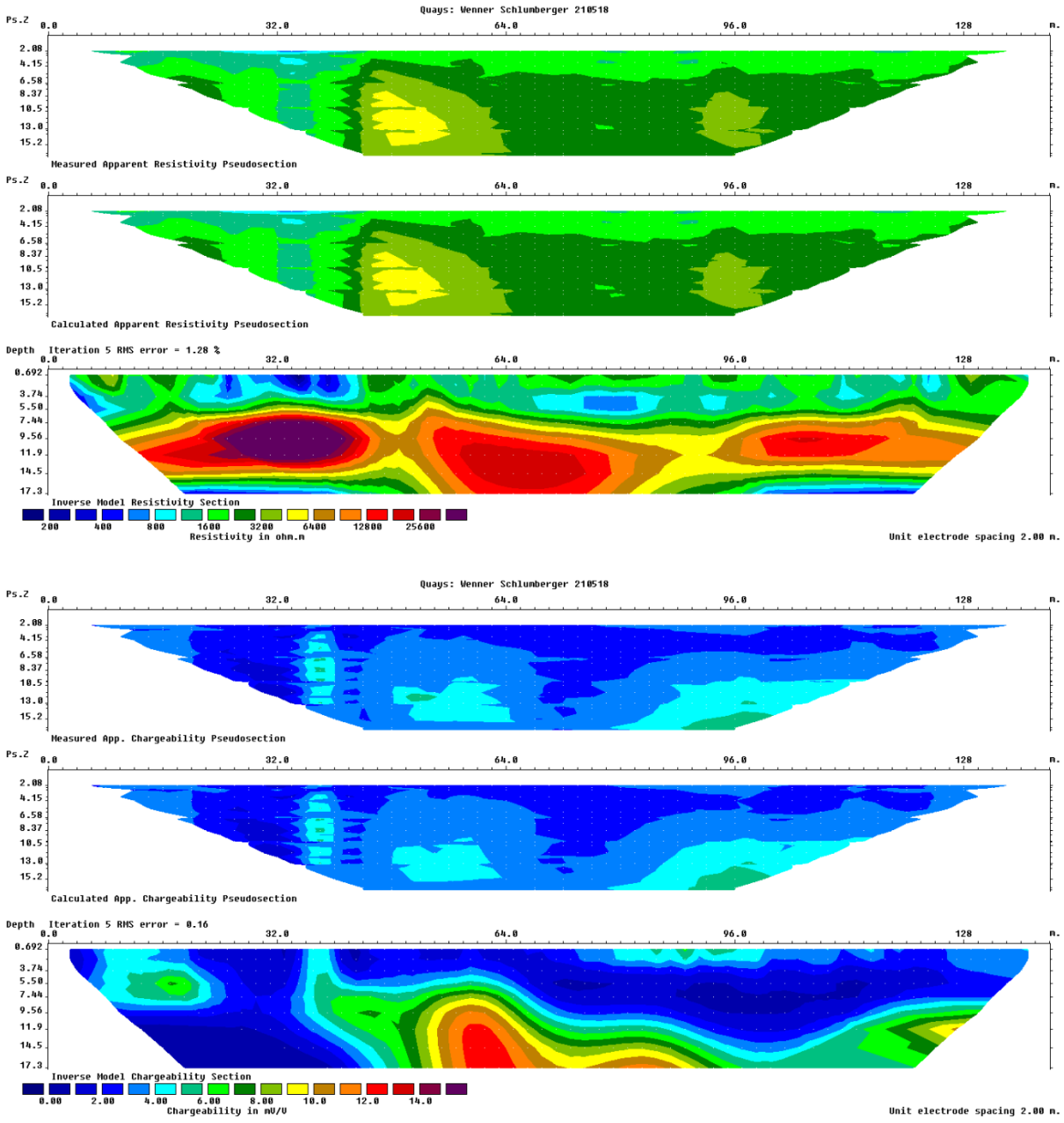

Figure B 8) The Quays, southwest side of road. Wenner-Schlumberger survey: pseudo-section, section calculated from model, inverse model section.

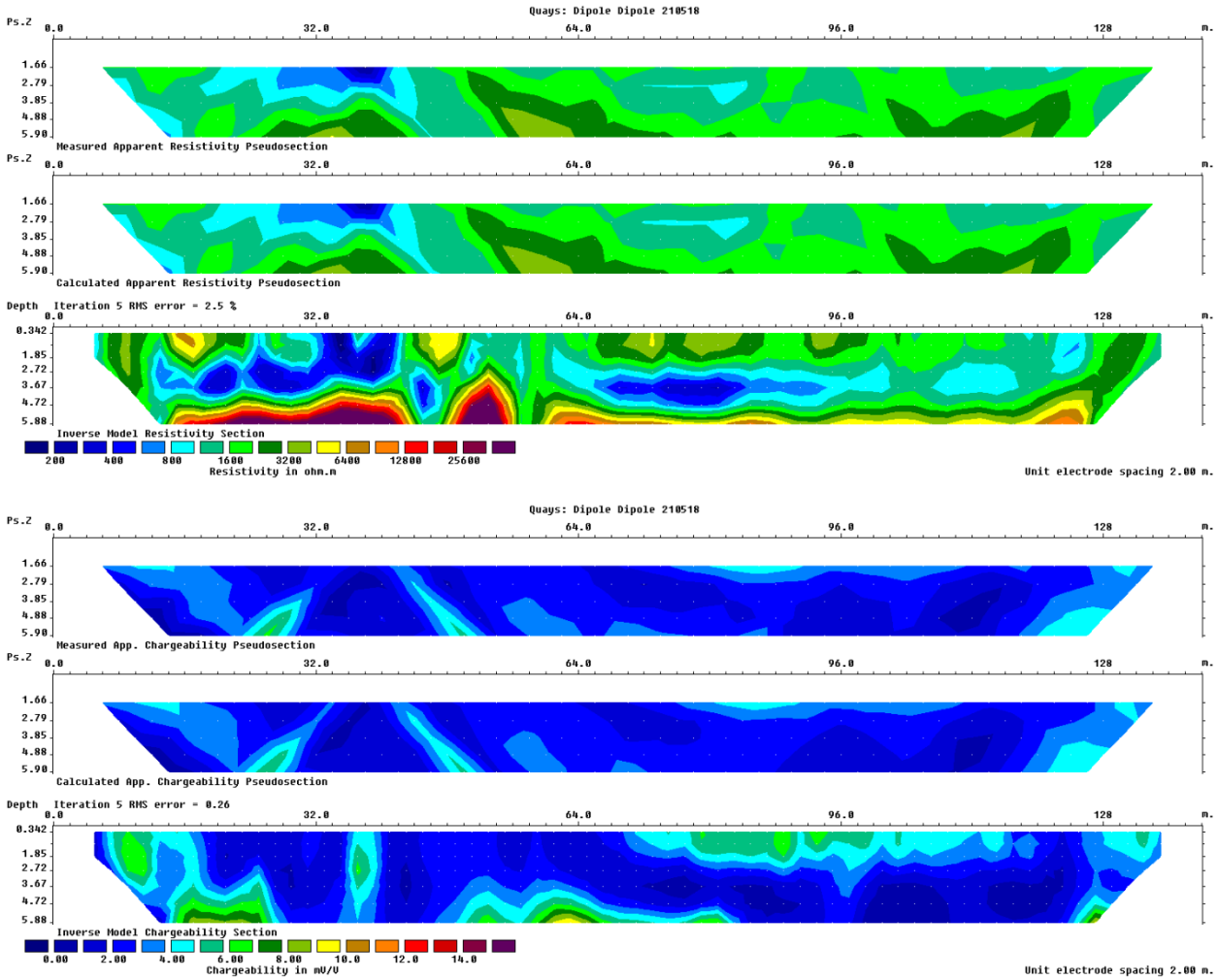

Figure B 9) The Quays, southwest side of road. Dipole-dipole survey: pseudo-section, section calculated from model, inverse model section. 2X vertical exaggeration.

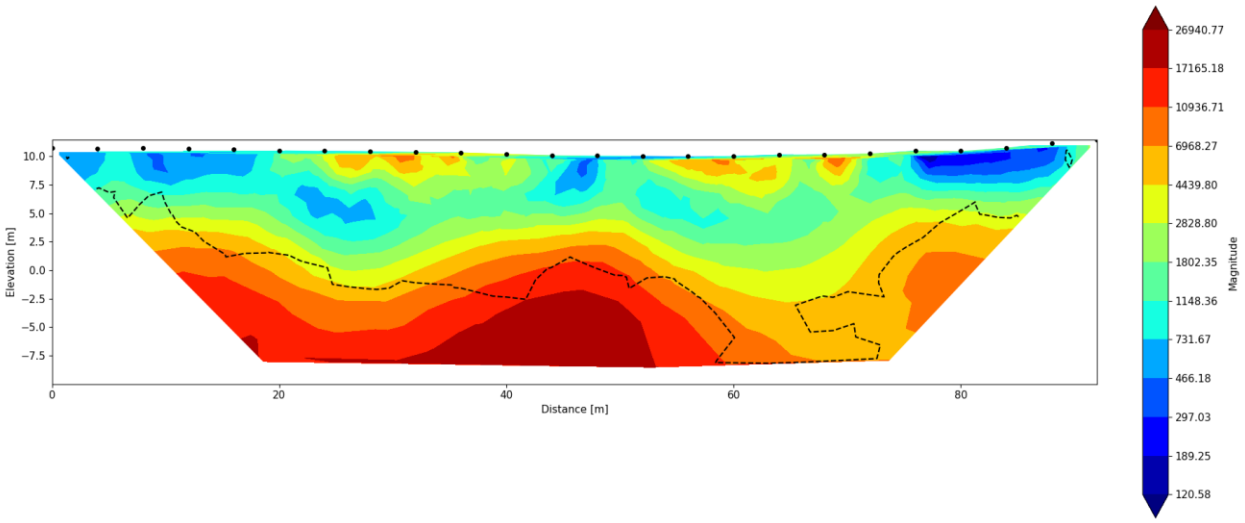

Figure B 10) Resistivity inversion model and DOI of Wenner-Schlumberger survey at the Bread and Cheese site. This model produced by RESIPy software.

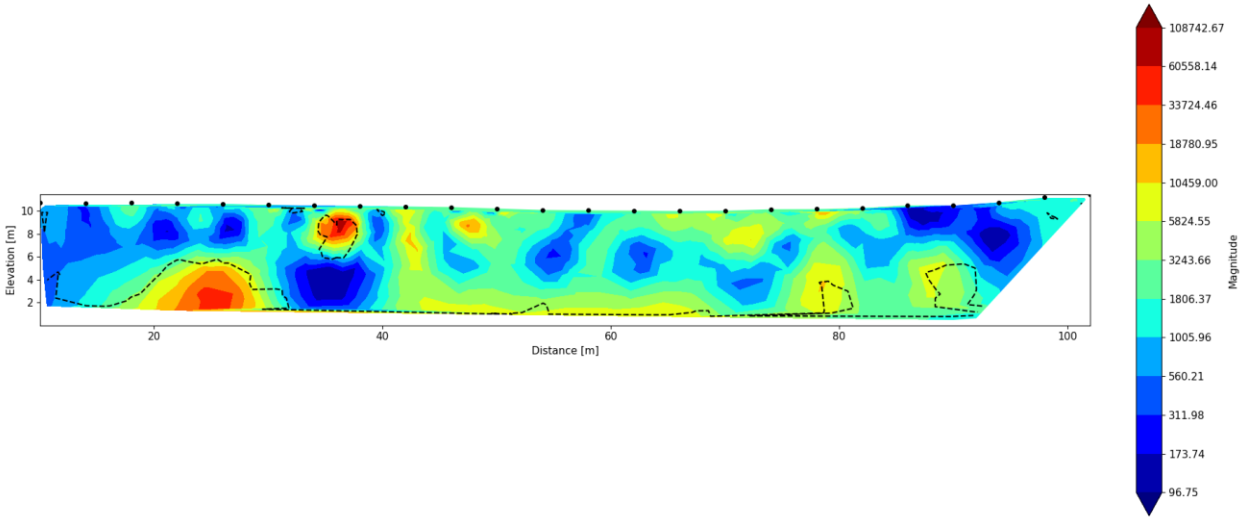

Figure B 11) Resistivity inversion model and DOI of Dipole-Dipole survey at the Bread and Cheese site, RESIPy software

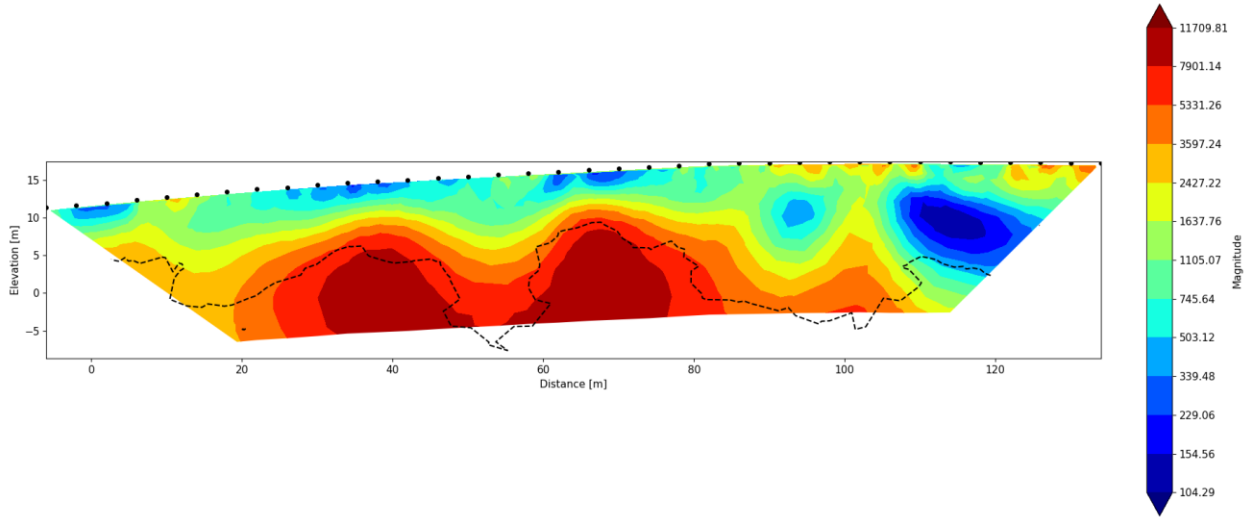

Figure B 12) Resistivity inversion model and DOI of Wenner-Schlumberger survey at the Cliff site, RESIPy software.

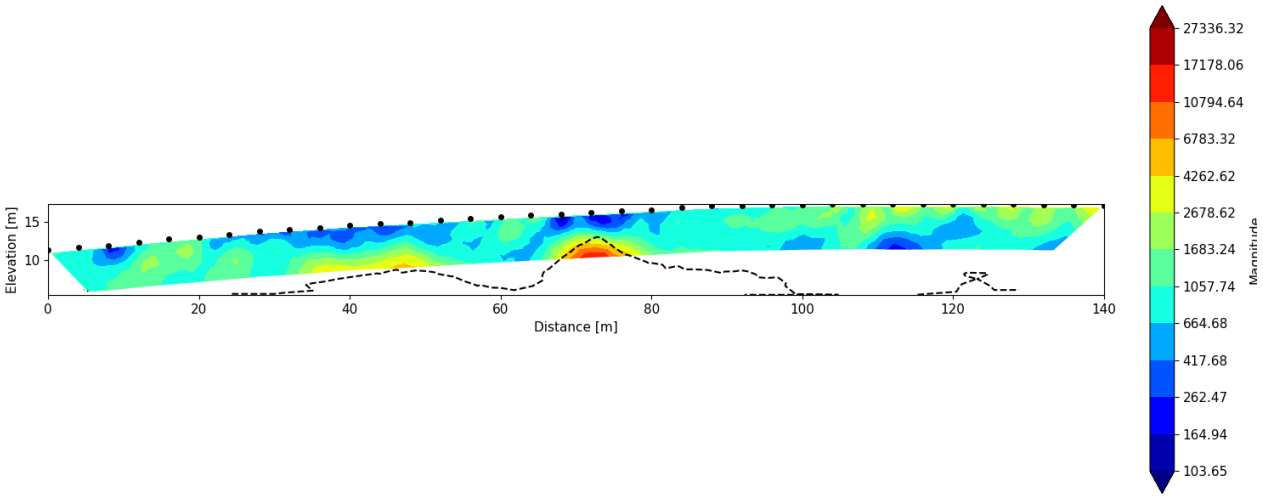

Figure B 13) Resistivity inversion model and DOI of Dipole-Dipole survey at the Cliff site, RESIPy software.

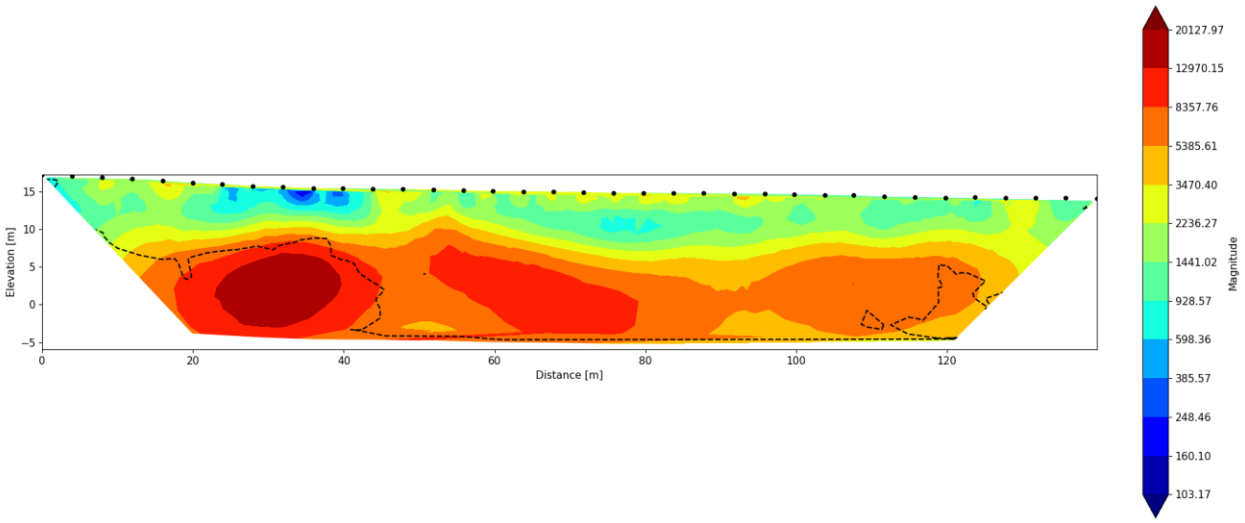

Figure B 14) Resistivity inversion model and DOI of Wenner-Schlumberger survey at the Quays, southwest side of road, RESIPy software.

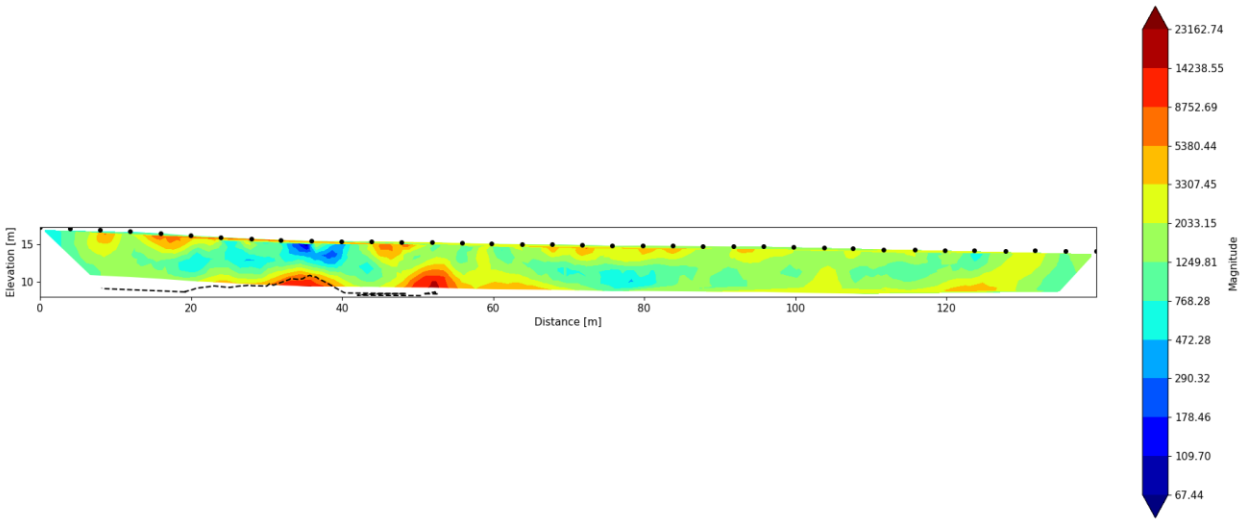

Figure B 15) Resistivity inversion model and DOI of Dipole-Dipole survey at the Quays, southwest side of road, RESIPy software.

Appendix C: Example *.dat file for RES2DINV

DCR/IP Processing

Data from the DCR/IP surveys were downloaded from the Syscal Junior instrument using Iris Instrument software Prosys II and exported to Excel. The data were formatted into Geotomo's 'general' format with topographic data appended, and saved as a *.dat file.

Inversions of the DCR and IP data were carried out using Geotomo's software RES2DINV version 3.56.73 with a dongle which allowed full use of the program features. Before reading the data, the inversion cell size was chosen to be half the electrode spacing (Inversion>Model discretization> Use model refinement), as recommended when there are large changes in resistivity. After the data file was read in, a least-squares inversion was carried out. The program produced the inverted model *.INV, which could then be displayed. In the Display menu, options to include the topography and set the vertical/horizontal scale to 1.0 were chosen. The horizontal plotting scale (i.e., pixels per electrode spacing) was chosen to be ~20 to fit the models neatly into the display window with appropriately sized text. The default colour scheme was used with user defined contour intervals – logarithmic intervals for resistivity and linear intervals for IP.

Table C 1) Example *.dat file for RES2DINV

Cliff: Wenner Schlumberger 210426					□ Title for graphs					
4					□ unit electrode spacing					
11					□ Array type (11 for general array)					
0					□ Array type (0 for non specific)					
Resistivity					□ Header					
0					□ 0 for resistivity (1 for resistance)					
491					□ number of data points					
2					□ Type of x-location, 2 for surface distance					
1					□ Flag for IP data, 0 for none, 1 if present					
Chargeability					□ header for chargeability					
mV/V					□ units for chargeability					
0.16	1				□ damping factors resistivity/charg??					
4	-6	0	6	0	-2	0	2	0	780.58	3.87
4	-2	0	10	0	2	0	6	0	825.46	4.03

4	2	0	14	0	6	0	10	0	1084.23	5.31
…										
number of electrodes, x and z locations of electrodes C1,C2,P1,P2 respectively										
(all z locations 0), resisitivity, IP (491 lines in total).										
…										
4	42	0	130	0	78	0	94	0	2789.35	12.51
4	46	0	134	0	82	0	98	0	2871.56	12.12
Topography in separate list					□ header					
2					□ indicates surface distance					
36					□ Number of topography data points					
-6	11.3				□ horizontal and vertical component					
-2	11.6									
…					36 points in total					
130	17.3									
134	17.2									
1					□ topo data point number with electrode 1					
0	0	0	0		□ end with a few zeros.					
0										
0										
0										

Appendix D: Sets of Xline GPR Profiles

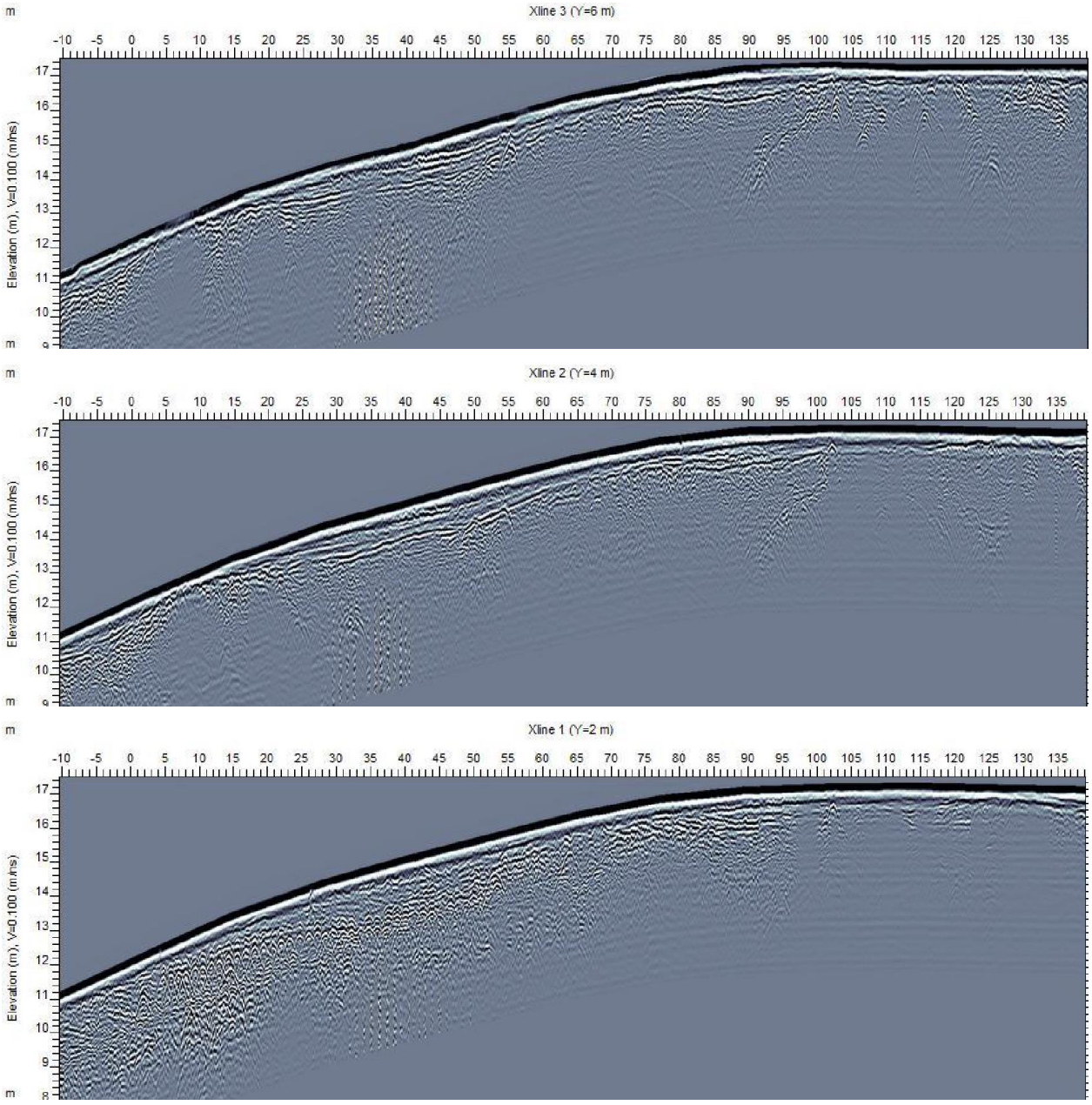

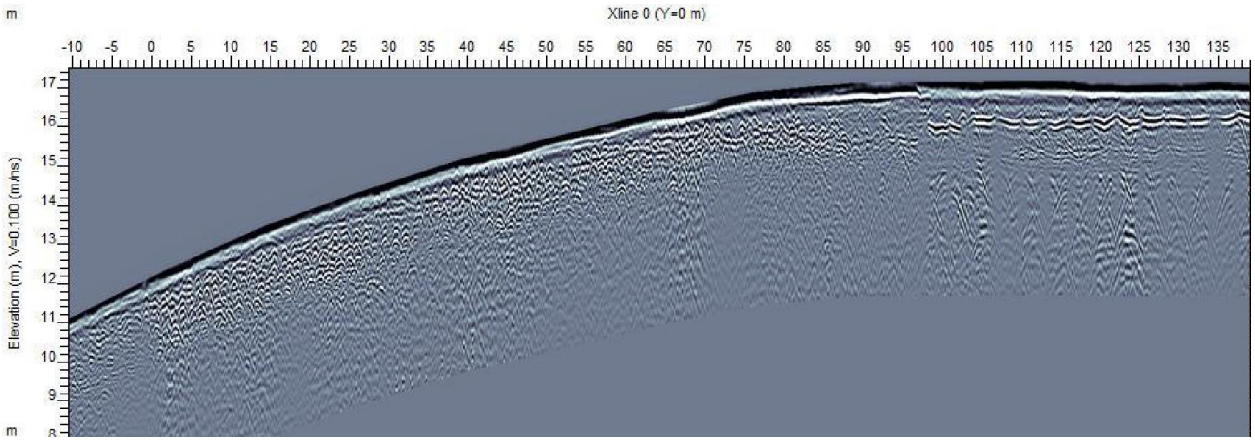

Figure D 1) The Cliff, GPR profiles, survey 2, ordered from NE to SW (bayward from top to bottom). Distance from NW to SE, wooden wall from 0 to ~98 m. 250 MHz antennas. Vertical exaggeration 5X.

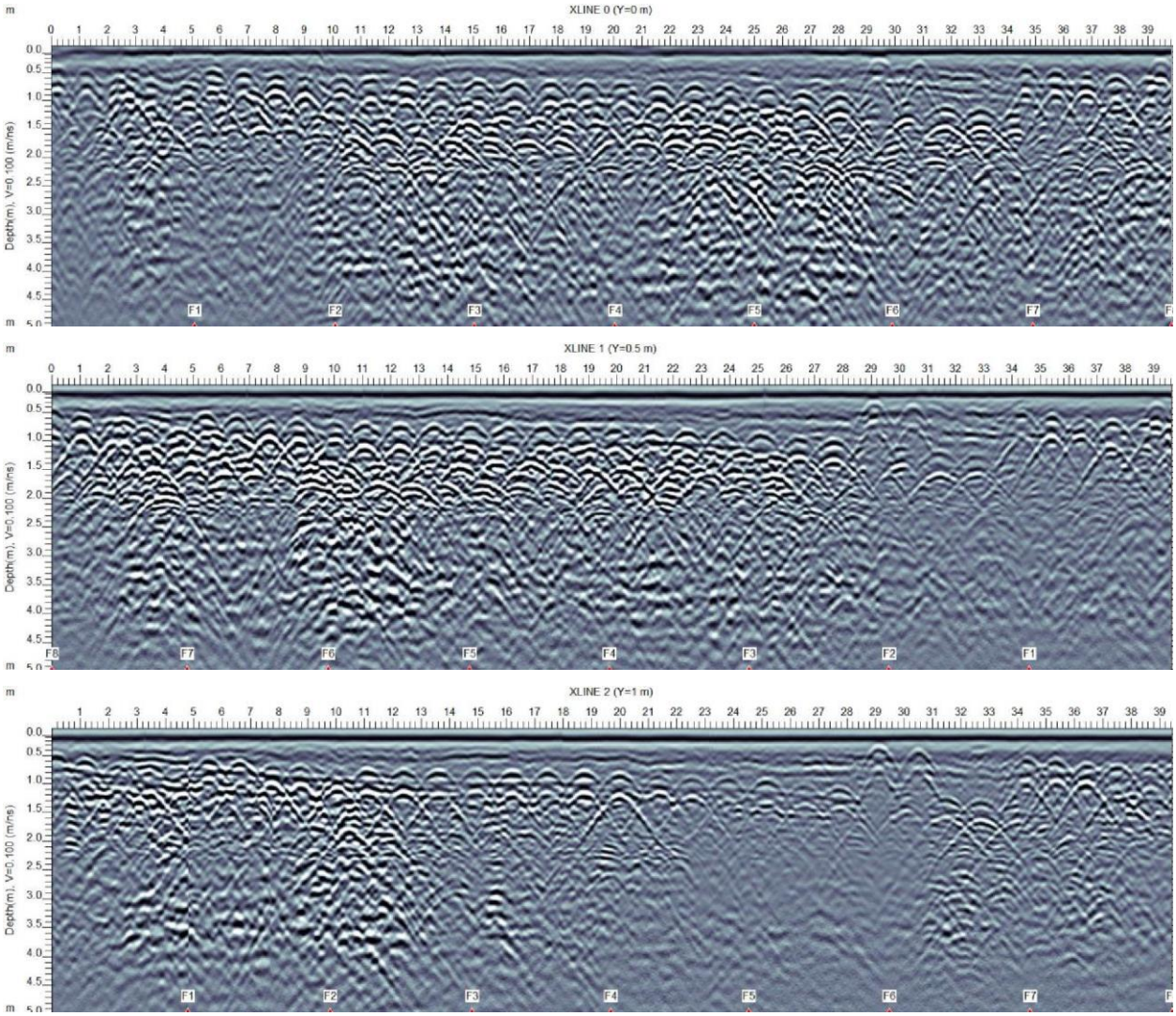

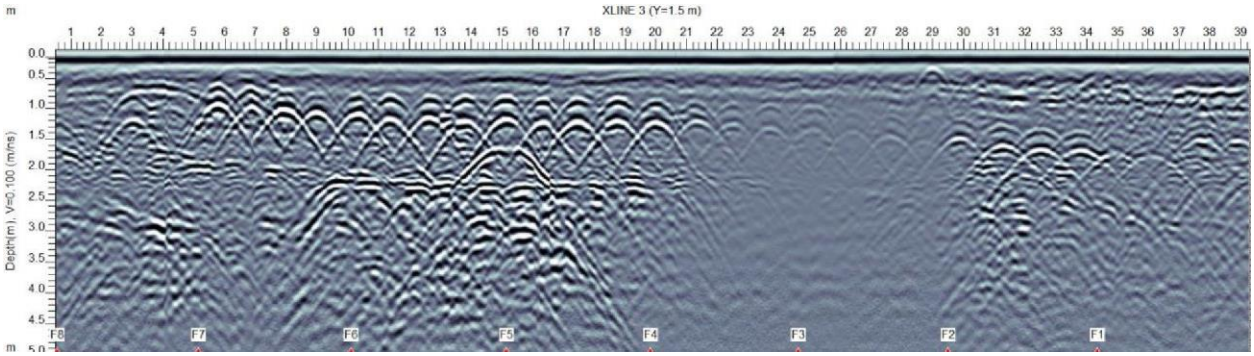
XLINE 3 (Y=1.5 m)
Depth(m), V=0.100 (m/ns)
F8
F7
F6
F5
F4
F3
F2
F1

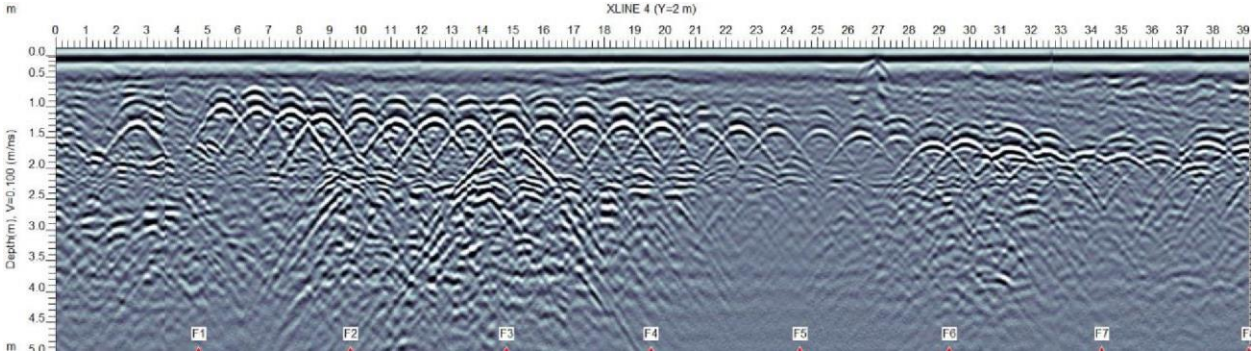
XLINE 4 (Y=2 m)
Depth(m), V=0.100 (m/ns)
F1
F2
F3
F4
F5
F6
F7

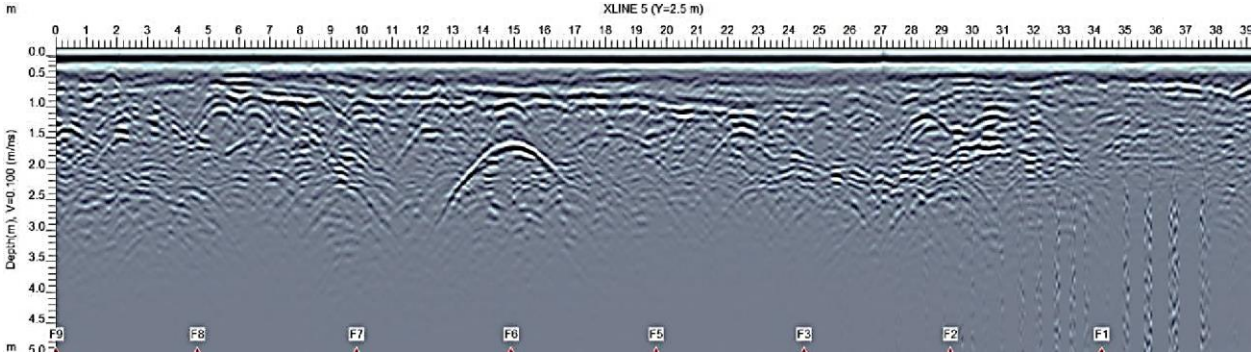
XLINE 5 (Y=2.5 m)
Depth(m), V=0.100 (m/ns)
F9
F8
F7
F6
F5
F3
F2
F1

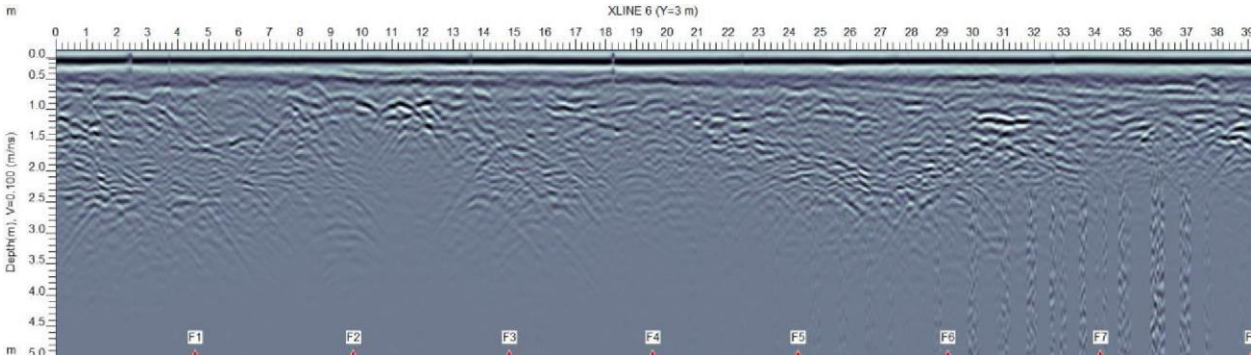
XLINE 6 (Y=3 m)
Depth(m), V=0.100 (m/ns)
F1
F2
F3
F4
F5
F6
F7

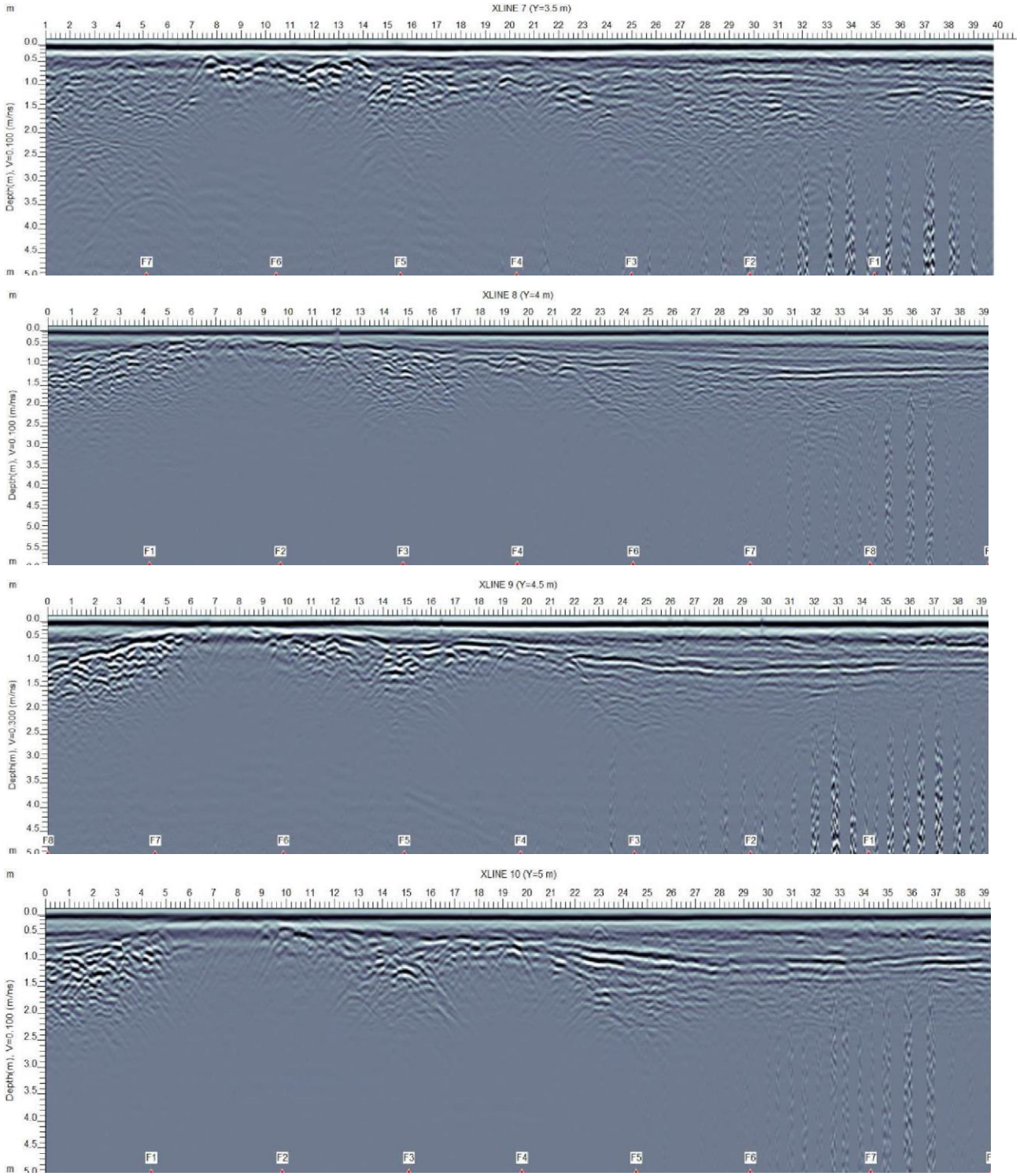
XLINE 7 (Y=3.5 m)
Depth(m), V=0.100 (m/ns)
F7
F6
F5
F4
F3
F2
F1
XLINE 8 (Y=4 m)
Depth(m), V=0.100 (m/ns)
F1
F2
F3
F4
F6
F7
F8
XLINE 9 (Y=4.5 m)
Depth(m), V=0.300 (m/ns)
F8
F7
F6
F5
F4
F3
F2
F1
XLINE 10 (Y=5 m)
Depth(m), V=0.100 (m/ns)
F1
F2
F3
F4
F5
F6
F7

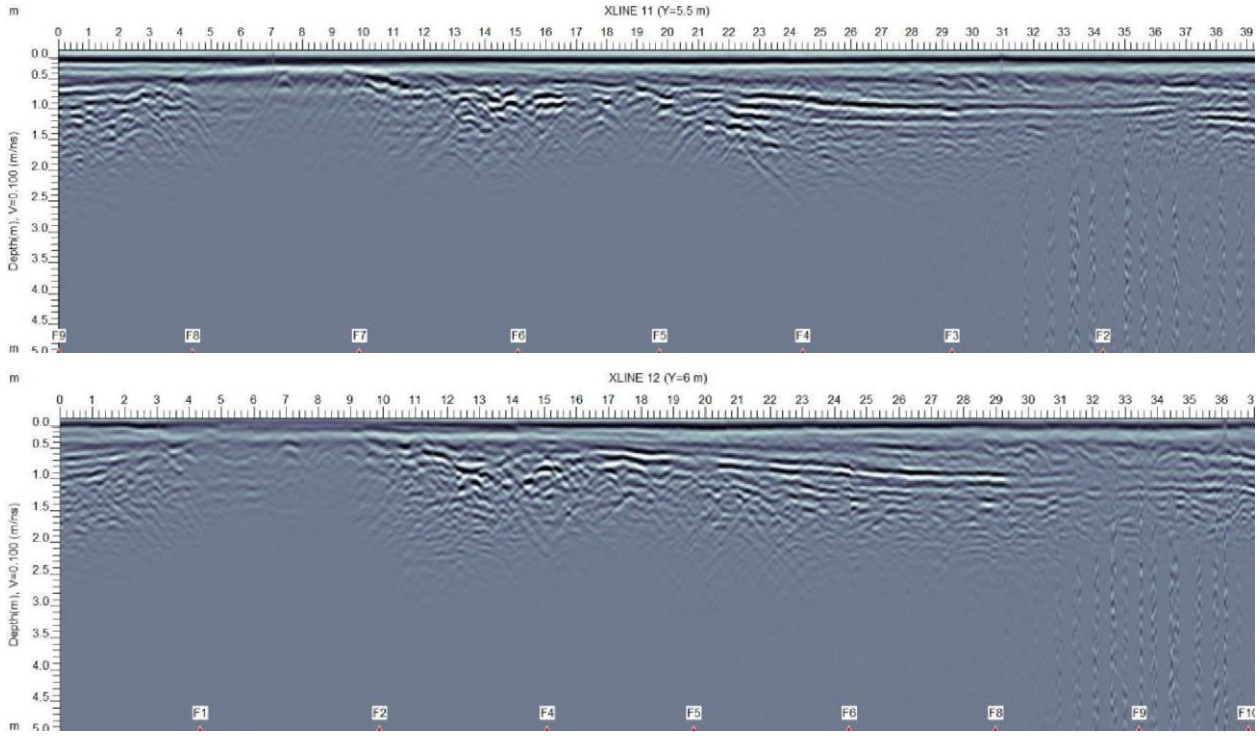

Figure D 2) Depicts the full set of Xline landward distances from the wall, without elevation corrections

Appendix E: The RTK static data for the base locations and the Rover points

RTK of the GPR point at Bread and Cheese site:

Table E 1) Location of the Base of the RTK, during GPR survey at Bread and Cheese site

Station	Easting	Northing	Elevation
Base1	364579.019	5241156.867	9.7633

Table E 2) GPR grid points' location at Bread and Cheese site.

Easting	Northing	Elevation	Y	X	Distance
364535.978	5241171.546	11.264	0	0	0
364539.874	5241170.955	11.1126	0	4	3.94
364543.845	5241170.475	10.9723	0	8	7.94
364547.797	5241169.895	10.8668	0	12	11.93
364551.71	5241169.388	10.749	0	16	15.88
364555.691	5241168.838	10.6483	0	20	19.90
364559.641	5241168.199	10.5218	0	24	23.90
364563.605	5241167.843	10.3973	0	28	27.88
364567.573	5241167.409	10.2788	0	32	31.87
364571.571	5241167.016	10.212	0	36	35.89
364575.518	5241166.698	10.1282	0	40	39.85
364579.549	5241166.317	10.1144	0	44	43.90
364583.515	5241165.923	10.1001	0	48	47.88
364587.501	5241165.61	10.0653	0	52	51.88
364591.394	5241165.15	9.8998	0	56	55.80
364591.443	5241165.115	9.8944	0	56	55.86
364595.46	5241164.809	9.9099	0	60	59.89
364599.411	5241164.392	9.9303	0	64	63.86
364603.378	5241163.94	9.9609	0	68	67.86
364607.37	5241163.644	9.9813	0	72	71.86
364611.338	5241163.146	10.0412	0	76	75.86
364615.29	5241162.862	10.1575	0	80	79.82
364619.279	5241162.537	10.3419	0	84	83.82
364623.222	5241161.932	10.5239	0	88	87.81
364627.172	5241161.553	10.7774	0	92	91.78
364631.205	5241161.257	11.0995	0	96	95.82
364536.184	5241172.986	11.311	1.5	0	0.00
364540.117	5241172.449	11.1317	1.5	4	3.97

364544.068	5241171.963	10.9955	1.5	8	7.95
364548.026	5241171.232	10.8677	1.5	12	11.98
364551.947	5241170.898	10.768	1.5	16	15.91
364555.96	5241170.419	10.6751	1.5	20	19.95
364559.73	5241169.754	10.5902	1.5	24	23.78
364563.72	5241169.591	10.4936	1.5	28	27.77
364567.559	5241169.076	10.4036	1.5	32	31.65
364571.723	5241168.597	10.3123	1.5	36	35.84
364575.657	5241168.239	10.2506	1.5	40	39.79
364579.607	5241167.974	10.2022	1.5	44	43.75
364583.674	5241167.441	10.1563	1.5	48	47.85
364587.616	5241167.182	10.1291	1.5	52	51.80
364591.686	5241166.695	10.0358	1.5	56	55.90
364595.612	5241166.311	10.0082	1.5	60	59.84
364599.543	5241165.913	9.9917	1.5	64	63.79
364603.516	5241165.479	10.0225	1.5	68	67.79
364607.6	5241165.012	10.0757	1.5	72	71.90
364611.532	5241164.654	10.1358	1.5	76	75.85
364615.531	5241164.24	10.2493	1.5	80	79.87
364619.514	5241164.033	10.3722	1.5	84	83.86
364623.403	5241163.407	10.5431	1.5	88	87.80
364627.38	5241163.019	10.7832	1.5	92	91.79
364631.36	5241162.778	11.1014	1.5	96	95.78
364536.427	5241174.47	11.3136	3	0	0.00
364540.39	5241173.931	11.1229	3	4	4.00
364544.376	5241173.441	10.9623	3	8	8.02
364548.294	5241172.679	10.8551	3	12	12.01
364552.218	5241172.369	10.7677	3	16	15.94
364556.171	5241171.894	10.6869	3	20	19.92
364559.779	5241171.182	10.6443	3	24	23.60
364563.89	5241171.101	10.5633	3	28	27.71
364567.687	5241170.555	10.4817	3	32	31.55
364571.803	5241170.088	10.4144	3	36	35.69
364575.87	5241169.747	10.3432	3	40	39.77
364579.66	5241169.457	10.2778	3	44	43.57
364583.801	5241168.957	10.2129	3	48	47.75
364587.87	5241168.663	10.1675	3	52	51.83
364591.899	5241168.16	10.1111	3	56	55.89
364595.804	5241167.808	10.0763	3	60	59.81
364599.71	5241167.4	10.0741	3	64	63.73
364603.775	5241166.938	10.1022	3	68	67.82
364607.871	5241166.525	10.1445	3	72	71.94
364611.745	5241166.138	10.1977	3	76	75.84

364615.737	5241165.741	10.2894	3	80	79.85
364619.547	5241165.529	10.3924	3	84	83.66
364623.629	5241164.92	10.5621	3	88	87.79
364627.589	5241164.48	10.8035	3	92	91.77
364631.502	5241164.272	11.087	3	96	95.69
364536.677	5241175.942	11.2722	4.5	0	0.00
364540.774	5241175.344	11.078	4.5	4	4.14
364544.65	5241174.906	10.8984	4.5	8	8.04
364548.554	5241174.154	10.7992	4.5	12	12.02
364552.413	5241173.862	10.7131	4.5	16	15.89
364556.342	5241173.389	10.6666	4.5	20	19.84
364559.794	5241172.764	10.6227	4.5	24	23.35
364564.077	5241172.567	10.567	4.5	28	27.64
364567.824	5241172.069	10.5166	4.5	32	31.42
364571.963	5241171.613	10.462	4.5	36	35.58
364576.035	5241171.249	10.3832	4.5	40	39.67
364579.736	5241170.965	10.3404	4.5	44	43.38
364583.847	5241170.464	10.2439	4.5	48	47.53
364588.088	5241170.154	10.2037	4.5	52	51.78
364592.147	5241169.652	10.1417	4.5	56	55.87
364595.984	5241169.298	10.0957	4.5	60	59.72
364599.939	5241168.892	10.0796	4.5	64	63.70
364603.992	5241168.425	10.1097	4.5	68	67.78
364608.07	5241167.99	10.1612	4.5	72	71.88
364611.902	5241167.634	10.2333	4.5	76	75.73
364615.996	5241167.263	10.2851	4.5	80	79.84
364619.649	5241167.025	10.353	4.5	84	83.50
364623.882	5241166.373	10.5049	4.5	88	87.78
364627.841	5241165.993	10.7171	4.5	92	91.76
364631.708	5241165.746	11.0035	4.5	96	95.63
364536.864	5241177.432	11.2584	6	0	0.00
364541.075	5241176.841	11.1047	6	4	4.25
364544.957	5241176.394	10.9178	6	8	8.16
364548.776	5241175.613	10.7354	6	12	12.06
364552.598	5241175.316	10.7218	6	16	15.89
364556.619	5241174.852	10.6635	6	20	19.94
364559.86	5241174.197	10.6275	6	24	23.25
364564.303	5241174.011	10.593	6	28	27.69
364568.064	5241173.452	10.541	6	32	31.49
364572.149	5241173.032	10.4876	6	36	35.60
364576.356	5241172.692	10.4384	6	40	39.82
364579.826	5241172.422	10.3633	6	44	43.30
364583.916	5241171.945	10.2943	6	48	47.42

364588.356	5241171.623	10.2205	6	52	51.87
364592.42	5241171.143	10.1664	6	56	55.96
364596.198	5241170.785	10.1115	6	60	59.76
364600.158	5241170.364	10.0142	6	64	63.74
364604.242	5241169.914	10.0981	6	68	67.85
364608.297	5241169.498	10.1513	6	72	71.93
364612.212	5241169.088	10.2085	6	76	75.86
364616.222	5241168.731	10.255	6	80	79.89
364619.77	5241168.492	10.3131	6	84	83.44
364624.106	5241167.856	10.4469	6	88	87.83
364628.081	5241167.462	10.6133	6	92	91.82
364631.891	5241167.225	10.9075	6	96	95.64

RTK of the DCR electrode points in the Bread and Cheese site, 21/03/23:

Table E 3) Base station position in the Bread and Cheese site.

Station	Easting	Northing	Elevation
Base1	364579.422	5241157.026	9.7395

Table E 4) Electrode points position of DCR survey in the south side of the Bread and Cheese site, (Bay ward).

Easting	Northing	Elevation	Electrode	Distance
364548.053	5241169.527	10.8866	1	0
364551.934	5241168.898	10.7688	2	4
364555.789	5241168.419	10.6416	3	8
364559.811	5241167.833	10.493	4	12
364563.772	5241167.421	10.3836	5	16
364567.764	5241167.098	10.3081	6	20
364571.735	5241166.737	10.1962	7	24
364575.702	5241166.476	10.1117	8	28
364579.674	5241165.809	10.1103	9	32
364583.666	5241165.534	10.102	10	36
364587.63	5241165.122	10.062	11	40
364591.562	5241164.799	9.8691	12	44
364595.571	5241164.347	9.878	13	48
364599.536	5241164.002	9.9247	14	52
364603.488	5241163.874	9.936	15	56
364607.484	5241163.432	9.9919	16	60
364611.482	5241163.074	10.0575	17	64
364615.429	5241162.7	10.1929	18	68
364619.427	5241162.332	10.3101	19	72

364623.376	5241161.966	10.5171	20	76
364627.335	5241161.548	10.7586	21	80
364631.308	5241161.142	11.085	22	84
364635.258	5241160.734	11.393	23	88
364639.213	5241160.635	11.8007	24	92

Table E 5) Position of some important points in Bread and Cheese site.

Easting	Northing	Elevation	Description
364654.546	5241159.53	13.5453	end of metal railing, past electrode 24
364639.087	5241159.951	11.8535	about 10cm S of metal railing
364639.127	5241160.118	11.8324	Other side of metal railing (closer to electrodes)
364623.343	5241161.286	10.6054	end of metal railing at gap
364622.011	5241161.424	10.5502	Start of metal railing after gap between stations 127 and 128. ~1.5 m E of wooden electricity pole.
364614.097	5241162.194	10.1951	Road side of railing (photo) Some wood railings perpendicular to metal railing
364606.564	5241162.766	9.9805	In front of DANGER COASTAL EROSION sign
364598.689	5241163.147	9.8835	Near wooden sign with "1" on it.
364593.584	5241164.706	9.8487	Midpoint of array (x=46)
364593.188	5241163.914	9.6976	toward railing (going down, close to scarp edge)
364593.171	5241163.531	9.3021	next to land side railing, surface sloping downward
364593.201	5241163.25	9.1212	end of railing
364587.031	5241164.005	10.0463	end of railing
364567.77	5241166.576	10.3602	end of railing
364548.177	5241168.593	10.9907	end of railing
364545.88	5241169.105	11.0199	end of railing

RTK of the DCR electrode points, Bread and Cheese site, 21/04/22

Table E 6) Base station position in the Bread and Cheese site.

Station	Easting	Northing	Elevation
Base1	364579.019	5241156.867	9.7633

Table E 7) Electrode points position of DCR survey in the North side of the Bread and Cheese site, (house side).

Easting	Northing	Elevation	Electrode	Distance
364547.024	5241176.881	10.7588	1	0
364550.95	5241176.321	10.6987	2	3.97
364554.882	5241175.752	10.7227	3	3.97

364558.768	5241175.208	10.6593	4	3.92
364562.717	5241174.534	10.6401	5	4.01
364566.708	5241174.306	10.5319	6	4.00
364570.692	5241173.606	10.4788	7	4.05
364574.667	5241173.559	10.4526	8	3.98
364578.607	5241173.247	10.3985	9	3.95
364582.649	5241173.111	10.3469	10	4.04
364586.602	5241172.961	10.2207	11	3.96
364590.575	5241172.629	10.0992	12	3.99
364594.637	5241172.1	10.0595	13	4.10
364598.609	5241171.638	10.0441	14	4.00
364602.549	5241171.134	10.0028	15	3.97
364606.556	5241170.793	10.0252	16	4.02
364610.502	5241170.4	10.1625	17	3.97
364614.475	5241170.083	10.172	18	3.99
364618.493	5241170.111	10.2488	19	4.02
364622.75	5241169.143	10.5037	20	4.37
364626.328	5241168.167	10.4749	21	3.71
364630.318	5241167.935	10.7564	22	4.00
364634.379	5241167.862	11.188	23	4.06
364638.121	5241167.283	11.4348	24	3.79

GPR points at the Cliff site on 21/05/06:

Table E 8) GPR grid points at the Cliff site.

Easting	Northing	Elevation	x	Y
363176.321	5241991.533	11.1618	0	0.5
363184.397	5241981.507	12.3685	12.5	0.5
363191.055	5241972.088	13.4753	25	0.5
363198.159	5241960.748	14.4292	37.5	0.5

363204.449	5241950.592	15.1767	50	0.5
363212.059	5241939.184	15.8436	62.5	0.5
363218.839	5241929.949	16.4673	75	0.5
363227.552	5241920.953	16.9042	87.5	0.5
363236.355	5241912.003	17.1462	100	0.5
363245.239	5241903.45	17.1771	112.5	0.5
363254.403	5241894.632	17.2256	125	0.5
363262.521	5241885.463	17.1687	137.5	0.5
363271.324	5241876.499	17.1752	150	0.5
363279.588	5241866.874	17.1686	162.5	0.5
363287.553	5241857.659	17.0759	175	0.5
363178.144	5241993.028	11.2926	0	3
363186.42	5241982.858	12.5025	12.5	3
363193.252	5241973.25	13.5744	25	3
363200.252	5241961.846	14.5079	37.5	3
363206.539	5241952.076	15.167	50	3
363214.006	5241940.784	15.9045	62.5	3
363220.75	5241931.607	16.4773	75	3
363229.437	5241922.613	16.9906	87.5	3
363238.122	5241913.717	17.2536	100	3
363247.028	5241905.162	17.3423	112.5	3
363256.207	5241896.421	17.3423	125	3
363264.358	5241887.093	17.2809	137.5	3
363273.294	5241878.264	17.2272	150	3
363281.415	5241868.684	17.2913	162.5	3
363289.416	5241859.134	17.134	175	3
363289.43	5241859.128	17.137	175	3
363180.04	5241994.751	11.3323	0	5.5
363188.462	5241984.319	12.55	12.5	5.5
363195.465	5241974.244	13.5601	25	5.5
363202.456	5241962.959	14.4735	37.5	5.5
363208.627	5241953.269	15.1146	50	5.5
363216.031	5241942.238	15.8933	62.5	5.5
363222.467	5241933.247	16.4449	75	5.5
363231.247	5241924.29	16.9745	87.5	5.5
363240.057	5241915.297	17.2983	100	5.5
363248.678	5241907.074	17.3903	112.5	5.5
363257.854	5241898.29	17.2842	125	5.5
363266.217	5241888.971	17.2134	137.5	5.5
363275.287	5241879.772	17.159	150	5.5
363283.46	5241870.113	17.2682	162.5	5.5
363291.181	5241860.933	17.2128	175	5.5

GPR grid points in the Cliff site, High Resolution Grids on 21/05/28:

Table E 9) Location of the RTK Base station during GPR Gridding positioning at the Cliff site.

Station	Easting	Northing	Elevation
Base1	363208.943	5241957.844	14.99

Table E 10) GPR grid points at the Cliff site.

Easting	Northing	Elevation	X	Y	Distance
363182.271	5241982.53	11.95	0	0	0
363182.695	5241982.828	12.03	0	0.5	0.52
363183.084	5241983.124	12.06	0	1	0.49
363183.453	5241983.446	12.13	0	1.5	0.49
363183.951	5241983.664	12.18	0	2	0.54
363185.26	5241978.765	12.59	5	0	5.07
363185.694	5241979.012	12.59	5	0.5	0.50
363186.101	5241979.364	12.63	5	1	0.54
363186.488	5241979.648	12.69	5	1.5	0.48
363186.8	5241979.961	12.64	5	2	0.44
363187.213	5241980.236	12.65	5	2.5	0.50
363187.637	5241980.563	12.66	5	3	0.54
363188.073	5241980.825	12.69	5	3.5	0.51
363188.453	5241981.173	12.69	5	4	0.52
363188.844	5241981.428	12.69	5	4.5	0.47
363189.21	5241981.768	12.71	5	5	0.50
363189.67	5241982.072	12.72	5	5.5	0.55
363190.004	5241982.512	12.70	5	6	0.55
363188.194	5241974.687	13.08	10	0	8.03
363188.574	5241974.937	13.12	10	0.5	0.45
363189.038	5241975.199	13.11	10	1	0.53
363189.44	5241975.514	13.14	10	1.5	0.51
363189.406	5241975.529	13.15	10	1.5	0.04
363189.891	5241975.734	13.16	10	2	0.53
363190.293	5241975.993	13.13	10	2.5	0.48
363190.727	5241976.262	13.18	10	3	0.51
363191.13	5241976.513	13.18	10	3.5	0.47
363191.563	5241976.763	13.20	10	4	0.50
363192.009	5241977.029	13.19	10	4.5	0.52
363192.373	5241977.313	13.19	10	5	0.46
363192.792	5241977.576	13.20	10	5.5	0.49
363193.25	5241977.921	13.11	10	6	0.57
363190.941	5241970.395	13.41	15	0	7.87

363191.357	5241970.729	13.50	15	0.5	0.53
363191.818	5241970.968	13.55	15	1	0.52
363192.257	5241971.198	13.57	15	1.5	0.50
363192.671	5241971.462	13.59	15	2	0.49
363193.079	5241971.696	13.58	15	2.5	0.47
363193.526	5241971.985	13.60	15	3	0.53
363193.973	5241972.198	13.60	15	3.5	0.50
363194.404	5241972.466	13.59	15	4	0.51
363194.823	5241972.706	13.61	15	4.5	0.48
363195.261	5241972.925	13.60	15	5	0.49
363195.68	5241973.186	13.61	15	5.5	0.49
363196.102	5241973.426	13.59	15	6	0.49
363193.54	5241966.318	13.82	20	0	7.56
363194.024	5241966.502	13.86	20	0.5	0.52
363194.418	5241966.779	13.88	20	1	0.48
363194.833	5241967.064	13.92	20	1.5	0.50
363195.262	5241967.342	13.94	20	2	0.51
363195.682	5241967.601	13.94	20	2.5	0.49
363196.123	5241967.897	13.94	20	3	0.53
363196.536	5241968.15	13.93	20	3.5	0.48
363196.96	5241968.433	13.97	20	4	0.51
363197.392	5241968.706	13.96	20	4.5	0.51
363197.762	5241968.996	13.94	20	5	0.47
363198.179	5241969.214	13.96	20	5.5	0.47
363198.581	5241969.519	13.96	20	6	0.50
363196.148	5241962.06	14.17	25	0	7.85
363196.603	5241962.283	14.20	25	0.5	0.51
363196.991	5241962.605	14.23	25	1	0.50
363197.377	5241962.914	14.25	25	1.5	0.49
363197.828	5241963.157	14.28	25	2	0.51
363198.239	5241963.445	14.30	25	2.5	0.50
363198.66	5241963.739	14.31	25	3	0.51
363199.04	5241963.995	14.31	25	3.5	0.46
363199.465	5241964.305	14.30	25	4	0.53
363199.871	5241964.585	14.29	25	4.5	0.49
363200.294	5241964.876	14.28	25	5	0.51
363200.694	5241965.162	14.26	25	5.5	0.49
363201.125	5241965.46	14.27	25	6	0.52
363198.892	5241957.906	14.56	30	0	7.88
363199.266	5241958.175	14.58	30	0.5	0.46
363199.729	5241958.446	14.58	30	1	0.54
363200.137	5241958.722	14.60	30	1.5	0.49
363200.536	5241959.059	14.63	30	2	0.52

363200.966	5241959.416	14.62	30	2.5	0.56
363201.402	5241959.605	14.61	30	3	0.48
363201.795	5241959.867	14.59	30	3.5	0.47
363202.231	5241960.189	14.59	30	4	0.54
363202.638	5241960.417	14.58	30	4.5	0.47
363203.056	5241960.765	14.56	30	5	0.54
363203.452	5241961.013	14.56	30	5.5	0.47
363203.82	5241961.283	14.57	30	6	0.46
363201.587	5241953.731	14.86	35	0	7.88
363202.033	5241953.976	14.90	35	0.5	0.51
363202.469	5241954.265	14.88	35	1	0.52
363202.824	5241954.578	14.88	35	1.5	0.47
363203.296	5241954.807	14.90	35	2	0.52
363203.703	5241955.061	14.87	35	2.5	0.48
363204.109	5241955.436	14.88	35	3	0.55
363204.53	5241955.623	14.86	35	3.5	0.46
363204.952	5241955.947	14.86	35	4	0.53
363205.386	5241956.224	14.84	35	4.5	0.51
363205.793	5241956.465	14.85	35	5	0.47
363206.18	5241956.755	14.84	35	5.5	0.48
363206.594	5241957.046	14.83	35	6	0.51
363204.28	5241949.551	15.20	40	0	7.84
363204.724	5241949.777	15.19	40	0.5	0.50
363205.135	5241950.057	15.20	40	1	0.50
363205.59	5241950.292	15.20	40	1.5	0.51
363206.015	5241950.573	15.19	40	2	0.51
363206.441	5241950.846	15.19	40	2.5	0.51
363206.887	5241951.1	15.18	40	3	0.51
363207.211	5241951.407	15.18	40	3.5	0.45
363207.714	5241951.641	15.18	40	4	0.55
363208.113	5241951.905	15.16	40	4.5	0.48
363208.557	5241952.175	15.13	40	5	0.52
363208.923	5241952.506	15.12	40	5.5	0.49
363209.362	5241952.797	15.07	40	6	0.53

Table E 11) GPR grid points at the Cliff site.

Easting	Northing	Elevation	X	Y
363176.321	5241991.533	11.1618	0	0.5
363184.397	5241981.507	12.3685	12.5	0.5
363191.055	5241972.088	13.4753	25	0.5
363198.159	5241960.748	14.4292	37.5	0.5

363204.449	5241950.592	15.1767	50	0.5
363212.059	5241939.184	15.8436	62.5	0.5
363218.839	5241929.949	16.4673	75	0.5
363227.552	5241920.953	16.9042	87.5	0.5
363236.355	5241912.003	17.1462	100	0.5
363245.239	5241903.45	17.1771	112.5	0.5
363254.403	5241894.632	17.2256	125	0.5
363262.521	5241885.463	17.1687	137.5	0.5
363271.324	5241876.499	17.1752	150	0.5
363279.588	5241866.874	17.1686	162.5	0.5
363287.553	5241857.659	17.0759	175	0.5
363178.144	5241993.028	11.2926	0	3
363186.42	5241982.858	12.5025	12.5	3
363193.252	5241973.25	13.5744	25	3
363200.252	5241961.846	14.5079	37.5	3
363206.539	5241952.076	15.167	50	3
363214.006	5241940.784	15.9045	62.5	3
363220.75	5241931.607	16.4773	75	3
363229.437	5241922.613	16.9906	87.5	3
363238.122	5241913.717	17.2536	100	3
363247.028	5241905.162	17.3423	112.5	3
363256.207	5241896.421	17.3423	125	3
363264.358	5241887.093	17.2809	137.5	3
363273.294	5241878.264	17.2272	150	3
363281.415	5241868.684	17.2913	162.5	3
363289.416	5241859.134	17.134	175	3
363289.43	5241859.128	17.137	175	3
363180.04	5241994.751	11.3323	0	5.5
363188.462	5241984.319	12.55	12.5	5.5
363195.465	5241974.244	13.5601	25	5.5
363202.456	5241962.959	14.4735	37.5	5.5
363208.627	5241953.269	15.1146	50	5.5
363216.031	5241942.238	15.8933	62.5	5.5
363222.467	5241933.247	16.4449	75	5.5
363231.247	5241924.29	16.9745	87.5	5.5
363240.057	5241915.297	17.2983	100	5.5
363248.678	5241907.074	17.3903	112.5	5.5
363257.854	5241898.29	17.2842	125	5.5
363266.217	5241888.971	17.2134	137.5	5.5
363275.287	5241879.772	17.159	150	5.5
363283.46	5241870.113	17.2682	162.5	5.5
363291.181	5241860.933	17.2128	175	5.5

RTK of the DCR survey, electrode points, Cliff site on 21/04/26

Table E 12) Location of the Base of the RTK, during DCR survey at the Cliff site.

Station	Easting	Northing	Elevation
Base1	363208.943	5241957.844	14.989

Table E 13) Electrode points position of DCR survey in the North side of the Cliff site, (house side).

Easting	Northing	Elevation	Electrode
363181.043	5241995.509	11.3025	1
363183.716	5241992.703	11.5964	2
363186.267	5241989.666	11.9269	3
363188.758	5241986.565	12.3467	4
363191	5241983.3	12.7231	5
363193.122	5241979.931	13.0369	6
363195.41	5241976.685	13.3868	7
363197.713	5241973.438	13.7581	8
363199.834	5241970.046	13.9977	9
363202.03	5241966.735	14.2903	10
363204.343	5241963.563	14.6204	11
363206.629	5241960.244	14.7883	12
363208.695	5241956.8	14.9716	13
363208.699	5241956.819	14.9588	13
363210.558	5241953.294	15.224	14
363212.844	5241950.081	15.4514	15
363215.132	5241946.781	15.652	16
363217.302	5241943.435	15.9047	17
363219.268	5241939.872	16.0645	18
363221.727	5241936.823	16.2974	19
363224.216	5241933.64	16.4714	20
363226.821	5241930.657	16.6406	21
363226.815	5241930.649	16.6424	21
363229.766	5241927.937	16.8913	22
363232.423	5241925.054	17.1236	23
363235.4	5241922.326	17.191	24
363238.467	5241919.92	17.2449	25
363241.457	5241917.285	17.339	26
363244.272	5241914.514	17.3655	27
363247.062	5241911.615	17.4366	28
363249.625	5241908.554	17.3637	29
363252.459	5241905.657	17.3733	30

363255.369	5241902.945	17.4101	31
363258.146	5241900.064	17.3499	32
363261.014	5241897.259	17.3487	33
363263.624	5241894.28	17.2695	34
363266.451	5241891.409	17.2628	35
363269.174	5241888.519	17.2177	36

Table E 14) Location of some important point at Cliff site.

Easting	Northing	Elevation	Description
363241.124	5241905.573	17.0046	transition from wood to metal bracing location
363244.887	5241901.796	17.0805	culvert 3
363251.617	5241906.287	17.3633	other side of road from culvert, water in ditch, rock gouge
363250.022	5241905.051	17.3652	start of fracture crossing road
363248.571	5241904.019	17.3449	West end of fracture in centre of road
363256.031	5241896.601	17.3455	East end of main fracture in centre of road
363250.574	5241907.92	17.3498	cement end of culvert 3

GPR grid points in Quays site on 21/05/13:

Table E 15) RTK base setup in bus turnaround near NE end of grid, Quays site.

Station	Easting	Northing	Elevation
Base1	363463.275	5240486.164	17.2761

Table E 16) GPR grid points at the Quays site.

Easting	Northing	Elevation	x	y	Distance
363452.52	5240476.606	17.2068	0	0	0
363449.622	5240479.287	17.0142	4	0	3.95
363446.819	5240482.087	16.7678	8	0	7.91
363443.809	5240484.811	16.6217	12	0	11.97
363440.934	5240487.707	16.2455	16	0	16.05
363438.282	5240490.582	15.9685	20	0	19.96
363435.801	5240493.684	15.6989	24	0	23.93
363433.179	5240496.653	15.5057	28	0	27.89
363430.575	5240499.654	15.4039	32	0	31.87
363427.89	5240502.63	15.3697	36	0	35.88
363425.278	5240505.644	15.3299	40	0	39.86
363422.451	5240508.449	15.3417	44	0	43.85
363419.658	5240511.354	15.316	48	0	47.88

363416.888	5240514.204	15.3048	52	0	51.85
363414.071	5240517.049	15.2277	56	0	55.85
363411.296	5240519.923	15.1063	60	0	59.85
363408.354	5240522.627	14.9625	64	0	63.85
363405.476	5240525.417	14.8137	68	0	67.85
363402.495	5240528.065	14.6923	72	0	71.84
363399.522	5240530.716	14.5783	76	0	75.82
363396.518	5240533.4	14.5084	80	0	79.85
363393.344	5240535.978	14.477	84	0	83.94
363390.294	5240538.65	14.4256	88	0	88.00
363387.325	5240541.13	14.3689	92	0	91.87
363384.36	5240543.693	14.3278	96	0	95.78
363381.247	5240546.427	14.2916	100	0	99.93
363378.272	5240548.992	14.2451	104	0	103.86
363375.219	5240551.547	14.1902	108	0	107.84
363372.116	5240554.117	14.1226	112	0	111.87
363369.044	5240556.715	14.0784	116	0	115.89
363365.979	5240559.228	14.0446	120	0	119.85
363362.872	5240561.729	14.0229	124	0	123.84
363359.782	5240564.269	14.0366	128	0	127.84
363356.606	5240566.696	14.0121	132	0	131.84
363353.448	5240569.096	14.0091	136	0	135.81
363350.066	5240571.275	14.0258	140	0	139.83
363346.759	5240573.576	13.9973	144	0	143.86
363343.487	5240575.835	13.9619	148	0	147.83
363451.532	5240475.463	17.2844	0	1.5	0.00
363448.631	5240478.22	17.0554	4	1.5	4.00
363445.692	5240481.034	16.8295	8	1.5	8.07
363442.783	5240483.766	16.6005	12	1.5	12.06
363439.903	5240486.654	16.3304	16	1.5	16.14
363437.15	5240489.638	16.0589	20	1.5	20.20
363434.711	5240492.631	15.7925	24	1.5	24.06
363431.947	5240495.695	15.6051	28	1.5	28.19
363429.454	5240498.653	15.4933	32	1.5	32.06
363426.742	5240501.719	15.4001	36	1.5	36.15
363424.193	5240504.644	15.3327	40	1.5	40.03
363421.297	5240507.413	15.34	44	1.5	44.04
363418.509	5240510.352	15.3115	48	1.5	48.09
363415.772	5240513.142	15.3067	52	1.5	52.00
363413.049	5240515.964	15.2228	56	1.5	55.92
363410.21	5240518.888	15.1216	60	1.5	59.99
363407.28	5240521.582	14.9826	64	1.5	63.97

363404.572	5240524.279	14.8586	68	1.5	67.79
363401.464	5240527.009	14.7434	72	1.5	71.93
363398.485	5240529.632	14.653	76	1.5	75.90
363395.51	5240532.36	14.5683	80	1.5	79.94
363392.242	5240534.922	14.5237	84	1.5	84.09
363389.347	5240537.544	14.4849	88	1.5	88.00
363386.385	5240539.982	14.4456	92	1.5	91.83
363383.278	5240542.698	14.3972	96	1.5	95.96
363380.298	5240545.246	14.3569	100	1.5	99.88
363377.298	5240547.872	14.3094	104	1.5	103.87
363374.191	5240550.482	14.2459	108	1.5	107.92
363371.149	5240552.997	14.2004	112	1.5	111.87
363368.058	5240555.523	14.1489	116	1.5	115.86
363364.95	5240558.112	14.1092	120	1.5	119.91
363361.909	5240560.6	14.0906	124	1.5	123.84
363358.866	5240563.113	14.0951	128	1.5	127.78
363355.633	5240565.538	14.0767	132	1.5	131.83
363352.543	5240567.874	14.0595	136	1.5	135.70
363349.172	5240570.088	14.0655	140	1.5	139.73
363345.896	5240572.327	14.0499	144	1.5	143.70
363342.63	5240574.611	14.0008	148	1.5	147.69
363450.484	5240474.389	17.2793	0	3	0.00
363447.541	5240477.177	17.0674	4	3	4.05
363444.581	5240479.978	16.8759	8	3	8.13
363441.683	5240482.731	16.6256	12	3	12.13
363438.793	5240485.58	16.3643	16	3	16.18
363435.964	5240488.702	16.0811	20	3	20.40
363433.533	5240491.7	15.8582	24	3	24.26
363430.876	5240494.664	15.6519	28	3	28.24
363428.326	5240497.632	15.5303	32	3	32.15
363425.607	5240500.685	15.4326	36	3	36.24
363423.097	5240503.622	15.3693	40	3	40.10
363420.205	5240506.42	15.3636	44	3	44.13
363417.441	5240509.332	15.3167	48	3	48.14
363414.723	5240512.078	15.2886	52	3	52.01
363412.004	5240514.894	15.2022	56	3	55.92
363409.211	5240517.678	15.1145	60	3	59.86
363406.262	5240520.48	15.0192	64	3	63.93
363403.686	5240523.032	14.9177	68	3	67.56
363400.46	5240525.851	14.8101	72	3	71.84
363397.485	5240528.518	14.7246	76	3	75.84
363394.563	5240531.149	14.6423	80	3	79.77

363391.244	5240533.809	14.5822	84	3	84.02
363388.358	5240536.399	14.5409	88	3	87.90
363385.421	5240538.83	14.5169	92	3	91.71
363382.188	5240541.669	14.4685	96	3	96.01
363379.366	5240544.056	14.4272	100	3	99.71
363376.294	5240546.748	14.3639	104	3	103.80
363373.145	5240549.355	14.3107	108	3	107.88
363370.133	5240551.849	14.2525	112	3	111.79
363367.18	5240554.32	14.1964	116	3	115.64
363363.962	5240556.958	14.1431	120	3	119.81
363360.898	5240559.476	14.1224	124	3	123.77
363357.963	5240561.887	14.1099	128	3	127.57
363354.681	5240564.371	14.1091	132	3	131.69
363351.724	5240566.616	14.0906	136	3	135.40
363348.307	5240568.82	14.0805	140	3	139.46
363345.002	5240571.098	14.054	144	3	143.48
363341.857	5240573.334	14.0265	148	3	147.34
363449.377	5240473.357	17.2578	0	4.5	0.00
363446.443	5240476.118	17.0786	4	4.5	4.03
363443.419	5240479.027	16.8782	8	4.5	8.22
363440.608	5240481.697	16.6406	12	4.5	12.10
363437.73	5240484.552	16.3859	16	4.5	16.16
363434.79	5240487.798	16.0684	20	4.5	20.54
363432.354	5240490.742	15.8687	24	4.5	24.36
363429.748	5240493.658	15.6815	28	4.5	28.27
363427.211	5240496.637	15.5413	32	4.5	32.18
363424.5	5240499.705	15.4188	36	4.5	36.27
363421.963	5240502.615	15.3678	40	4.5	40.13
363419.037	5240505.447	15.3738	44	4.5	44.21
363416.321	5240508.286	15.3124	48	4.5	48.14
363413.695	5240510.954	15.2668	52	4.5	51.88
363410.919	5240513.857	15.1796	56	4.5	55.90
363408.109	5240516.732	15.0896	60	4.5	59.92
363405.221	5240519.437	15.0068	64	4.5	63.87
363402.693	5240521.919	14.9314	68	4.5	67.42
363399.463	5240524.709	14.8309	72	4.5	71.68
363396.44	5240527.406	14.7623	76	4.5	75.74
363393.488	5240530.077	14.6752	80	4.5	79.72
363390.173	5240532.782	14.6111	84	4.5	83.99
363387.363	5240535.261	14.5695	88	4.5	87.74
363384.427	5240537.712	14.5293	92	4.5	91.57
363381.09	5240540.622	14.462	96	4.5	95.99

363378.424	5240542.885	14.414	100	4.5	99.49
363375.293	5240545.627	14.3574	104	4.5	103.65
363372.074	5240548.338	14.3021	108	4.5	107.86
363369.111	5240550.758	14.2506	112	4.5	111.69
363366.249	5240553.163	14.1893	116	4.5	115.43
363362.962	5240555.87	14.1467	120	4.5	119.68
363359.962	5240558.295	14.1259	124	4.5	123.54
363357.031	5240560.722	14.1	128	4.5	127.35
363353.742	5240563.198	14.1032	132	4.5	131.46
363350.882	5240565.385	14.0884	136	4.5	135.06
363347.429	5240567.633	14.0685	140	4.5	139.18
363344.116	5240569.887	14.018	144	4.5	143.19
363341.001	5240572.094	14.007	148	4.5	147.01

Table E 17) Location of some important measured points at the Quays site.

Easting	Northing	Elevation	Description
363421.564	5240500.217	15.4405	culvert 1
363429.526	5240505.775	14.998	culvert 1 (approx other end)
363401.782	5240530.286	14.4994	E end of double guard railing over inlet, just inside railing
363393.357	5240537.709	14.3531	just inside railing, narrowest verge on seaward side, photo taken looking down
363390.462	5240540.411	14.2742	approx location where W side of inlet meets the road
363387.332	5240543.131	14.2026	W end of double railing over inlet
363382.242	5240547.555	14.1087	100 m' mark for grid, on railing
363373.314	5240555.422	13.9813	mark on railing, some feature seen in GPR
363373.361	5240555.418	13.9788	mark on railing, some feature seen in GPR
			Beyond W end of grid
363342.409	5240578.556	13.7926	W end of metal guard railing
363331.272	5240582.668	13.587	mark on road, some feature seen in GPR
363320.767	5240586.061	13.4445	mark on road, some feature seen in GPR
363319.455	5240580.234	13.3979	culvert 2 (plastic) on SW (house) side of road
363307.538	5240587.746	13.5414	middle of road where pavement changes (newer pavement to SE)
363293.5	5240593.688	13.5451	middle of road
363282.659	5240600.886	13.602	middle of road, over a crack in the tarmac crossing the road
363274.041	5240607.509	13.7963	middle of road, over a crack in the tarmac crossing the road
363265.921	5240614.794	14.1061	middle of road, end of GPR LINE01

363327.578	5240588.741	13.074	over culvert 2, on NE (ocean) side of road
363329.103	5240590.056	12.8993	over culvert 2, on NE (ocean) side of road
363330.153	5240590.615	12.5421	over culvert 2, on NE (ocean) side of road
363330.4	5240590.838	12.333	over culvert 2, on NE (ocean) side of road

RTK of the DCR survey at the house side of the road, starting in the NE:

Table E 18) RTK base setup in bus turnaround near NE end of grid, during the DCR survey.

Station	Easting	Northing	Elevation
Base1	363463.275	5240486.164	17.2761

Table E 19) Electrodes position of the DCR survey line in house side of the road, starting in the NE.

Easting	Northing	Elevation	Electrode	x	Distance
363448.797	5240472.311	17.2442	1	0	0
363445.803	5240474.954	17.0583	2	4	3.99
363442.93	5240477.668	16.8444	3	8	7.95
363440.012	5240480.34	16.6574	4	12	11.90
363437.267	5240483.351	16.4196	5	16	15.98
363434.605	5240486.298	16.1258	6	20	19.95
363432.027	5240489.286	15.9251	7	24	23.89
363429.38	5240492.334	15.6982	8	28	27.93
363426.796	5240495.336	15.5619	9	32	31.89
363424.154	5240498.397	15.4122	10	36	35.94
363421.56	5240501.342	15.3757	11	40	39.86
363418.853	5240504.272	15.3605	12	44	43.85
363416.192	5240507.266	15.2939	13	48	47.86
363413.281	5240510.033	15.2583	14	52	51.87
363410.251	5240512.642	15.1297	15	56	55.87
363407.32	5240515.257	15.0436	16	60	59.80
363404.234	5240517.85	15.0016	17	64	63.83
363401.23	5240520.502	14.9561	18	68	67.84
363398.084	5240522.843	14.8874	19	72	71.76
363394.799	5240525.166	14.7834	20	76	75.78
363391.72	5240527.728	14.8148	21	80	79.79
363388.678	5240530.284	14.7699	22	84	83.76
363385.625	5240532.809	14.7278	23	88	87.72
363382.493	5240535.386	14.6884	24	92	91.78
363379.475	5240538.103	14.683	25	96	95.84
363376.529	5240540.649	14.5884	26	100	99.73

363373.443	5240543.398	14.5225	27	104	103.86
363370.595	5240545.914	14.455	28	108	107.66
363367.696	5240548.75	14.2761	29	112	111.72
363364.549	5240551.344	14.2633	30	116	115.80
363361.56	5240554.017	14.1752	31	120	119.81
363358.65	5240556.65	14.1908	32	124	123.73
363355.556	5240559.315	14.1114	33	128	127.82
363352.091	5240561.218	14.1837	34	132	131.77
363349.014	5240563.712	14.1321	35	136	135.73
363349.099	5240563.779	14.1288	35	136	135.84
363345.679	5240565.93	14.0429	36	140	139.88

Table E 20) Location of some of the important measured point during DCR survey, Quays site.

Easting	Northing	Elevation	Description
363433.647	5240485.494	16.1048	edge of ditch next to electrode 5
363432.721	5240484.692	15.3764	middle of ditch
363421.693	5240500.182	15.3759	edge of ditch over culvert 1
363426.167	5240506.393	15.2297	mark on railing
363417.926	5240503.623	15.2973	start of embankment (~2m high) west of ditch (ends at culvert 1)
363393.932	5240526.169	14.7551	start of curb on road, east end of embankment
363393.158	5240537.828	14.3172	at narrow edge over inlet
363387.224	5240543.103	14.2232	west end of double railing
363387.918	5240528.837	14.853	east end of cleared land with fill